

Spectroscopic and Computational Techniques for the Analysis of Photochemically Driven Reactions

A thesis submitted in partial fulfilment of the requirements for the award of

Doctor of Philosophy

September 2019

By

Thomas Matthew Stonelake

STATEMENT 1

This thesis is being submitted in partial fulfilment of the requirements for the degree of PhD

Signed _____ Date _____

STATEMENT 2

This work has not been submitted in substance for any other degree or award at this or any other university or place of learning, nor is it being submitted concurrently for any other degree or award (outside of any formal collaboration agreement between the University and a partner organisation)

Signed _____ Date _____

STATEMENT 3

I hereby give consent for my thesis, if accepted, to be available in the University's Open Access repository (or, where approved, to be available in the University's library and for inter-library loan), and for the title and summary to be made available to outside organisations, subject to the expiry of a University-approved bar on access if applicable.

Signed _____ Date _____

DECLARATION

This thesis is the result of my own independent work, except where otherwise stated, and the views expressed are my own. Other sources are acknowledged by explicit references. The thesis has not been edited by a third party beyond what is permitted by Cardiff University's Use of Third Party Editors by Research Degree Students Procedure.

Signed _____ Date _____

WORD COUNT _____

(Excluding summary, acknowledgements, declarations, contents pages, appendices, tables, diagrams and figures, references, bibliography, footnotes and endnotes)

Acknowledgements

My sincerest and deepest thanks to Dr. Joseph Beames, for his advice and assistance throughout this project. I couldn't hope for a better supervisor.

I'd like to thank my parents, Peter and Julie, for supporting me throughout this degree. Without their support and guidance, I would never have gotten this far. I'd like to thank my sister, Emily, for supporting me and for giving me lifts to and from the train station, I promised her I'd put her in my acknowledgments. I want to thank Anisha for being there with me at every step of the way through this.

I would like to thank the Engineering and Physical Sciences Research Council (EPSRC) for funding my degree program.

Additionally, I would like to thank the Pope group at Cardiff University for supplying the iridium complexes discussed in this work, and the Fallis group for supplying the tetrazolium compounds.

Preface

Chapter 3 consists of my contributions to work that has been published previously in the paper 'Ligand-Tuneable, Red-Emitting Iridium (III) Complexes for Efficient Triplet-Triplet Annihilation Upconversion Performance' by Phillips et al, published in Chemistry, a European Journal, DOI: 10.1002/chem.201801007 .

Chapter 4, Section 4.6 and all subsections therein contain my contributions to work that has been published previously in the paper 'Dual visible/NIR emission from organometallic iridium (III) complexes' by Phillips et al, published in the Journal of Organometallic Chemistry, DOI: 10.1016/j.jorganchem.2019.04.019

It is anticipated that this work will form the basis of at least two further publications, one consisting of data from and text contained in Chapter 4, Sections 1-5, and the

second consisting of the data and text contained in Chapter 5. Both papers are in preparation.

Table of Contents

Acknowledgements	iv
Preface	iv
List of Figures	x
List of Tables	xiv
List of Equations	xv
Abstract	1
1. Introduction and Background	3
1.1 Background	3
1.2 Transient/Flash Photolysis Spectroscopy	9
1.3 Computational Background	26
1.4 Aims and objectives	30
1.4.1 Ir ^{III} Complexes.....	30
1.4.2 Triphenyltetrazolium compounds.....	30
1.4.3 Cavity Ringdown Spectrometer.....	31
1.5 Summary	31
2. Experimental	34
2.1 Transient/Flash Photolysis Spectrometer	34
2.1.1 Transient Absorption Spectra.....	36
2.1.2 Transient Kinetics.....	37
2.2 Computational	39
2.2.1 Iridium Complexes.....	39
2.2.2 Tetrazolium and Formazans.....	41
2.3 Sample Preparation	41
2.3.1 Iridium Complexes.....	41
2.3.2 Tetrazolium and Formazan.....	42
3. Transient Spectroscopic and Computational Analysis of Red-Emitting Iridium (III) Quinoxaline Complexes	45
3.1 Introduction to Iridium Complexes	45
3.2 Complex Structures	53
3.3 Steady State Absorption Spectra	56
3.3.1 Steady State UV-Vis Absorption.....	56
3.3.2 Simulation of Singlet-to-Singlet Transitions and Orbital Analysis.....	57
3.3.3 Simulation of Spin-forbidden Absorption.....	63
3.3.4 Simulation of Steady State Absorption Spectrum.....	64
3.4 Emission Spectra	65
3.5 Transient Absorption Spectra	67

3.5.1 Transient Absorption Spectra	67
3.5.2 Simulation of Triplet-to-Triplet Absorption	70
3.6 Transient Kinetics	71
3.7 Conclusion	73
4. Effect of Ligand Structure on the Spectroscopic Properties of Iridium (III) Complexes	76
4.1 Ligand Variations	76
4.1.1 Ancillary Ligand Variation	76
4.1.2 Cyclometallating Ligand Variation	77
4.2 Steady State Absorption Spectra	80
4.2.1 Picolinate-Based Complexes	80
4.2.1.1 Steady State UV-Vis Absorption	80
4.2.1.2 Simulation of Singlet-to-Singlet Transitions and Orbital Analysis	82
4.2.1.3 Simulation of Steady State Spectrum	85
4.2.2 Pyrazinate-Based Complexes	88
4.2.2.1 Steady State UV-Vis Absorption	88
4.2.2.2 Simulation of Singlet-to-Singlet Transitions and Orbital Analysis	90
4.2.2.3 Simulation of Steady State Spectrum	92
4.2.3 Diquinoxaline-Pyridine Complexes	95
4.2.3.1 Steady State UV-Vis Absorption	95
4.2.3.2 Simulation of Singlet-to-Singlet Transitions and Orbital Analysis	97
4.2.3.3 Simulation of Steady State Spectrum	101
4.3 Emission Spectra	103
4.3.1 Picolinate-Based Complexes	103
4.3.2 Pyrazinate-Based Complexes	105
4.3.3 Diquinoxaline-Pyridine Complexes	106
4.4 Transient Absorption Spectra	109
4.4.1 Picolinate-Based Complexes	109
4.4.1.1 Transient Absorption Spectra	109
4.4.1.2 Simulation of Triplet-to-Triplet Absorption	113
4.4.2 Pyrazinate-Based Complexes	114
4.4.2.1 Transient Absorption Spectra	114
4.4.2.2 Simulation of Triplet-to-Triplet Absorption	116
4.4.3 Diquinoxaline-Pyridine Complexes	117
4.4.3.1 Transient Absorption Spectra	117
4.5 Transient Kinetic Measurements	118
4.5.1 Picolinate-Based Complexes	118
4.5.2 Pyrazinate-Based Complexes	121
4.5.3 Diquinoxaline-Pyridine Complexes	122
4.6. DFT Analysis of Benzoquinoxaline Ir (III) Complexes	123
4.6.1 Molecular Orbital Decomposition	124
4.6.2 Simulation of Spectroscopic Features	126
4.6.2.1 Simulation of Complex Features	126
4.6.2.2 Simulation of Ligand Emission	129
4.7 Discussion of Ligand Effects	130
4.7.1 Comparison of Bipyridine, Picolinate and Pyrazinate Effects in Quinoxaline Complexes	130
4.7.2 Effect of Extended Conjugation on Quinoxaline Ligand	133
4.7.3 Speculative Prediction of Complex Properties	133
4.8 Conclusion	133

5. Inhibiting the Photoreductive Pathway of 2,3,5-Triphenyltetrazolium via Selective Substitution	137
5.1 Introduction and Background	137
5.2 Compound Structures	140
5.3 Steady State UV-Vis Absorption Spectra	141
5.3.1 Triphenyltetrazolium (TTP)	141
5.3.1.1 Steady State UV-Vis Absorption	141
5.3.1.2 Molecular Orbital Decomposition Analysis	142
5.3.1.3 Simulation of Excited States	144
5.3.1.4 Triphenylformazan (TPF)	145
5.3.2 3,5-diF Triphenyltetrazolium (3,5-diF TTP)	146
5.3.2.1 Steady State UV-Vis Absorption	146
5.3.2.2 Molecular Orbital Decomposition Analysis	146
5.3.2.3 Simulation of Excited States	148
5.3.3 2,6-diF Triphenyltetrazolium (2,6-diF TTP)	149
5.3.3.1 Steady State UV-Vis Absorption	149
5.3.3.2 Molecular Orbital Decomposition Analysis	150
5.3.3.3 Simulation of Excited States	151
5.3.4 2,6-diMethyl, 4-Methyl, 4-Tert-butyl Triphenyltetrazolium (2,6-diMe TTP)	152
5.3.4.1 Steady State UV-Vis Absorption	152
5.3.4.2 Molecular Orbital Decomposition	153
5.3.4.3 Simulation of Excited States	154
5.4. Flash Photolysis Study	155
5.4.1 Triphenyltetrazolium (TTP)	155
5.4.2 3,5-diF Triphenyltetrazolium (3,5-diF TTP)	164
5.4.3 2,6-diF Triphenyltetrazolium (2,6-diF TTP)	167
5.4.4 2,6-diMethyl, 4-Methyl, 4-Tert-butyl Triphenyltetrazolium (2,6-diMe TTP)	170
5.5 Emission Spectra	171
5.5.1 Triphenyltetrazolium (TTP)	171
5.5.2 3,5-diF Triphenyltetrazolium (3,5-diF TTP)	173
5.5.3 2,6-diF Triphenyltetrazolium (2,6-diF TTP)	176
5.5.4 2,6-diMethyl, 4-Methyl, 4-Tert-butyl Triphenyltetrazolium (2,6-diMe TTP)	179
5.6 Transient Kinetic Study	181
5.6.1 Triphenyltetrazolium (TTP)	182
5.6.2 2,6-diF Triphenyltetrazolium (2,6-diF TTP)	184
5.7 Mass Spectrometry	186
5.7.1 Triphenyltetrazolium (TTP)	187
5.7.1.1 Oxidised Photocoupled Product	192
5.7.2 2,6-diF Triphenyltetrazolium (2,6-diF TTP)	193
5.8 Conclusion	195
6. Design and Development of a mid-IR Cavity Ringdown Spectrometer	197
6.1. Introduction and Background	197
6.1.1 Cavity Ringdown Spectroscopy	197
6.1.2 Herriott Cell	200
6.1.3 Criegee Intermediates	201
6.2. Design and Components	203
6.2.1 Main Cavity	203
6.2.2 Re-injection Cavity	206
6.2.3 Alignment of Cavity	207

6.3	Conclusion and Future Work	210
	Summary and Perspective	212
	Iridium (III) Complexes	212
	Triphenyltetrazolium Compounds	215
	Development of a Cavity Ringdown Infrared Spectrometer	217
	Appendices	220
	Effect of Ligand Structure on the Spectroscopic Properties of Iridium (III) Complexes	220
	Picolinate Complexes	220
	Ir(L2) ₂ (pico).....	220
	Ir(L3) ₂ (pico).....	223
	Ir(L4) ₂ (pico).....	226
	Ir(L5) ₂ (pico).....	229
	Ir(L6) ₂ (pico).....	232
	Ir(L7) ₂ (pico).....	235
	Pyrazinate Complexes	238
	Ir(L5) ₂ (pyra)	238
	Ir(L7) ₂ (pyra)	241
	Benzoquinoxaline Complexes	244
	Ir(L9) ₂ (bpy)	244
	Ir(L10) ₂ (bpy)	245
	Ir(L11) ₂ (bpy)	247
	Di-quinoxaline-Pyridinyl Complexes.....	249
	[Ir(L13) ₂]PF ₆	249
	Inhibiting the Photoreductive Pathway of 2,3,5-Triphenyltetrazolium via Selective Substitution.....	251
	Bibliography.....	252

List of Figures

Figure 1 Electromagnetic spectrum and its approximate domain of atomic and molecular interactions.	3
Figure 2 Chemical equations for the two photolytic dissociation processes of ozone in the troposphere and the reaction of singlet oxygen with water vapour to form hydroxyl radicals. Superscript refers to spin state.	7
Figure 3 Diagram illustrating spin-allowed absorption and emission, using model singlet ground and excited state potential energy surfaces. The lengths of the blue and red arrows are indicative of a Stokes' shift induced through the application of Kasha's rule (typically via collisional energy transfer to the bath)	13
Figure 4 A Jablonski diagram for an arbitrary chemical system, showing the relation between the singlet ground state, S_0 , and a singlet excited state, S_n , and triplet excited states, T_n and T_1 , as well as the processes that allow the interchange between them.	16
Figure 5 Adaptation of Fig.3 illustrating spin-allowed transient absorption (red arrow). Without the initial pump, there would be no absorption at the corresponding red wavelength. The lifetime of S_1 dictates for how long the transient red wavelength absorption can be observed.	19
Figure 6 Typical Slater (left) and Gaussian (right) profile curves, as a function of an arbitrary variable r . These plots are indicative of functions used to model electronic orbitals. Slater functions are a better representation of electronic expectation values away from a nucleus but are more computationally costly to use.	28
Figure 7 Diagram of the transient absorption/flash photolysis spectrometer used in this work, (Edinburgh Instruments LP920), from above.	34
Figure 8 ICCD spectrum of Xe flash lamp emission spectrum. This lamp is used as the probe in the LP920 spectrometer, which limits the wavelengths over which transient features can be observed. At the edges of this spectrum, as the intensity decreases, there is increased noise in the transient spectra.	37
Figure 9 Morse potential diagram showing an example of the Franck-Condon vertical transitions for spin-forbidden absorption and phosphorescent emission to and from a triplet state, beginning and ending at the singlet ground state.	40
Figure 10 Simplified description of ligand field induced d-orbital splitting	46
Figure 11 Molecular orbital diagrams of π acceptor (top) and π donor (below) bonding with a transition metal.	47
Figure 12 Examples of different Ir^{III} complexes, all of which are viable phosphors. $\text{Ir}(\text{bpy})_3$ is perhaps the most well known of these compounds, and forms the basis for much of the literature spectroscopic work on these complexes. The latter two are novel complexes, for which the spectroscopy is reported herein.	48
Figure 13 Four complexes previously studied by Schmidbauer et al.	52
Figure 14 The seven quinoxaline-based complexes analysed in this chapter and the basis of the ligands used to form them	54
Figure 15 Comparison of the simulated (blue) structure with the experimentally determined crystal structure (brown) for the L5 complex, showing excellent agreement between them. The RMSD value between these two is 0.339 Å. Structures compared and rendered in Chimera software package and POV-RAY.	55
Figure 16 Normalised absorption spectra of the 7 complexes. The labels refer to the complexes as shown in Fig 14. The spectra are all qualitatively similar, but with band shifts discussed in the text. Wavelengths <260 nm omitted due to instrument limitations.	56
Figure 17 Renderings of the simulated frontier molecular orbitals for the calculated singlet ground state of $\text{Ir}(\text{L1})_2(\text{bpy})$	60
Figure 18 Comparison of simulated spectrum of $\text{Ir}(\text{L1})_2(\text{bpy})$ (red) with the steady state spectrum acquired (black).	64
Figure 19 The normalised emission spectra of the complexes listed by their constituent ligands. The L7 complex was examined in both oxygenated and nitrogenated conditions to determine if there was any oxygen influence on the band position. The peak maxima of each complex emission are shown inset for clarity, magnified to emphasise the position with respect to wavelength.	66
Figure 20 Transient absorption spectrum of the $[\text{Ir}(\text{L1})_2(\text{bpy})]\text{PF}_6$ complex in chloroform, obtained at a 50 ns delay from the laser pulse.	68

Figure 21 Simulated triplet absorption spectrum for the Ir(L1) ₂ (bpy) complex in chloroform. This spectrum corresponds to TD-DFT calculations of excited electronic triplet states, arising from the triplet ground state. The spectrum is a convolution of computed transitions for ease of comparison. _____	70
Figure 22 Transient kinetic measurements of the Ir(L1) ₂ (bpy) complex. The top trace is an emission trace, the bottom three are difference in optical density traces. All are fitted to a mono-exponential decay function, an example of a fit is shown in red on the top trace. Fit errors in nanoseconds are shown in parentheses. _____	71
Figure 23 The 7 iridium complexes synthesised using picolinate (inset) ancillary ligands. Again, the ligand labels from this figure will be used to identify the complexes in the text. _____	76
Figure 24 The 3 iridium complexes synthesised using pyrazinate (inset) as an ancillary ligand. _____	77
Figure 25 The benzoquinoxaline based iridium complexes discussed in this chapter _____	78
Figure 26 The diquinoxaline-pyridine iridium complexes discussed in this chapter _____	79
Figure 27 Comparison of the steady state absorption spectra of the picolinate-based complexes, normalised. _____	81
Figure 28 The calculated Kohn-Sham molecular orbitals of the Ir(L1) ₂ (pico) complex, rendered with the Avogadro software package, shown for illustrative purposes. _____	84
Figure 29 TD-DFT simulation (black) of the absorption spectrum of Ir(L1) ₂ (pico) (red). The convolution of the TD-DFT data is discussed in the text. The spectra are qualitatively similar, but show an energetic offset, commonly observed in TD-DFT calculations. _____	87
Figure 30 Steady state UV-Vis absorption spectra for the pyrazinate-based complexes. _____	89
Figure 31 The calculated Kohn-Sham molecular orbitals of the Ir(L2) ₂ (pyra) complex, rendered with the Avogadro software package, shown for illustrative purposes _____	91
Figure 32 Comparison of TD 50-50 simulated (black) and experimental (red) absorption spectra for the Ir(L2) ₂ (pyra) complex. _____	94
Figure 33 Normalised UV-Vis absorption spectra of the two bis-tridentate diquinoxaline-pyridinyl complexes in chloroform. _____	95
Figure 34 Normalised steady state absorption spectra of the free L12 ligand and its associated iridium complex in chloroform. _____	97
Figure 35 Thickened wireframe representation of the Ir(L12) ₂ complex with the 3 moieties of one of the ligands highlighted. These areas of each ligand are used to provide a more effective molecular orbital decomposition of the system. _____	98
Figure 36 Renderings of the frontier molecular orbitals of the L12 complex, for illustrative purposes. _____	99
Figure 37 The experimental and simulated steady state spectra of the Ir(L12) ₂ complex. In this case, there are a wide array of triplet transitions, and it is not immediately clear how they contribute to the spectrum. Therefore, in this case, the triplet state positions have not been convoluted, but are overlaid as vertical lines to designate position only. _____	102
Figure 38 The emission spectra of the picolinate-quinoxaline iridium complex set, normalised to peak maxima for comparison purposes. _____	103
Figure 39 The emission spectra of the pyrazinate-quinoxaline complexes, normalised to peak maxima for comparison purposes. _____	105
Figure 40 Normalised emission spectra of the two diquinoxaline-pyridinyl complexes in chloroform. Spectra normalised to peak maxima for comparison purposes. _____	106
Figure 41 Normalised emission intensities of the two complexes at various dilutions, showing a clear spectral response to complex concentration. The top trace of each complex represents a concentration of approximately 100 μM, with each subsequent trace representing a halving of concentration. _____	108
Figure 42 Time resolved emission spectra of the free L12 ligand in chloroform at two different gate delays, that is the delay of the camera in observing the emission after photoexcitation. _____	109
Figure 43 Transient absorption spectrum of the Ir(L1) ₂ (pico) complex in chloroform at a time delay of 50 ns from the laser pulse. _____	110
Figure 44 Comparison of the TA spectra of the picolinate set of complexes. The major features show a progression as the quinoxaline substituents are adjusted, exhibiting a bathochromic shift. All spectra obtained at a 50 ns delay from the laser pulse. _____	112
Figure 45 The simulated triplet-to-triplet absorption spectrum of Ir(L1) ₂ (pico), again convoluted for ease of viewing, as described previously. _____	113
Figure 46 Comparison of the transient absorption spectra of the pyrazinate-based complexes, obtained at 50 ns from the laser pulse. _____	115

Figure 47 The simulated triplet-to-triplet absorption spectrum of Ir(L2) ₂ (pyra), again convoluted for ease of viewing, as described previously. _____	116
Figure 48 Transient absorption spectra of the two diquinoxaline-pyridinyl complexes in chloroform, obtained at a 50 ns delay from the laser pulse. _____	117
Figure 49 Transient kinetic measurements of the Ir(L1) ₂ (pico) complex. The top trace is an emission measurement, all other traces are emission background subtracted Δ OD measurements. All measurements are fitted to a mono-exponential decay function in the Origin 9 software package and lifetimes are displayed next to the trace. _____	119
Figure 50 Transient kinetic traces of the major features of the Ir(L2) ₂ (pyra) complex. Fit errors in nanoseconds are shown in parentheses. _____	121
Figure 51 Kinetic traces of the major features of the transient spectra of [Ir(L12) ₂]PF ₆ (left) and [Ir(L13) ₂]PF ₆ (right) complexes in chloroform. Wavelengths and lifetimes of each trace are inset, with lifetime fit errors in nanoseconds in parentheses. _____	122
Figure 52 Comparison of the optimised singlet (blue) and triplet (brown) geometries of Ir(L8) ₂ (bpy) (RMSD = 0.141 Å) _____	127
Figure 53 Simulated L8 emission (blue), superimposed on the Ir(L8) ₂ (bpy) (black) and L8 ligand emission (red). _____	129
Figure 54 Comparison of the emission spectra of the L2 variant of each complex type. These spectra are overlaid to highlight the effect of the ancillary ligand on the emission peak maximum and normalised to the peak maxima for comparison purposes. _____	130
Figure 55 The chemical structure of 2,3,5-triphenyltetrazolium, with the positions of the tetrazolium ring numbered. _____	137
Figure 56 The eight conformers of triphenylformazan considered in this work. _____	138
Figure 57 The basis compound triphenyltetrazolium and the photocoupled and formazan products formed from its photoreduction. _____	139
Figure 58 The proposed mechanism of the photoreaction of triphenyltetrazolium, leading to the formation of triphenylformazan and the photocoupled product species. _____	139
Figure 59 The three substituted variants of TTP involved in this study. _____	140
Figure 60 Normalised UV-Vis absorption spectrum of TTP in acetonitrile (100 μ M) (black trace). The TD-DFT derived spectrum is also displayed (red trace). _____	141
Figure 61 Rendered frontier molecular orbitals of the singlet ground state of triphenyltetrazolium. _____	144
Figure 62 Normalised steady state UV-Vis absorption spectrum of triphenylformazan in acetonitrile (10 μ M) (black trace). The TD-DFT derived spectrum is also displayed (red trace). _____	145
Figure 63 Percentage contribution of each of the groups to the frontier orbitals of the singlet ground state of 3,5-diF triphenyltetrazolium. _____	147
Figure 64 Rendered frontier molecular orbitals of the singlet ground state of 3,5-diF triphenyltetrazolium. _____	148
Figure 65 Normalised UV-Vis absorption spectrum of 2,6-diF TTP in acetonitrile (100 μ M). The TD-DFT singlet-to-singlet spectrum is also displayed, derived from the calculated singlet ground state. _____	149
Figure 66 Rendered frontier molecular orbitals of the singlet ground state of 2,6-diF TTP _____	151
Figure 67 Normalised UV-Vis absorption spectrum of 2,6-diMe TTP in acetonitrile (100 μ M). The TD-DFT derived spectrum of singlet-to-singlet transitions calculated from the singlet ground state is also displayed. _____	152
Figure 68 Rendered frontier molecular orbitals of the singlet ground state of 2,6-diMe TTP _____	154
Figure 69 Luminescence subtracted transient absorption/FLP spectrum of TTP (100 μ M) in acetonitrile at different time delays from the laser pulse (λ_{ex} = 266 nm). All spectra are placed on their own scale to allow comparison, due to intensity differences. _____	156
Figure 70 Successive acquisitions of luminescence corrected transient absorption/FLP spectra at the same time delay from a sample of TTP in acetonitrile (100 μ M), demonstrating the progressive alteration of the sample composition with cumulative light exposure. _____	159
Figure 71 Luminescence corrected transient absorption/FLP spectra of TTP (100 μ M) in acetonitrile under flow at a variety of different gate delays relative to pulse (λ_{ex} = 266 nm) _____	161
Figure 72 Luminescence corrected transient absorption spectrum of TPF in acetonitrile (10 μ M) (λ_{ex} = 266 nm) _____	163

Figure 73 Luminescence corrected transient absorption/FLP spectrum of 3,5-diF TTP (100 μ M) in acetonitrile at different time delays from the laser pulse ($\lambda_{\text{ex}} = 266$ nm). All spectra are placed on their own scale to allow comparison, due to intensity differences. _____	164
Figure 74 Luminescence corrected transient absorption/FLP spectra of 3,5-diF TTP (100 μ M) in acetonitrile under flow at a variety of different delays relative to pulse ($\lambda_{\text{ex}} = 266$ nm) _____	166
Figure 75 Luminescence corrected transient absorption/FLP spectrum of 2,6-diF TTP (100 μ M) in acetonitrile at different time delays from the laser pulse ($\lambda_{\text{ex}} = 266$ nm). _____	168
Figure 76 Luminescence corrected transient absorption/FLP spectra of 2,6-diF TTP (100 μ M) in acetonitrile at different time delays from the laser pulse, acquired using the PMT/monochromator detector system ($\lambda_{\text{ex}} = 266$ nm). _____	169
Figure 77 Luminescence corrected transient absorption/FLP spectrum of 3,5-diF TTP (100 μ M) in acetonitrile at 50 ns delay from the pulse ($\lambda_{\text{ex}} = 266$ nm) _____	170
Figure 78 Emission spectra of the TTP compound (100 μ M) at 50 ns from the laser pulse, multiple acquisitions ($\lambda_{\text{ex}} = 266$ nm), static cell. _____	171
Figure 79 Emission spectra of the TTP compound in acetonitrile (100 μ M) under flow at 50 ns from the laser pulse ($\lambda_{\text{ex}} = 266$ nm). Smoothing applied for presentation purposes. _____	173
Figure 80 Emission spectra of the 3,5-diF TTP compound in acetonitrile (100 μ M) at 50 ns from the laser pulse, multiple acquisitions ($\lambda_{\text{ex}} = 266$ nm), static cell. _____	174
Figure 81 Emission spectra of the 3,5-diF TTP compound in acetonitrile (100 μ M) under flow at 50 ns from the laser pulse ($\lambda_{\text{ex}} = 266$ nm). Smoothing applied for presentation purposes. _____	175
Figure 82 Emission spectra of the 2,6-diF TTP compound in acetonitrile (100 μ M) at 50 ns from the laser pulse, multiple acquisitions ($\lambda_{\text{ex}} = 266$ nm) _____	176
Figure 83 Emission spectra of the 2,6-diF TTP compound in acetonitrile (100 μ M) at 20 ns from the laser pulse ($\lambda_{\text{ex}} = 266$ nm) acquired using wavelength stepped PMT mapping. Smoothing applied for presentation purposes. _____	177
Figure 84 Emission spectra of the 2,6-diF TTP compound in acetonitrile (100 μ M) at 30 ns from the laser pulse ($\lambda_{\text{ex}} = 266$ nm). Smoothing applied for presentation purposes. _____	178
Figure 85 Emission spectra of the 2,6-diMe TTP compound in acetonitrile (100 μ M) at 50 ns from the laser pulse, first three acquisitions ($\lambda_{\text{ex}} = 266$ nm) _____	179
Figure 86 Emission spectra of the 2,6-diMe TTP compound in acetonitrile (100 μ M) at 50 ns from the laser pulse, multiple acquisitions ($\lambda_{\text{ex}} = 266$ nm) _____	180
Figure 87 Luminescence corrected kinetic transient absorption spectrum of TTP in acetonitrile (100 μ M) at 390 nm ($\lambda_{\text{ex}} = 266$ nm). For presentation purposes smoothing has been applied. _____	182
Figure 88 Kinetic emission spectra of TTP in acetonitrile (100 μ M) ($\lambda_{\text{ex}} = 266$ nm). For presentation purposes smoothing has been applied. _____	183
Figure 89 Luminescence corrected kinetic transient absorption spectrum of 2,6-diF TTP in acetonitrile (100 μ M) at 390 nm and 490 nm ($\lambda_{\text{ex}} = 266$ nm). _____	184
Figure 90 Kinetic emission spectra of 2,6-diF TTP in acetonitrile (100 μ M) ($\lambda_{\text{ex}} = 266$ nm). For presentation purposes smoothing has been applied. _____	185
Figure 91 Time-of-flight mass spectrum of TTP in acetonitrile (100 μ M), no laser exposure. _____	187
Figure 92 Time-of-flight mass spectrum of TTP in acetonitrile (100 μ M), 2 hours laser exposure. _____	188
Figure 93 Time-of-flight mass spectrum of TTP in acetonitrile (100 μ M), 10 minutes laser exposure _____	189
Figure 94 Time-of-flight mass spectrum of TTP in acetonitrile (100 μ M), 45 minutes laser exposure _____	190
Figure 95 Time-of-flight mass spectrum of degassed TTP in acetonitrile (100 μ M), 10 minutes laser exposure. _____	191
Figure 96 Time-of-flight mass spectrum of degassed TTP in acetonitrile (100 μ M), 45 minutes laser exposure. _____	192
Figure 97 Theorised structure for the oxidised photocoupled product. _____	192
Figure 98 Time-of-flight mass spectrum of 2,6-diF TTP in acetonitrile (100 μ M) _____	193
Figure 99 Time-of-flight mass spectrum of 2,6-diF TTP in acetonitrile (100 μ M), 2 hours laser exposure. _____	194
Figure 100 Diagram of an off-axis injection optical cavity setup with one reflection shown. _____	198

Figure 101 Ozonolysis of an example alkene, forming a Criegee intermediate and a ketone via a primary ozonide. An R3, R4 CI and R1, R2 ketone are also possible. _____	201
Figure 102 Basic reaction coordinate showing the syn- and anti- conformers of a simple Criegee intermediate _____	202
Figure 103 Side-on (top) and end-on (bottom) views of the spectrometer system in development. ____	205
Figure 104 Above view diagram of the cavity ringdown setup in development. _____	206
Figure 105 Spot patterns traced by the red diode alignment beam on the surfaces of the aluminium alignment mirror (top left), the opposing cavity mirror (top right) in optic mounts from initial optical cavity testing, and on the surface of the secondary cavity mirror mounted in the sample chamber (bottom). _____	208
Figure 106 Comparison of the signal obtained through the optical cavity with and without the re-injection mirror in position. _____	209

List of Tables

Table 1 Table depicting the absorption transitions for the singlet ground state to first singlet excited state as calculated using TD-DFT and a CAM-B3LYP level of theory. The values in parentheses are the onsets of the experimentally determined UV-Vis absorption ¹ MLCT feature and are used for comparison. _____	58
Table 2 MO contributions to the first 5 singlet to singlet excitations for the [Ir(L1) ₂ (bipy)]PF ₆ complex. _____	59
Table 3 Table depicting the percentage contributions of each of the main components of the complex to the frontier orbitals of the L1 Ir complex, as determined by the GaussSum software package. Figures are rounded to the nearest integer. _____	60
Table 4 Frontier orbital energy gap for the singlet ground states of the bipyridine complexes _____	62
Table 5 Calculated values for the spin forbidden absorption and emission of the complexes. The experimental values are shown in parentheses for comparison. _____	63
Table 6 Maximum peak values for the emission of the complexes. Simulated values shown in parentheses _____	67
Table 7 The peak maxima values for the transient absorption spectra of the 7 complexes, focussing on the clear features observed in figure 20. _____	69
Table 8 Lifetimes for the transient features of the complexes. For brevity, the feature positions are approximated. Fit errors in nanoseconds are shown in parentheses. *No lifetime could be obtained from the PMT measurements of the L3 complex bleach, due to lack of sufficient resolution _____	72
Table 9 Percentage contributions of each component of the Ir(L1) ₂ (pico) complex to the frontier molecular orbitals. _____	82
Table 10 The first five singlet excited states of the Ir(L1) ₂ (pico) complex and the molecular orbitals involved in these transitions. _____	84
Table 11 Vertical transition spin-forbidden absorption wavelengths for the picolate complexes. _____	85
Table 12 Moiety contributions to the frontier orbitals of the L2 variant of the pyrazinate complex _____	90
Table 13 The wavelength, force oscillator strengths and contributing molecular orbital transitions of the first 5 singlet-to-singlet excited states for the Ir(L2) ₂ (pyra) complex. _____	92
Table 14 Computed values for the vertical spin-forbidden absorption and emission for the pyrazinate complexes. Experimental values are shown in parentheses. _____	93
Table 15 Calculated electronic component of the spin-forbidden absorption between the singlet ground state and the excited triplet state of the diquinoxaline-pyridine complexes. _____	96
Table 16 The decomposition analysis of the singlet ground state frontier orbitals of Ir(L12) ₂ _____	99
Table 17 The wavelength, force oscillator strengths and contributing molecular orbital transitions of the first 5 singlet-to-singlet excited states for the Ir(L12) ₂ and Ir(L13) ₂ complexes. Molecular orbital contributions less than 10% have been omitted for clarity _____	100
Table 18 The emission peak maxima of the picolate complexes, ordered by their wavelength values. Computationally derived T ₁ – S ₀ vertical transition values are shown in parentheses. _____	104
Table 19 The emission peak maxima of the pyrazinate complexes, ordered by their wavelength values. _____	106
Table 20 Experimentally determined emission centres for the L12 and L13 complexes. Simulated vertical transition estimates shown in parentheses. _____	107

Table 21 Average lifetimes of the picolinate complexes, shown alongside the substituents of the complexes. _____	120
Table 22 Lifetimes of transient kinetic features of the diquinoxaline-pyridine complexes, $[\text{Ir}(\text{L12})_2]\text{PF}_6$ and $[\text{Ir}(\text{L13})_2]\text{PF}_6$. Fit errors in nanoseconds are shown in parentheses after each lifetime. _____	123
Table 23 Percentage contribution of each group to the frontier molecular orbitals of the L8 bipyridine complex. _____	124
Table 24 Percentage contribution of each group to the frontier molecular orbitals of the L11 bipyridine complex. _____	125
Table 25 Calculated electronic component of the spin-forbidden absorption and emission between the singlet ground state and the excited triplet state for each of the benzoquinoxaline complexes. _____	126
Table 26 RMSD values for the geometry difference between the singlet and triplet geometries of the benzoquinoxaline complexes. _____	127
Table 27 The wavelength, force oscillator strengths and contributing molecular orbital transitions of the first 5 singlet-to-singlet excited states for the $\text{Ir}(\text{L8})_2(\text{bpy})$ complex. _____	128
Table 28 Singlet ground state HOMO to LUMO gaps for the picolinate and pyrazinate complexes, ordered from highest energy difference to lowest. _____	131
Table 29 Average energies for the singlet state frontier orbitals of the complex sets _____	132
Table 30 Percentage contribution of each of the groups to the frontier orbitals of the singlet ground state of triphenyltetrazolium. _____	143
Table 31 The first five calculated singlet states of triphenyltetrazolium from the singlet ground state. _____	144
Table 32 The first five calculated singlet states of 3,5-diF triphenyltetrazolium from the singlet ground state. _____	148
Table 33 Percentage contribution of each of the groups to the frontier orbitals of the singlet ground state of 2,6-diF triphenyltetrazolium. _____	150
Table 34 The first five calculated singlet states of 2,6-diF triphenyltetrazolium from the singlet ground state. _____	151
Table 35 Molecular orbital contributions from each of the constituent groups of the calculated geometry of singlet 2,6-diMe TTP _____	153
Table 36 The first five excited singlet states of 2,6-diMe TTP _____	154

List of Equations

Equation 1 Beer-Lambert law. A = light absorbed by the material, T_0 = transmission of light through reference, T = transmission of light through sample, ϵ = molar extinction coefficient, C = concentration of species, l = path length of light through sample. _____	9
Equation 2 Morse potential function. r = internuclear distance, D_e = well depth, k_e = force constant at well minimum, r_e = equilibrium bond distance. _____	12
Equation 3 Difference in optical density for a selected wavelength. $I_0(\lambda)$ = intensity prior to excitation, $I_t(\lambda)$ = intensity after excitation. _____	17
Equation 4 B3LYP electron exchange-correlation energy. _____	27
Equation 5 Calculation used by the L900 spectrometer software to derive a transient absorption spectrum. $I_p(\lambda)$ = probe background intensity, $I_T(\lambda)$ = measurement intensity, $I_F(\lambda)$ = fluorescence background intensity. _____	35
Equation 6 Empty cavity decay rate. k = decay rate coefficient, τ = ringdown time, L = distance between mirrors, R = reflectivity of mirrors, c = speed of light. _____	198
Equation 7 Mean distance travelled by light within the cavity, L_{eff} . _____	198
Equation 8 The relationship of transmitted intensity to absorptivity. I = transmitted intensity, I_0 = initial intensity, t = time, k = decay rate, L_{cov} = round-trip cavity losses, l_{RT} = cavity round-trip length, t_{RT} = cavity round-trip time, α = absorption coefficient of sample, c = speed of light, C = concentration of sample, ϵ = molar extinction coefficient of sample. _____	199
Equation 9 The stability region of a re-injection cavity. L = mirror separation, R_{RIM} = radius of re-injection mirror, R_F = radius of front cavity mirror. _____	207

Abstract

A variety of spectroscopic techniques are employed for the analysis of chemical interactions instigated by photonic excitation. Steady state absorption and emission spectroscopy is useful for characterising photostable compounds and performing constitutional analysis of samples pre and post reaction, but often cannot provide information on reaction intermediates, excited states or reaction dynamics. To address these areas, transient spectroscopic techniques can be used, involving pump-probe measurements to induce a photochemical or photophysical process and monitor it as a function of wavelength and time. In this work, both steady state and transient spectroscopic techniques were used to interrogate and characterise a number of novel photoactive species, supported throughout by computational chemistry approaches. Firstly, this includes a number of novel Ir^{III} complexes, synthesised by the Pope group at Cardiff University. These complexes, which largely contain quinoxaline derivatives, display highly tuneable photophysical properties with respect to subtle ligand variation. This tuneability was analysed, both experimentally and computationally, with respect to ligand structure and, using this ligand library set, tuning properties of similar ligands are predicted. Secondly, similar techniques were employed to analyse the photoreduction of a photosensitive compound, 2,3,5-triphenyltetrazolium, and three similar chemical variants, supplied by the Fallis group at Cardiff University. Tetrazolium compounds are useful as chemical indicators: their reduction reaction is associated with a colour change, and as such it would be advantageous to inhibit the photochemical reduction to prevent false positives in the chemical reduction process. Through chemical variation of the tetrazolium the photoreaction can be inhibited, and through spectroscopic analysis of this reaction new photochemical pathways are proposed. Finally, initial steps in the development of a gas phase multi-pass absorption spectrometer for the analysis of trace chemical intermediate species have been undertaken.

1. Introduction and Background

1.1 Background

A chemical compound's response to electromagnetic radiation exposure reveals many of its defining characteristics, and the field of spectroscopy is concerned with studying molecular response to electromagnetic radiation and developing new methods to maximise knowledge of chemical compounds through observing this response.

Through this process, information can be garnered about a vast array of molecular properties, including, but not limited to, molecular structure and molecular packing, electronic properties and vibrational properties. This assists chemists on a daily basis in their pursuit of optimising chemicals for use in every walk of life, from drug discovery to housing construction and clothing manufacture. Perhaps one of the most obvious spectroscopic tests that can be carried out on molecular system is evaluating colour, which arises from a combination of the degree of light absorbed, scattered or emitted by a substance, as a function of wavelength. From the careful measurement of a compounds response to a range of wavelengths of incident light, the absorptive properties of that chemical species can be obtained, called an absorption spectrum, that generally functions as a unique 'fingerprint' for that compound. Similarly, a compound can emit light following light exposure, which can also be used to glean information about its electronic properties and characterise it.

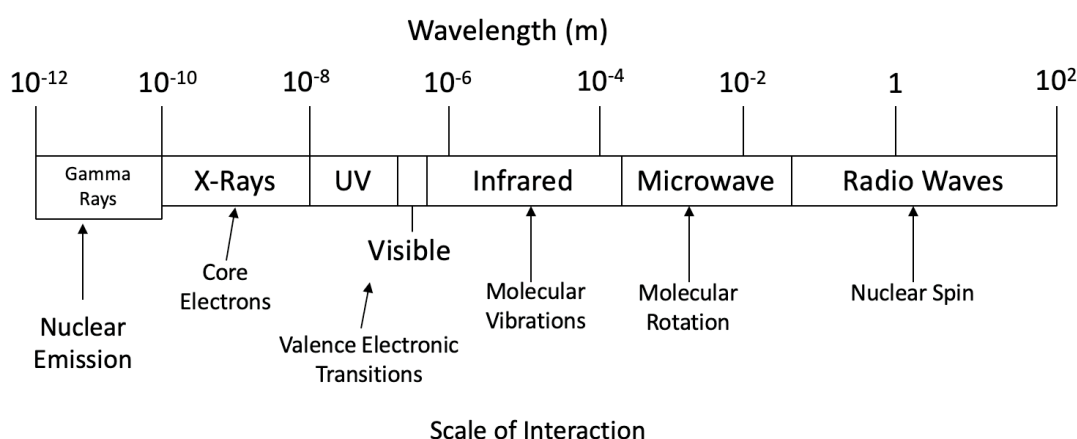


Figure 1 Electromagnetic spectrum and its approximate domain of atomic and molecular interactions.

Absorption and emission spectra are most commonly recorded over the ultraviolet (UV), visible and infrared (IR) portions of the electromagnetic spectrum, and typically provide information on the structural and electronic properties of compounds, as shown in figure 1. Using this information, chemical and photophysical processes can be studied and their mechanisms of action elucidated by examining changes in spectra during and following irradiation. From such examinations, compounds with desirable properties can be isolated and tailored for use in commercial applications. For example, brightly emitting compounds in displays¹, light-harvesting compounds in solar panels², and as photosensitisers for applications such as photonic upconversion³, a process using energy transfer from multiple absorptive compounds to produce an emission wavelength shorter than the excitation wavelength. All of these require specific, consistent responses to known stimuli, so spectroscopy is used to screen compounds to assess their potential usefulness in these areas. Beyond merely identifying a compound via its 'fingerprint', spectroscopic characterisation allows the determination of mechanisms that lead to certain behaviours, such as absorption and emission, and thus allows for the prediction of behaviours in similar compounds, a vital component in rational design. This enables much time and effort to be spared in synthesising and screening compounds, as the deeper understanding of how structural and electronic properties relate to photophysical and photochemical properties can allow for the processing of compounds with desired qualities using theoretical methods, selecting likely candidates for synthesis and confirmatory analysis.

Transition metal complexes are favoured for their brightly coloured emission properties, owing to intense metal-ligand interactions. Third row transition metal complexes, such as those based on Iridium (III) (Ir^{III}), are widely used due to their very strong spin-orbit coupling,^{4,5} enabling intense, long-lived luminescence through access to the triplet manifold. Iridium (III) complexes, which are a group of complexes upon which this thesis focuses, can feature a large variety of structures, currently in use across a wide range of fields and applications, including as photosensitisers, chemical ion sensors⁶ and light emitting devices, such as OLEDs (organic light emitting diodes). Ir^{III} complexes have been used as photosensitisers for catalytic reactions, such as the reduction of water⁷⁻¹¹ to generate hydrogen, as well as functioning directly as light-

driven catalysts in asymmetric photoredox reactions.^{12,13} Their versatile structural properties allow them to function well as analytical probes, with an example being a novel tri-aryl boron containing Ir^{III} species developed by Xu *et al* for fluoride detection via the deactivation of phosphorescence in the complex following fluoride attachment to the boron moiety, quenching the triplet state whilst leaving singlet fluorescent ligand states still active.¹⁴ Their use in OLED applications is extensive, with a wide variety of ligand architectures being employed with emission wavelengths spanning the entire visible spectrum.^{15–20} These devices generally achieve efficient emission through electrical stimulation of the phosphorescent complex used.

Iridium complexes tend to be well suited for these roles, as they can possess strong absorption bands in the visible region of the electromagnetic spectrum, which makes them attractive for use across many of the applications stated above. In addition, they also exhibit intense, discrete emission bands, with structure-dependent wavelength maxima.^{21–23} This tuneability of these brightly emitting compounds is an extremely favourable property, as it means there exists a vast library of compounds with similar photophysical attributes, yet varying emission wavelengths. This arises largely from the wide selection of ligands that can be complexed to the metal centre. Through the careful selection of ligands, compounds can be produced which have the desired properties for a role. For example, the broad tuning of emission wavelength via extension of ancillary ligand conjugation in Ir^{III} complexes for live cell imaging by Zhao *et al*, as the complexes synthesised by the group display intense phosphorescence with low cytotoxicity across wavelengths extending from 450 – 850 nm.²⁴ Spectroscopic analysis has been used to determine commonalities between the behaviours of groups of iridium (III) complexes, and from these observations, rational design can be used to effectively engineer variants of these complexes with the desired absorption and emission properties.^{25–27}

Spectroscopic analysis also extends into assessing a compounds stability under the operating conditions of the application its being employed in, as many compounds display photosensitivity to certain wavelengths, particularly higher energy wavelengths such as those in the UV and visible regions. Photodegradation will shorten a

compounds operational lifespan and potentially create issues with its functioning in an application. An example of this would be 2,3,5-triphenyltetrazolium chloride (TTC), a compound commonly used in testing the viability of seeds that failed to germinate.^{28,29} The test relies on the reduction of the tetrazolium species to a corresponding compound called 1,3,5-triphenylformazan (TPF), which is accompanied by a colour change from colourless to deep red. This occurs in aerobically active seeds but will not occur in inactive ones. Metabolically active tissue will also be able to induce this reduction enzymatically, via agents such as dehydrogenases and NADH.³⁰ For this reason, various tetrazolium salts are commonly used to test for cytotoxicity,^{31,32} cell viability,³³ and in fluorometric assays for determining cell redox activity.³⁴ Triphenyltetrazolium can also be employed as a redox indicator for detecting 1,1-dimethylhydrazine, used as a rocket fuel, which is highly toxic and volatile, posing a carcinogenic risk as well as being a potential environmental hazard.³⁵ The TTC-based indicator strips developed by Minin *et al* were highly sensitive to the presence of 1,1-dimethylhydrazine, able to detect airborne concentrations of 0.006 mg ml⁻¹, and the reduction reaction was noted to possess radical character through an in-situ EPR (electron paramagnetic resonance) study.³⁵ This is in keeping with previous experiments that suggests that the reduction of TTC and the oxidation of TPF both feature a tetrazolium ring-based radical species intermediate reported by Neugebauer *et al*.^{36,37}

Another increasingly important field of development is that of atmospheric spectroscopy, the study of the composition of air in different regions of the world. This is important for assessing the quality of the air in different environments and at different times of the day and year, as this has ramifications for the health of populations living in them. The chemistry of the lower stratum of the atmosphere, namely the troposphere, varies most significantly based on geolocation. In rural or 'pristine' environments the chemical composition of the troposphere tends to be dominated by biogenic emissions such as terpenoid compounds,³⁸ whilst urban environments have much greater quantities smaller anthropogenic molecules, such as acetone and formaldehyde, as a consequence of human activities. The concentration of different compounds in tropospheric air also alters significantly with the seasons

and with the time of day, as a result of changing temperatures, light conditions and activities.^{39–42} For example, OH radicals have a significantly greater concentration during the day than at night as their dominant formation pathway is the solar photolysis of ozone,⁴³ shown in figure 2. Developing an understanding of the human impact upon the atmosphere, and in turn the environmental impacts of biogenic and anthropogenic tropospheric emissions upon human health, have been of vital importance since the industrial revolution.



Figure 2 Chemical equations for the two photolytic dissociation processes of ozone in the troposphere and the reaction of singlet oxygen with water vapour to form hydroxyl radicals. Superscript refers to spin multiplicity.

As the chemical composition of the troposphere is often in flux, understanding the finer chemical composition can be challenging when using more conventional spectroscopic techniques, due to the low concentrations of many important chemical species. In recent years, the knowledge of tropospheric chemical composition has increased greatly with refined and novel spectroscopic investigations of species such as HONO, HOONO and HOOO.^{44–49} Specialist techniques employing the use of multi-pass optical cells are widely used in the field of atmospheric study, both for examining the atmospheric composition through absorption spectroscopy, and for studying chemical reactions between species. Since the late 1990s cavity ringdown spectroscopy (CRDS) has become a commonly used absorption spectroscopy technique, with incredibly high sensitivities due to its achievement of very long path lengths. It has seen increasing use in analysing atmospheric constituents which is vital for the development atmospheric models.^{50–52} CRDS began as a technique used to precisely measure the reflectivity of dielectric mirrors, which were rapidly developing towards total reflection thanks to developments in ion sputtering film deposition

methods.⁵³ This posed a challenge, as the methods used prior to this were no longer sufficient, as the difference between the rejected light intensity and the laser output were too small to effectively determine directly. CRDS was developed as a solution, as by measuring the decay time of an empty cavity, one can accurately relate the cavity length and this decay time to the reflectivity of the mirrors.

Computational studies can aid chemical analysis immensely, as computational chemistry can provide a deeper insight into the changes in electronic and geometric structure of a molecule and can be used to great effect in assigning the origin of an emission or absorption band. Density functional theory (DFT) studies are frequently employed in the characterisation of Ir^{III} complexes for the assignment of band origins and assessment of ligand effects, as DFT can provide good qualitative insight into electronic and geometric structure with a relatively low computational expense.^{54–59} As an example of this, Shi *et al* used DFT techniques to evaluate comprehensively the properties of four similar Ir^{III} complexes based around substituted phenylpyridine and N-hetero carbene ligand structures, determining the energy gap between the highest occupied molecular orbital (HOMO) and lowest unoccupied molecular orbital (LUMO), one of the most important properties with respect to the tuning of these complexes, as well as ligand contributions to those orbitals.⁶⁰ Absorption and emission spectra for each of the four complexes were also able to be simulated and conclusions about ligand effects inferred from comparison between these properties for each of the complexes, one of the most significant and powerful uses of this methodology, as it allows for the estimation of properties of novel ligand structures prior to synthesis.

In this work, several compounds are examined for their photophysical properties, using a variety of spectroscopic and computational techniques. A series of iridium (III) complexes are analysed to determine the effect ligand structure has on their emissive properties and to determine their electronic structure which underpins their spectroscopy. A selection of tetrazolium compounds are also analysed using similar techniques to determine whether the photoreduction reaction to the corresponding formazan can be inhibited. In this way, a combined computational and spectroscopic methodology is employed in an effort to elucidate properties in more robust and

insightful capacity than could be accomplished through either method used in isolation.

1.2 Transient/Flash Photolysis Spectroscopy

Steady state spectroscopic methods, such as UV-Vis or infrared absorption and emission, are commonplace in modern chemical laboratories. They are useful in applications ranging from molecular characterisation to studying reaction kinetics. These techniques can provide a wealth of information on the rovibronic structure of a molecule under interrogation and can be used to provide everything from structural to mechanistic information, and therefore are often vital in chemical characterisation. Steady state UV-vis absorption spectroscopy involves probing a sample with a light source across a range of wavelengths spanning the UV-vis region, extending slightly into the near-infrared (typically $\sim 200 \text{ nm} < \lambda < 800 \text{ nm}$) and observing the characteristic wavelengths absorbed by the sample. A solution phase, steady-state absorption spectrum is obtained by continuously irradiating the sample and simultaneously recording the transmitted light intensity through the sample. Through comparison of this transmitted light intensity with that of an appropriate reference (an identical experimental apparatus but without the presence of the sample species), one can derive the wavelength dependent absorption of the sample. This absorption spectrum is readily obtained through application of the Beer-Lambert law:

$$A = \log_{10} \left(\frac{T_0}{T} \right) = \epsilon Cl$$

***Equation 1** Beer-Lambert law. A = light absorbed by the material, T_0 = transmission of light through reference, T = transmission of light through sample, ϵ = molar extinction coefficient, C = concentration of species, l = path length of light through sample.*

The Beer-Lambert law describes several factors that result in the attenuation of light when travelling through a material. These factors include the molar extinction coefficient, ϵ , which is a fundamental property of the sample, and describes how strongly the material interacts with light for a given wavelength; the concentration, C , of the sample; and the path length (l) of the interrogating beam through the sample.

For an absorbing sample, typically as the concentration of the sample increases, or as the path length increases, so does the measured absorption. The molar extinction coefficient will vary with wavelength, characteristic of the electronic properties of the compound being examined.

Before extending the discussion of molecular structure further, it is worth noting that by monitoring the light transmission through the sample, there are of course other properties that could lead to a change in observed transmitted light intensity, for example light scattering. Light scattering will result in disruption of the interrogating beam used to analyse the sample, causing the observed intensity to decrease, which could lead to a false assessment of the sample absorptivity at that wavelength. Scattering is most commonly caused by small particulate in solution, but bubbles of gas in a strongly aerated solution, imperfections in the sample cell, or even density fluctuations in a solution can also lead to significant scattering. Another related cause of reduction in observed intensity could be due to reflection from larger particulate present in solution. Differences between the sample and reference containers can also lead to a change in the observed intensities, as a significantly higher reflectivity of the reference cuvette compared to the sample cuvette would lead to a reduction in observed absorbance and vice versa. Errors in the instruments design can also lead to observed differences in light intensity. Most spectrophotometers in use today rely on a monochromator to select the wavelength being observed by the detector, which will respond to light of any given frequency, producing a signal from incident photons of any wavelength within its operational range. The resolution of an such instrument will depend on the spectral bandwidth of the monochromator, normally defined as the full-width half-maximum of the light selected for and permitted through, in wavelength space. A spectral bandwidth of a nanometre would mean that a significant intensity of light from $\sim 349 - 351$ nm would be expected to be observed at a selected wavelength of 350 nm, for example, resulting in a larger signal than would be expected. This would not be expected to be a large source of error for most applications of spectrophotometers however, as the absorption bands observed are generally much broader than the spectral bandwidth of the monochromator.

Where there is more than one absorbing species at a given wavelength, the absorption spectrum observed will be a combination of the absorptive properties of each species. As the path length will remain the same for all species in the solution, the factors determining total absorption will be the concentrations of the present species and their respective molar extinction coefficients for that wavelength. The sum of each species Beer-Lambert law expression will be therefore equivalent to the absorption observed.

Crucially, the property of the system one is interested in examining through UV-Vis absorption spectroscopy is the molar extinction coefficient, which can be readily related to the electronic structure of the molecule. Typically, a non-irradiated stable polyatomic molecule in solution is found in its lowest energy electronic configuration, normally a closed-shell singlet. When exposed to an incident photon of sufficient energy, the system can undergo promotion to a higher energy electronic excited state, absorbing the photon in the process. This absorption can thus be observed in a steady UV-Vis spectrometer, with the energy gap between the two electronic states being equivalent to the energy of the absorbed photon. As a consequence of the Pauli exclusion principle, each atomic or molecular orbital can hold up to two electrons, each with an opposing spin number, with a value of either $+\frac{1}{2}$ or $-\frac{1}{2}$. A system containing only fully paired electrons is designated as being in the 'singlet' spin state, as determined by the expression $n = 2S + 1$, where S is the net spin of the system and n is the spin multiplicity. Given that all the electrons in a singlet system are paired, the net spin is 0, resulting in a value of 1. For a system with one unpaired electron, the S value is $\frac{1}{2}$, resulting in a multiplicity of 2, otherwise known as a doublet. For systems with two unpaired electrons with the same spin number the net spin is 1, resulting in a multiplicity of 3, called a triplet state. Singlet states can also possess two unpaired electrons following excitation to an excited electronic state whilst preserving spin. This is one of the rules governing electronic transitions, called selection rules. The spin selection rule states that the S value cannot change during a transition from one electronic state to another. Transitions that obey this rule are described as 'spin-allowed', whilst transitions that break this rule are described as 'spin-forbidden.' The other selection rule governing electronic transitions is known as the Laporte selection

rule. It applies to centrosymmetric systems, and states that transitions between orbitals with the same symmetry are forbidden.

In addition to electronic energy levels, molecules will possess a number of vibrational energy levels. A nonlinear polyatomic molecule possesses $3N - 6$ vibrational modes, where N is the number of atoms. This arises from a consideration of the degrees of translational, rotational and vibrational degrees of freedom the molecule possesses in 3D space and removal of the 3 translational and 3 rotational degrees of freedom, one for each perpendicular axis. Transitions between the vibrational modes of a molecule can be examined using an infrared absorption spectrometer, as the scale of the energy gaps between the modes corresponds to that region of the electromagnetic spectrum. Vibrational modes can be visualised graphically by considering a single bond coordinate at a time. By considering the internuclear separation of a bond, a visualisation of vibrational modes along that bond can be constructed, called a Morse potential diagram. In the Morse potential diagram, the energy levels of the system as a function of internuclear separation is depicted, producing a curve known as a potential well. The potential is produced by the following relationship:

$$V'(r) = D_e \left(1 - e^{-\sqrt{k_e/2D_e}(r-r_e)} \right)^2$$

Equation 2 Morse potential function. r = internuclear distance, D_e = well depth, k_e = force constant at well minimum, r_e = equilibrium bond distance.

As the two nuclei of the bond being considered near one another, the Coulombic repulsion forces between them will raise the energy of the system. When the separation between them is increased, the system will also experience an increase in energy due to the decrease in efficient overlap between the molecular orbitals of the two, until the two molecules are sufficiently far apart as to be considered non-interacting, meaning the energy will plateau, and remain unchanged for any subsequent increase in r . This is the bond dissociation energy. Electronic transitions can be represented on the diagram, with additional vibrational potentials at higher energies representing the vibrational mode structure at these higher electronic states. Electronic absorption and emission between different electronic states is represented

by the movement up to higher vibrational levels and down to the ground state surface, respectively. Below in figure 3 is a Morse potential diagram depicting a singlet-to-singlet spin-allowed transition between two surfaces, meaning there is no change in the net spin of the system. The excited state surface is represented by S_n , whilst the ground state is represented by S_0 .

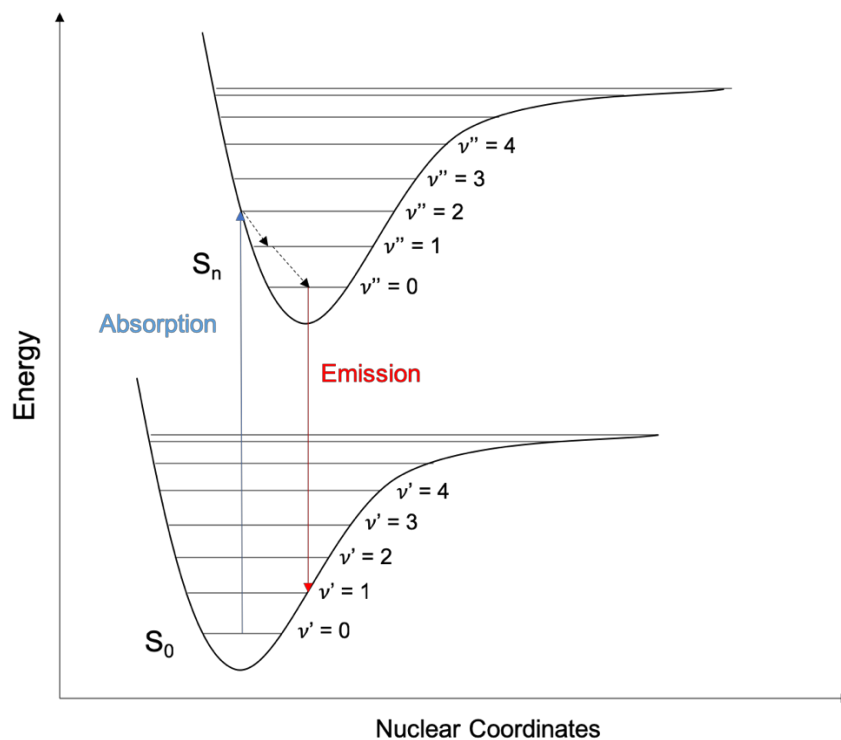


Figure 3 Diagram illustrating spin-allowed absorption and emission, using model singlet ground and excited state potential energy surfaces. The lengths of the blue and red arrows are indicative of a Stokes' shift induced through the application of Kasha's rule (typically via collisional energy transfer to the bath)

The likelihood of promotion to any given excited state depends on the degree of overlap between the vibrational wavefunctions of accessible vibrational states of the ground and excited electronic states at any particular set of nuclear coordinates. This is called the Franck-Condon principle, and the degree of overlap between wavefunctions of vibrational levels will give rise to a vibronic absorption spectrum. If a transition is to take place between two potential energy surfaces that are identical in shape, and vertically offset with identical minimum energy bond lengths in the given coordinate, then the $v=0 \leftarrow v=0$ transition will be the most intense. In reality, potential energy surfaces will not be identical, nor will they typically be solely vertically offset, but will

be offset in the bond coordinate as well. For the above example, which shows potential energy surfaces offset in the bond coordinate, the $2 \leftarrow 0$ transition is highlighted, which may present the most intense absorption peak in a vibronic spectrum, but the $1 \leftarrow 0$, $3 \leftarrow 0$ etc. transitions are also probable, and will show reduced intensities of absorption, at wavelengths corresponding to the vertical transition energies. Similarly, the $0 \leftarrow 2$ transition would also have a large Franck-Condon factor, however in most scenarios the population in $v=2$ of the ground state will be less than that in $v=0$, and thus the experimentally observed vibronic feature will show a lower absorbance.

After absorption of a photon has occurred, in the most simplistic of examples, intramolecular vibrational energy redistribution, alongside intermolecular solute-to-solvent vibrational energy transfer, will cause rapid relaxation of the system to low lying vibrational levels of the lowest excited state of a particular spin multiplicity (often coined 'Kasha's rule').⁶¹ From here the system can electronically relax through emission of a photon, which in turn can be experimentally collected to garner an emission spectrum. The relaxation of the system, toward the minimum energy geometry of the excited state potential energy surface, prior to emission of a photon leads to the emission spectrum being red-shifted with respect to the absorption spectrum. This shift is coined a Stokes shift. The absorption and emission profiles, and their absolute position in energy space, can, in principle, be derived directly from an understanding of the potential energy surfaces of the ground and excited states, and derivation of the vibrational structure within each global or local minima. From there, one can examine the overlap of the vibronic wavefunctions in the two electronic states of interest and explicitly compute the electronic band profile of any absorption feature. In solution, explicit detection of vibronic features is often precluded by broadening caused by a multitude of effects including collisional broadening caused by variations in transition energy due to impacts with other molecules in solution, the Doppler shifts caused by variations of the velocities of sample in solution and the intrinsic broadening of spectral lines due to the uncertainty principle. Gas-phase spectra will be less affected by the collisional broadening aspect due to the much

lower particle densities, which is the most significant factor, resulting in discernible linewidths becoming measurable.

Figure 3 shows only the singlet manifold for a sample system. In reality, there are additional manifolds of alternate spin multiplicities, perhaps most significantly a set of triplet electronic states that exist within the same energy space. For most small organic species, the triplet manifold plays little role in the photophysics of the system, however as the size of the system increases, or alternatively when heavy atoms are added to the system, the probability of intersystem crossing (ISC) increases in the excited states, that is population transferring from the initially prepared singlet manifold to the triplet manifold. The rate of ISC is governed by the degree of vibrational overlap between the two states, as well as the degree of spin-orbit coupling, which is the coupling of an electrons spin to its orbital angular momentum. This effect can make the previously spin-forbidden transitions of singlet-to-triplet and vice versa allowed. Following ISC to a triplet state from the singlet ground state, the molecule will undergo vibrational relaxation to the lowest triplet state, T_1 , before radiatively relaxing back to the singlet ground state. As this radiative relaxation process is also spin-forbidden, it occurs on a much longer average timescale than that of a spin-allowed emissive process, commonly on the $>\mu\text{s}$ scale. Spin-forbidden emissive processes are known as phosphorescence, whilst spin-allowed emissive processes are known as fluorescence. Both of these processes will display a series of allowed vibronic transitions in the same manner as the absorption transitions described previously, with the $0 \rightarrow 1$ fluorescence transition shown on the Morse potential diagram in fig. 3. Fig. 4, below, shows the relationship between singlet and triplet electronic states as a function of energy for an arbitrary chemical system in the form of a Jablonski diagram. Spin allowed absorption of a photon and resultant fluorescence from a singlet excited state is shown, as well as the pathways associated with intersystem crossing to a triplet state and subsequent phosphorescence (formally spin forbidden emission). Also shown is non-radiative internal conversion between two triplet states, which is also possible between singlet excited states and the ground state, but which is omitted here for clarity.

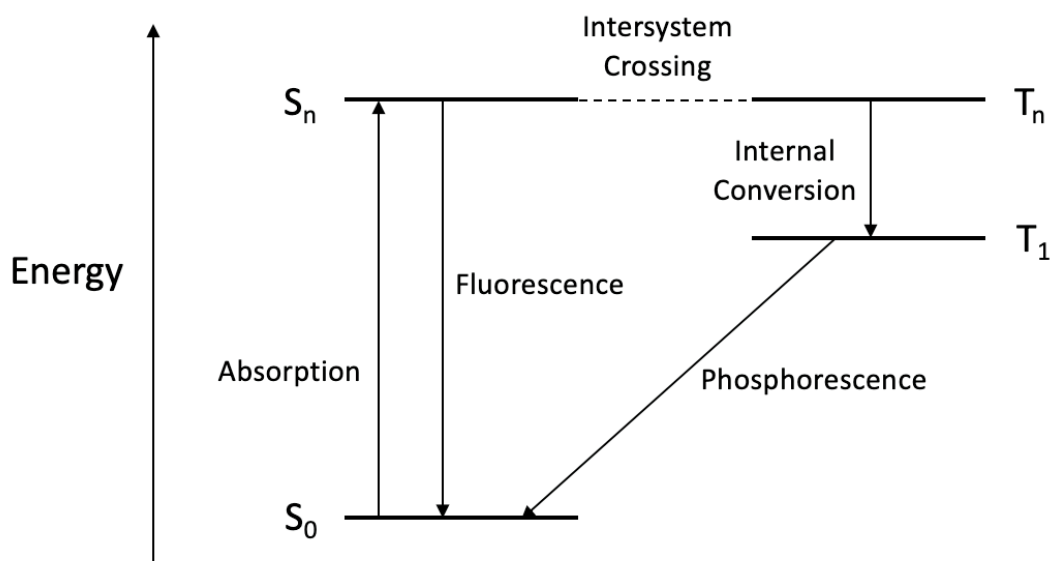


Figure 4 A Jablonski diagram for an arbitrary chemical system, showing the relation between the singlet ground state, S_0 , and a singlet excited state, S_n , and triplet excited states, T_n and T_1 , as well as the processes that allow the interchange between them.

In some cases, the excited state potential energy surfaces cannot be described by Morse potentials, but instead are repulsive with respect to a particular bonding coordinate of the molecule (typically $n-\sigma^*$ or $\pi-\sigma^*$), and nuclear relaxation on this potential energy surface leads to bond fission. This leads to a fundamental change to the chemical composition of the sample, as the bond will separate, normally homolytically, meaning each of the atoms involved in bonding retains an electron from the original bond. This generates a highly reactive species called a diradical, in reference to its doubly free radical nature. These species tend to be short lived, either recombining shortly after formation or more commonly reacting with something else in solution or undergoing a further intramolecular reaction.

Transient spectroscopy is an analytical technique used to study the excited states of sample molecules and monitor the development of those states with time. It differs from steady state spectroscopy in the aspect that the state or states being interrogated are short-lived, progressing over time, hence 'transient' spectroscopy. This is accomplished by inducing a physical or chemical change in a sample being

examined and monitoring these changes using time resolved absorption or emission spectroscopy. The type of change induced in the sample can vary depending on the sample conditions and the manner in which the change is induced. For the purposes of this thesis, the two key types of spectra recorded and discussed are:

1. Transient absorption spectra: a pulsed light source is used to induce the photon driven formation of transient excited electronic states, which subsequently relax back to the ground state, without a permanent change in the chemical composition of the sample or
2. Laser flash photolysis: a pulsed light source is used to induce the photon driven formation of new chemical species. In this case, the excited state population of the sample branches between relaxation to the ground state, and bond cleavage or molecular transformation and thus the ground state population of the sample does not recover at $t = \infty$.

The apparatus used in both measurements is identical, with the distinction between the two types of spectra arising solely from the effect photons have on the sample.

In this thesis, the transient absorption spectra recorded are pump-probe spectra, where the transient species are photonicly induced. In order to record these spectra the sample is exposed to a low power, broadband light source (probe) which, when monitored, provides a transmission spectrum of the sample. At some time, either prior to, or during, the probe excitation of the sample, a higher intensity pulsed light source initiates an alteration of the ground state population. This alteration is observed as changes in the absorption spectrum as a function of time. Spectra are plotted as a difference in optical density of the sample after excitation, abbreviated as ΔOD , which corresponds to:

$$\Delta OD (\lambda) = \log_{10} \frac{I_0(\lambda)}{I_t(\lambda)}$$

Equation 3 Difference in optical density for a selected wavelength. $I_0(\lambda)$ = intensity prior to excitation, $I_t(\lambda)$ = intensity after excitation.

An increase in ΔOD obtained corresponds to a reduction in transmitted light at a given wavelength, whilst a negative ΔOD value means an increase in transmission. A positive ΔOD value typically corresponds to an increase in absorption relative to the ground state as a result of the absorption of an excited state, (ESA). This is due to the detector responding to an attenuation in the intensity of the probe light passing through the sample due to absorption from the excited state induced by the pump source to subsequent higher excited states. A negative value corresponds to a decrease in absorption relative to the ground state of the chemicals under investigation, and is most often assigned as a ground state bleach (GSB): the removal of ground state population induced by the pump excitation, assuming the ESA is shifted in wavelength relative to the ground state absorption spectrum. This GSB results from depletion of the ground state population resulting in the reduction of light absorption at wavelengths corresponding to the ground state steady state absorption spectrum of the sample. This results in more probe light being transmitted by the sample at these wavelengths, and thus perceived by the detector, relative to a probe background measurement without the laser. If, for example, 40% of the sample population was promoted to a higher excited state by an excitation pulse, this would result in a substantial depletion of intensity of the previously observed steady state absorption spectrum of ground state molecules. Emission from the sample following pump excitation can also cause a negative ΔOD value to be observed, which can be corrected for by active background subtraction through deconvolution of the spectra using an emission spectrum of the sample created by the pump. Similarly, the pump can potentially induce stimulated emission in the sample during the excitation pulse. For this reason, the pump light source is frequently positioned perpendicularly to the probe light source, to allow for the observation of the samples luminescence with minimal scattering effects incurred from the laser.

The lifetimes of features observed in the transient spectra can yield great insight into the dynamics of the system being studied. Through observation of the lifetimes of different states (examination of signal magnitude attributed a spectroscopic feature with respect to time), information on the nature of the state responsible for the signal

can be gleaned. An example of this would be the observed duration of emission features, as fluorescence will have a markedly shorter lifetime than phosphorescence, often coincident with the pump pulse. Similarly, if an emission feature extends into the hundreds of nanoseconds it's likely originating from a triplet state. From comparison of the lifetimes of GSB, ESA and emission features, different spectroscopic features can be attributed to different states or species, as the difference in dynamics would suggest they arise from different origins. Conversely, correlation between the lifetimes of features can be used to attribute them to the same spectroscopic processes. An example would be if a bleach and a transient absorption feature shared similar lifetimes, they could be attributed to the same process: the depletion of a ground state absorption band via promotion of the molecule to an excited state, generating a GSB feature, and the subsequent absorption band of that excited state generating an ESA. Both features would decay at the same time, indicative of the induced excited state decaying back to the ground state, restoring the ground state absorption feature and reducing the magnitude of the ESA.

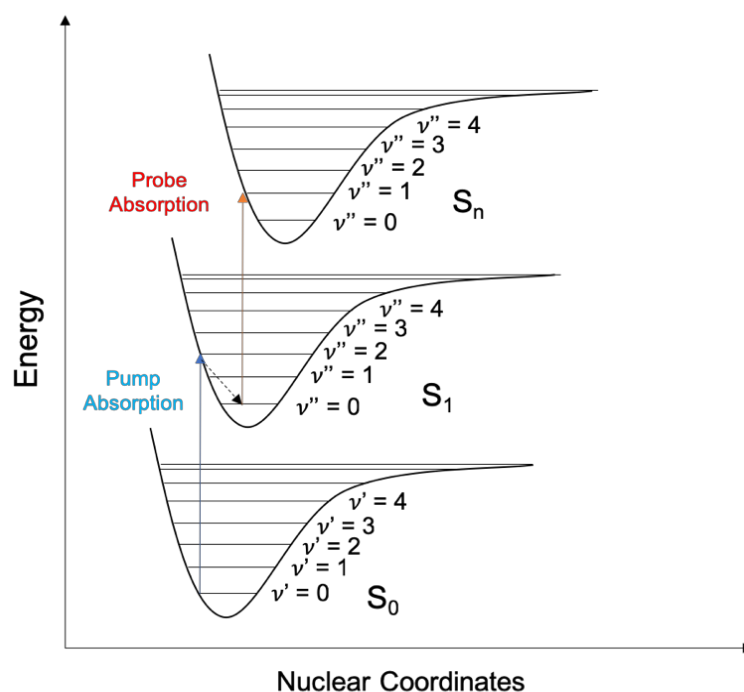


Figure 5 Adaptation of Fig.3 illustrating spin-allowed transient absorption (red arrow). Without the initial pump, there would be no absorption at the corresponding red wavelength. The lifetime of S_1 dictates for how long the transient red wavelength absorption can be observed.

In order to design a set of experimental conditions under which to record a pump-probe transient absorption or flash photolysis spectrum, the wavelength of the pump source has to be carefully selected. This information can be taken from a cursory look at the steady state absorption spectrum of the interrogated molecule. Firstly, the pump wavelength should be chosen so as to be at a wavelength suitable to induce an electronic transition in the molecule – thus one would normally attempt to use a wavelength corresponding to a peak maximum from the steady state spectrum. The pump wavelength will also impact the nature of the spectrum itself, as the range of energetically accessible excited states will change with the wavelength used to drive the excitation. If the wavelength selected is too low in energy, there may be few features visible within the spectrum, or alternatively the photon energy may not be sufficient to reach a state suitable to promote photochemical change. Conversely, if the goal of the experiment is to examine the spectroscopy of a molecule non-destructively, choosing a wavelength too high in energy may damage the molecule through photolysis. In the event the aim of the study is to monitor the photodegradation dynamics of the sample then this is not necessarily a problem. For experiments involving testing the photostability of a species in ambient sunlight, a high energy (<350 nm) pump wavelength might also not be appropriate.

Lasers are a commonly used pump source due to their monochromatic nature, their relatively short pulse durations but high powers, and their potential for wavelength tunability. This affords for more precise preparation of specific excited states, with high probability within the laser beam volume, and to afford the study of the evolution of the transient species with time. Time evolution of the transient species can be monitored in two manners. Firstly, the pump can be chosen to have a short time with respect to the probe, such that the probe is effectively continuous, and the probe can then be monitored as a function of time after the probe pulse. Alternatively, if the pump and probe have similar temporal widths, then the time delay between pump and probe can be scanned and the total probe-induced signal monitored as a function of delay time. This latter methodology is most commonly employed in ultrafast measurements, whereas the former is more common in experiments with time resolutions lower than ~ 100 fs. The reason for this discrepancy is that for continuous

monitoring of the probe signal after the pump is limited by the time response of the detectors and electronics, whereas, in order to achieve time resolution $< \sim 100$ ps one must bypass the inherent electronic time limitation of the equipment, and instead create a pump-probe delay using an optical delay scheme. The majority of the data presented in this report is shown on a timescale > 1 ns, and therefore the discussion will focus on instrumentation based on a pseudo-continuous probe with respect to the pump.

To facilitate the acquisition of the most useful ΔOD spectra, the probe source and detection ranges should ideally have as wide a range as possible in wavelength space: a sensitive ΔOD spectrum can only be acquired for wavelengths where the probe has an intense, reliable and stable output. Significant intensity fluctuations in the probe will increase the noise in the instrument, inducing increased error in the measurements. This would manifest as an increase or decrease in ΔOD for wavelengths affected by the fluctuation, as the intensity of the reference pulse would differ from that of the measurement pulse, which to the detector would be indistinguishable from the sample response. A method of combatting this effect would be to run multiple repeat measurements and average them, as fluctuations in the lamp are likely to be random in nature, compared to the signal from the sample, which should be consistent, barring photodegradation. Signal is therefore distinguishable from noise in terms of standard deviations from the noise floor. The output range of the probe source is also an important consideration, as the experimental error in observed ΔOD between the reference and measurement will become more significant if the output signal of the probe source is not very intense at a given wavelength. This is true if the range of pulse-to-pulse fluctuations of the probe source remains constant with output wavelength, as the degree of noise as a percentage of the total calculated difference will be more significant at less intense wavelengths. As an example, consider two probe wavelengths: one at the peak of the probes output and another near the minimum. If the peak output wavelength has an average observed intensity of 40,000 counts and the near-minimum wavelength has an average of 2000 counts, then for a global average intensity deviation of 500 counts, the noise will be vastly

more significant as a percentage of the total intensity for the lower intensity wavelength than for the peak output. Here, 'count' refers to the intensity output of the ICCD spectral camera detector system, described in more detail in the experimental chapter of this thesis. Counts are the unit of intensity and are subject to gain parameters within the detector system, and so do not necessarily refer to individual photon count events. Typically, the probe source intensity decays away from its central wavelength, such that at the edges of the spectral output range of a probe source the noise dramatically increases. Therefore, an ideal probe source should have some degree of intensity and short-term stability across the desired wavelength range of observable molecular transitions. The long-term stability of the probe source with time is another essential factor: if the probe intensity is unstable on the timescale of the molecular relaxation/photon driven chemical change, then quantifying timescales for these processes will become unreliable. Similarly, the detector system used must have a high sensitivity in order to be able to quantify relatively small changes in intensity between two measurements caused by the spectroscopic properties of the transient state. This sensitivity can be improved by using a cooled detector system, either by cryogenically cooling the sensor or, more commonly, thermoelectrically using a Peltier cooler system, lowering the noise floor through decreasing the dark level of the detector, that is noise generated through currents in the detector sensor. The probe and pump source can also be allowed to thermally equilibrate prior to measurements being acquired, reducing the variation in intensity between pulses.

The selection of the detector system is also an important factor in designing instrumentation, particularly for compounds in the gas phase where spectra are far more defined, although this is less of an issue in the solution phase due to broadening effects. The detector systems used are high resolution with respect to the application requirements, with the smallest discernible features being around the nanometre scale, much smaller than the width of the features being examined. For most modern systems, intensified charge coupled devices (ICCD) are used, normally in an array format, allowing for the acquisition of entire spectra with each pump or probe pulse. These camera detectors normally have controllable exposure times and can be set to acquire data after a time delay relative to the pump. A broadly accessible timeframe is

desirable for transient measurements, allowing for the study of different spectroscopic events. Sub-nanosecond transient absorption techniques are often referred to as 'ultrafast' transient absorption, and primarily study the picosecond and femtosecond timescales. These ultrafast techniques are used to study electron dynamics, such as examining electron dynamics and energy redistribution. On the nanosecond to microsecond timescale, chemical reaction dynamics and emission is typically studied, and these can sometimes extend into the millisecond and greater time regimes. Most instruments will have technical limitations that dictate which timescale they can observe; for instance, the xenon arc lamp used as a probe source in many transient spectrometers will operate in a pulsed configuration limited to a few milliseconds, restricting the maximum timescale.

Finally, it is worth noting some of the additional complexities that are evident when investigating flash photolysis as opposed to simple transients. A flash laser photolysis (FLP) spectrum will typically show ESA features indicative of the starting material (as in transient spectra), features due to chemical intermediates produced over the course of the reaction and features due to the final products of the reaction, all likely evolving over different timescales, both growing and decaying, and also potentially changing with successive measurements as the sample contained within the pump-probe volume is irrevocably altered. Therefore, care must be taken when studying such systems, as the composition of the interrogated volume may alter with successive acquisitions, meaning that averaging applied to measurements over successive pump-probe shots will potentially contain spectral features of reaction products formed by previous exposure, obscuring the true reaction dynamics. In short, the volume probed will change over the course of a multiple acquisition averaged measurement and will not have the same molecular composition during final measurement compared to the first. To compensate for this, a lower number of acquisitions can be used, reducing the number of pump-probe pulses averaged together to obtain a result, although this can have an impact on the quality of the acquisition. An alternative would be to use a method of replenishing the sample between pulses, such as a flow system. This requires larger volumes of sample but allows for the prevention of build-up of products from a photon-driven chemical reaction by clearing them away and replacing

them with fresh starting material. In a similar fashion, the reaction conditions of the flash photolysis reaction must be carefully controlled. Solvent environment, atmospheric conditions and temperature are all considerations that could affect the rate and outcome of a chemical reaction, and these conditions can also affect the outcome of a flash photolysis experiment.

It is important to choose a solvent that is transparent at the probe wavelength range in order to prevent the attenuation of the interrogating beam, as well as any distortions the absorption spectrum of the solvent would introduce to the transient spectrum. Likewise, it is very important that the solvent does not have appreciable absorption intensity at the pump wavelength, as this will potentially directly convolute the transient spectra obtained in addition to potentially inducing an unwanted reaction with the sample due to the induction of a more energetic excited state. It's also important to choose a solvent system that can effectively dissolve both the sample being studied and any known photoproducts, as insufficient solubility can cause the precipitation of these photoproducts, leading to increased scatter in the signal and potential damage to the sample vessel and instrumentation from exposure of the solid to the pump beam. An example would be the deposition of a photoproduct precipitate on the inside surface of the sample cuvette due to the use of an incompatible solvent. Atmospheric conditions are an important factor, as the presence of airborne species dissolved in solution, namely oxygen, can have implications for an experiment involving the creation of highly energetic excited states. The creation of triplet states using the pump source can lead to interactions with dissolved oxygen resulting in quenching of the sample, reducing the observed lifetime of its features, and potentially oxidation following a reaction with the induced excited state oxygen species this quenching can create. Another effect induced by the solution is solvatochromism, the shifting of a compounds spectral features through interaction with its solvent environment.

Flash photolysis was first developed following World War 2, by R. G. W. Norrish and G. Porter at Cambridge University, following efforts to investigate short-lived intermediates and free radicals, as well as develop new techniques to determine

reaction kinetics.⁶² Following on from their early work using intense light sources to generate and study the decay of methylene in 1947,⁶³ they adopted the use of flash tubes used for photography in order to develop a technique by which they could generate large amounts of radicals from simple compounds and study them spectroscopically.⁶⁴ The original apparatus used a high intensity flash generated by a gas-discharge flash tube placed parallel to the reaction chamber lasting a few milliseconds to induce a photoreaction. The intensity and duration of the flashes generated were dictated by the type of flash lamp used, with initial energies of up to 10 kJ being generated from a single discharge. This represented a substantial increase in the power available to drive reactions over existing methods and was used to induce and study the decomposition of a variety of different chemical species, including NO₂, as well as induce photochemical reactions, including that of acetone and ketene. Observations made by the pair at this time note that the rapid induction of these reactions with such relatively high pulse intensities produced unexpected results in some of the cases. In 1951, they published a spectroscopic study interrogating the hydrogen-oxygen explosion reaction induced via the flash photolysis of NO₂.⁶⁵ Kinetics to study the induced reaction were derived by sampling the absorption spectrum of the mixture every 200 microseconds, using a probe flash 50 microseconds in duration controlled by a timing wheel. Norrish and Porter won the Nobel prize for chemistry in 1967, alongside M. Eigen for his similar work using electrical and sonic impulses, for their work studying reaction intermediates induced by flash photolysis.

Subsequent work developing flash photolysis spectrometers led to more powerful and shorter pulses via the refinement of the flash tube methodology, and eventually the adoption of amplified photomultiplier cells as a means of detection coupled with a xenon arc lamp used as the probe source.⁶⁶ These adjustments were to allow for greater time resolution than the spectrographic plates used up to that point, offering resolutions of around a microsecond. The development of pulsed laser systems led to the next major improvement in the field of flash photolysis, allowing high pulse powers and excitation times on the nanosecond timescale.⁶⁷

1.3 Computational Background

Computational chemistry calculations are extremely useful tools for analysing chemical interactions, as they allow the simulation of electronic properties and molecular interactions, and thus a method for the analysis of molecular states, from electronic states to rotational states. They can also be used to forge a link between experimental properties and experimentally derived properties, that may be challenging to deduce from experiment alone. Thus they can be a powerful method of deriving and testing mechanisms of chemical reactions.

There are a variety of methods employed to compute molecular properties, ranging from computationally cheap methods based solely on classical mechanics, through to those that provide an excellent quantum mechanical descriptions of molecular systems and that deal with both static and dynamic electron correlation. Lying somewhere between these two limits is density functional theory (DFT). DFT uses the principle that the energy of a system is directly related to the electron density of the system, and so calculations made are based upon this relationship. DFT differs in its approach to *ab initio* methods in its use of spatially dependent electron density functionals to determine the properties of many-electron systems. This is an alternative to, for example Hartree-Fock theory which is an *ab initio* method that employs approximate solutions to the Schrodinger equation by constructing molecular orbitals from linear combinations of atomic orbitals.

The use of DFT also provides access to time dependent DFT (TD-DFT), which allows the calculation of excited state properties. TD-DFT is a response method, based on the ground state electron density computed in the original DFT ansatz. A mathematical description of TD-DFT is beyond the scope of this thesis, however it is worth noting that TD-DFT provides a very computationally efficient way of calculating excited state energies, and in some cases energy gradients and vibrational frequencies. In addition, TD-DFT calculations provide information on transition energies, transition properties (e.g. the contributions of molecular orbitals to electronic transitions) and oscillator strengths for electronic transitions.

DFT requires a functional to approximate the electron correlation and exchange energies of a molecular system. There are a range of functionals, each designed for different uses, but the most commonly used functional is a hybrid functional called B3LYP (standing for Becke, 3 parameter, Lee-Yang-Parr). This functional is often chosen as it offers good accuracy over a range of chemical problems, with relatively low computational expense⁶⁸. Hybrid DFT functionals employ a mixture of the electron exchange-correlation energy, determined by either experimental methods or estimated by another *ab initio* method and the exact Hartree-Fock value. The equation B3LYP employs for the electron exchange-correlation energy is shown below:

$$E_{xc}^{B3LYP} = E_c^{LDA} + E_x^{LDA} + a_c(E_c^{GGA} - E_c^{LDA}) + a_x(E_x^{GGA} - E_x^{LDA}) + a_0(E_x^{HF} - E_x^{LDA})$$

Equation 4 B3LYP electron exchange-correlation energy.

a_0 , a_c and a_x are fitting coefficients and have values of 0.2, 0.81 and 0.72 respectively, and were derived from the fitting of formation energies of small molecules. The term E_x^{HF} is the Hartree-Fock exact exchange functional. The terms E_c^{GGA} and E_x^{GGA} are both generalised gradient approximations; the exchange functional Becke 1988 (B-88) and correlation functional of Lee, Yang and Parr respectively.^{69,70} E_c^{LDA} and E_x^{LDA} are the local density approximation functionals for the correlation and exchange respectively.

For certain calculations, for example time-dependent DFT calculations in this work, an augmented version of B3LYP is used, called the Coulomb attenuating method or CAM-B3LYP. This method includes additional terms for more accurately modelling long distance interactions. Long distance interactions, within a chemical thesis, can be somewhat of a misnomer, and indeed herein the most pertinent ‘long range interaction’ is that of an electron in a high lying orbital, hence the use of this functional when computing excited state properties. CAM-B3LYP comprises of 0.19 Hartree-Fock

and 0.81 B-88 exchange interaction at short range and then 0.65 Hartree-Fock to 0.35 B-88 at long range.⁶⁸

Atomic orbitals are modelled in most computational methods with the use of basis sets. Basis sets are a representation of the orbitals that make up the electronic structure of atoms, comprised of a set of functions that approximately describe the shape of these atomic orbitals. The basis sets that offer the best description of atoms are those that use Slater-type orbital functions, based on hydrogen-like orbital approximations as these are capable of describing the electron probabilities accurately, with exponential decay at long range from the nucleus but also satisfy Kato's cusp condition at short range. However, Slater-type orbitals are computationally expensive to work with, as integral calculations are challenging to perform with linear combinations. As such the most commonly used basis sets are Gaussian functions to describe orbitals (most commonly called Gaussian-type orbitals, or GTOs), as this offers far easier mathematical description of linear combinations of orbitals within a molecule and decreases computational workload by 4-5 orders of magnitude compared to Slater-type orbitals. More Gaussian functions are required in a basis set to derive a similar description of an orbital as afforded by Slater type functions, but this still does not offset the gain in efficiency from the ease of computation. Examples of the two functions can be seen in figure 6.

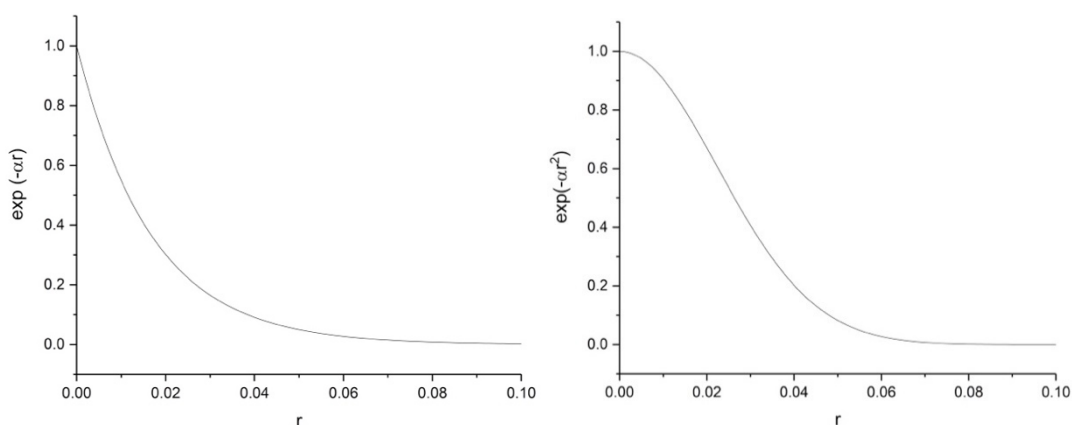


Figure 6 Typical Slater (left) and Gaussian (right) profile curves, as a function of an arbitrary radial distance variable r . These plots are indicative of functions used to model electronic orbitals. Slater functions are a better representation of electronic expectation values away from a nucleus but are more computationally costly to use.

There exists a wide variety of basis sets in use, differentiated by the type and amount of functions used to describe the orbitals. A basis set that contains the minimum number of functions to describe an atom is called a minimal basis set, describing each orbital with a single function. Additional functions are then included in more complete basis sets in order to account for polarisation and to add flexibility, enabling the more complete modelling of *d* and *f* type orbitals. Many basis sets also include 'diffuse' functions, which normally take the form of an exponential component to more accurately model the non-zero electron interaction 'tail' present at large distances from the nucleus, which a purely Gaussian description would find difficult to emulate. Larger atoms, such as those found at the core of transition metal complexes, can require the use of larger basis sets to describe the transition metal core electrons than those used to describe the lighter atoms that make up the ligand structure.⁷¹

Density functional theory has been increasingly employed in the analysis of chemical systems, largely due to the advent of more powerful available computers and the relatively computationally cheap nature of DFT. The development of more user-friendly commercial computational software, such as the Gaussian 09 software used in this work, also contributed to the more widespread use of these methods. Whilst DFT does often fail to produce quantitatively exact results, its capacity to provide qualitatively sound analysis at a computationally cheap cost makes it a powerful tool in aid of both chemical analysis and prediction of chemical and spectroscopic properties. The use of DFT in assisting with the assignment of spectroscopic features observed in transition metal complexes is a good example of this, as the methods described above can provide accurate simulations of the absorption and emission spectra of these complexes, as well as allow for the assessment of the molecular orbitals involved in those transitions.^{71,72}

1.4 Aims and objectives

1.4.1 Ir^{III} Complexes

The aim of this thesis with regards to the analysis of the Ir^{III} complexes presented here was to investigate their spectroscopic properties of a range of complexes and determine their chemical origin, ultimately leading towards an understanding of ligand structure on photophysical characteristics. A joint spectroscopic and computational methodology will be developed to yield insights into changing spectroscopic profiles caused by ligand substitution relative to a reference complex, upon which the all other complexes are derived. The combination of experimental and computational approaches will provide insights into the underlying electronic effects that ligand substitution or alteration has on the complex. In this way, with reference to a basis complex, it is sought to predict the photophysics of novel, as yet synthesised Ir^{III} complexes. If this predictive methodology can be efficiently developed, it may be possible to predict a suitable Ir^{III} complex structure to suit academic/commercial applications (towards rational design).

1.4.2 Triphenyltetrazolium compounds

The interrogation of 2,3,5-triphenyltetrazolium and three of its chemical variants is undertaken with the objective of determining whether the photochemical reduction of the parent tetrazolium can be inhibited through selective substitution of the N-phenyl moieties. The aim was to inhibit the formation of a photocoupled product, theorised to form following photoexcitation of the parent tetrazolium compound (optically clear), which subsequently or concomitantly leads to generation of an associated (coloured) formazan. This colour changing reaction is widely used as a reduction indicator, however the presence of light may be a false positive that this project seeks to eliminate. Using a combined spectroscopic and computational methodology, the photosensitivities of each of the compounds are investigated, along with an investigation of photoreaction products.

1.4.3 Cavity Ringdown Spectrometer

The aim of the development of the multipass optical cavity spectrometer is to construct a highly sensitive infrared absorption spectrometer for the study of high-energy, short-lived trace gas phase intermediates, called Criegee intermediates. The aim of this project is to develop an understanding of the rates of decay and potential chemical interactions of Criegee intermediates derived from select tropospheric significant alkenes, such as isoprene, which will be generated in the laboratory using the photolysis of diiodoalkanes, or other synthetic routes. A multi-pass absorption spectrometer is required to observe these species due to their very low concentrations and fast reaction kinetics, so enhanced path lengths techniques like cavity ringdown spectroscopy can provide sufficient sensitivities to observe and characterise them.

1.5 Summary

The information contained within this chapter provide an introduction and a context to the following work. The experimental and computational techniques discussed above form the basis of the analysis within the following thesis, and so it is important to provide a background to them here prior to further discussion. Transient spectroscopy and flash photolysis are similar, but distinct in the key aspect of the effect they have on the sample, so it is essential that this distinction is made and that the reader be aware of the basis of these techniques in order to contextualise the majority of the following thesis. Background to these techniques is also provided to demonstrate the usefulness of these techniques in analysing chemical systems and to further inform as to the mechanism of action of a flash photolysis/transient spectrometer. Much of this thesis also relies on the use of the computational techniques discussed above to aid in the assessment of the phenomena observed through experiment, so it is essential to provide an overview of the methods employed. The computational portion of the analysis used relies on density functional theory throughout, so the introduction above should serve as sufficient to understand the methodology of the following analysis. A more in-depth discussion of the specific apparatus used is provided at the opening of each relevant chapter, as well as in the following experimental chapter.

2. Experimental

2.1 Transient/Flash Photolysis Spectrometer

The compounds analysed in this work were interrogated using a transient absorption/flash photolysis spectrometer (Edinburgh Instruments LP920) that was acquired and upgraded during the course of this project. The sample is placed in the centre of the instrument in a cuvette and exposed to radiation in a perpendicular pump-probe arrangement. The probe used is a xenon flash-lamp positioned on-axis to the detector system, with a spectrally stable pulse time of approximately 2.5 ms, which is used as a background for a transient measurement. The pump excitation source used is a laser (Continuum Surelite Nd:YAG, 1064, 532, 355 and 266 nm, 10 Hz) with a pulse time of approximately 10 ns. The wavelengths employed in this thesis were 355 nm (pulse power ~1 mJ) and 266 nm (pulse power ~1 mJ). The laser input is situated 90° relative to the probe input and detector, allowing the simultaneous excitation of the sample by both inputs and mitigating interference or damage to the detector from the laser, whilst also allowing the option to obtain emission measurements.

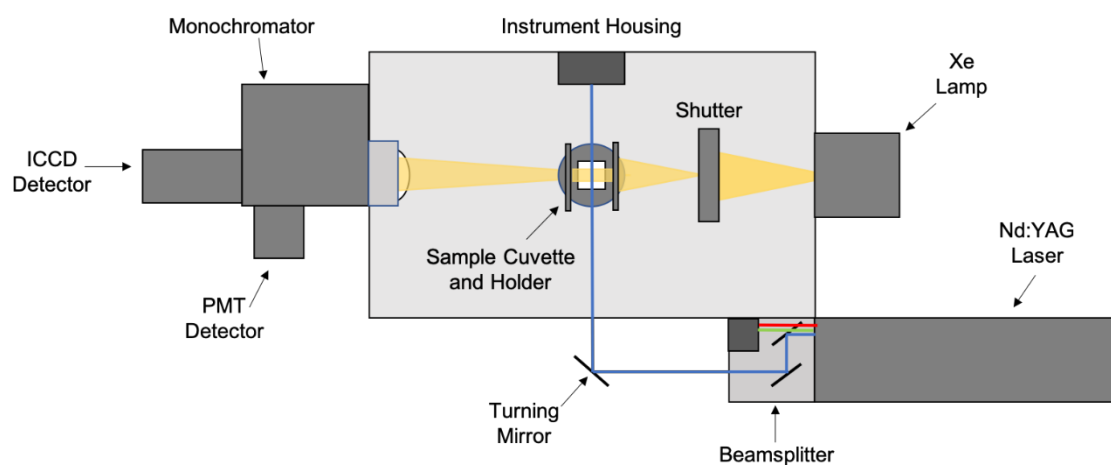


Figure 7 Diagram of the transient absorption/flash photolysis spectrometer used in this work, (Edinburgh Instruments LP920), from above.

The instrument itself has two modes of detection: an intensified charge-coupled device (ICCD) detector unit and a second detector unit with light from the sample transmitted by a monochromator grating. In the latter case, either a photomultiplier

tube (PMT) (200 – 900 nm) or InGaAs (900 – 2000 nm) detector unit can be used, depending on the wavelength range required, although only the PMT detector is used in this work. The ICCD was added to the instrument along with additional shutter equipment for the flash lamp during the course of the project, enabling much more rapid acquisition of spectra than using the PMT, as well as providing more control over the sample exposure.

The flash-lamp is spectrally stable for the majority of the duration of the pulse, save for a stabilisation period at the beginning, where the lamp is voltage overdriven to initiate radiation. Subsequent to that, once the lamp is stable with respect to both intensity and emission spectrum, the early part of the pulse period is used as a spectral background, with the laser pulse timed to occur at a set interval after the lamp has stabilised, for example 0.5 ms. The laser pulse will excite the sample, inducing a change in the sample spectral response to the probe lamp. A trio of measurements is made for any given mode of operation, kinetic or spectral, allowing for a change in optical density to be obtained: a measurement of the sample using just the flash-lamp, a measurement with both the lamp and the laser pulse and finally a measurement using just the laser, with the lamp shuttered. The measurement with just the lamp serves as a probe background, whilst the laser only measurement is an emission background. Using these three spectra and the equation below (equation 5), an emission subtracted ΔOD spectra can be obtained, detailing changes in absorption due to the excitation of the sample.

$$\Delta OD(\lambda) = \log_{10} \left(\frac{I_p(\lambda)}{I_T(\lambda) - I_F(\lambda)} \right)$$

Equation 5 Calculation used by the L900 spectrometer software to derive a transient absorption spectrum. $I_p(\lambda)$ = probe background intensity, $I_T(\lambda)$ = measurement intensity, $I_F(\lambda)$ = fluorescence background intensity.

A ΔOD spectrum is a measure of the change in optical density of a sample following excitation. It is therefore in this case a representation of the difference between the samples ground state and that of the excited state or photoinduced product of the

sample. A negative value on a ΔOD spectrum represents a decrease in opacity at the corresponding wavelength and a positive value represents an increase. An increase generally means that the excited state or photo-product absorbs more light at that wavelength than the initial state did prior to excitation. A decrease corresponds to bleaching due to depletion of the ground state, removing a transition that was previously being accessed by the lamp input at that wavelength, resulting in more of the lamp light passing through the excited state solution and to the detector. Emission of the sample following excitation would also appear as a decrease in a ΔOD spectrum, but these are generally subtracted by the emission background. Stimulated emission is not explicitly distinguished relative to fluorescence or phosphorescence by the equipment used here and is likely subtracted along with the emission background.

2.1.1 Transient Absorption Spectra

When using the ICCD as a detector, entire spectra can be obtained from a single measurement for the range 200 – 900 nm. This is limited, however, by the probe lamp output, shown in figure 8 below. A comparison of a lamp-only spectrum and one in which the laser is also used to excite the sample yields a ΔOD spectrum. This measurement is not inherently time-resolved, but a delay relative to the laser pulse can be set, and a combination of these spectra can give an indication of the evolution of the transient with time. The term ‘transient absorption’ is used to refer to these spectra despite the lack of time information, as they are the absorption spectra of transient species and this terminology is used throughout this thesis. This terminology is commonly used within literature in this field.

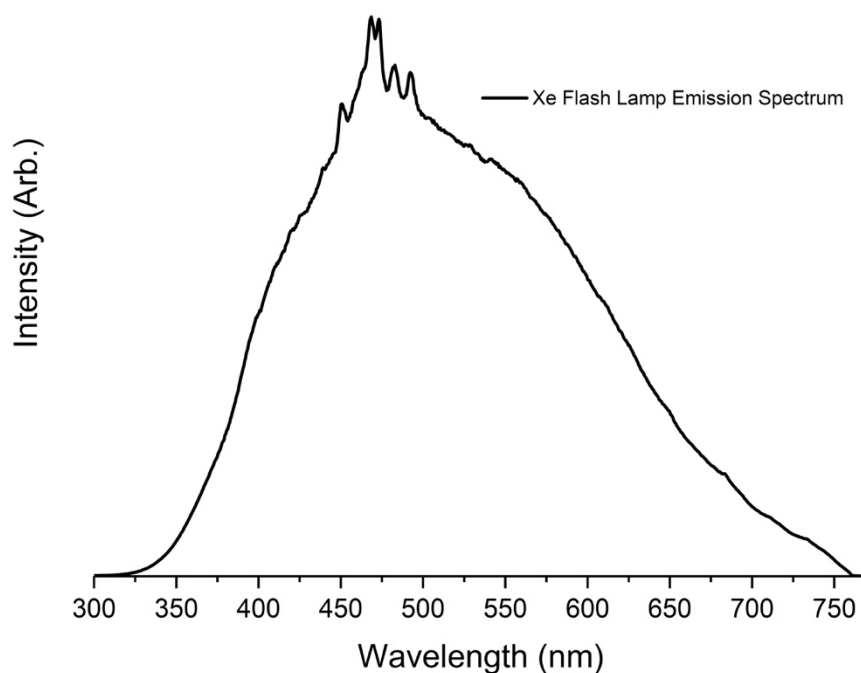


Figure 8 ICCD spectrum of Xe flash lamp emission spectrum. This lamp is used as the probe in the LP920 spectrometer, which limits the wavelengths over which transient features can be observed. At the edges of this spectrum, as the intensity decreases, there is increased noise in the transient spectra.

Emission spectra of the sample can also be obtained by exciting the sample with the laser only, as the laser input axis is positioned at 90° relative to the detector lamp axis, allowing for acquisition of the emission of the sample with minimal interference from the excitation source. Due to the inherent variation in pulse output and lack of available means to accurately monitor input power, quantum yield data is unable to be obtained using this instrumentation and is not directly relevant to the analysis presented herein.

2.1.2 Transient Kinetics

The detector module can be set up to use a photomultiplier tube (PMT) or Indium-Gallium-Arsenic (InGaAs) detector in pairing with a monochromator, allowing for time-resolved ΔOD spectra to be obtained for narrow bands of wavelengths in a similar manner to the above ICCD. The PMT offers good responsivity for the range 200 – 900 nm. The detection method allows the observation of changes in the absorption of the sample following laser excitation with time. This enables feature lifetimes to be

obtained for spectroscopic features observed in the transient absorption trace and the emission trace obtained by the ICCD.

The PMT is a vacuum tube that uses a series of dynodes, electrodes that release additional electrons when struck by an incident electron, in conjunction with an anode and cathode to translate a photonic signal into an electrical signal whilst simultaneously amplifying it. The photons are incident upon the cathode and cause the ejection of electrons as per the photoelectric effect, which then impact upon the first dynode triggering a cascade of electrons that eventually reach the anode on the other side of the tube and generate a signal. This method intrinsically amplifies the incident signal and is highly sensitive, leading to good detectivity and therefore is appropriate for use when detecting even weak output signals. However, the PMT is unable to distinguish between incident wavelengths, requiring the use of the monochromator to select the desired wavelength. The monochromator used in this work is typically operated with a bandwidth of 2.05 nm, as this gives a reasonable signal to noise ratio without impacting the accuracy of the results, as most features studied are relatively broad in wavelength space. The oscilloscope used to digitise the output from the detector has a temporal resolution of around 4 ns and the laser pulse duration of around 10 ns means that early time data will have some inherent error due to this for certain wavelengths, although some of the compounds studied in this work typically possess transient features with lifetimes 1-3 orders of magnitude larger than this, meaning kinetic lifetimes can still be reliably deduced from the data obtained without further treatment. The PMT can be used to obtain spectral data by performing a wavelength map. This map involves obtaining a kinetic profile of the chosen wavelength range, stepping the wavelength by a fixed amount between measurements. By choosing a time value after the onset of the laser pulse and obtaining the intensity for each of the examined wavelengths at that point, a transient spectrum can be obtained for that timescale. This mode of measurement is inappropriate to be employed for the light-sensitive compounds due to deleterious effects on the sample with progressive measurements, meaning the spectrum would not be consistent throughout. This method can be used to examine the early timeframe of a compounds response in lieu of the ICCD detection system, as the laser

intensity is too high for the ICCD to safely examine close to the onset of the pulse, as well as providing an alternative measurement to corroborate the measurements of the ICCD at later timescales.

2.2 Computational

2.2.1 Iridium Complexes

The complex structures were optimised in the Gaussian 09 software package on both the lowest singlet and triplet spin states. The complexes were modelled as monocationic where applicable and without the PF₆ pairing ion. The complexes were optimised using the B3LYP functional, using the 6-31G* basis set for the lighter atoms and the Stuttgart-Dresden core potential and basis set for the iridium. The complexes properties were computed in an implicit chloroform solvent using a self-consistent reaction field model, which simulates the solvent effects by treating the complex within a dielectric continuum ($\epsilon = 4.7113$). Very tight convergence criteria and an ultrafine integration grid were used for all optimisations. All optimisations were confirmed as minima through harmonic vibrational frequency calculations.

Stationary point energy calculations were performed for each of the optimised geometries for the opposing spin state to the optimization process, freezing the geometry but evaluating the energy. This gives the triplet energy at the singlet geometry and vice versa for each of the complexes. Using these stationary point calculations in conjunction with the geometry optimisations, the vertical transitions between the ground states of the singlet and triplet states can be determined, $T_1 \leftarrow S_0$ corresponding to spin forbidden absorption (blue, fig 9) and $T_1 \rightarrow S_0$ (red, fig 9) corresponding to spin forbidden emission. The energy difference between the singlet geometry, triplet spin state stationary point calculation and the singlet state geometry optimisation should correspond to the photon energy of the spin forbidden absorption, per the Franck-Condon principle. Figure 9 is similar to figure 3 in appearance, save for the higher energy state being a triplet state in this case, and is shown here purely for illustrative purposes. In reality the triplet and singlet manifolds may have differing minimum energy geometries along the schematic bond coordinate,

and may have higher/lower energies. Following on from this, the difference between the triplet optimised geometries and the stationary point singlet state energy calculation performed using this geometry corresponds to the emission energy.

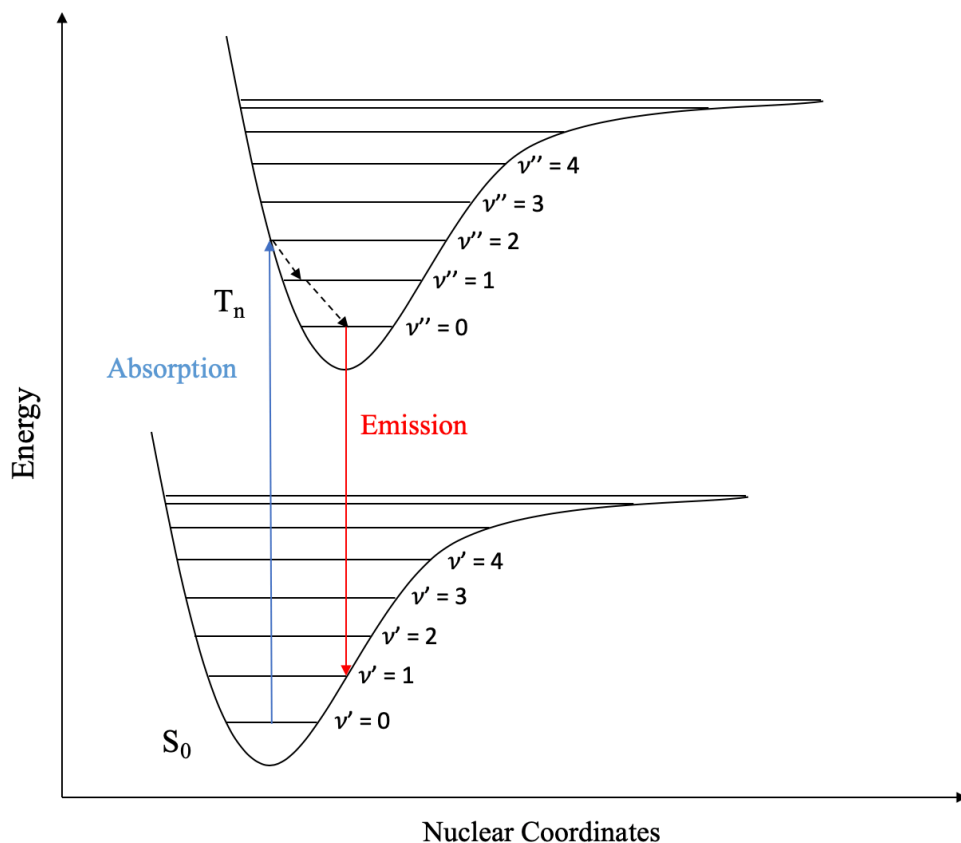


Figure 9 Morse potential diagram showing an example of the Franck-Condon vertical transitions for spin-forbidden absorption and phosphorescent emission to and from a triplet state, beginning and ending at the singlet ground state.

As there will be a geometric difference in the complex when it is in the triplet state compared to the singlet state, the adiabatic $\nu = 0 \leftarrow \nu = 0$ transition will not be vertical. Owing to the fact that electronic transitions occur effectively instantaneously on the timescale of nuclear motion, per the Born-Oppenheimer approximation, the transitions between electronic states will be dictated by the degree of overlap between the wavefunctions of the two electronic states at that point, leading to favoured transitions where $\Delta\nu \neq 0$. As per Kasha's rule, after photoexcitation, the molecule will rapidly relax non-radiatively via internal conversion to its lowest electronic and vibrational excited state, and it is from this state emission is most likely

to occur. This gives rise to a Stokes shift as a result of the change in nuclear geometry, whereby the emission is lower in energy than the photon absorbed.

Spin-allowed absorption features were simulated using time-dependent (TD-DFT) calculations with the same criteria as above, using the CAM-B3LYP functional. Molecular orbital decomposition was performed using the GaussSum software package based on calculations performed at the singlet minimum energy optimised geometries for each complex.

2.2.2 Tetrazolium and Formazans

All tetrazolium and formazan structures were optimised using the Gaussian 09 software package in the electronic ground singlet state, without counterions present in the case of the tetrazolium compounds. The B3LYP functional was used in conjunction with the 6-31G* basis set and all calculations were performed with very tight convergence criteria with an ultrafine integration grid. The compounds were evaluated in an implicit acetonitrile solvent using a self-consistent reaction field model, simulating solvent effects with a dielectric continuum ($\epsilon = 35.688$). TD-DFT calculations were used to simulate the spectra of the compounds from the singlet ground states using the CAM-B3LYP functional and otherwise identical specifications. Molecular orbital decomposition was performed using the GaussSum software package based on molecular orbital calculations performed at the singlet state. In both cases, additional information about specific calculations are provided in the text, for example details on spectral convolution, or details of more advanced calculated spectroscopic properties.

2.3 Sample Preparation

2.3.1 Iridium Complexes

All iridium complexes in this work were provided in powder form following synthesis by the Pope group at Cardiff University. Their purity and structures were confirmed by the Pope group using ^1H and ^{13}C NMR as well as high resolution mass spectrometry. Samples of each were dissolved in HPLC-grade chloroform and placed in a quartz

cuvette for all spectroscopic measurements. Based on absorption spectra acquired, 355 nm was chosen as the pump excitation wavelength for transient absorption measurements, as it was the lowest photon energy pump wavelength available with strong absorption by the complexes that provided access to the full visible emission spectrum of each compound. The use of a shorter pump wavelength, such as 266 nm, might prove damaging to the complex (for example, 266 nm radiation is more likely to induce photodissociation from high lying repulsive potential energy surfaces) whilst not necessarily providing any more useful spectroscopic information over the region interrogated by the probe lamp. All spectroscopic experiments were conducted at room temperature (approx. 20 °C).

2.3.2 Tetrazolium and Formazan

The tetrazolium and formazan compounds in this work were provided in powder form following synthesis by the Fallis group at Cardiff University. Their synthesis was confirmed using ^1H and ^{13}C NMR as well as mass spectrometry. Samples of each were dissolved in HPLC-grade acetonitrile at a concentration of 100 μM for the tetrazoliums and 10 μM for the triphenylformazan and placed in a quartz cuvette for all spectroscopic measurements. Based on absorption spectra acquired, 266 nm was chosen as the pump excitation wavelength for transient absorption measurements, as this was the only available output wavelength at which the compounds possessed a strong absorption cross-section. All spectroscopic experiments were conducted at room temperature (approx. 20 °C).

The degassing procedure used for the atmospheric controlled mass spectrum study utilised a specialised cuvette with a tap, for sealing the vessel and allowing inlet and outlet of gases, and a bulb portion, for freezing the sample. The cuvette apparatus was connected to a Schlenk vacuum gas manifold equipped with a vacuum pump and nitrogen output line. The aqueous sample was stored in the bulb compartment and this portion was submerged in liquid nitrogen until the sample became solid. At this point, the vacuum line was used to extract the atmosphere from the cuvette apparatus

whilst keeping the sample frozen. The nitrogen line was used to refill the apparatus whilst the sample was allowed to thaw. This procedure was repeated eight times, then the tap was sealed on the cuvette apparatus to maintain the nitrogen atmosphere and it was removed from the Schlenk manifold.

3. Transient Spectroscopic and Computational Analysis of Red-Emitting Iridium (III) Quinoxaline Complexes

3.1 Introduction to Iridium Complexes

The organometallic complexes studied in this work are Ir^{III} complexes, formed from organic ligands coordinated to an iridium metal core. Organometallic transition metal complexes have an electronic structural configuration that is defined by the interaction of the metal core with the molecular orbitals of the ligands bound to them. Iridium (III) complexes are of 5d⁶ character due to the 3+ cationic nature of the iridium atom, with partially occupied *d* orbitals which are degenerate in free space. Under the influence of the field caused by the molecular orbitals of a ligand set, this degeneracy is removed. An octahedral configuration with six metal-ligand bonds destabilises the d_z² and d_x² - y² orbitals relative to free space, whilst the remaining three orbitals, the d_{xy}, d_{xz} and d_{yz} orbitals, are lowered in energy. The members of the two sets are degenerate with respect to the other members, and the difference in energy between the two sets is labelled 'Δ_o' in octahedral structures, which is known as the ligand field splitting parameter. The removal of degeneracy occurs due to the orientation of the ligands with respect to the metal centre (under an appropriate symmetry group) in the octahedral bonding configuration, as the d_x² - y² and d_z² orbitals are oriented directly along the metal-ligand bond axis, resulting in them interacting with the ligands to form σ bonding (an associated antibonding) orbitals, whilst the remaining three are orientated between the metal-ligand bonds, do not lead to σ bonding contributions to the molecular orbitals of the system, and thus are considered non-bonding. This is shown in figure 10. The orbitals formed are designated t_{2g} and e_g, forming the HOMO and LUMO respectively, under the O_h point group. The terminology 'octahedral' is commonly used in organometallic chemistry to describe complexes coordinated with 6 bonding sites, even if they may not necessarily belong to the O_h point group.

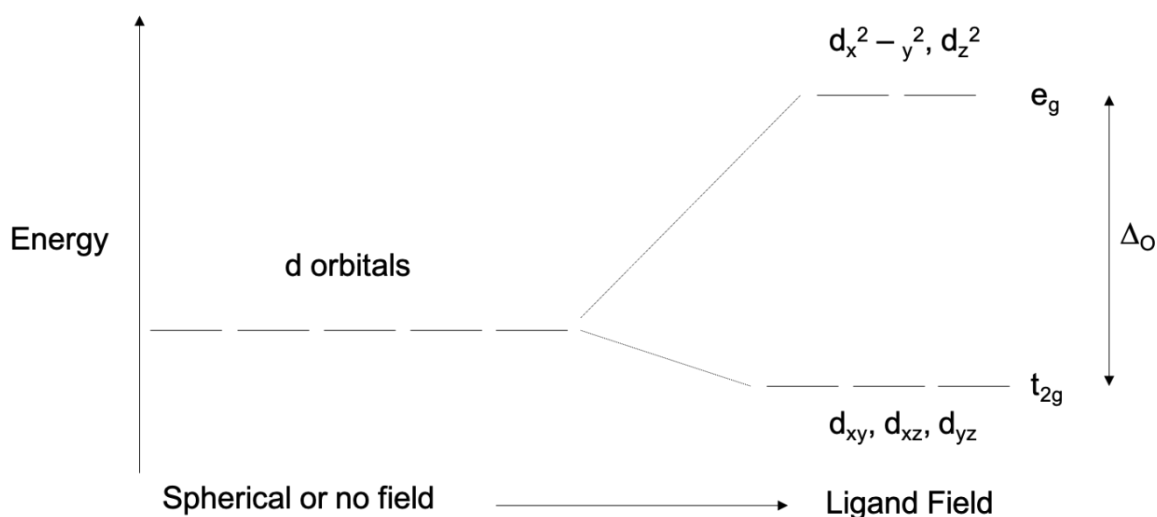


Figure 10 Simplified description of ligand field induced d-orbital splitting

A phenomenon known as π -backbonding can occur whereby π^* orbitals centred on the LUMO of a ligand can interact with them, resulting in electron donation from the metal. The magnitude of Δ_o can be altered by the π acceptor or donator character of ligands coordinated to the metal, as well as by the properties of the metal itself, such as charge and position within the transition metal group. Ligands can be listed according to their π acceptor/donor character and thus by the impact they have on Δ_o , in what is known as the spectrochemical series. π acceptor ligands, also known as 'strong field' ligands, such as CN^- and CO increase Δ_o through bonding with the d_{xy} , d_{yz} and d_{xz} orbitals, accepting electrons from the metal and producing a new set of bonding orbitals lower in energy relative to these non-bonding orbitals. π donating ligands are ligands where the inverse occurs, and the ligand donates electrons to the metal. This lowers the magnitude of Δ_o through the generation of an anti-bonding orbital higher in energy than that of the non-bonding metal orbitals d_{xy} , d_{yz} and d_{xz} . These effects are shown in figure 11.

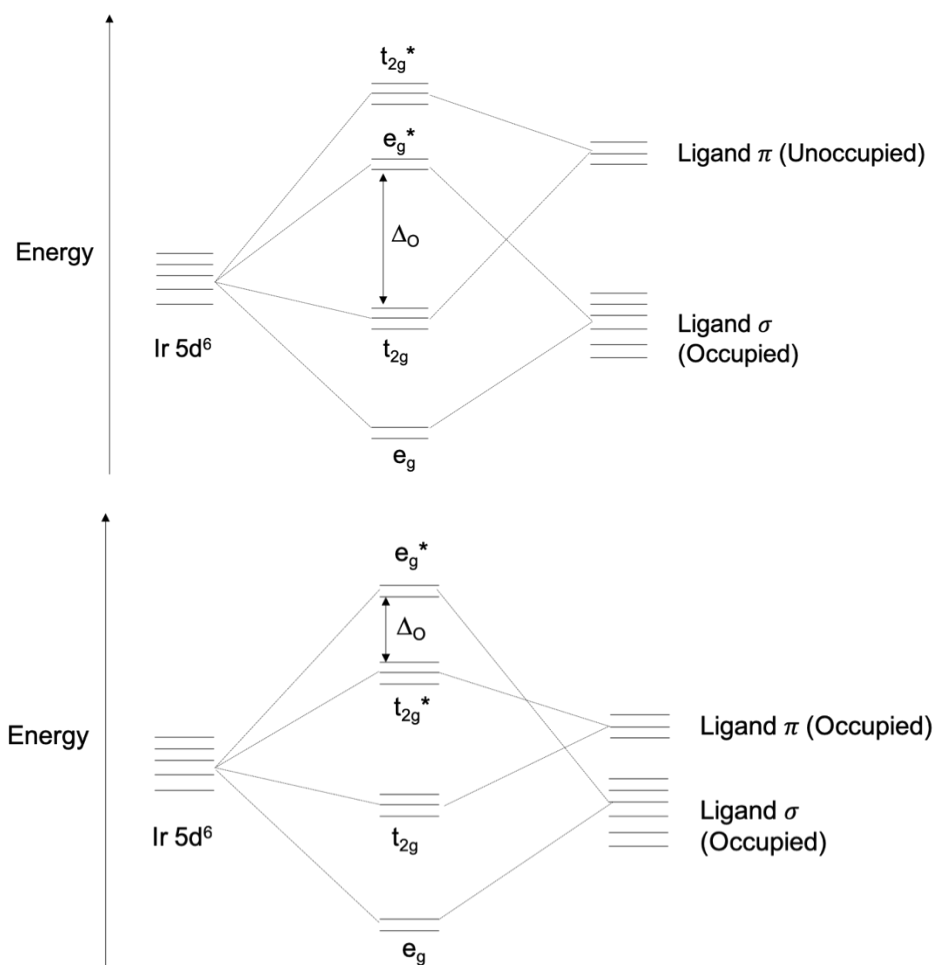


Figure 11 Molecular orbital diagrams of π acceptor (top) and π donor (below) bonding with a transition metal.

The magnitude of Δ_O results in the complex as a whole being labelled either low- or high-spin, where electrons occupy either the t_{2g} orbitals (in the case of low-spin) by pairing up, or fill both the t_{2g} and e_g orbitals in an unpaired manner, starting with the t_{2g} (in the case of high-spin). This occurs due to Hund's rule, which states that the lowest energy configuration is the one with the greatest value of spin multiplicity across degenerate HOMO/SOMO levels. Whether a complex is high- or low-spin depends on whether the energetic cost of spin pairing is greater than that of Δ_O , i.e. whether or not it is most energetically efficient to doubly occupy the t_{2g} orbitals or singly occupy the t_{2g} and e_g orbitals, overcoming Δ_O . Ir^{III} octahedral complexes are predominantly low-spin, regardless of ligand field strength, due in part to the position

of iridium in its transition metal series and the charge on the cation itself, which increases ligand field strength.

Ligands can coordinate to octahedral Ir^{III} complexes through more than one bonding site per ligand. Whilst the most simplistic organometallic complexes might have a single σ -bond per ligand, common with smaller ligands (e.g. CoF₆³⁻ or Fe(CO)₅), larger ligands can bind to the metal core through multiple sites. This is termed chelation, and ligands that perform this type of bonding are described as polydentate ligands, with a classic example being EDTA. The simplest polydentate ligands are bidentate and tridentate ligands, which coordinate with 2 and 3 bonds respectively. All of the novel iridium complexes discussed in this work are composed of either bidentate or tridentate ligands. Chelation reduces the likelihood that a complex will undergo ligand substitution to lower coordinating molecules, as, for example, the entropy of the system would decrease if two monodentate ligands were to replace a bidentate ligand, providing a degree of stability against substitution by molecules in solution e.g. water. In the octahedral geometry, 3 bidentate ligands can generally be accommodated in a complex, or 2 tridentate ligands. In the event that the ligands are all identical, the complex is described as being 'homoleptic', and 'heteroleptic' if this is not the case.

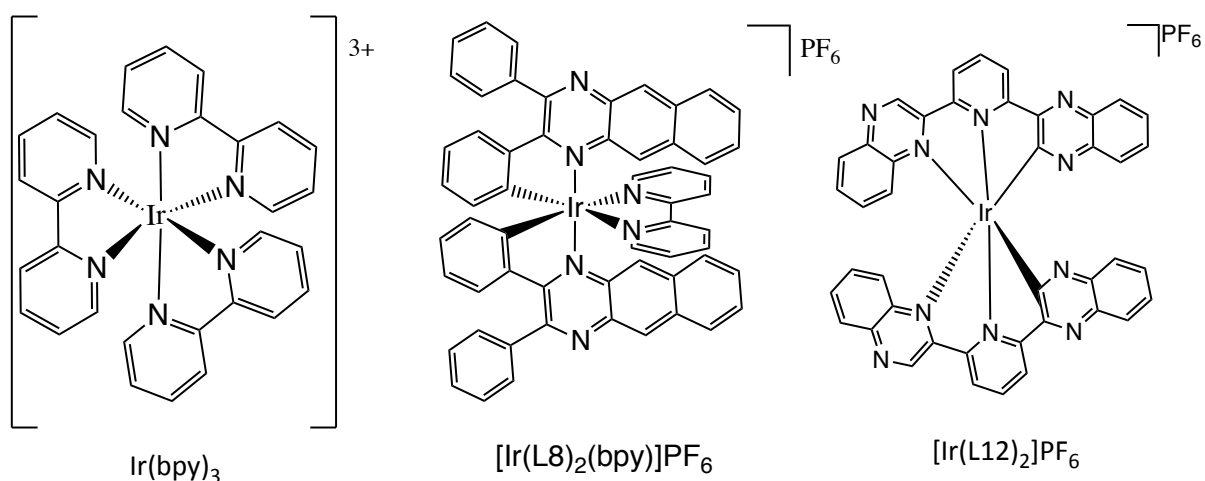


Figure 12 Examples of different Ir^{III} complexes, all of which are viable phosphors. Ir(bpy)₃ is perhaps the most well known of these compounds, and forms the basis for much of the literature spectroscopic work on these complexes. The latter two are novel complexes, for which the spectroscopy is reported herein.

In fig. 12 above, three examples of Ir^{III} complexes can be seen. The Ir(bpy)₃ complex is an example of a homoleptic bidentate complex, with all three ligands identical and coordinating via two bonding sites. The [Ir(L8)₂(bpy)]PF₆ and [Ir(L12)₂]PF₆ complexes, examined in this work, are examples of a heteroleptic bidentate complex and a homoleptic tridentate complex respectively. The ligand structure of the L8 bipyridine complex is a common one in the field of Ir^{III} complex development, which takes the form Ir(C[^]N)₂(anc), where the C[^]N ligand is known as a cyclometallating ligand, coordinating via a C – X and a N – X bond to the metal centre, whilst the ‘anc’ is designated as an ‘ancillary’ ligand, in this case bipyridine. All the bidentate complexes in this thesis are of this form.

One of the most prominent uses of iridium complexes are as ‘phosphors’, a term used here to describe light-emitting substances. Phosphors are generally stimulated using photoexcitation, although electrophosphorescent devices, such as those found in OLED displays, rely on electronic stimulation. Phosphors are distinguished by their emissive properties, with emission lifetimes ranging from the nanosecond timescale to the >1 millisecond timescale and with a wide variety of chemical structures and properties which can change the wavelengths of emission. Phosphors are used in a range of applications that require the production or harnessing of light and thus are designed and/or chosen to suit the commercial application. Other considerations like chemical inertness and low toxicity are also important, given that phosphors are commonly used in consumer applications such as televisions and lightbulbs. An ideal phosphor would therefore be one with highly tuneable, discrete emissive properties, with a corresponding tuneable lifetime, and high absorption cross-section in the visible region for ease of excitation in applications such as solar light harvesting or display screens using a backlight. Longer lifetimes are advantageous for applications such as lighting equipment, particularly in signage for use in the event of an emergency, which often has to be visible in low light conditions. Shorter lifetime applications would include computer monitors or other displays, where an intense, colour tuneable, short-lived discrete emission would be ideal in order to provide a clear picture with minimal blurring from frame to successive frame caused by residue from a prior excitation.

Photostability is another priority when choosing a phosphor. Most applications desire a phosphor which can be repeatedly electronically excited prior to emission, and does not bleach or fade over repeated excitations. Phosphors should not be the limiting factor in an application and therefore are often required to be photostable over several years, without appreciable degradation. Degradation may also occur through chemical reaction with other species in the operating environment, so it is essential to choose a good combination of phosphor and environment to ensure that unwanted deleterious reactions do not occur. Possible sources of trace or bulk co-reactants include any cofactors in solution, the atmosphere the phosphor is stored under, and the solvent and container materials themselves. The photostability of the phosphor can also influence chemical stability: the phosphor should not have highly reactive excited states, such that photoexcitation increases the rate of self-reaction or reaction with other environmental species. Of course, it is perfectly viable to alter the environment to reduce chemical reactivity, rather than changing the phosphor. However, the more inert the phosphor species, typically the more versatile it is.

Electronic quenching is another important consideration in choosing a phosphor. If the phosphor has a high collisional quenching cross section within the chosen environment, this may shorten the excited state lifetime and reduce the emission quantum yield to a point where the phosphor is no longer viable for the particular application. This is often a significant consideration when the phosphor may be in solution and also in the presence of molecular oxygen, which is a common and relatively significant quencher of excited triplet state.

Finally, one must choose a phosphor based on more consumer-driven practical considerations. One must consider the toxicity of the phosphor, where once again, a more chemically inert phosphor typically has the advantage of being less likely to be a health hazard. When choosing or designing a light-emitting compound, the expense, the ease of synthesis and the waste created in the synthesis should be evaluated. Most phosphors are for commercial applications are mass produced so the synthesis process should be as simple and inexpensive as possible, preferably allowing for modification to the phosphor chemical structure, as this is often where the

spectroscopic tuneability of light emitting compound classes derives. In addition, it is advantageous if the synthesis does not produce significantly toxic by-products: ease of disposal, social care and cost all should factor into this.

Many of these ideal phosphor properties apply to iridium (III) complexes, hence their widespread usage in this field. Iridium (III) complexes generally feature high efficiency luminescence owing to their high capacity for accessing singlet excited states, but also triplet excited states via inter-system crossing,⁷³ commonly considered to be near unitary following excitation,⁷⁴ and consequently can possess potentially 100% efficient emission with respect to electroluminescent excitation.⁷⁵ The large spin-orbit coupling constants typical of Ir^{III} complexes, which are on average significantly higher than comparable complexes based around other transition metals,^{74,76} are what enable inter-system crossing to occur. Spin orbit coupling is a relativistic effect that arises through the coupling of an electron's spin to its orbital angular momentum, causing formally spin-forbidden processes to become allowed. The triplet states responsible for phosphorescence are most commonly metal-to-ligand (³MLCT) and ³ $\pi - \pi^*$ ligand-to-ligand charge transfer (³LLCT) in nature.^{72,76,77} The metal-to-ligand and ligand-to-ligand charge transfer transitions, which are readily accessible within the visible region in Ir^{III} complexes, means that subtle changes to the ligand structure often result in changes to the emissive properties of the complex. Due to the enormous number of potential ligand structures that can be complexed to the iridium core, these systems offer superb fine-tuning of luminescence through ligand adjustment in this way.^{76,78,79}

In addition to providing high-efficiency luminescence, the multitude of states accessible to Ir^{III} complexes mean that they frequently have large molar extinction coefficients in the short-wavelength visible and UV regions,⁷⁹⁻⁸¹ although absorption cross-sections are generally reduced in the region >500 nm. Ligand centred (LC) transitions, $\pi - \pi^*$ and $n - \pi^*$ in nature, which are responsible for very intense, short-wavelength (<300 nm) absorption features are commonly observed in Ir^{III} complexes.^{79,81} ^{1,3}LLCT between cyclometallating ligands and ^{1,3}MLCT transitions arising from the 5d orbitals centred around the metal produce less intense absorption features extending to longer wavelengths relative to those of the LC transitions (300 –

500 nm).^{74,79,81} Through the use of cyanine dyes it has been demonstrated that absorption can be extended into the near infrared,⁸² broadening the potential applications of these phosphors.

Ir^{III} complexes have been synthesised that display excellent photostability, having long service lifetimes, and are highly resilient to repeated and protracted photoexcitation.^{74,83} The photostability of a chosen complex is highly dependent on the nature and structure of the ligands used, however, generally overcoming photodegradation remains a major challenge in the development of Ir^{III} complexes.⁸⁴ Studies into photodegradation reveal that it is often a complex process, dependent on a multitude of factors including the solvent environment and atmosphere.⁸⁴ A study into four homoleptic bidentate Ir^{III} complexes, based around $\text{Ir}(\text{ppy})_3$, by Schmidbauer *et al.* analysed a variety of conditions to elucidate some of these factors and their relative effects.⁸⁴ The complexes used were 3 substituted forms of the $\text{Ir}(\text{ppy})_3$ complex, shown in fig. 13. The study monitored the concentration of each complex as a function of irradiation time, using an LED light source of 350 mW power at 400 nm. It was found that the $\text{Ir}(\text{ppy})_3$ base complex displayed the greatest photostability, whilst the substituted versions underwent relatively rapid degradation, with the *piq* and *F, CN-ppy* versions of the complex exhibiting the poorest stability. The authors showed that halogenated solvents generally exacerbated the photonically induced degradation of the complexes, when compared to toluene, with evidence of halogenated by-products found via mass spectra following exposure.

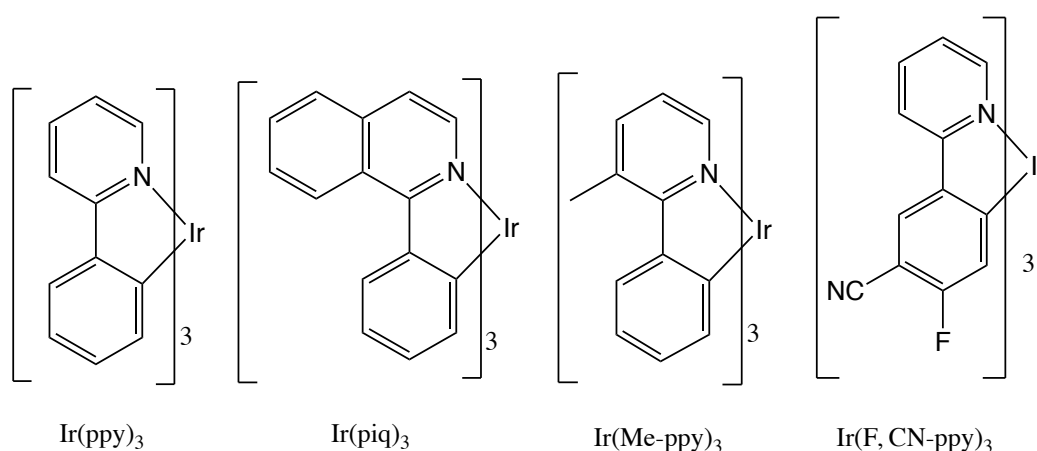


Figure 13 Four complexes previously studied by Schmidbauer *et al.*

The interactions of the complexes with diatomic oxygen were also considered, as Ir^{III} complexes are noted to have very good sensitizer properties due to their ready access to excited triplet states and emissive state energy tuneability and thus are able to interact with oxygen in its native triplet state to produce singlet oxygen in solution. Through an atmospheric study, the removal of an oxygen-rich atmosphere was found to significantly reduce the rate of degradation in the Ir(piq)₃ complex, whilst the opposite effect was had on the rate of degradation for the Ir(ppy)₃ and Ir(Me-ppy)₃ complexes. The reasoning for this phenomenon is that the Ir(piq)₃ more readily undergoes chemical attack from the singlet oxygen generated in solution, whilst the other two are efficiently quenched by oxygen in solution, removing the possibility of degradation via the complex triplet state. This is evident in mass spectra and infrared absorption spectra of the complexes acquired following irradiation, with more prominent oxidation products being observed for the Ir(piq)₃ than either of the other two in an oxygen-rich environment, and evidence of ligand dissociation for the Ir(ppy)₃ and Ir(Me-ppy)₃ complexes under an inert atmosphere. This study demonstrates the difficulty of designing a stable complex, as all the elements of the operating conditions can be unique to each complex, with even very structurally similar complexes behaving in opposing ways under the same conditions.

3.2 Complex Structures

To investigate the tuneability of Ir^{III} complexes, a novel set of Ir^{III} quinoxaline complexes were synthesized by the Pope group at Cardiff University and are characterized herein using steady state and transient absorption spectroscopy, assisted by a DFT computational techniques. The complexes in this initial study all share the same general structure, comprised of two quinoxaline ligands and a bipyridine ligand coordinated to an iridium core. All the complexes are monocationic and paired to PF₆ counterions. For brevity, complexes are referred to by their ligand number, i.e. 'complex L1' is shorthand for [Ir(L1)₂(bpy)]PF₆.

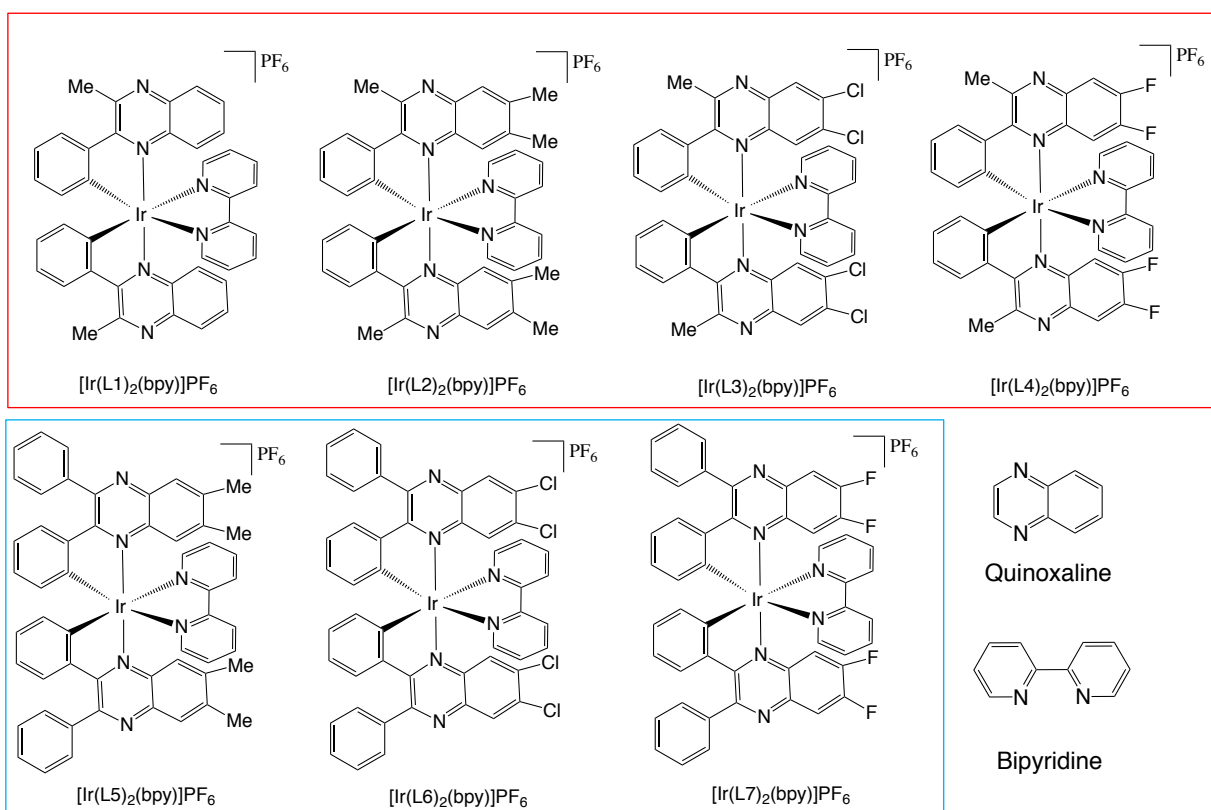


Figure 14 The seven quinoxaline-based complexes analysed in this chapter and the basis of the ligands used to form them

Complex L1 forms the basis of the set, and the remaining 6 complexes can be divided into two sets based on the substitution of the heterocyclic ring located on the backbone of the quinoxaline ligand. As can be observed in figure 14, these sets are distinguished by substitution with either a methyl group (red boxed set) or a phenyl ring (blue boxed set), with L2 – L4 directly analogous to L5 – L7 save for this difference. The complexes exhibit similar spectral profiles, with largely identical absorption and emission spectra, but feature distinct, fine shifts to the band onset and λ_{max} values. This effect is due to the change in ligand substitution. All the complexes feature a broad emission band between 570 – 750 nm. The absorption spectra of the complexes display three main features: a strong, broad series of absorption bands between 250 – 300 nm, a less intense absorption feature between 350 – 450 nm and a weak, broad absorption band centred at around 500 nm.

Each of the complexes in this series were investigated using the DFT-based methods described in section 2.2.1. In order to validate the methodological approach, at least in

terms of the DFT-derived molecular structure, the computationally optimised geometries are compared to those obtained from x-ray diffraction crystallography. Only L2, L3 and L7 were able to be isolated as crystals, and in each case the computationally derived geometric parameters were in very good agreement with those obtained experimentally. As an example of this, figure 15 shows the singlet ground state geometry determined for the L5 complex superimposed on the experimentally derived structure acquired using x-ray diffraction crystallography.

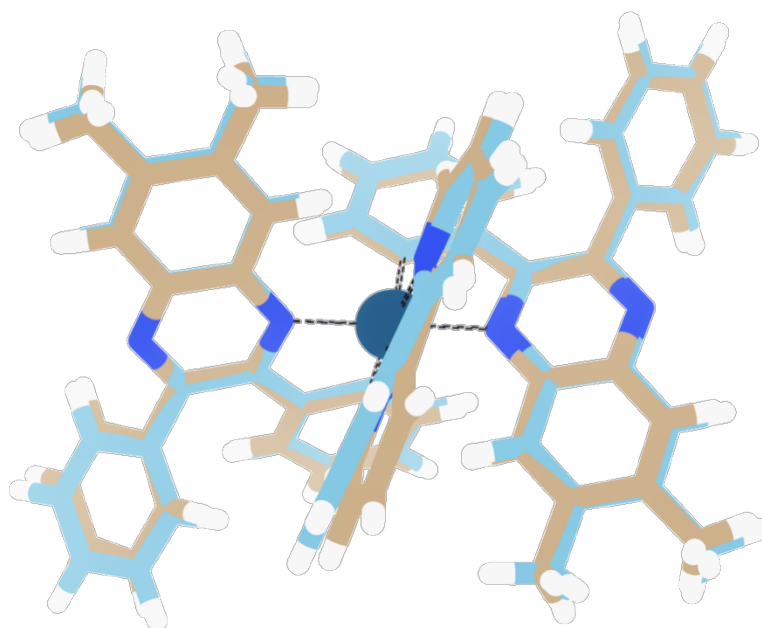


Figure 15 Comparison of the simulated (blue) structure with the experimentally determined crystal structure (brown) for the L5 complex, showing excellent agreement between them. The RMSD value between these two is 0.339 Å. Structures compared and rendered in Chimera software package and POV-RAY.

3.3 Steady State Absorption Spectra

3.3.1 Steady State UV-Vis Absorption

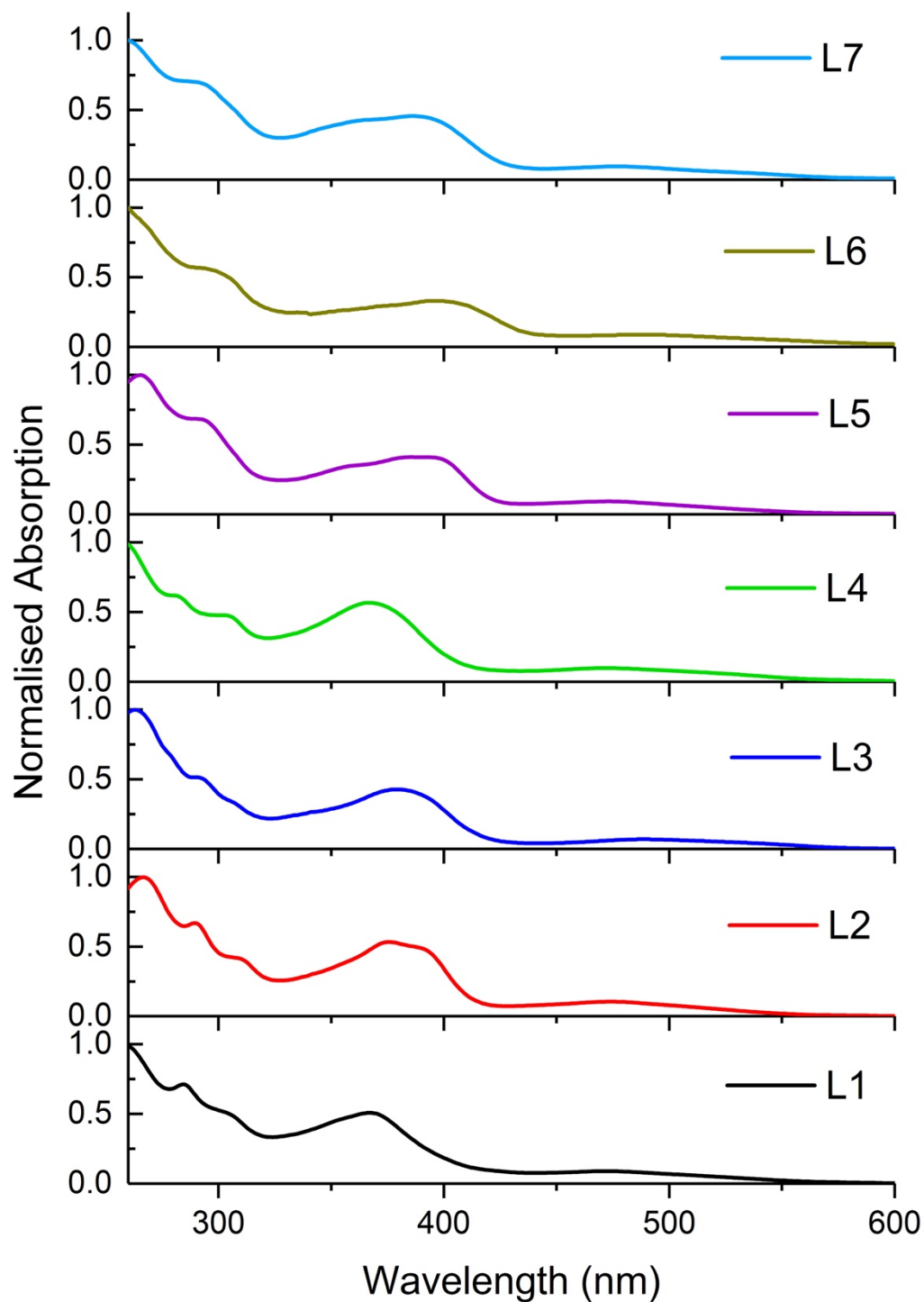


Figure 16 Normalised absorption spectra of the 7 complexes. The labels refer to the complexes as shown in Fig 14. The spectra are all qualitatively similar, but with band shifts discussed in the text. Wavelengths <260 nm omitted due to instrument limitations.

The steady state UV-Vis absorption spectra, seen in figure 16, of the complexes all feature three broad absorption bands, defined from their onset rather than their maxima, as each band is a composite of contributions from multiple states and it is thus not a fair representation to discuss them in terms of maxima. Using L1 as a reference, methyl substituting the quinoxaline ligand slightly bathochromically shifts the absorption bands <450 nm, whilst substituting with chlorine (L3) bathochromically shifts all features of the spectrum. Substituting with fluorine (L4) induces a very slight hypsochromic shift to all features. The L5 – L7 group follow the same trend as their L2 – L4 analogues with the phenylated set being slightly bathochromically shifted. The phenylated set L5 – L7 also produce spectra seemingly with a lower spectral definition than their methylated counterparts, with broader, less structured absorption bands. It is not clear what the origin of this effect is, however, it could be an effect of additional vibrational broadening, or a slight reduction in separation between electronic states.

The different responses of the spectroscopic features to changes in the complex structure is suggestive of different origin states of each of these features. Prior literature suggests that the short wavelength band arises from ligand centred transitions, whilst the longer wavelength bands originate from singlet metal-to-ligand charge transfer and spin-forbidden singlet-to-triplet metal-to-ligand charge transfer.^{79,81} Therefore, at this stage the high intensity absorption bands with onsets <325 nm and <450 nm are assigned as arising from singlet-to-singlet spin-allowed ligand-centred (¹LC) and metal-to-ligand (¹MLCT) transitions respectively, given their strong intensity and high energy. The band with onset at around 550 nm is assigned as a singlet-to-triplet spin-forbidden metal-to-ligand (³MLCT) absorption, consistent with the lower energy gap generally found between the S₀ and T₁ state in Ir^{III} complexes and also consistent with the lower probability of this spin-forbidden process occurring and thus a reduced absorption cross-section.

3.3.2 Simulation of Singlet-to-Singlet Transitions and Orbital Analysis

Time dependent DFT calculations were performed on the optimised singlet state structures using the long-range interaction corrected CAM-B3LYP level of theory in

order to obtain simulations of the UV-Vis absorption spectra and an approximation of the primary absorption features. This serves to assist in the assignment of the absorption bands given above, and to assist in the understanding of the subtle band shifts observed in the steady state UV-Vis absorption spectra. Table 1 below depicts the first calculated spin-allowed singlet transitions from the singlet ground state of each complex, compared with the experimentally determined onset of the corresponding band.

Complex	$S_0 \rightarrow S_1$ Absorption (nm)
[Ir(L1) ₂ (bpy)]PF ₆	405 (372)
[Ir(L2) ₂ (bpy)]PF ₆	402 (402)
[Ir(L3) ₂ (bpy)]PF ₆	419 (406)
[Ir(L4) ₂ (bpy)]PF ₆	409 (394)
[Ir(L5) ₂ (bpy)]PF ₆	406 (417)
[Ir(L6) ₂ (bpy)]PF ₆	423 (428)
[Ir(L7) ₂ (bpy)]PF ₆	414 (418)

Table 1 Table depicting the absorption transitions for the singlet ground state to first singlet excited state as calculated using TD-DFT and a CAM-B3LYP level of theory. The values in parentheses are the onsets of the experimentally determined UV-Vis absorption ¹MLCT feature and are used for comparison.

The computational values are a close approximate of the experimental values, albeit not exact, supporting the assignment of the absorption band as spin allowed absorption. The discrepancy in values can be accounted for through consideration of the geometry sampled, as the experimental band is likely made up of absorption contributions from a variety of different ground state geometries, whilst only one is considered in the DFT treatment. Band onsets are reported here in place of absorption peak maxima as it was felt this gives the most reliable/reproducible information. In many cases in the spectra reported in this thesis, absorption features have a complex structure suggesting that multiple absorption bands are overlapping. This will skew any attempt to report band maxima, whilst band onsets are more likely to arise from a

single electronic transition and are easier to identify in a spectrum. In order to evaluate the individual contribution of molecular orbitals to the ¹MLCT excitations, orbital decomposition was performed for the first five excited states, constituting an integral part of the TD-DFT evaluation of the complexes. Those results are shown below for the [Ir(L1)₂(bipy)]PF₆ complex in table 2.

Orbital Contribution to Excited States	
Excited State	Contributing Transitions
1 (405.09 nm, f=0.0267)	HOMO -> LUMO (88.16%)
2 (400.70 nm, f=0.1539)	HOMO -> LUMO +1 (83.98%)
3 (344.89 nm, f=0.0104)	HOMO -> LUMO +2 (91.20%)
4 (326.01 nm, f=0.1264)	HOMO -3 -> LUMO (26.90%) HOMO -2 -> LUMO +1 (10.65%) HOMO -1 -> LUMO (35.23%)
5 (323.01 nm, f=0.1769)	HOMO -2 -> LUMO (33.42%) HOMO -1 -> LUMO +1 (50.12%)

Table 2 MO contributions to the first 5 singlet to singlet excitations for the [Ir(L1)₂(bipy)]PF₆ complex.

Visualisation of the frontier molecular orbitals (shown in figure 17 for the L1 complex) and decomposition analysis (table 3) were used to help determine the nature of charge transfer within the complexes induced by excitation. This is accomplished by examining the frontier orbitals of the complexes and determining the percentage contributions that various moieties within the complex contribute to each orbital. From the spectra and table, both reported above, it appears that the longest wavelength ¹MLCT transitions, which occur on the edge of the visible spectrum, predominantly involve excitation from the HOMO to the LUMO or LUMO +1. In addition, it appears that these are the spectral features that are most sensitive to ligand substitution, and therefore these will form the focus of further discussion below. In order to determine the nature of these excitations, i.e. the degree of MLCT character vs intraligand character, a formal decomposition analysis was performed

using the GaussSum software package utilising Mulliken population analysis calculations.

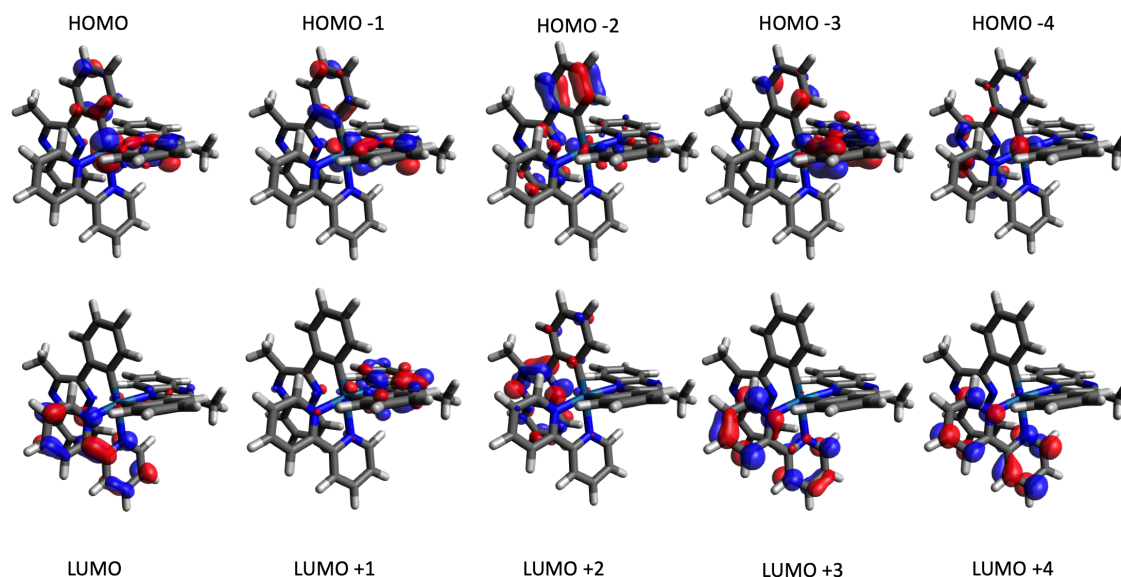


Figure 17 Renderings of the simulated frontier molecular orbitals for the calculated singlet ground state of Ir(L1)₂(bpy)

[Ir(L1) ₂ (bipy)]PF ₆	Moiety Contribution to Orbital (%)			
	Ir (5d)	Bipy	Quinoxaline 1	Quinoxaline 2
LUMO +4	1	67	16	16
LUMO +3	2	79	9	9
LUMO +2	2	97	0	1
LUMO +1	4	1	47	48
LUMO	3	2	48	47
HOMO	33	2	33	33
HOMO -1	3	1	48	48
HOMO -2	10	1	44	45
HOMO -3	22	3	38	37
HOMO -4	17	0	43	40

Table 3 Table depicting the percentage contributions of each of the main components of the complex to the frontier orbitals of the L1 Ir complex, as determined by the GaussSum software package. Figures are rounded to the nearest integer.

From table 3 above, it can be seen that the HOMO is evenly divided between the iridium atom and the two quinoxaline ligands, whilst the LUMO and LUMO +1 show predominantly quinoxaline character. This holds broadly true for the whole set of complexes, with only minor variations in the values. This suggests that the long wavelength singlet absorption bands observed in the steady state UV-Vis spectrum of the complex are MLCT in character, with some electron density transitioning from the central metal atom to the quinoxaline ligands in the excited state. The seven complexes display C_2 symmetry, demonstrating the quinoxalines near degenerate character, and this is reflected in the percentage contributions in table 3, with molecular orbitals delocalised over both quinoxaline ligands with even contributions from each. It is worth noting that analysis of an alternative, asymmetric geometry initially utilised gave a differing account of the contributions, with degeneracy between the quinoxalines lost and a larger contribution from the bipyridine moiety. However, there is no evidence that this asymmetric geometry is present, as it is not formed in the synthesis process as confirmed by x-ray diffraction crystallography, and so is not considered in this work.

The simulated singlet-to-singlet transitions principally arise from the low-lying occupied orbitals and are mainly into the LUMO and LUMO +1, suggesting that the absorption bands of this complex are to MLCT and LLCT in character. The low-lying singlet excited states of the complexes also exhibit predominantly quinoxaline occupation, explaining the band shift introduced by the adjustment of the substituents of these ligands seen in the absorption spectra. The energy gap between the HOMO and LUMO were also assessed in order to examine the effects of the quinoxaline substitution.

Complex	HOMO (eV)	LUMO (eV)	ΔE (eV)
[Ir(L1) ₂ (bpy)]PF ₆	-6.21	-3.1	3.11
[Ir(L2) ₂ (bpy)]PF ₆	-6.12	-2.98	3.14
[Ir(L3) ₂ (bpy)]PF ₆	-6.39	-3.39	3
[Ir(L4) ₂ (bpy)]PF ₆	-6.32	-3.25	3.07
[Ir(L5) ₂ (bpy)]PF ₆	-6.11	-3.01	3.1
[Ir(L6) ₂ (bpy)]PF ₆	-6.38	-3.42	2.96
[Ir(L7) ₂ (bpy)]PF ₆	-6.31	-3.28	3.03

Table 4 Frontier orbital energy gap for the singlet ground states of the bipyridine complexes

As can be seen from table 4 above, in conjunction with table 6 in section 3.4 below, the ordering of the energy differences between the frontier orbitals of the singlet states matches that of the complex emission λ_{\max} , discussed in more detail in section 3.4. The substitution of the quinoxaline ligands impacts upon both occupied and unoccupied orbital energies: the orbital energies of the halogenated complexes are lower than those of the L1, L2 and L5 complexes, suggesting that the halogen substitution stabilises the system as a whole. In all cases the HOMO of the phenylated version of a complex is slightly less stable than its methylated counterpart, e.g. L6 has a slightly higher energy value than L3. Methylated complexes (L2 and L5) have the least stable frontier orbitals, featuring a substantial raising of the HOMO relative to the L1 basis complex. The LUMO and HOMO of the complexes both experience the same effect due to the substituents, i.e. both are stabilised or destabilised relative to the L1 complex, but they do not experience this effect equally, which is what gives rise to the differing energy gaps between them. This can be rationalised when the decomposition analysis is taken into account, as the HOMO is composed from roughly even contributions from the iridium and quinoxaline moieties, whilst the LUMO is composed primarily of contributions from the quinoxalines. Thus, it stands to reason that any

stabilising or destabilising influence from quinoxaline substituents would generally impact upon the energy of the unoccupied orbitals to a greater extent than the HOMO. The standard deviations of the orbital energies provide a qualitative picture of this, where the HOMO has a variance of 0.12 eV, and the LUMO of 0.18 eV.

3.3.3 Simulation of Spin-forbidden Absorption

Calculations of the spin-forbidden vertical transition energies can be performed by evaluating the energy of the first triplet state of the complex, at the geometry of the singlet ground state minimum. The simulated and estimated experimentally determined values are compared in table 5 below.

Complex	$S_0 \rightarrow T_1$ Absorption (nm)
[Ir(L1) ₂ (bpy)]PF ₆	541 (477)
[Ir(L2) ₂ (bpy)]PF ₆	533 (474)
[Ir(L3) ₂ (bpy)]PF ₆	565 (500)
[Ir(L4) ₂ (bpy)]PF ₆	552 (480)
[Ir(L5) ₂ (bpy)]PF ₆	540 (479)
[Ir(L6) ₂ (bpy)]PF ₆	572 (501)
[Ir(L7) ₂ (bpy)]PF ₆	555 (483)

Table 5 Calculated values for the spin forbidden absorption and emission of the complexes. The experimental values are shown in parentheses for comparison.

These ³MLCT computed absorption band positions are significantly red-shifted in comparison to those reported in table 1 for the ¹MLCT bands. Although the calculations performed in this manner do not provide oscillator strengths for such ³MLCT spin-forbidden transitions, one can assume they will be substantially lower in intensity than their spin-allowed singlet counterparts, and therefore these calculations

provide additional support for the assignment of the longer wavelength (> 400 nm) steady state absorption bands as $^3\text{MLCT}$ in character.

3.3.4 Simulation of Steady State Absorption Spectrum

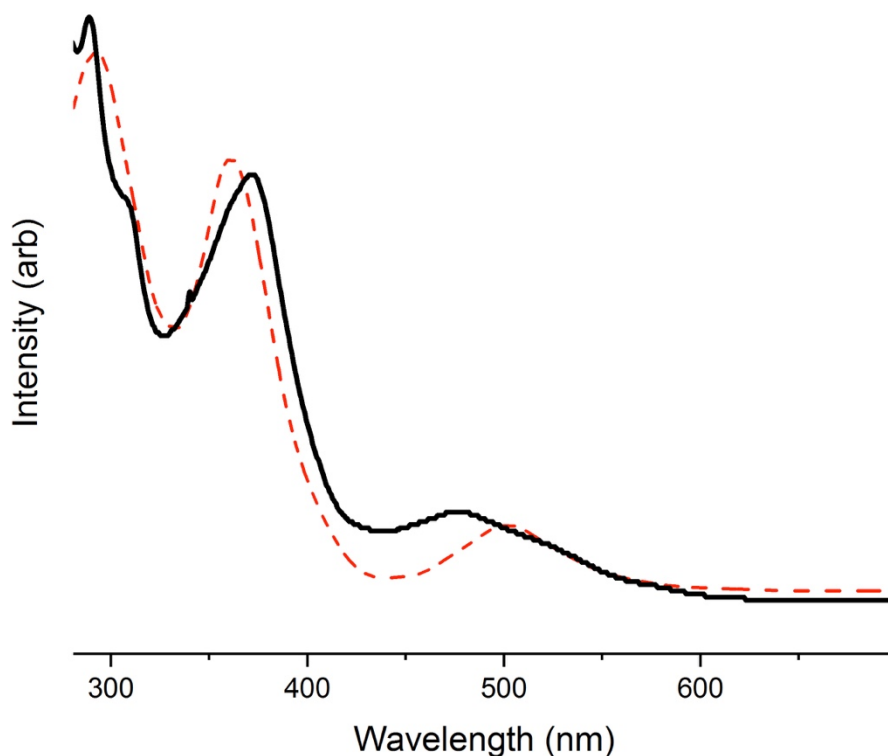


Figure 18 Comparison of simulated spectrum of $\text{Ir}(\text{L1})_2(\text{bpy})$ (red) with the steady state spectrum acquired (black).

The steady state absorption spectrum of the $\text{Ir}(\text{L1})_2(\text{bpy})$ complex was simulated in a more complete fashion, evaluating the $\text{S}_1/\text{T}_1 \leftarrow \text{S}_0$ transitions in a strictly non-vibronic manner. 2000 ground state singlet geometries were sampled from an uncoupled harmonic Wigner distribution in the NewtonX computational software suite, forming a ground state quantum distribution. Excitation energies and oscillator strengths were then calculated for the first 20 singlet excited states and the first 5 triplet excited states for each geometry, convoluted (0.1 eV linewidth) and then summed, producing the spectrum represented by the dashed red line visible in figure 18. This method displays remarkable agreement with experiment, but is computationally expensive, requiring approximately a month of available computational resources to complete, and so was only enacted for the L1 complex. Although this is a small part of the overall

project, the remarkable agreement that is achievable here demonstrates the capacity of this method, which is often applied to small molecular systems, but rarely extended to systems of this size. This clearly illustrates that this technique, whilst expensive, can be used to model band positions, band widths and also to relatively accurately position spin forbidden absorptions (albeit that in this instance the spin forbidden oscillator strength is scaled to fit the simulation – all transitions computed were given identical oscillator strengths regardless of computed geometry). It is believed this is the first approach of it's kind to large complex systems such as this, although other work has since been published, yet again showing it's significance.⁸⁵

3.4 Emission Spectra

One of the primary features of interest in this study is the shifting of the emission bands of the complexes with substitution. The emission spectra of the complexes were recorded using the ICCD camera. As in the previous measurements, the complexes were all pumped at 355 nm. The spectra are shown below in figure 19, normalized for comparison purposes, with an inset displaying the emission maxima for ease of comparison.

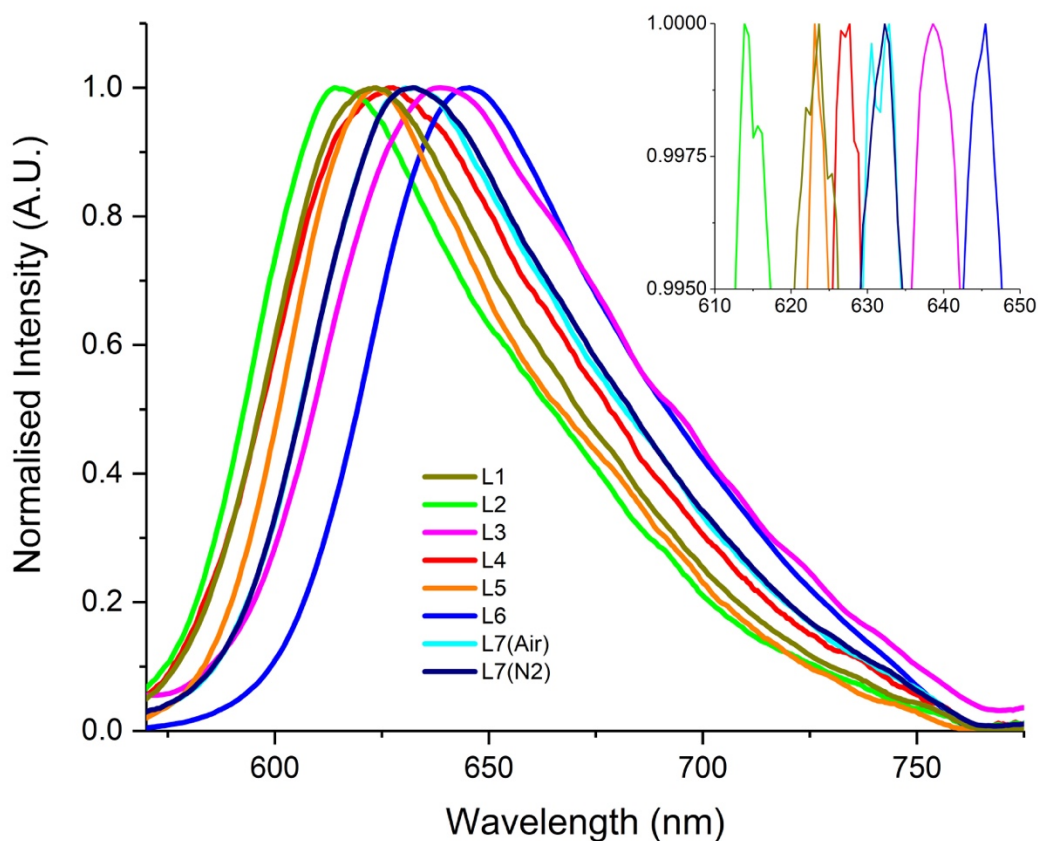


Figure 19 The normalised emission spectra of the complexes listed by their constituent ligands. The L7 complex was examined in both oxygenated and nitrogenated conditions to determine if there was any oxygen influence on the band position. The peak maxima of each complex emission are shown inset for clarity, magnified to emphasise the position with respect to wavelength.

From the spectra in figure 19 above, it can be seen that the complexes all share the same general profile with the onset and peak maximum being ligand dependent. The L7 complex was examined under both atmospheric and degassed conditions to determine if the presence of dissolved oxygen had an influence on the band positions. The absolute intensity of the emission peak was reduced under atmospheric conditions but the peak position and shape remained unchanged, as can be seen in the above figure 19. This suggests that oxygen functions as a quencher for the excited state of the complexes, reducing quantum yield, but doesn't appear to complex with the system or induce significant geometric change.

Complex	λ_{max} (nm)
[Ir(L1) ₂ (bpy)]PF ₆	623 (691)
[Ir(L2) ₂ (bpy)]PF ₆	617 (698)
[Ir(L3) ₂ (bpy)]PF ₆	638 (708)
[Ir(L4) ₂ (bpy)]PF ₆	626 (692)
[Ir(L5) ₂ (bpy)]PF ₆	622 (723)
[Ir(L6) ₂ (bpy)]PF ₆	645 (730)
[Ir(L7) ₂ (bpy)]PF ₆	632 (716)

Table 6 Maximum peak values for the emission of the complexes. Simulated values shown in parentheses

From table 6 it is apparent that the complex emission follows a similar trend as the absorption features, as the peak maximum values are shifted depending on the substitution of the quinoxaline ligands. The one exception to this trend is that the methyl substituted L2 complex shows a hypsochromic shift relative to the L1 complex. The halogenated complexes L3 and L4 display bathochromic shifts, with the L3 complex once again displaying the most red-shifted features. The phenylated complexes (L5 – L7) follow the same pattern as their methylated counterparts, albeit slightly bathochromically shifted in all cases. The calculated vertical transition values show a reasonable quantitative match for the experimentally determined values, but more significantly are a good qualitative match, correctly simulating the order of energy of emission from each of the complexes.

3.5 Transient Absorption Spectra

3.5.1 Transient Absorption Spectra

Transient absorption measurements were obtained for the complexes using the ICCD as a mode of detection. The pump laser was tuned to 355 nm, as all the complexes feature a strong absorption at that wavelength. The complexes were dissolved in chloroform and measurements were performed without degassing. The transient

absorption spectrum of the L1 complex is shown below in figure 20 as an example spectrum.

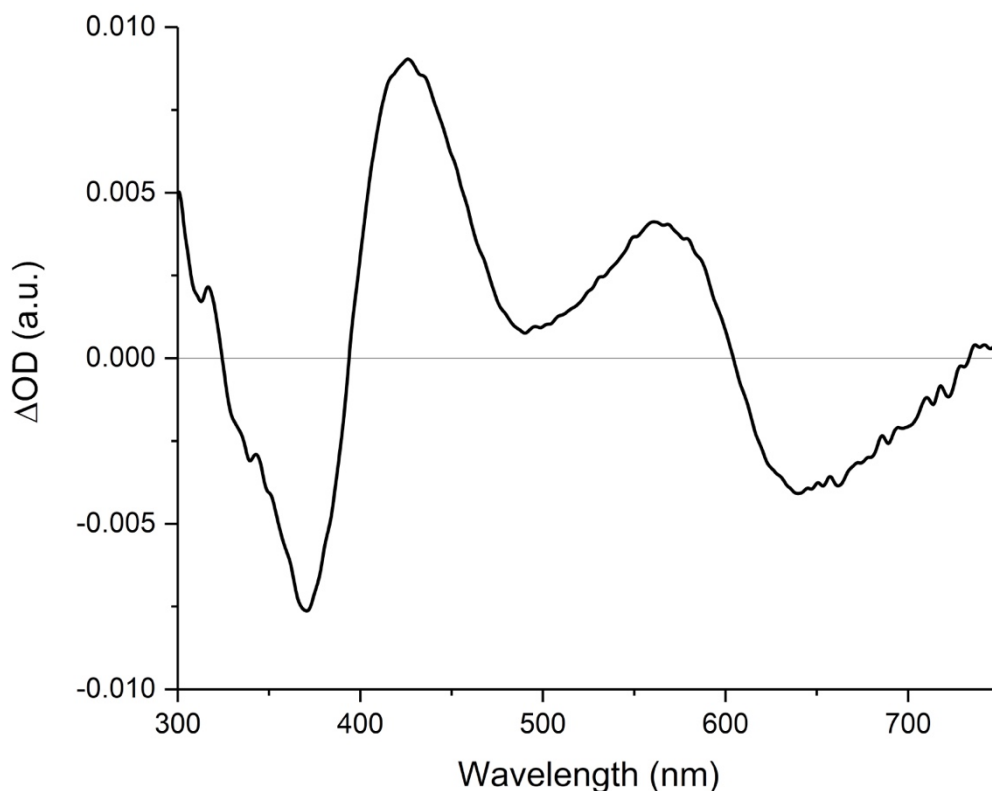


Figure 20 Transient absorption spectrum of the $[\text{Ir}(\text{L1})_2(\text{bpy})]\text{PF}_6$ complex in chloroform, obtained at a 50 ns delay from the laser pulse.

This spectrum is archetypical of the set of complexes, as they all possess the four major features visible above. As with the ground state absorption spectrum, the features are bathochromically or hypsochromically shifted relative to this example spectrum depending on the substitution of the quinoxaline ligands. The negative feature between 325 – 400 nm is assigned as a bleach, arising from the depletion of the ground state absorption band. The positive features between 400 – 600 nm are assigned to triplet – triplet absorptions and are due to absorptive transitions of the excited state decreasing the amount of light from the probe reaching the detector when compared to the ground state. The feature at 600 – 750 nm is assigned to the emission of the complex, as this spectrum is not emission background corrected, and

this feature corresponds closely to the observed emission. A table of the transient absorption and bleach λ_{max} values for each of the complexes is shown below.

Complex	Bleach (nm)	Transient Abs. 1 (nm)	Transient Abs. 2 (nm)
[Ir(L1) ₂ (bpy)]PF ₆	370	430	560
[Ir(L2) ₂ (bpy)]PF ₆	375	420	565
[Ir(L3) ₂ (bpy)]PF ₆	378	435	580
[Ir(L4) ₂ (bpy)]PF ₆	370	425	565
[Ir(L5) ₂ (bpy)]PF ₆	360	435	575
[Ir(L6) ₂ (bpy)]PF ₆	415	450	590
[Ir(L7) ₂ (bpy)]PF ₆	356	439	581

Table 7 The peak maxima values for the transient absorption spectra of the 7 complexes, focussing on the clear features observed in figure 20.

The transient spectra exhibit similar peak shifting behaviour as the conventional absorption spectra. The values for all complexes are reasonably close to one another with the exception of the L6 complex, which is significantly red shifted in comparison to the others. With the exception of the L4 complex, the complexes that feature halogenated quinoxaline ligands have bathochromically shifted features relative to the others. The phenyl substituted set (L5-L7) also experience a bathochromic shift.

3.5.2 Simulation of Triplet-to-Triplet Absorption

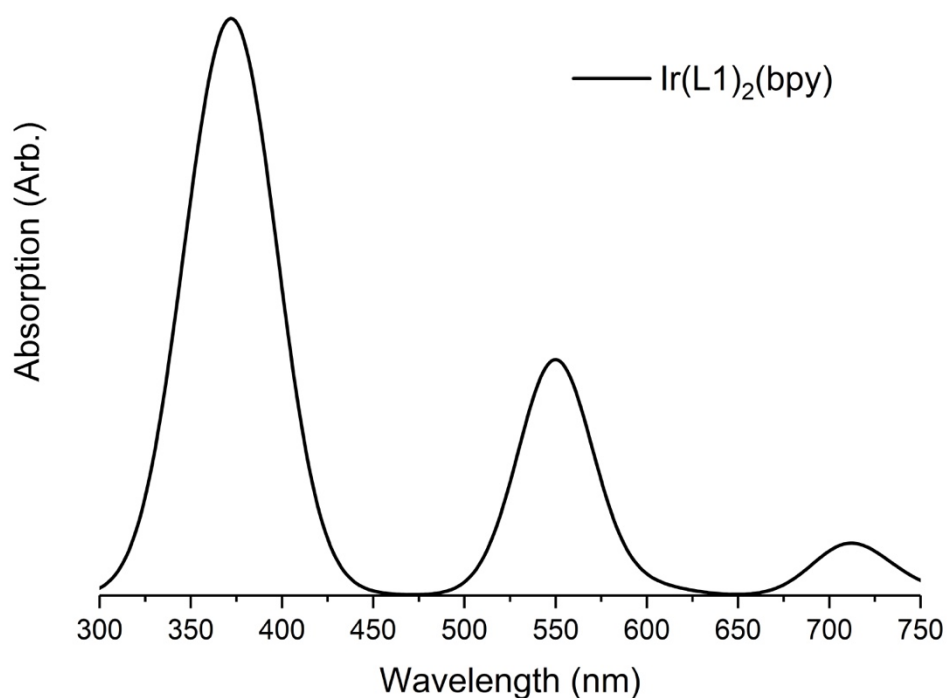


Figure 21 Simulated triplet absorption spectrum for the Ir(L1)₂(bpy) complex in chloroform. This spectrum corresponds to TD-DFT calculations of excited electronic triplet states, arising from the triplet ground state. The spectrum is a convolution of computed transitions for ease of comparison.

The simulated triplet-to-triplet absorption spectrum for the L1 complex, seen in figure 21, shows qualitative similarities to the observed transient absorption spectrum, including a strong absorption band in the shorter wavelength portion of the spectrum and a weaker absorption band between 500 – 600 nm. These observations hold true for the entire bipyridine complex set, with three distinct absorption bands visible in the wavelength region probed by the transient experiments, supporting the assignment of the transient spectrum as spin-allowed triplet excited state absorption. The transient absorption spectrum is a convolution of the absorption spectrum of the excited state and the bleaching of the ground state absorption spectrum, accounting for the visual differences between the simulated and experimental TA spectra. The TA spectrum is also not background subtracted in this case, meaning there is distortion from the phosphorescent emission of the complex.

3.6 Transient Kinetics

The kinetics of the processes observed using the ICCD were examined using the photomultiplier tube (PMT) detector system. A monochromatic grating used in conjunction with this detector enables wavelengths to be isolated and examined with respect to time.

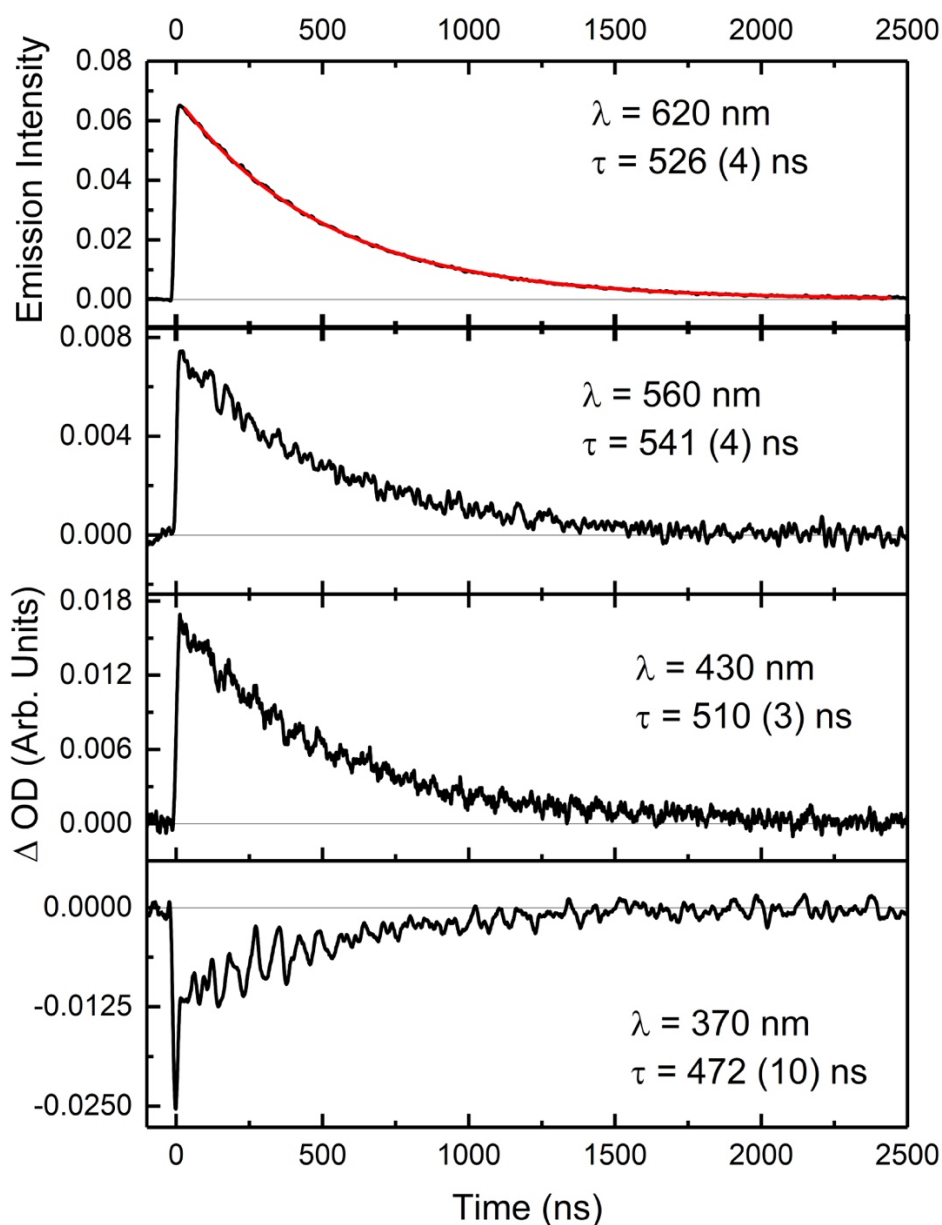


Figure 22 Transient kinetic measurements of the Ir(L1)₂(bpy) complex. The top trace is an emission trace, the bottom three are difference in optical density traces. All are fitted to a mono-exponential decay function, an example of a fit is shown in red on the top trace. Fit errors in nanoseconds are shown in parentheses.

The transient kinetics of the major features of the $[\text{Ir}(\text{L1})_2(\text{bpy})]\text{PF}_6$ complex can be seen in figure 22. Each of the various transient absorption and emission features exhibited by any given complex bear similar lifetimes to each other and each feature can be fit to a mono-exponential decay function, suggesting a single state of origin. Given that this state is likely a triplet state, this suggests that intersystem crossing occurs at a very high rate as, save for the sharp onset of the bleach feature at 370 nm, no evidence of any features that could correspond to an additional singlet-to-singlet process or any other process are visible in the kinetics. Qualitatively, all complexes exhibit these features suggesting that the same or similar processes occur for each complex, with the quantitative differences in absorption and emission wavelength and lifetimes ascribed to the perturbative effects of the different quinoxaline substituents. All features display a complete return to baseline, suggesting that no permanent chemical change has been induced by the photoexcitation process. The transient absorption and the emission feature lifetime values tend to correlate more closely, which is ascribed to the greater resolution of these measurements resulting in a better fit for the function. The short wavelength bleach tends to be weaker and less resolved when analysed with the PMT. This is likely due to the less intense and reliable lamp output at this wavelength band. This effect is likely responsible for the observed shorter lifetimes of the bleach features.

Complex	Bleach (~360 nm) (ns)	Abs. (~440nm) (ns)	Abs. (~560 nm) (ns)	Em. (~630 nm) (ns)
Ir(L1)₂(bpy)	472 (10)	510 (3)	541 (4)	526 (4)
Ir(L2)₂(bpy)	392 (20)	445 (3)	431 (4)	447 (3)
Ir(L3)₂(bpy)	*	406 (1)	397 (3)	445 (2)
Ir(L4)₂(bpy)	469 (6)	495 (2)	475 (4)	474 (4)
Ir(L5)₂(bpy)	434 (19)	447 (1)	441 (1)	455 (1)
Ir(L6)₂(bpy)	560 (2)	417 (1)	409 (2)	433 (2)
Ir(L7)₂(bpy)	478 (24)	490 (1)	504 (3)	499 (2)

Table 8 Lifetimes for the transient features of the complexes. For brevity, the feature positions are approximated. Fit errors in nanoseconds are shown in parentheses. *No lifetime could be obtained from the PMT measurements of the L3 complex bleach, due to lack of sufficient resolution

From the above table, it can be seen that the error in the bleach is more substantial than in the other measurements. The L1 complex exhibits the longest average lifetime for the features, whilst the L3 and L6 complexes exhibit the shortest. Phenylated versions of complexes exhibit longer average lifetimes than their methylated analogues, e.g. the L5 complex has an average lifetime of 447 ns (discounting the bleach feature), whilst the L2 complex has an average of 441 ns. An exception to this rule is the L4 and L7 fluorinated complex pair, where the L4 has slightly longer-lived features than the L7. These complexes exhibit long-lived features as well, suggesting that halogenation alone isn't the cause of shorter lifetimes.

3.7 Conclusion

Seven iridium (III) complexes were evaluated and it was found that their spectroscopic features are variable depending on the nature of the substituents of their quinoxaline ligands. The variations are generally subtle and predictable with respect to their effect on the spectroscopy of the base complex, the $[\text{Ir}(\text{L1})_2(\text{bpy})]\text{PF}_6$ complex in this chapter. All complexes show broadly similar features, with variations primarily involving the shifting of absorption and emission band positions. Transient spectroscopy and kinetics have also been shown to be useful for characterisation of the complexes and for developing an understanding of the origins of the processes involved when combined with the theoretical DFT approach. The transient absorption spectra of the complexes have a distinct profile with 4 major features in the 300 – 700 nm: a ground state bleach, two excited state absorptions and a long wavelength visible emission, and these features show a clear shift with ligand variation. These features are more useful for characterising the complexes than their steady-state absorption spectra, as they are far more distinct from one another and show a more predictable variation with ligand substitution. The lifetimes of the four features of any one of the complexes all fall within a similar time range and fit a mono-exponential profile, leading to the assignment of a single excited state of origin for each. Given the long-lived nature of the features, extending into the hundreds of nanoseconds, this excited state is assigned as a triplet state, with the emission assigned as phosphorescence, as the spin-forbidden nature of the transitions to and from the excited state results in a lower

probability and thus a protracted lifetime in comparison with those resulting from spin-allowed singlet-singlet transitions.

The use of computational techniques, namely the relatively low-cost DFT analysis used here, in predicting the direction and extent of the band shifting caused by a given ligand in relation to a basis complex allows for the beginning of a rational design scheme to be established. Although the DFT study was unable to exactly match the band positions of the spectroscopic features numerically, the ordering of the relative shift in peak maximum positions between the complex emissions were accurately assessed, suggesting that the ligand substitution effects are being accurately modelled with respect to the basis complex, the unsubstituted L1 variant in this case. This shows promise as an analytical tool for the creation of novel complexes, as the relatively low resource and time expense of a DFT study allows for the pre-screening of potential complexes for desired spectroscopic properties prior to synthesis within a laboratory. Molecular orbital decomposition analysis was useful in providing insights into the nature of electron density within the complexes, with results suggesting that the HOMO of each complex is divided evenly between the iridium centre of the complex and the two quinoxaline moieties, whilst the LUMO is predominantly quinoxaline centred. This observation strengthens the argument that the absorption features of the complexes are MLCT in nature, and that the emission is likewise LMCT.

4. Effect of Ligand Structure on the Spectroscopic Properties of Iridium (III) Complexes

4.1 Ligand Variations

4.1.1 Ancillary Ligand Variation

Following the work on the complexes discussed in the previous chapter, an additional set of similar complexes, visible in figure 23, were developed in order to examine the effect that the ancillary ligand has on the absorptive and emissive properties of the complex. To this end, a new set of complexes were synthesised by the Pope group featuring the same variations of bidentate quinoxaline ligands as those discussed in the previous chapter but bound to a picolinate ancillary ligand in place of the bipyridine. The main differences this affected were a change in overall charge of the complex, as the picolinate complexes are neutral and do not form a salt with a paired anion, and the loss of overall complex symmetry due to the asymmetrical picolinate. This symmetry loss has an important impact on the properties that shall be discussed further in the chapter.

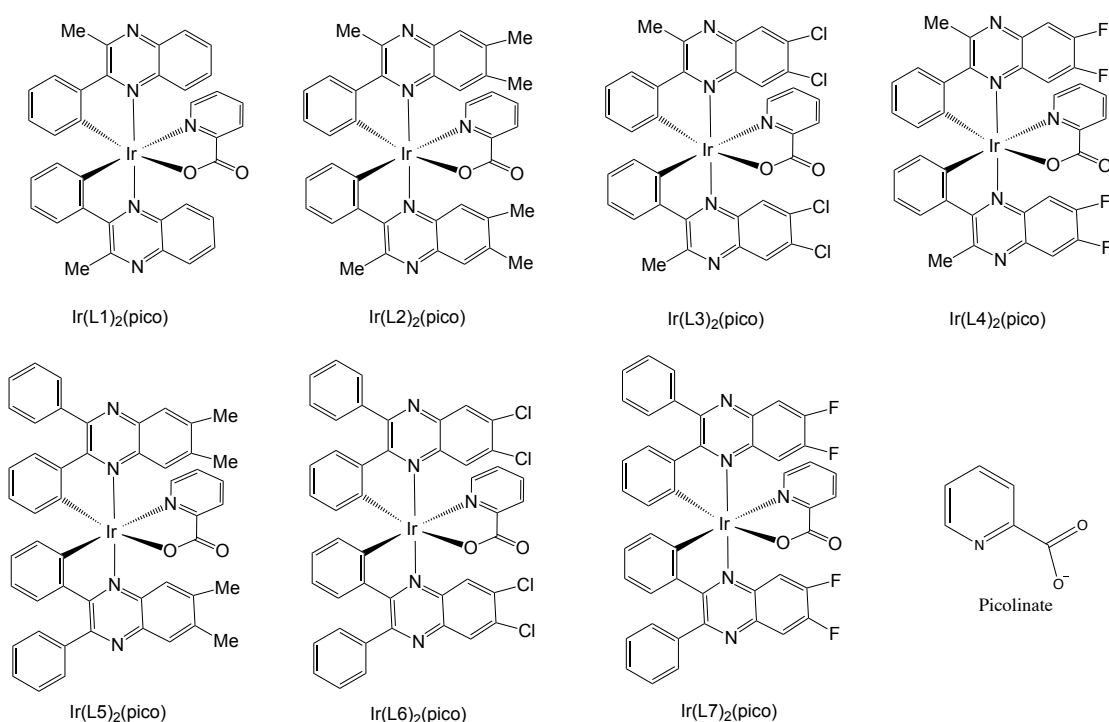


Figure 23 The 7 iridium complexes synthesised using picolinate (inset) ancillary ligands. Again, the ligand labels from this figure will be used to identify the complexes in the text.

A selection of complexes were also made using pyrazinate ancillary ligands, seen in figure 24, utilising the L2, L5 and L7 quinoxaline ligands, in order to further compare the effects of the ancillary ligand on the overall spectroscopic properties of the complex. This allows for the control of multiple variables within the total set of compounds. As the pyrazinate and picolinate ligands are remarkably similar, bearing only one atom difference between them, it would be expected that the complexes incorporating them will exhibit a smaller spectroscopic difference relative to one another than when either are compared to their bipyridine analogues. The combination of quinoxaline and ancillary ligand effects allows for far greater tunability, meaning a complex can be created with spectroscopic properties to suit more given applications.

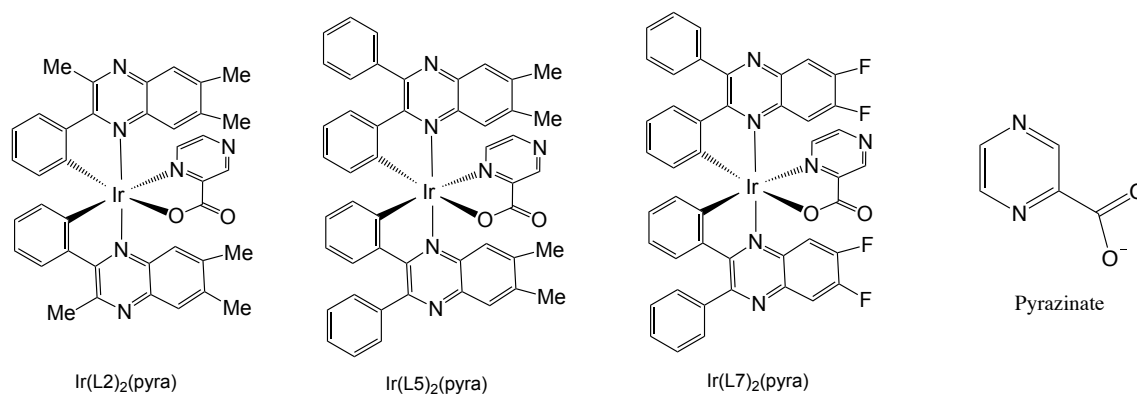


Figure 24 The 3 iridium complexes synthesised using pyrazinate (inset) as an ancillary ligand.

4.1.2 Cyclometallating Ligand Variation

In addition to studying the effect of adjusting the ancillary ligand, the effect of altering the structure of the backbone of the cyclometallating ligand was also examined. Two different approaches were attempted, one employing adjustments to the bidentate quinoxaline ligands through the addition of a phenyl ring to the backbone of the quinoxaline, using a benzoquinoxaline basis as the cyclometallating ligand and the original bipyridine ancillary ligand, seen in figure 25. The other approach uses two diquinoxaline ligands which have a tridentate bonding mode, meaning that an ancillary ligand is not present here.

The structure of the benzoquinoxaline ligands differs from the quinoxaline ligands previously developed, with two phenyl rings attached to the main backbone of the ligand, with substituents attached to the *para* carbon of each. Four benzoquinoxaline ligand variations were synthesised, featuring H, Br, Me and -OMe groups as the substituents. This allows for the exploration of subtle variations between the complexes in a similar fashion to the quinoxaline complex systems examined previously. All four of these complexes are monocationic in nature and synthesised in the form of hexafluorophosphate salts.

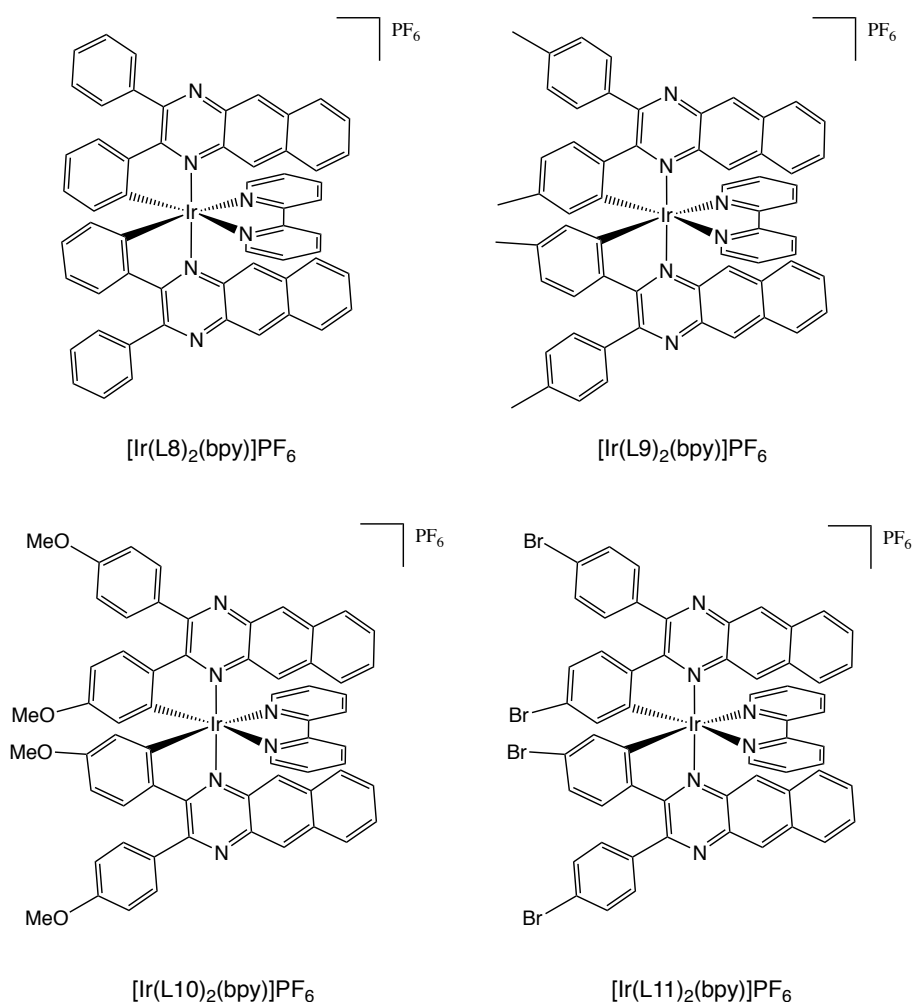


Figure 25 The benzoquinoxaline based iridium complexes discussed in this chapter

The tridentate diquinoxaline ligands used in the third set of complexes are formed of two quinoxaline groups bridged by a pyridine ring. The two quinoxaline moieties are

bonded with different orientations to a pyridine ring, resulting in different bonding modes to the iridium metal core in the complex with one quinoxaline bonding via a carbon atom and the other bonding via a nitrogen atom. The pyridine ring bonds to the iridium atom via the nitrogen heteroatom, resulting in a tridentate ligand overall. Two variations of this ligand type were synthesised: the base diquinoxaline-pyridine ligand and a dimethylated quinoxaline form, which shares the general structure of the base ligand save for the substitution of methyl groups on the terminal positions of the quinoxaline moieties. Both of these complex variations are monocationic in nature and synthesised paired to hexafluorophosphate counterions, seen in figure 26.

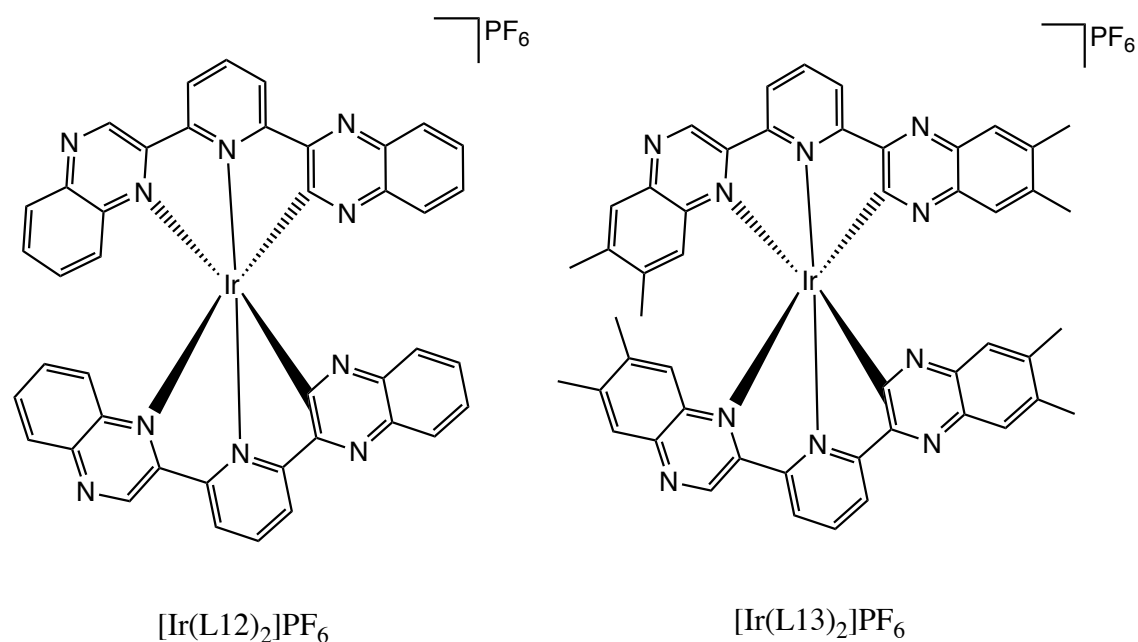


Figure 26 The diquinoxaline-pyridine iridium complexes discussed in this chapter

The diquinoxaline-pyridine complexes are fully analysed using steady state and transient absorption, emission and DFT techniques, whilst the benzoquinoxaline complexes are examined using DFT only.

4.2 Steady State Absorption Spectra

4.2.1 Picolinate-Based Complexes

4.2.1.1 Steady State UV-Vis Absorption

The complexes that utilise picolinate ancillary ligands feature broadly similar absorption spectra to their bipyridine counterparts from the previous chapter, each featuring three main components, albeit the features are slightly bathochromically shifted when making a direct comparison of the peak values of each feature. The qualitative similarity of the spectra suggest that the features arise from similar transitions between the molecular orbitals of the complex. The spectral similarities suggest and support the argument made in the previous chapter that the unoccupied frontier orbitals involved in these transitions are located primarily on the quinoxaline ligands, as significant ancillary ligand involvement would likely cause a more pronounced alteration to the shape of the spectra, however the slight bathochromic shift observed here relative to the bipyridine suggests that the ancillary ligand does have a minor influence on these transitions. The spectra display large absorption bands between 250 – 300 nm, a smaller absorption band between 350 – 450 nm and a broad, weak band between 450 – 700 nm. The two more intense, lower wavelength features are ascribed to $^1\text{MLCT}$ transitions as their intensity suggests a high probability of the transitions occurring, indicative of a spin-allowed nature. The longer wavelength band is assigned to a $^3\text{MLCT}$ transition, given its low intensity and longer wavelength, indicating a low probability of transition consistent with the selection rule forbidden nature of the spin change involved. These spin-forbidden transitions are weakly allowed in the case of iridium complexes due to spin-orbit coupling.

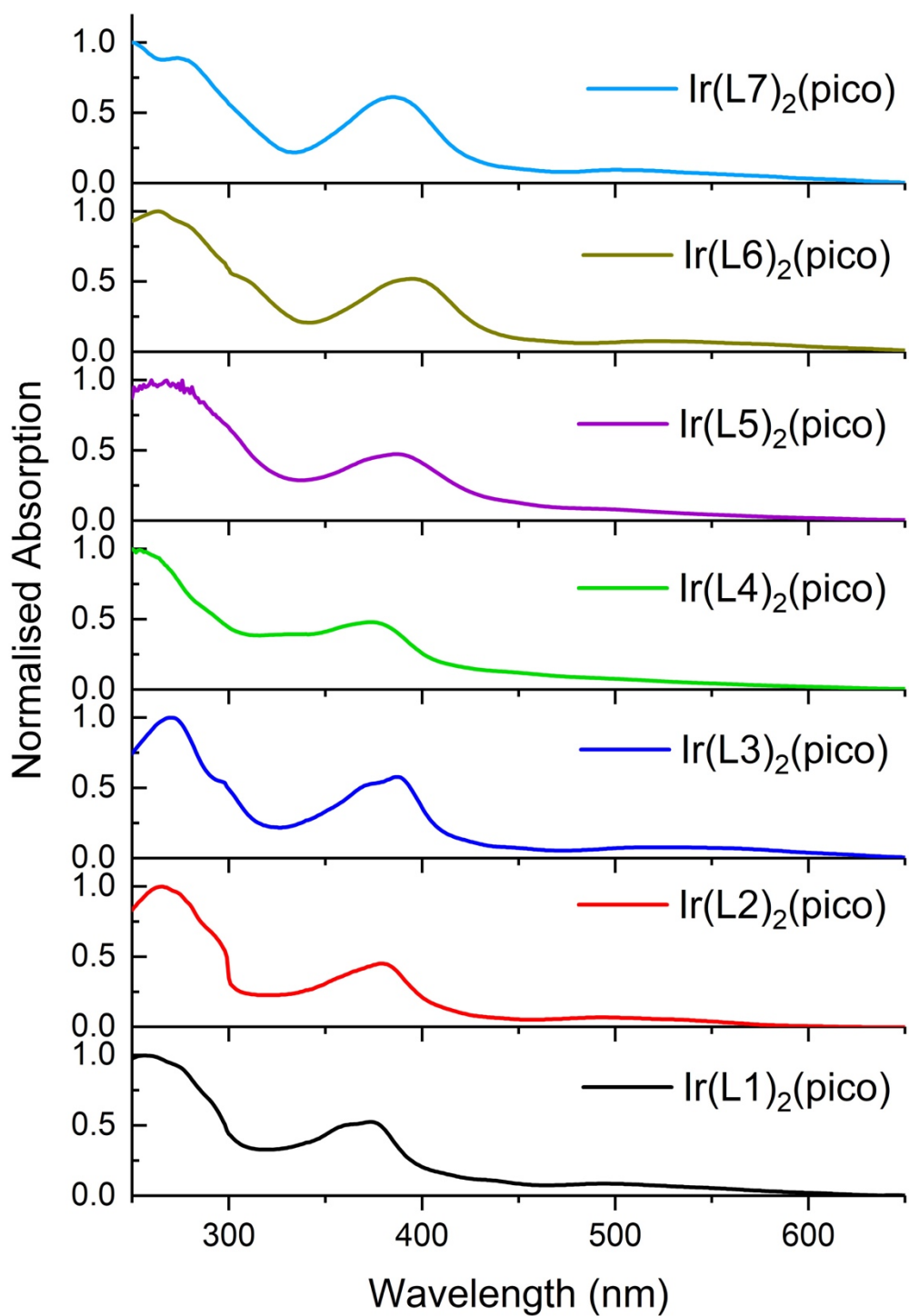


Figure 27 Comparison of the steady state absorption spectra of the picolate-based complexes, normalised.

As can be seen in the above figure 27, the ordering of the spectroscopic features of the complexes are the same as in the bipyridine case from the previous chapter.

4.2.1.2 Simulation of Singlet-to-Singlet Transitions and Orbital Analysis

Molecular orbital decomposition analysis of the calculated singlet state geometries of the picolinate-based complexes allows for more in-depth analysis of the transitions involved in the rest of the DFT analysis, such as the TD-DFT or vertical transition calculations. This in turn can lend a much greater insight into the processes behind the characterisation spectra analysed in the previous section and allow for evaluation of the effects the ligand alterations have on the electronic structure of the molecules. The molecular orbitals of the complexes were once again analysed using the GaussSum software package.

Ir(L1)₂(pico)	Moiety Contribution to Molecular Orbital (%)			
	Ir (5d)	Picolinate	Q1	Q2
LUMO +4	1	1	78	21
LUMO +3	1	23	15	62
LUMO +2	2	96	2	0
LUMO +1	4	1	59	36
LUMO	4	1	36	59
HOMO	40	4	29	27
HOMO -1	43	14	23	20
HOMO -2	9	8	51	32
HOMO -3	34	5	14	47
HOMO -4	14	19	54	13

Table 9 Percentage contributions of each component of the Ir(L1)₂(pico) complex to the frontier molecular orbitals.

The Ir(L1)₂(pico) complex is used as an example above. As can be seen in the above table 9, the electron density is divided relatively evenly across the iridium core and the quinoxaline ligands for the occupied orbitals, with the picolinate contributing less than 20% of the total. The unoccupied molecular orbitals are predominantly localised on the quinoxaline ligands, with the exception LUMOs +2 and +3, which feature strong

contributions from the picolinate moiety. From this examination of the HOMOs and LUMOs, it can be seen that most transitions are again expected to be $^1\text{MLCT}$ in character.

A noteworthy feature of the picolinate complexes is the complete loss of degeneracy between the quinoxalines. In the previous chapter, the bipyridine-based complexes are near symmetrical, resulting in the two quinoxaline ligands being effectively degenerate. This was reflected in the decomposition analysis, as the amount of orbital density contribution from each of the quinoxalines was identical. In the case of the picolinate-based complexes, this is no longer the case. The asymmetry introduced through the use of the picolinate ancillary ligand results in the loss of degeneracy between the quinoxalines, resulting in a division of their orbital contributions, although the energy difference between them is very small. This results in an interesting parity between the quinoxalines, evident in the above table in the form of pairs of orbitals that have identical contributions from the metal and picolinate, but differing contributions from each of the quinoxalines. The LUMO and LUMO +1 form one such pair and it can be seen how the quinoxalines contribute the same total amount for each orbital within the pair and their contributions are mirrored by the other, e.g. for the LUMO Q1 contributes 36% and Q2 contributes 59%, but for the LUMO +1 the inverse is true. An effect similar to this can be seen in the bipyridine orbitals, but to a far lesser degree, as the difference between the quinoxaline contributions was only a few percent at most. This orbital splitting leads to transitions that are very similar in energy. This behaviour is observed across the picolinate-based complexes and continues into the higher unoccupied orbitals. The renderings of the orbitals for $\text{Ir}(\text{L1})_2(\text{pico})$ can be seen in figure 28 below.

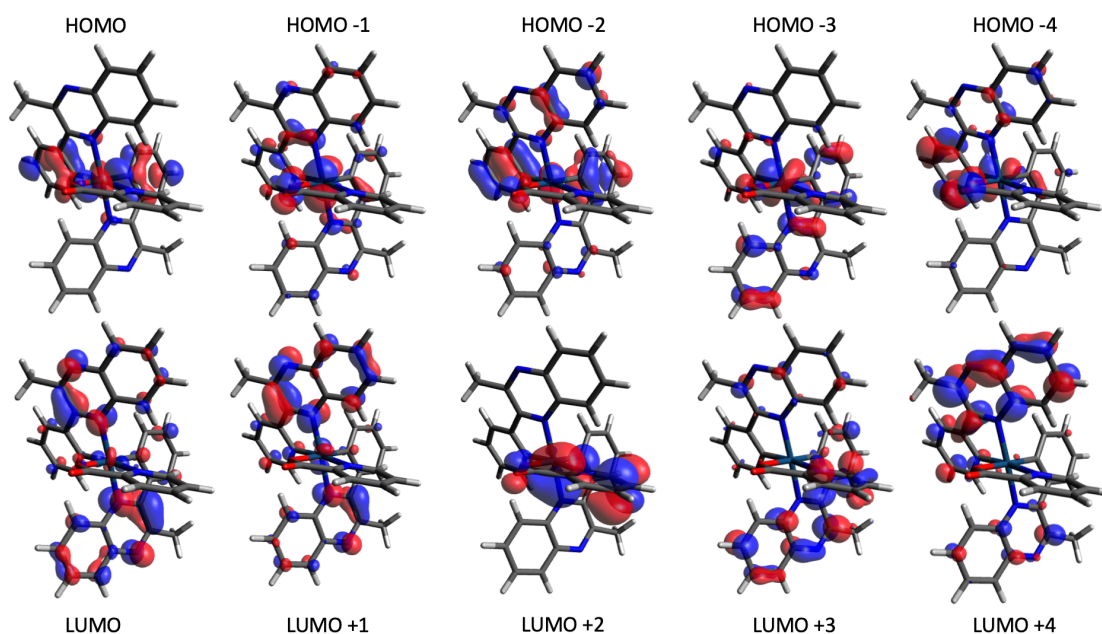


Figure 28 The calculated Kohn-Sham molecular orbitals of the $\text{Ir}(\text{L1})_2(\text{pico})$ complex, rendered with the Avogadro software package, shown for illustrative purposes.

The simulation of the absorption and emission spectra were carried out using TD-DFT and stationary point calculations as in the case of the bipyridine complexes. TD-DFT calculations are useful for simulating spin-allowed absorption transitions, as well as giving insight into the orbitals that contribute to those transitions and the extent to which they contribute. The results of the singlet TD-DFT calculations for the first five singlet excited states are shown below in table 10, again using the $\text{Ir}(\text{L1})_2(\text{pico})$ complex as an archetype.

Excited State	Contributing Transitions
1 (423.97 nm, $f = 0.0349$)	HOMO \rightarrow LUMO (87%)
2 (415 nm, $f = 0.1237$)	HOMO \rightarrow LUMO +1 (84.24%)
3 (343.01 nm, $f = 0.089$)	HOMO -2 \rightarrow LUMO (36.71%) HOMO -1 \rightarrow LUMO (42.68%)
4 (329.34 nm, $f = 0.0442$)	HOMO -1 \rightarrow LUMO +1 (20.79%) HOMO -1 \rightarrow LUMO +1 (48.2%)
5 (321.19 nm, $f = 0.1511$)	HOMO -3 \rightarrow LUMO (38.05%) HOMO -2 \rightarrow LUMO +1 (15.04%)

Table 10 The first five singlet excited states of the $\text{Ir}(\text{L1})_2(\text{pico})$ complex and the molecular orbitals involved in these transitions.

The low-lying excited states correspond well with the secondary ¹MLCT band (350 – 450 nm) assigned in the absorption spectrum of this complex. The first two excited state transitions are a good example of the effect the pseudo-degenerate splitting of the orbitals has on the spectra, as the contributing transitions originate from the same occupied orbitals and proceed to either the LUMO or the LUMO +1 with similar percentages as the other. Subsequent excited states do not reveal particularly meaningful information about the spectra, beyond that there are many short-wavelength, high oscillator strength transitions which correspond well with the main ¹MLCT absorption band observed in the conventional absorption spectrum.

4.2.1.3 Simulation of Steady State Spectrum

The vertical transitions of the complexes were calculated using optimised geometries for the lowest energy at the singlet spin state and stationary points for the opposing spin state from these geometries and are shown in table 11. These offer an approximation of the ³MLCT absorption band centre wavelength utilising the Franck-Condon principle.

Complex	S ₀ to T ₁ Abs. (nm)
Ir(L1) ₂ (pico)	578
Ir(L2) ₂ (pico)	568
Ir(L3) ₂ (pico)	608
Ir(L4) ₂ (pico)	586
Ir(L5) ₂ (pico)	579
Ir(L6) ₂ (pico)	618
Ir(L7) ₂ (pico)	597

Table 11 Vertical transition spin-forbidden absorption wavelengths for the picolinate complexes.

These values take into account only the purely electronic aspects of the transition, and so will not reflect exactly the experimental values.

The TD 50-50 command in the Gaussian 09 software package was used in an attempt to simulate the absorption spectrum in its entirety, as any spin-forbidden absorption bands are missing from the conventional singlet TD calculation. The TD 50-50 command assesses the excited states of both singlet and triplet spin configurations from a singlet ground state, allowing for a far more complete approximation of the spectra. This process is similar to the previous calculations of the triplet state energies, but is capable of yielding energies of triplet states above T_1 . A disadvantage of this technique is that Gaussian 09 is unable to estimate the oscillator strength of any transitions involving a change in spin state and hence unable to determine the probability of any singlet-to-triplet transitions. In an attempt to overcome this, Gaussian distributions were fitted to the TD-DFT produced spectrum, centred around the first five singlet-to-triplet transition values with equal intensity and width assigned to each and this was used to produce a simulation of the total absorption spectrum. An additional complication is that it is likely the response ansatz for TD-DFT will generate a T_1 state energy which is less reliable than using a triplet ground state DFT approach. However, as can be seen, this has little impact on qualitatively describing the spectra. The Ir(L1)₂(pico) complex is once again used as an archetype here, shown in figure 29.

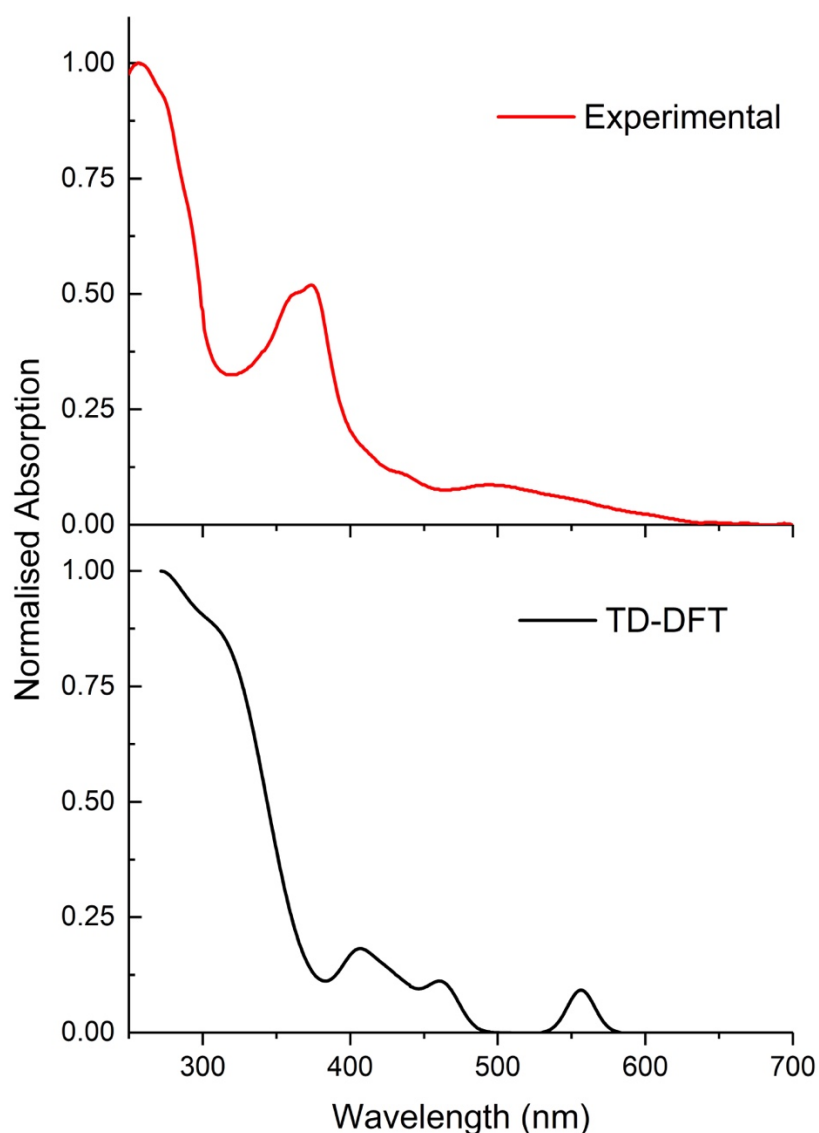


Figure 29 TD-DFT simulation (black) of the absorption spectrum of $\text{Ir}(\text{L1})_2(\text{pico})$ (red). The convolution of the TD-DFT data is discussed in the text. The spectra are qualitatively similar, but show an energetic offset, commonly observed in TD-DFT calculations.

As can be observed above, the simulated spectrum is not a good quantitative fit for the experimentally determined one, as the energy of the features have all been underestimated by the calculation, bathochromically shifting the spectrum significantly. However, qualitatively it matches the spectrum well given the relatively low cost of the calculation and strengthens the argument that the weak feature observed centred at 500 nm in the absorption spectrum is $^3\text{MLCT}$ in character, as this third major feature is lacking in the purely spin-allowed singlet-to-singlet TD-DFT

calculation. It is important to note that the breadth of the features in these simulated spectra is artificial, as the simulation occurs under gas phase conditions with only a dielectric constant to simulate the solvation effects, meaning that line-broadening effects have to be introduced to the transitions simulated using an applied Gaussian function. This effect can also slightly perturbate the appearance of the spectrum.

4.2.2 Pyrazinate-Based Complexes

4.2.2.1 Steady State UV-Vis Absorption

The pyrazinate-based complexes once again exhibit similar features to the picolinate and bipyridine-based counterparts, shown in figure 30.

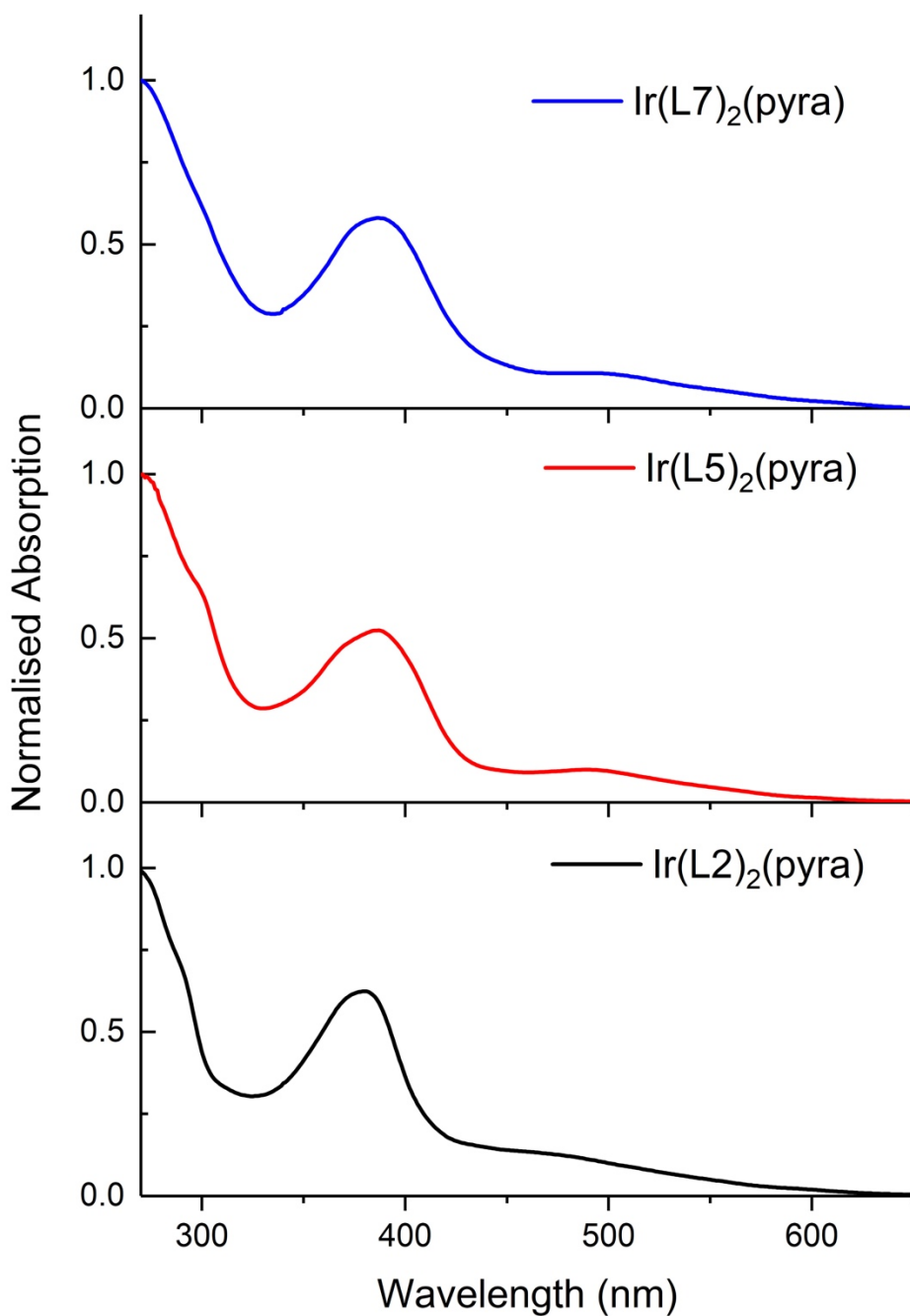


Figure 30 Steady state UV-Vis absorption spectra for the pyrazinate-based complexes.

The spectra show very little difference between one another, an exception being that the L2 and L5 complexes have a more prominent shoulder feature at around 300 nm. The band formally assigned as the ³MLCT absorption band displays a discernible red-shift in the L5 and L7 cases when compared with the L2 complex, presenting as a more distinct feature separate from the ¹MLCT absorption band in the region 320 – 450 nm. Again, the complexes displaying such close spectral similarity suggests that the

spectroscopy of all are derived from the same underlying process, with the relative energies of the molecular orbitals involved in these transitions being subject to minor perturbations induced by the selective alteration of the quinoxaline ligands.

4.2.2.2 Simulation of Singlet-to-Singlet Transitions and Orbital Analysis

Analysis of the orbitals of the pyrazinate complexes followed the same procedure as above. This yielded similar results to the picolate complexes in that the degeneracy of the quinoxaline ligands which was a primary feature of the bipyridine complexes had been lost, again likely due to the lack of symmetry of the complexes when compared to the original set.

Ir(L2) ₂ (pyra)	Moiety Contribution to Orbital (%)			
	Ir (5d)	Pyrazinate	Quinoxaline 1	Quinoxaline 2
LUMO +4	1	9	81	9
LUMO +3	1	88	7	3
LUMO +2	4	77	0	19
LUMO +1	3	10	47	39
LUMO	4	10	48	38
HOMO	38	4	28	30
HOMO -1	28	7	29	36
HOMO -2	19	9	30	42
HOMO -3	22	4	51	23
HOMO -4	21	5	34	41

Table 12 Moiety contributions to the frontier orbitals of the L2 variant of the pyrazinate complex

The L2 complex variant is used here as an example due to the similarity across the complex set. As can be observed in the above table 12, the distribution of electron density across the complex is broadly similar to the previous complexes, with a roughly even distribution found across the occupied orbitals but a predominantly ligand-based distribution across the unoccupied orbitals. This depletion of the iridium-based electron density suggests again that the transitions involved in the spectroscopy of these is metal-to-ligand charge transfer in nature. An important difference to note is

that in the pyrazinate complexes the distribution of electron density between the quinoxaline ligands is not equal overall, with one quinoxaline contributing more across the frontier orbitals. The overall contribution of the quinoxaline ligands is similar to that of previous complexes however. The rendered molecular orbitals of the L2 pyrazinate complex are shown in figure 31 below.

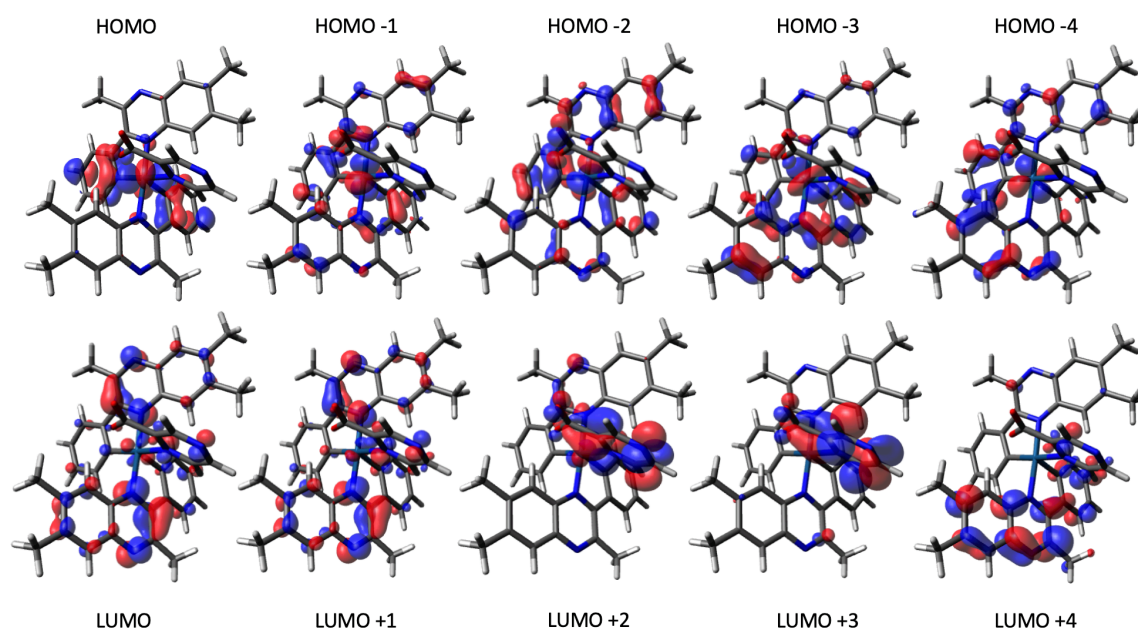


Figure 31 The calculated Kohn-Sham molecular orbitals of the $\text{Ir}(\text{L2})_2(\text{pyra})$ complex, rendered with the Avogadro software package, shown for illustrative purposes

The pyrazinate also contributes far more to the low-lying unoccupied molecular orbitals than in previous complexes, suggesting a more active role in the transitions at the expense of one of the quinoxaline ligands, most notably in the LUMO +2 in the example given.

TD-DFT calculations were performed to estimate the energy of the singlet and triplet states from the singlet ground states of the complexes, as well as to estimate the progression of triplet states from the calculated triplet state minimum energy geometry. Vertical transitions were again also assessed using the minimum energy geometries for each of the states and stationary point energy calculations for the opposing spin state from each of these geometries, allowing for a full simulation of the

experimentally measured spectra. Table 13 shows the first 5 singlet excited states for the Ir(L2)₂(pyra) complex.

Excited State	Contributing Transitions
1 (416.4 nm, f = 0.0466)	HOMO → LUMO (85.41%)
2 (407.26 nm, f = 0.1651)	HOMO → LUMO +1 (80.63%)
3 (347.97 nm, f = 0.016)	HOMO → LUMO +2 (84.46%)
4 (337.1 nm, f = 0.0897)	HOMO -2 → LUMO (56.09%) HOMO -1 → LUMO (18.6%)
5 (325.11 nm, f = 0.0832)	HOMO -3 → LUMO (17.63%) HOMO -2 → LUMO +1 (21.11%) HOMO -1 → LUMO +1 (35.73%)

Table 13 The wavelength, force oscillator strengths and contributing molecular orbital transitions of the first 5 singlet-to-singlet excited states for the Ir(L2)₂(pyra) complex.

The singlet-to-singlet TD-DFT calculations show similar results to those of the picolinate complexes, which is to be expected given the close structural similarity between these two sets. The largest contributions are predominantly directed to the LUMO and LUMO +1, meaning there are strong ¹MLCT transitions at wavelengths in keeping with the medium intensity feature observed in the absorption spectrum of this complex. The lack of any singlet based excited state beyond 416 nm strengthens the argument that the low intensity features longer in wavelength are due to spin-forbidden processes involving the triplet state.

4.2.2.3 Simulation of Steady State Spectrum

The vertical transitions of these complexes were calculated using the same methods as above, approximating the electronic component of the state change from singlet to triplet and vice versa utilising the energy optimised geometries of those states and stationary point calculations for one state from the other states geometry, i.e the singlet-to-triplet absorption was calculated by performing an energy evaluation for the triplet state from the singlet state geometry and determining the difference between the singlet and triplet energies for that geometry. The results are shown in table 14.

Complex	S ₀ to T ₁ (nm)	T ₁ to S ₀ (nm)
Ir(L2) ₂ (pyra)	563	685 (632)
Ir(L5) ₂ (pyra)	573	703 (641)
Ir(L7) ₂ (pyra)	589	714 (651)

Table 14 Computed values for the vertical spin-forbidden absorption and emission for the pyrazinate complexes. Experimental values are shown in parentheses.

The vertical transition values correctly predict the energy ordering of the emission for the set of complexes, with the L2 having the shortest wavelength emission of all, then the L5 followed by the L7. This again demonstrates the utility of this method to quickly and accurately assess a set of complexes to determine what effect a ligand alteration would have on its emissive properties relative to a basis complex, and to what extent.

A TD = 50-50 calculation was also run for each of the complexes in order to more completely simulate the spectra. As for the picolate case, the simulated spectra are quantitatively imprecise but match the qualitative aspects of the absorption spectra reasonably well. Figure 32 shows the simulated and experimental steady state spectra of Ir(L2)₂(pyra).

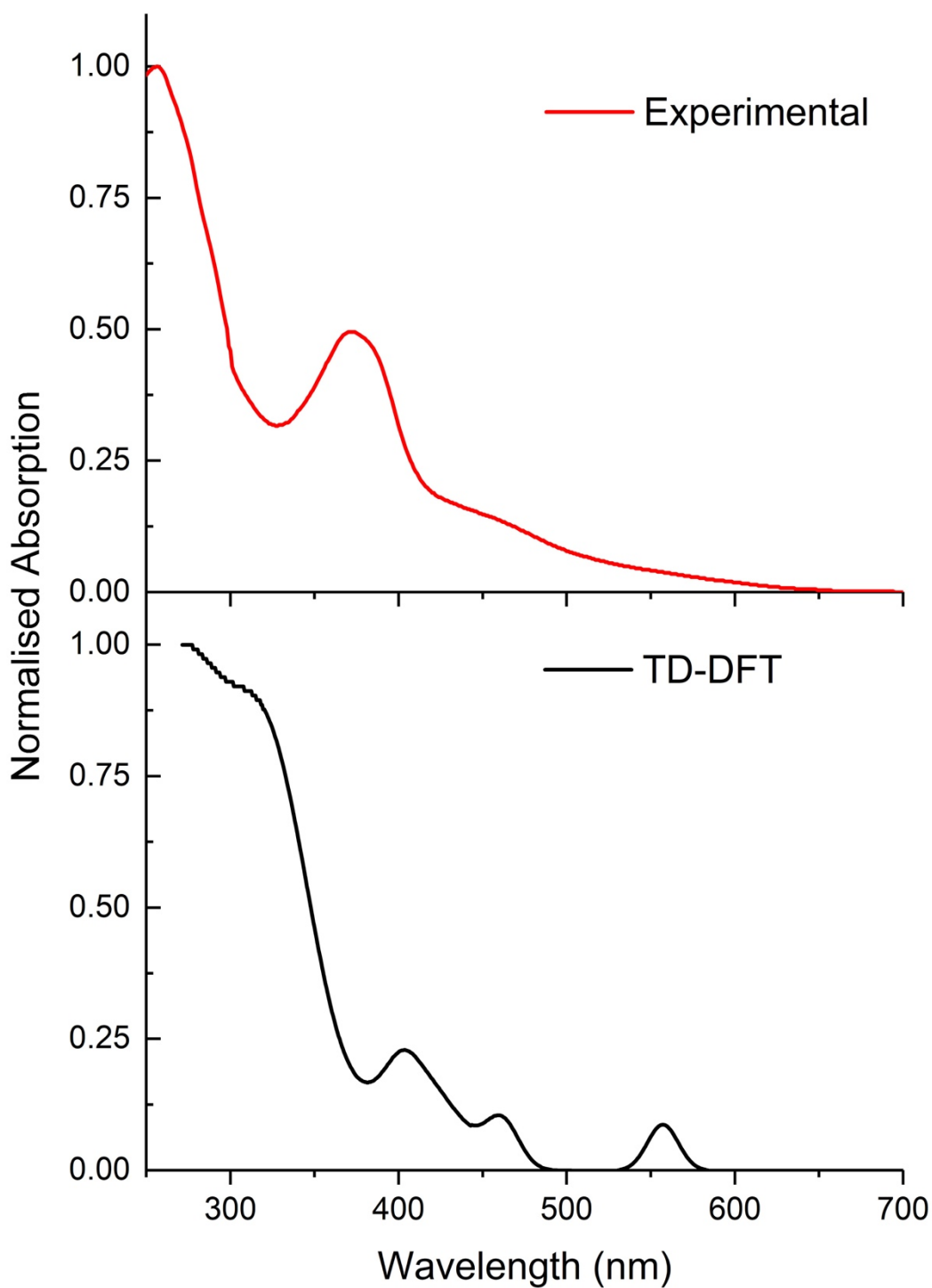


Figure 32 Comparison of TD 50-50 simulated (black) and experimental (red) absorption spectra for the $\text{Ir}(\text{L2})_2(\text{pyra})$ complex.

The inclusion of the singlet-to-triplet states was carried out in the same manner as the picolinate complex set by fitting Gaussian distributions to the centre wavelengths of the spin-forbidden transitions. The same scaling was used for all triplet transitions, as it wasn't possible to determine the relative strengths of each from the DFT calculation

due to the spin-forbidden nature of the transitions. This would introduce some degree of error, as it's unlikely that each spin-forbidden transition is equally probable, and thus this technique is more of qualitative use than quantitative. Nonetheless, despite these issues, the simulated spectra are very useful for determining which components of the experimental spectra are due to changes in spin state. As can be seen in the simulated spectrum in the above figure, the two features between 450 and 600 nm are due to singlet-to-triplet transitions, which matches the two low-intensity, broad features between 410 and 700 nm in the absorption spectrum.

4.2.3 Diquinoxaline-Pyridine Complexes

4.2.3.1 Steady State UV-Vis Absorption

The steady state UV-Vis absorption spectra of the two tridentate complexes are shown below in figure 33.

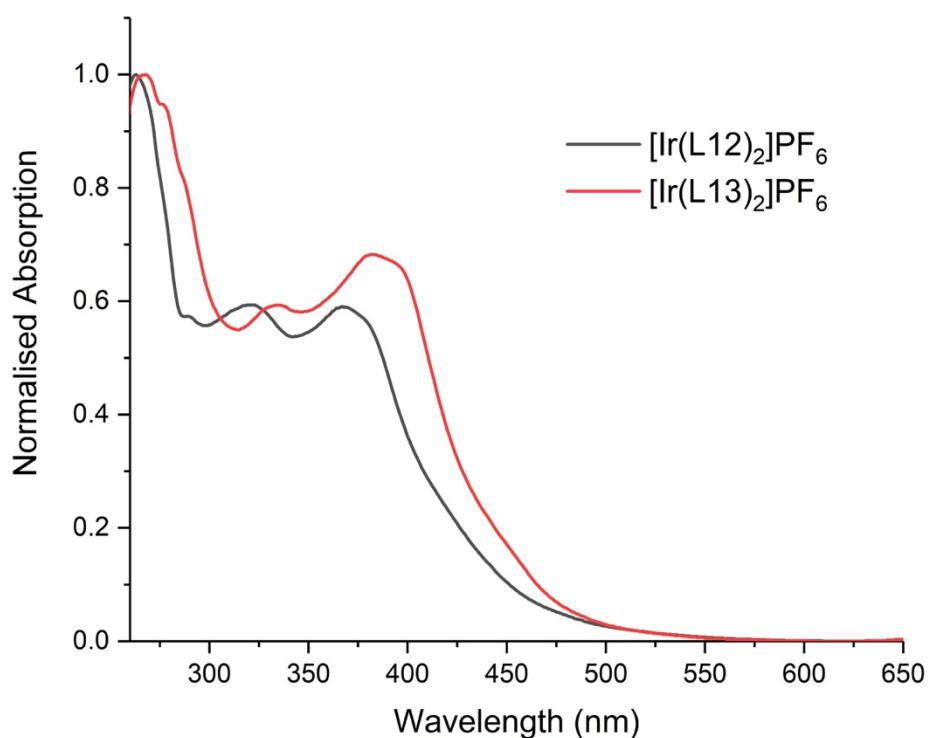


Figure 33 Normalised UV-Vis absorption spectra of the two bis-tridentate diquinoxaline-pyridinyl complexes in chloroform.

The two complexes show a profile that differs significantly from the bidentate complexes discussed so far in this thesis, such as the presence of multiple pronounced

absorption features in the 300 – 400 nm region. Both complexes show a strong absorption <300 nm with visible shoulder features. Whilst previously the bidentate complexes have shown a trio of broad, distinct features, these complexes show a more coherent joined band, with several maxima. Both complexes show a prominent feature in the region 350 – 400 nm, which has a sloping feature extending to ~550 nm. This slope contains a visible low-intensity shoulder feature in both cases that's ascribed to spin-forbidden singlet-triplet absorptions, likely ³MLCT/³ILCT (intraligand charge transfer) in nature, discussed in more detail in the DFT study section of this chapter. The methylated L13 complex shows a clear bathochromic shift in all features of the spectrum, which is otherwise identical in overall profile, save for some relative intensity differences, to the L12 basis complex. Vertical transition estimates of the spin-forbidden portion of the absorption spectrum were performed and are shown in table 15.

Complex	S ₀ → T _n Abs. (nm)
[Ir(L12) ₂]PF ₆	444
[Ir(L13) ₂]PF ₆	527

Table 15 Calculated electronic component of the spin-forbidden absorption between the singlet ground state and the excited triplet state of the diquinoxaline-pyridine complexes.

The spin-forbidden vertical transitions fall in a similar region as the previously studied complexes and suggest that the shoulder peak observed at the longer wavelengths (>425 nm) in the steady state spectra are due to promotion to the triplet state. There is a significantly lower calculated energy of absorption for the L13 complex compared to the L12 complex, suggesting that in this case, methylation of the quinoxaline ligand has substantially reduced the energy gap between the ground and excited state.

The free ligand of the L12 complex was also analysed as a comparison, and its steady state UV-Vis absorption spectrum is shown below in figure 34, contrasted with that of the L12 complex.

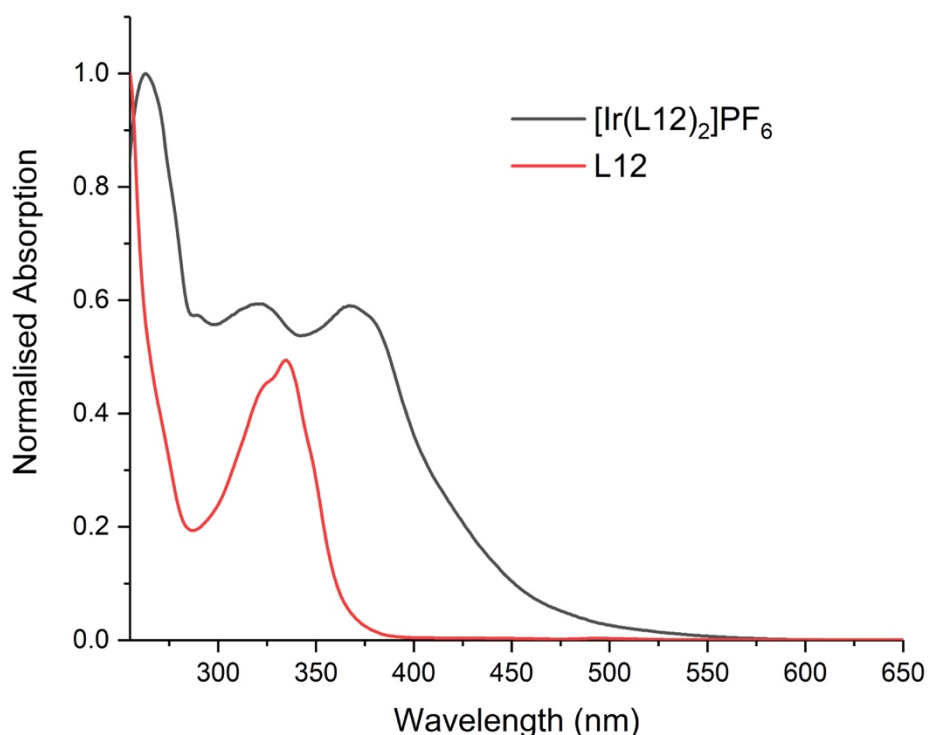


Figure 34 Normalised steady state absorption spectra of the free L12 ligand and its associated iridium complex in chloroform.

From the comparison between the free ligand and the complex, the absorption band between 300 – 370 nm can be ascribed to ligand centred transitions, as similar features can be observed in the absorption spectrum of the free diquinoxaline-pyridinyl ligand.

4.2.3.2 Simulation of Singlet-to-Singlet Transitions and Orbital Analysis

Molecular orbital decomposition analysis was performed on the L12 and L13 based complexes using the GaussSum software package in the same procedure as above, but using different grouping criteria, to reflect the larger ligand structure and reduced number of total ligands. Each ligand was divided into three separate moieties, the C-quinoxaline, N-quinoxaline and pyridinyl groups, with the iridium metal core constituting its own group. This enables a more in-depth examination of the complex contributions when compared to treating each whole ligand as an individual group,

which is unlikely to reveal anything meaningful about the electronic structure of the complexes.

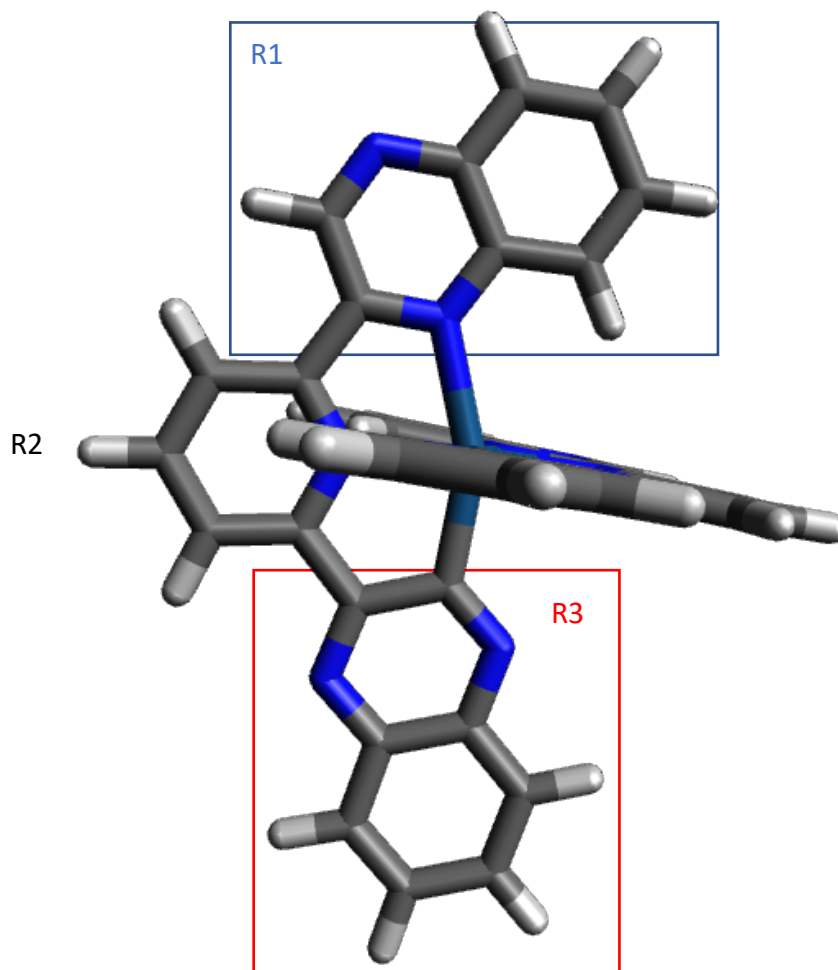


Figure 35 Thickened wireframe representation of the $\text{Ir}(\text{L12})_2$ complex with the 3 moieties of one of the ligands highlighted. These areas of each ligand are used to provide a more effective molecular orbital decomposition of the system.

The three groups chosen above in figure 35 are the same for each ligand, although only one is highlighted for example purposes here. The results of the decomposition analysis for the frontier orbitals of the singlet ground state are shown below, with each of the ligand groups labelled.

Ir(L12) ₂	Ir (5d) (%)	L1 R1 (%)	L1 R2 (%)	L1 R3 (%)	L2 R1 (%)	L2 R2 (%)	L2 R3 (%)
LUMO +4	1	33	15	0	34	15	0
LUMO +3	1	0	21	28	0	21	28
LUMO +2	1	1	19	29	1	20	29
LUMO +1	4	38	11	0	35	10	0
LUMO	4	34	12	1	37	13	1
HOMO	29	2	3	30	2	3	30
HOMO -1	8	3	3	38	3	4	40
HOMO -2	10	2	5	40	2	4	37
HOMO -3	6	1	3	42	1	4	43
HOMO -4	7	3	4	39	3	4	39

Table 16 The decomposition analysis of the singlet ground state frontier orbitals of Ir(L12)₂

As can be observed from the above table 16, the two ligands in the L12 complex are functionally degenerate, with contribution values falling within a few percentage points of each other where they differ at all for each of the equivalent moieties of each ligand for any given orbital. This behaviour is reminiscent of the pseudo-degeneracy seen in some of the other iridium complexes in this work. The L13 complex behaves in a similar fashion as the L12. Renderings of the frontier molecular orbitals of the L12 complex are shown in figure 36 below.

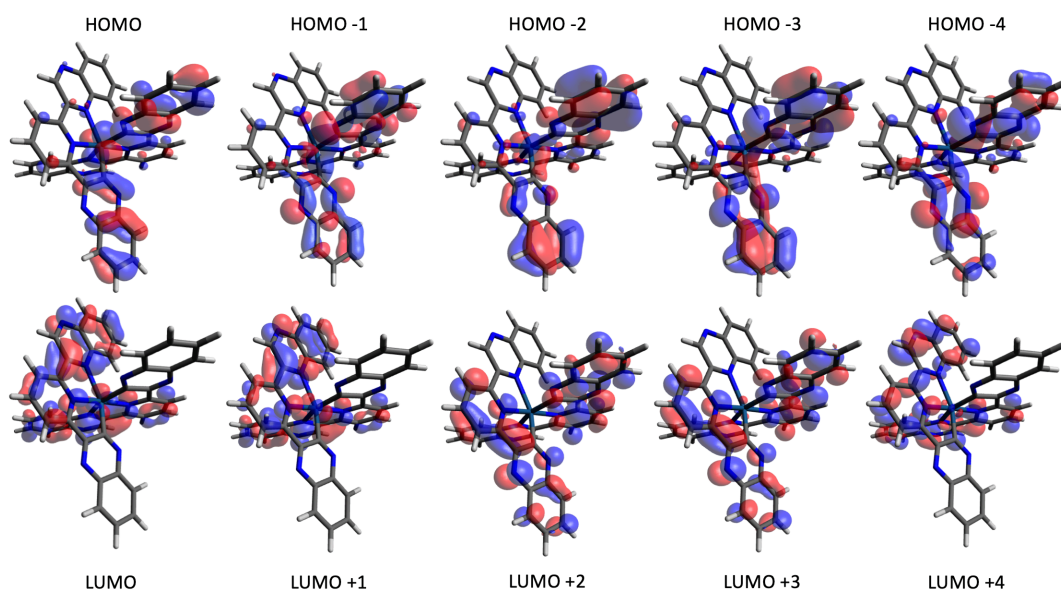


Figure 36 Renderings of the frontier molecular orbitals of the L12 complex, for illustrative purposes.

The first five singlet-to-singlet transitions of the complexes were derived from the singlet geometry using TD-DFT calculations and the results are depicted below in table 17.

[Ir(L12) ₂]PF ₆	
Transition	Contributing MOs
1 (383.91 nm, f = 0.0099)	HOMO → LUMO (76.8%)
2 (383.64 nm, f = 0.0179)	HOMO → LUMO +1 (74.68%)
3 (354 nm, f = 0.0011)	HOMO -5 → LUMO +3 (29.22%) HOMO -4 → LUMO +2 (47.06%)
4 (352.64 nm, f = 0.0007)	HOMO -5 → LUMO +2 (35.74%) HOMO -4 → LUMO +3 (40%)
5 (350.12 nm, f = 0.0067)	HOMO -7 → LUMO +1 (11.99%) HOMO -6 → LUMO (40.22%)

[Ir(L13) ₂]PF ₆	
Transition	Contributing MOs
1 (389.73 nm, f = 0.0218)	HOMO → LUMO +1 (77.21%)
2 (388.5 nm, f = 0.0162)	HOMO → LUMO (79.17%)
3 (352.33 nm, f = 0.0024)	HOMO -6 → LUMO +3 (23.81%) HOMO -4 → LUMO +2 (45.35%)
4 (350.92 nm, f = 0.0003)	HOMO -6 → LUMO +2 (10.57%) HOMO -5 → LUMO +2 (29.27%) HOMO -4 → LUMO +3 (38.64%)
5 (349.04 nm, f = 0.0311)	HOMO -6 → LUMO (27.34%) HOMO -5 → LUMO (21.7%) HOMO -3 → LUMO (11.74%)

Table 17 The wavelength, force oscillator strengths and contributing molecular orbital transitions of the first 5 singlet-to-singlet excited states for the Ir(L12)₂ and Ir(L13)₂ complexes.

Molecular orbital contributions less than 10% have been omitted for clarity

The above tables show that the lowest energy transitions expected from the spin-allowed component of the UV-Vis absorption spectra extend only as far as 380 – 390 nm, in keeping with the results of the spin-forbidden vertical transitions in the attribution of longer wavelength absorption bands (400 – 500 nm) to spin-forbidden processes. The magnitude of spin-forbidden absorption therefore appears to be far more significant in the tridentate complexes than in the bidentate complexes, given

the relatively high intensity of absorption beyond the wavelengths that are ascribed to singlet-singlet processes. This behaviour is evidently a hallmark of iridium (III) quinoxaline complexes, owing to their high degree of spin-orbit coupling allowing formally spin-forbidden processes to occur. Combination of these results with the decomposition analysis shows that the first and second transitions are composed of charge transfers from the Ir centre and R3 moieties to the R1 and R2 moieties, possessing mixed $^1\text{MLCT}/^1\text{LLCT}/^1\text{ILCT}$ character. The low oscillator strengths of these early transitions are likely due to the low wavefunction overlap expected between the R3 moieties and R1 and R2 moieties, due to their spatial separation. One would expect that the spin-forbidden absorption and emission would reflect this also, possessing mixed charge transfer character, given that the unoccupied molecular orbitals of the complexes are ligand dominated.

4.2.3.3 Simulation of Steady State Spectrum

The TD = 50-50 method of simulating the spin-allowed and spin-forbidden transitions was used here once again. Here the first 20 singlet-to-triplet transitions are shown on the spectrum as lines with equal intensities assigned to each, for clarity. This is to once again provide a qualitative assessment of the positions of spin-forbidden absorption bands.

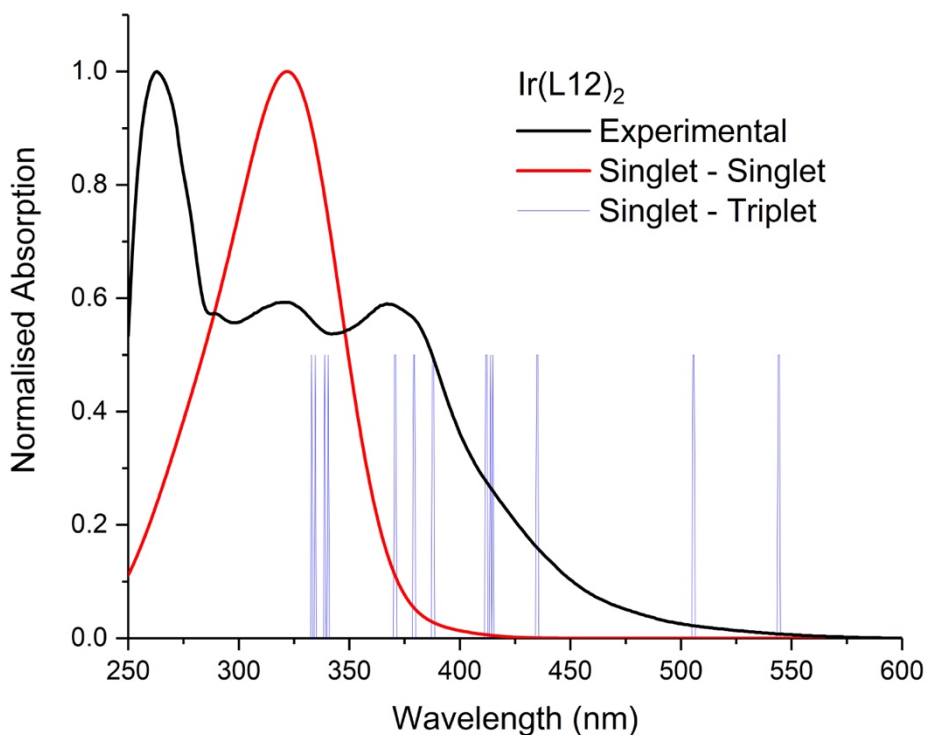


Figure 37 The experimental and simulated steady state spectra of the Ir(L12)₂ complex. In this case, there are a wide array of triplet transitions, and it is not immediately clear how they contribute to the spectrum. Therefore, in this case, the triplet state positions have not been convoluted, but are overlaid as vertical lines to designate position only.

As can be observed in the above figure 37, the spin-forbidden bands of the simulated spectrum correspond closely to the longer wavelength portion of the experimental steady state spectrum, which cannot be explained solely using the spin-allowed portion of the simulated spectrum. This suggests that the intensity of the singlet-to-triplet transitions are greater in the tridentate complexes. Each line in the singlet-to-triplet portion of the simulated spectrum corresponds to a pair of transitions very near to one another in energy, suggestive of pairs of transitions originating from the metal to each of the ligands.

4.3 Emission Spectra

4.3.1 Picolinate-Based Complexes

The set of complexes utilising a picolinate ancillary ligand has a general emission profile shape identical to that of the bipyridine set; each complex exhibits a single broad emission feature, ascribed to a $^3\text{LMCT}$ transition. The position of maximum of the emission band of each complex is once again dependent on the substituents of the quinoxaline ligands. This band position ordering is also identical to that of their bipyridine counterparts, with the L2 ligand presenting a hypsochromic shift relative to the L1 case and the rest being bathochromically shifted to varying degrees. The halogenated complexes, L3, L4, L6 and L7, all show the largest red-shift, with the phenyl-substituted complexes L6 and L7 displaying a slightly greater shift than their methyl-substituted partners. The emission spectra of the picolinate complexes are shown below in figure 38.

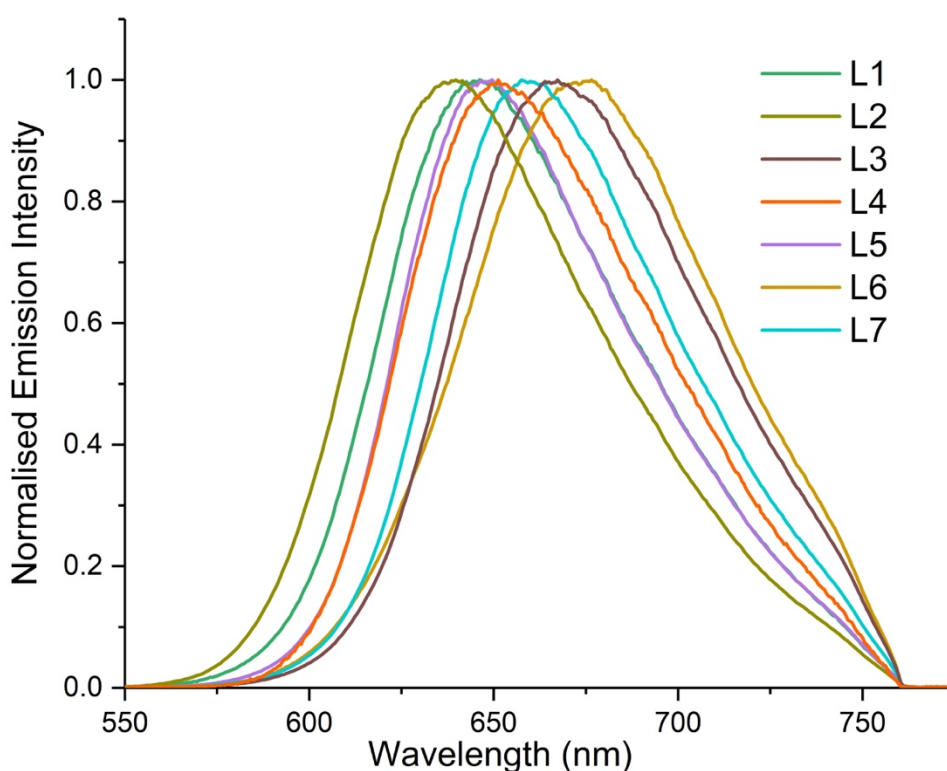


Figure 38 The emission spectra of the picolinate-quinoxaline iridium complex set, normalised to peak maxima for comparison purposes.

The set as a whole is bathochromically shifted compared to their bipyridine analogues, occurring within the region 550 – 770 nm. This indicates that the ancillary ligand also has an influence on the band position, despite DFT evidence indicating that the frontier molecular orbitals ascribed to the transition were predominantly centred on the quinoxaline ligands and the metal centre in the bipyridine case. Given the qualitative similarity of the spectra of the picolinate complexes as well as the significant structural similarities to their bipyridine counterparts, a similar electron density distribution would be expected of them, and this will be discussed in further detail in the DFT section of this chapter. The ancillary ligand is clearly shown by these spectra to be playing a significant role in the spectral properties of the complexes, as the picolinate group emission maxima are red-shifted by values between 24 – 41 nm relative to their bipyridine analogues.

Complex	Emission Peak (nm)	Quinoxaline Substituent
Ir(L2)₂(pico)	638 (689)	CH ₃ , CH ₃
Ir(L1)₂(pico)	646 (697)	CH ₃ , H
Ir(L5)₂(pico)	648 (705)	Ph, CH ₃
Ir(L4)₂(pico)	652 (710)	CH ₃ , F
Ir(L7)₂(pico)	656 (722)	Ph, F
Ir(L3)₂(pico)	667 (739)	CH ₃ , Cl
Ir(L6)₂(pico)	680 (751)	Ph, Cl

Table 18 The emission peak maxima of the picolinate complexes, ordered by their wavelength values. Computationally derived $T_1 - S_0$ vertical transition values are shown in parentheses.

Comparison of the simulated emission values with the experimental results, seen in table 18, show that the applied computational method, as in the previous chapter, underestimates the energy of the emission significantly. An important result to note, however, is the qualitative estimation of the emission wavelength ordering, and hence the effect of quinoxaline substitution, is correct. This emphasises the use of these DFT techniques as an inexpensive way to predict the properties of a complex in advance of synthesising them, and hence informing the design process of iridium complexes. The use of a known complex as a standard greatly aids this process, as it's easier to determine the effect an alteration to ligands would have when compared to a simpler

base compound, the L1 compound in the case of the picolinate and bipyridine based complexes.

4.3.2 Pyrazinate-Based Complexes

The pyrazinate-based complexes once again exhibit a single, identically shaped emission profile with a quinoxaline ligand dependent maximum position, shown in figure 39. The ordering of the three complexes matches the previous trend, with the L2 complex showing the shortest wavelength emission peak, followed by the L5 and L7.

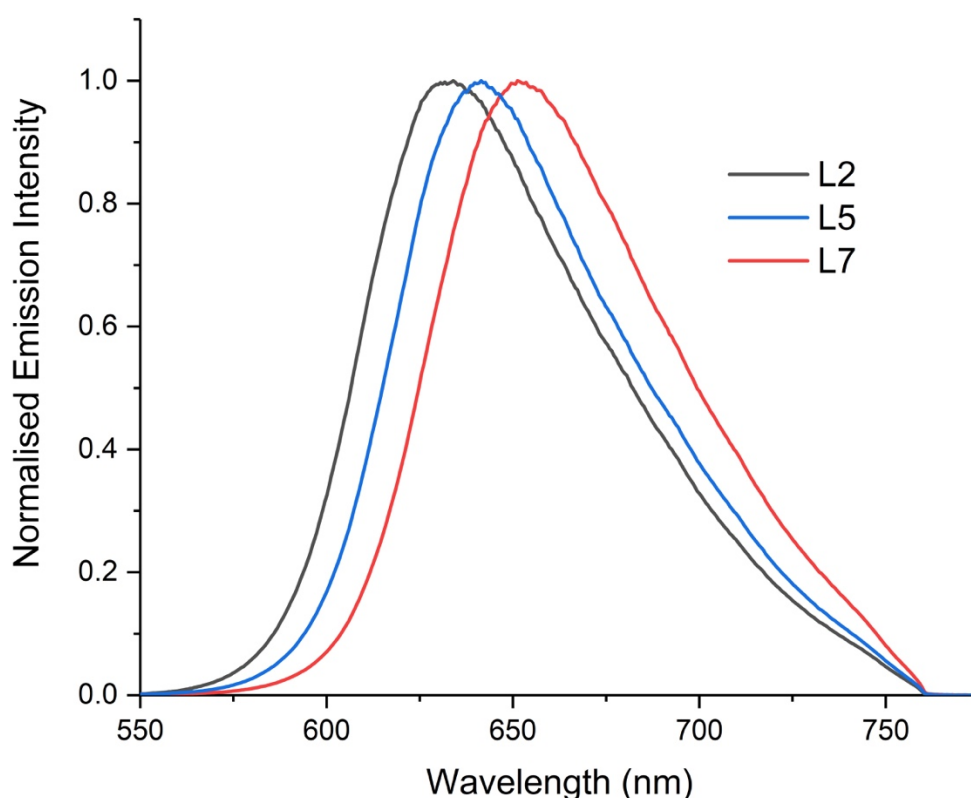


Figure 39 The emission spectra of the pyrazinate-quinoxaline complexes, normalised to peak maxima for comparison purposes.

The spectra are once again bathochromically shifted relative to the bipyridine equivalent set. The pyrazinate based complexes are slightly blue-shifted relative to the picolinate set, which is expected due to the slight change between these two ligands. This hypsochromic shift is consistent across the complexes, as they retain the ordering influenced by the quinoxaline substituents. These features highlight the tuneability of these complexes, as through the adjustment of the quinoxalines a fine tuning can be

achieved whilst careful selection of the ancillary ligand can allow for broad or fine adjustment of the band positions. The emission peak values are shown in table 19 below.

Complex	Emission Peak (nm)	Quinoxaline Substituent
Ir(L2) ₂ (pyra)	631	CH ₃ , CH ₃
Ir(L5) ₂ (pyra)	641	Ph, CH ₃
Ir(L7) ₂ (pyra)	652	Ph, F

Table 19 The emission peak maxima of the pyrazinate complexes, ordered by their wavelength values.

4.3.3 Diquinoxaline-Pyridine Complexes

Both of the diquinoxalinepyridinyl complexes display two emission bands with a concentration-dependent relative intensity. The emission spectra of the complexes at a higher concentration are shown below in figure 40.

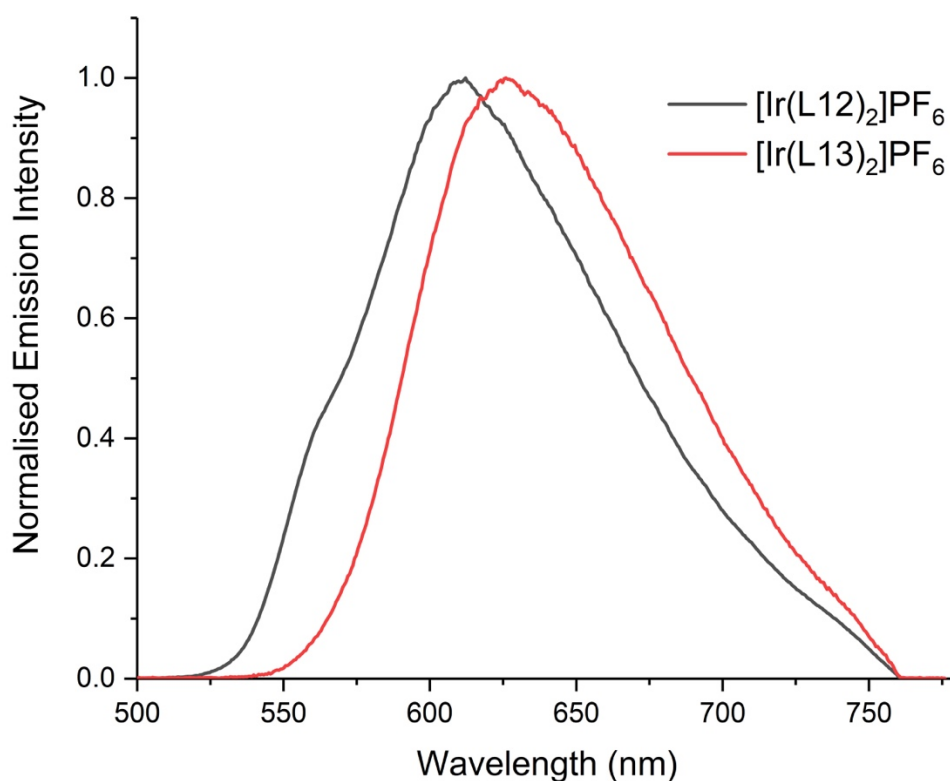


Figure 40 Normalised emission spectra of the two diquinoxaline-pyridinyl complexes in chloroform. Spectra normalised to peak maxima for comparison purposes.

The emission spectra of both complexes are broadly identical in profile. The L12 complex has an emission maximum centred at approximately 607 nm whilst the L13 complex displays a maximum at around 625 nm. The features of the L13 complex are once again bathochromically shifted relative to those of the L12 complex, highlighting the importance of overall structure with regards to the effect ligand alterations have, as this is the opposite outcome to that observed in the bidentate quinoxaline sets of complexes. Both complexes show a slight shoulder feature, most prominently in the L12 complex and visible in the above figure 40 in the region 550 – 575 nm.

Complex	T ₁ → S ₀ Em. (nm)
[Ir(L12) ₂]PF ₆	607 (698)
[Ir(L13) ₂]PF ₆	625 (689)

Table 20 Experimentally determined emission centres for the L12 and L13 complexes.

Simulated vertical transition estimates shown in parentheses.

The results of the vertical transition estimation, shown in table 20, are a good match for experiment, with predicted wavelengths falling within the same region as the complex emission, supporting the assignment of the long-lived emission feature being spin-forbidden in nature. The estimation of the relative energies of the emission centres of the complexes has the opposite outcome to that observed experimentally however, with the L13 complex having a shorter wavelength emission centre than the L12 complex.

The relative intensity of the emission features were found to alter with the concentration of the complex in solution, suggestive of each complex having two emission features with separate states of origin, shown in figure 41. The shoulder peak was not present in the pure chloroform solvent, ruling out contamination.

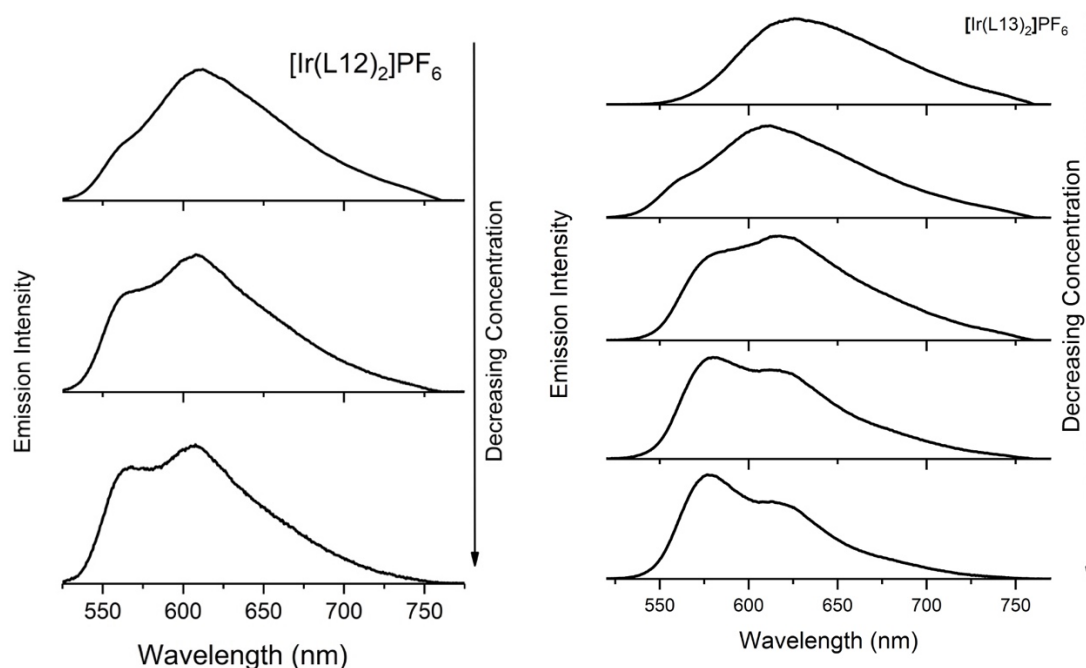


Figure 41 Normalised emission intensities of the two complexes at various dilutions, showing a clear spectral response to complex concentration. The top trace of each complex represents a concentration of approximately 100 μM , with each subsequent trace representing a halving of concentration.

The shift in relative intensity of the two emission bands in each case is attributed to the differing properties of their states of origin. The longer wavelength emission band that wanes in intensity is attributed to a spin-forbidden phosphorescent process as in the cases studied elsewhere in this work, whilst the lower wavelength emission that gains in relative intensity is ascribed to ligand-centred spin-allowed fluorescent transitions. As the latter are significantly more probable than the former, the emission from these transitions will generally be more intense. Whilst the breadth of the two different features convolutes the spectra overall, the concentration study above demonstrates two clear peak wavelengths within the spectra of each complex, and kinetic emission data recorded for each of the peak maxima supports this hypothesis and is discussed in the kinetics section of this chapter. The emission spectrum of the non-complexed L12 ligand was also recorded and is displayed below in figure 42.

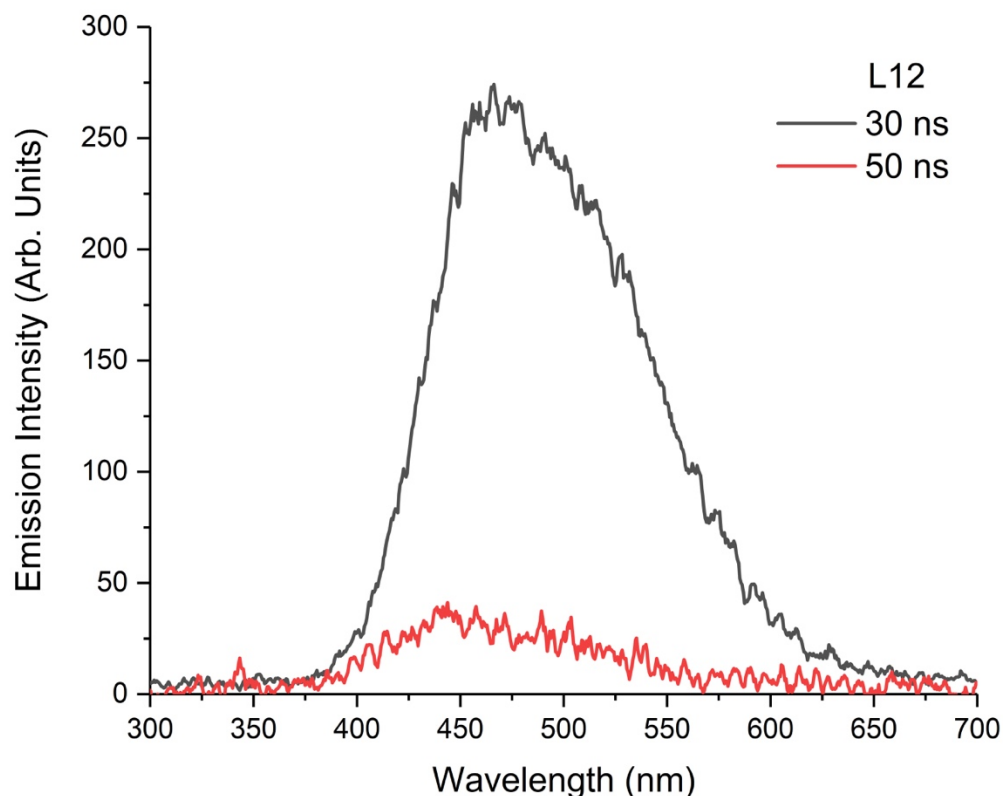


Figure 42 Time resolved emission spectra of the free L12 ligand in chloroform at two different gate delays, that is the delay of the camera in observing the emission after photoexcitation.

The emission spectrum of the free ligand shows a considerable decay with time, as the above figure shows. This is more reminiscent of fluorescence than the long-lived phosphorescent emission typically displayed by iridium complexes.

4.4 Transient Absorption Spectra

4.4.1 Picolinate-Based Complexes

4.4.1.1 Transient Absorption Spectra

As is to be expected from their structural and spectroscopic similarities, the picolinate-based complexes exhibit transient spectra nearly identical to the bipyridine analogues. The method by which the spectra were obtained was slightly improved via the use of emission background subtraction, allowing the removal of the negative-going features caused by the emission of the complex giving a more accurate representation of the complex absorption profile in the 550 – 770 nm region. The complexes all feature a

prominent bleach feature at around 350 – 400 nm, ascribed to the depletion of the ground state ¹MLCT absorption band. The spectra also exhibit strong increases in optical density in the regions 400 – 520 nm and 550 – 670 nm. A broad feature is also visible beyond 650 nm, but this is likely due to poor lamp response beyond this wavelength.

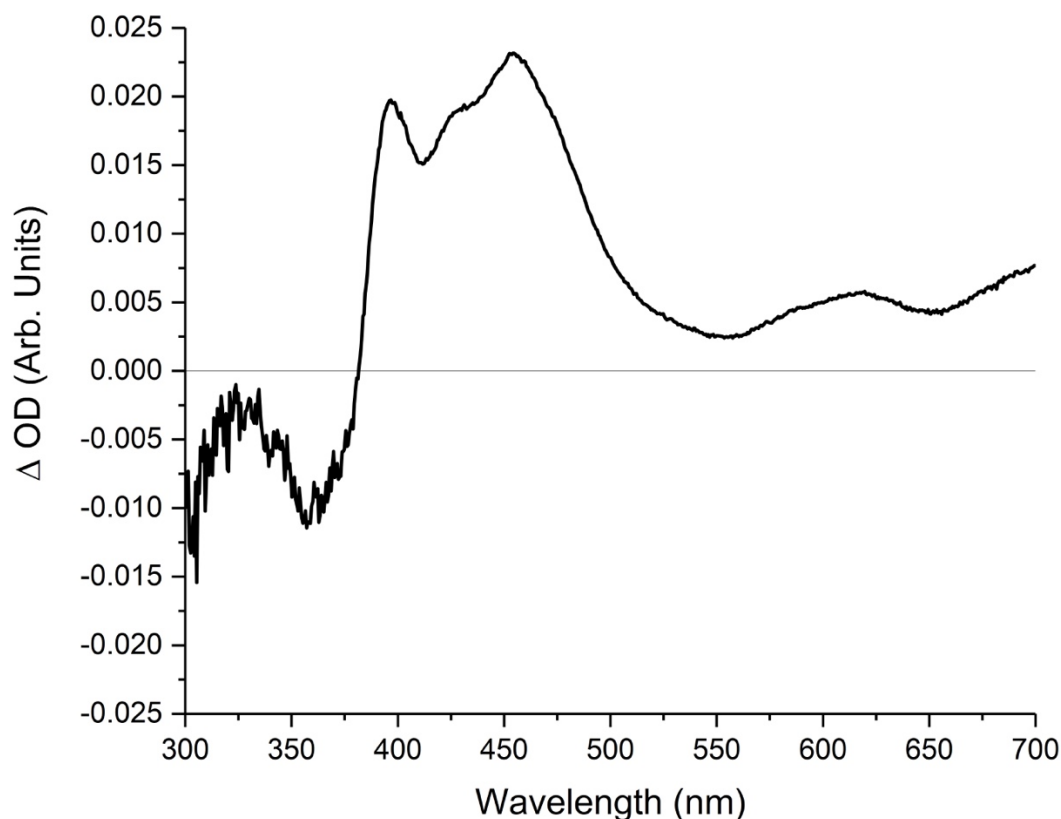


Figure 43 Transient absorption spectrum of the Ir(L1)₂(pico) complex in chloroform at a time delay of 50 ns from the laser pulse.

The TA spectrum of the L1 variant of the picolinate-based complex is displayed above in figure 43 for exemplary purposes, as it's broadly typical of the complexes as a whole and is also used as a reference for the effects of quinoxaline ligand substitution within the group. Whilst the spectra of these complexes are broadly similar to the bipyridine complexes, there are some noteworthy differences. The absorption features visible between 400 – 520 nm are distinct and feature multiple separate peaks, in contrast to the bipyridine complexes where they are generally a single, broad peak. This is likely due to the different molecular orbitals involved in the transitions ascribed to the peaks

being altered to differing degrees by the ancillary ligand change, resulting in the shifting of some features to greater degrees than others. The broad, single feature observed in the bipyridine case is likely due to overlap between multiple features which have since become distinct in the case of the picolinate-based complexes. This is discussed more in the DFT section of this chapter and is an excellent example of the use of transient absorption spectroscopy in the characterisation of these complexes, as it shows substantially more discernible detail than the conventional UV-Vis absorption spectra.

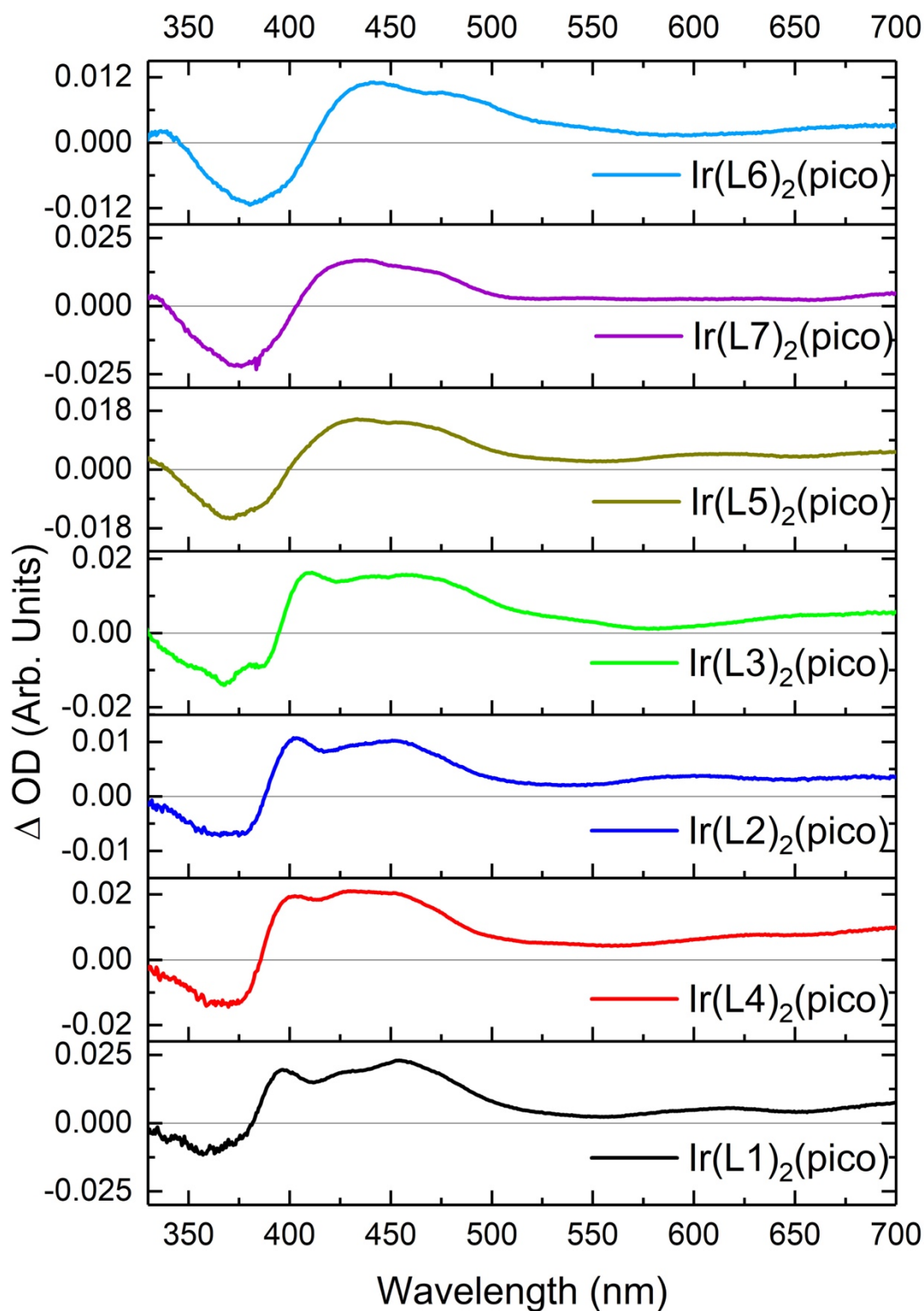


Figure 44 Comparison of the TA spectra of the picolinate set of complexes. The major features show a progression as the quinoxaline substituents are adjusted, exhibiting a bathochromic shift. All spectra obtained at a 50 ns delay from the laser pulse.

As can be observed in the above comparison of the spectra in figure 44, the different features undergo slightly differing degrees of bathochromic shift depending on the

quinoxaline ligand used. The transient absorption spectra also follow the same ordering as the conventional absorption spectra in terms of the positions of the major features in this regard. The phenyl substituted quinoxaline complexes L5 – L7 show much broader absorption features when compared to the methylated complexes L1 – L4, as well as a more pronounced and broader bleach feature.

4.4.1.2 Simulation of Triplet-to-Triplet Absorption

A separate TD calculation was performed from the triplet state of each complex in order to assess the transitions that could be responsible for the features observed in the transient absorption spectra of the complexes. The resulting calculations describe a series of strong absorptions between 300 – 550 nm, with a series of weaker transitions between 550 – 750 nm, in general agreement with the observed spectrum. A simulated spectrum of the Ir(L1)₂(pico) complex is shown below in figure 45.

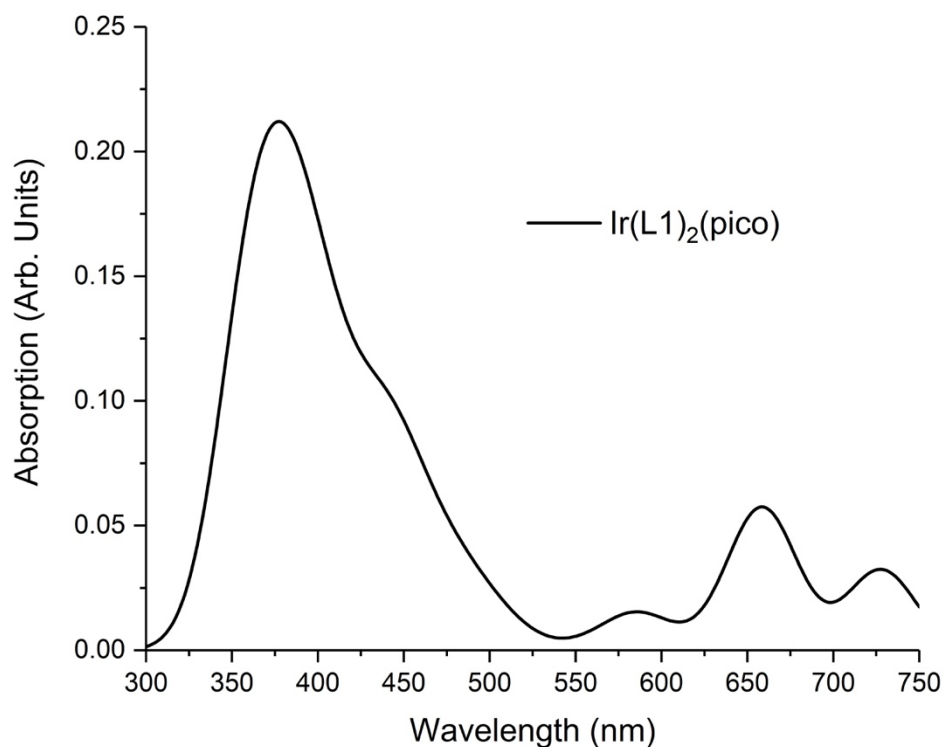


Figure 45 The simulated triplet-to-triplet absorption spectrum of Ir(L1)₂(pico), again convoluted for ease of viewing, as described previously.

The absorption spectrum above was simulated by applying a Gaussian distribution line broadening function to simulated spectral lines. The resulting spectrum is a good qualitative fit for the observed transient absorption spectrum, with a strong absorption band at shorter wavelengths and a series of weaker absorptions beyond 550 nm. The simulated spectra reflect the greater degree of complexity present in the picolinate-based complex compared to the bipyridine equivalent from the previous chapter. The prominent shoulder peak visible in the absorption at 300 – 540 nm is indicative of a multitude of relatively strong absorption features, which is observed in the transient absorption spectrum of the molecule.

4.4.2 Pyrazinate-Based Complexes

4.4.2.1 *Transient Absorption Spectra*

The pyrazinate ancillary ligand doesn't appreciably alter the general shape of the spectra of the complexes when compared to the picolinate set. The limited number of complexes in this set makes it more difficult to draw conclusions about the effect of altering the quinoxaline ligands, but due to the similarity with the picolinate and bipyridine sets some inferences can be made through comparison. The transient absorption spectra of the pyrazinate complex set is shown in figure 46 below.

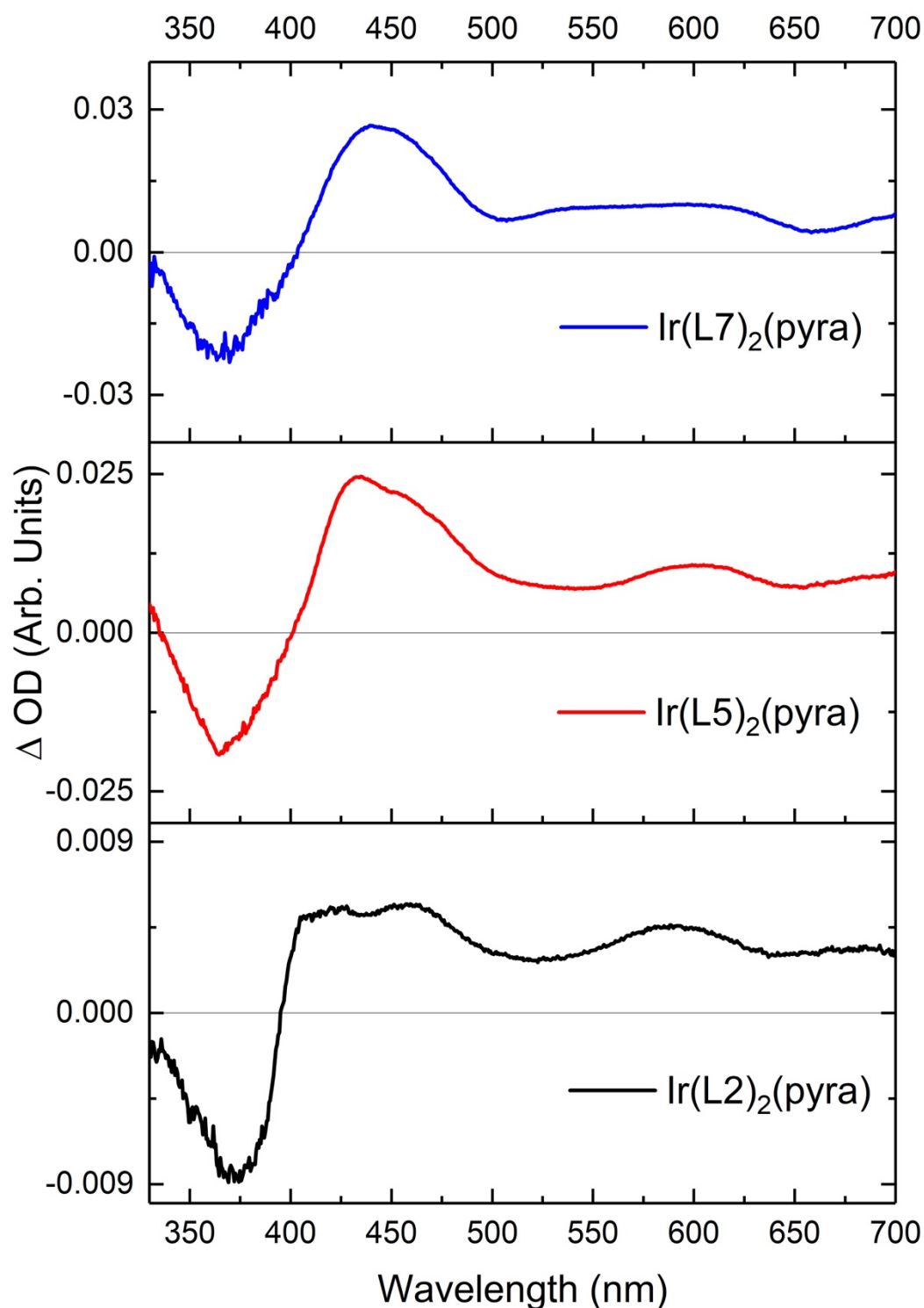


Figure 46 Comparison of the transient absorption spectra of the pyrazinate-based complexes, obtained at 50 ns from the laser pulse.

The two complexes in the set with phenylated quinoxaline ligands, L5 and L7, both exhibit the pronounced bleach and broader, less distinct absorption features seen in their picolinate-based complex equivalents for instance, supporting the argument that

the phenyl group is what causes this effect in the TA spectra. The shifting due to the quinoxaline substituent change is again present here, evidenced most prominently by the maximum of the absorption feature between 400 – 500 nm, as this occurs at ~400 nm in the L2 complex, ~430 nm in the L5 complex and ~440 nm in the L7 complex. The transient absorption spectra of the complex set as a whole is slightly bathochromically shifted in comparison to the picolinate set.

4.4.2.2 Simulation of Triplet-to-Triplet Absorption

The triplet TD-DFT calculations predict a prominent absorption feature between 300 – 480 nm, with contributions from many low-lying occupied orbitals into the LUMO and LUMO +1. There are also a series of less prominent absorptions at longer wavelengths, between 500 and 800 nm. The simulated spectrum of the L2 pyra complex is shown below in figure 47.

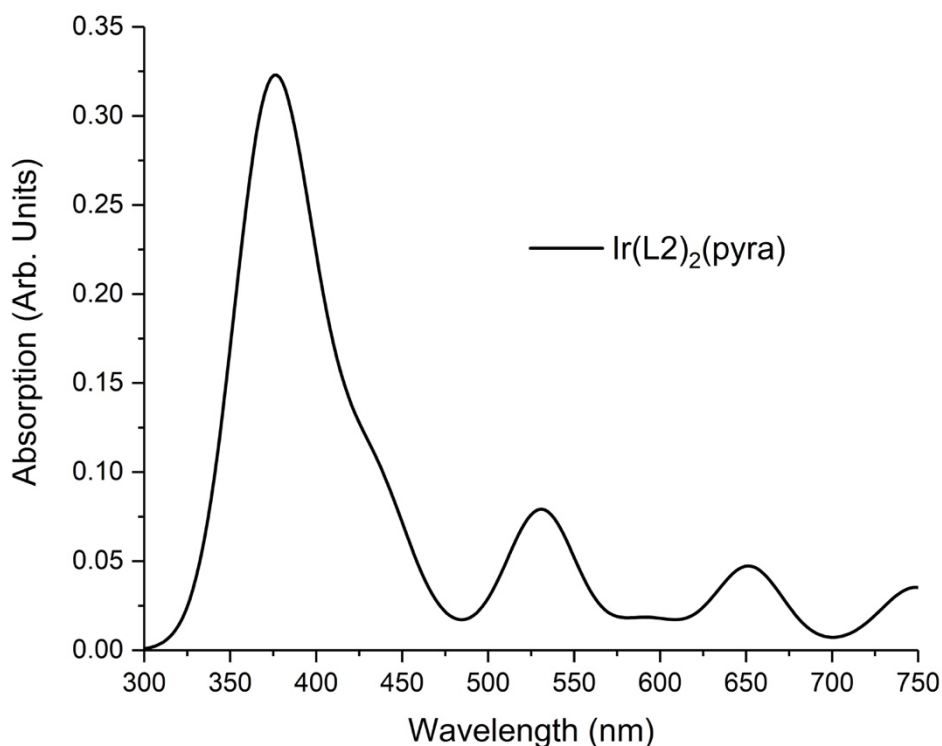


Figure 47 The simulated triplet-to-triplet absorption spectrum of Ir(L2)₂(pyra), again convoluted for ease of viewing, as described previously.

4.4.3 Diquinoxaline-Pyridine Complexes

4.4.3.1 Transient Absorption Spectra

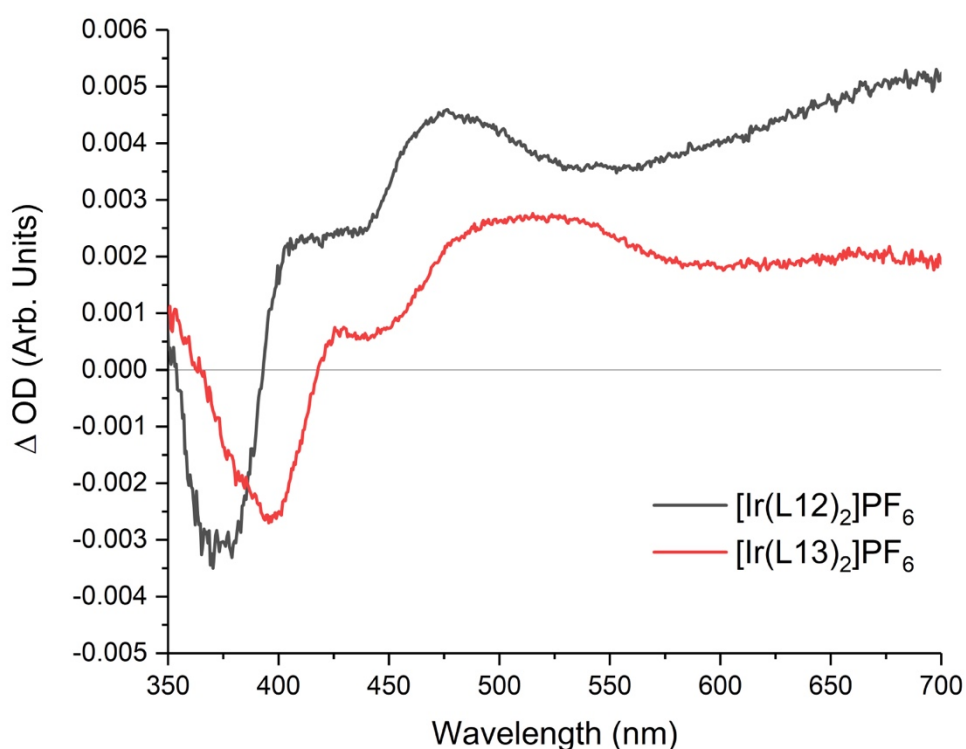


Figure 48 Transient absorption spectra of the two diquinoxaline-pyridinyl complexes in chloroform, obtained at a 50 ns delay from the laser pulse.

The two diquinoxaline-pyridinyl complexes present near-identical transient absorption spectra, shown in figure 48, with a set of features that bear a resemblance to the bidentate complexes already discussed. The prominent bleach feature visible in both is ascribed to a depletion of the ground state absorption bands observed at $\sim 350 - 425$ nm, as there's a close alignment between the onset and maxima of each. The increases in optical density observed between $450 - 525$ nm in the L12 complex and $475 - 600$ nm in the L13 complex are ascribed to triplet-to-triplet absorption bands and are clearly broader in the L13 complex case. These absorption bands are likely predominantly ILCT and LLCT in origin. The previously studied bidentate quinoxaline complexes also displayed similar absorption bands in their transient spectra and in those cases, particularly the picolinate set, the absorption band was shown to be a composition of different absorption features with a structure. It is highly likely that a similar phenomenon is being observed here, as the breadth of the absorption feature overall can be dictated by the degree to which the substituents shift each of the

absorption features that make up the overall band. Both complexes also display a broad increased optical density feature in the longer wavelength region of the spectra, significantly more pronounced in the case of the L12 complex. This is again proving to be a hallmark of quinoxaline-based iridium complexes, as this feature can be observed in the transient spectra of the bidentate complexes previously examined. This broad, long wavelength absorption band is also ascribed to transitions arising from the lowest energy triplet state to higher triplet states.

4.5 Transient Kinetic Measurements

4.5.1 Picolinate-Based Complexes

Analysis of the complexes using the PMT and monochromator detector system shows that the picolinate complexes all have similar lifetimes, with the features displayed by an individual complex all bearing similar decay profiles. The lifetimes of the absorption and emission features are similar and can all be fitted to a mono-exponential decay function, suggesting a single state of origin for each feature. This origin is attributed to the T_1 state, with the long decay lifetime corresponding to the T_1 to S_0 relaxation process, as the relatively long decay lifetimes are indicative of phosphorescence. Kasha's rule would dictate that the complex would rapidly non-radiatively relax to the T_1 state from any higher triplet states it was initially excited to, or converted over to via intersystem crossing, prior to relaxation via phosphorescent emission. The transient kinetic spectra of the L1 picolinate complex are shown in figure 49 below.

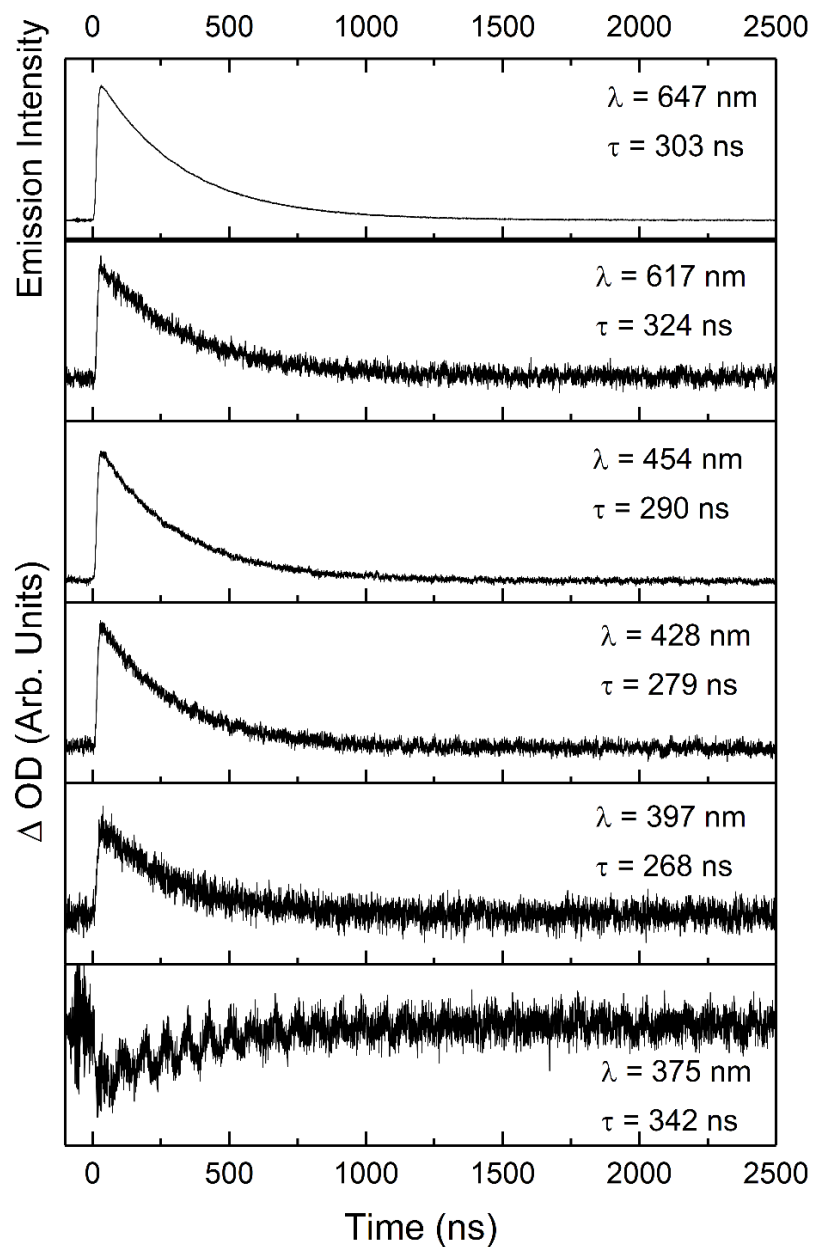


Figure 49 Transient kinetic measurements of the $\text{Ir}(\text{L1})_2(\text{pico})$ complex. The top trace is an emission measurement, all other traces are emission background subtracted ΔOD measurements. All measurements are fitted to a mono-exponential decay function in the Origin 9 software package and lifetimes are displayed next to the trace.

Whilst the lifetimes of the complexes are all within a similar range, the average lifetimes of the complexes show a clear dependency on the nature of the quinoxaline ligands, in keeping with the behaviour of the complexes in general.

Complex	Average Lifetime (ns)	Quinoxaline Substituent
Ir(L3) ₂ (pico)	263	CH ₃ , Cl
Ir(L4) ₂ (pico)	267.4	CH ₃ , F
Ir(L7) ₂ (pico)	270	Ph, F
Ir(L6) ₂ (pico)	292.8	Ph, Cl
Ir(L1) ₂ (pico)	301.4	CH ₃ , H
Ir(L2) ₂ (pico)	320.7	CH ₃ , CH ₃
Ir(L5) ₂ (pico)	324.9	Ph, CH ₃

Table 21 Average lifetimes of the picolate complexes, shown alongside the substituents of the complexes.

As can be seen from the above table 21, the lifetimes of the features are on average shorter for complexes that contain halogens. Phenyl ring substitution on the quinoxaline moiety also appears to extend the lifetime of the features.

4.5.2 Pyrazinate-Based Complexes

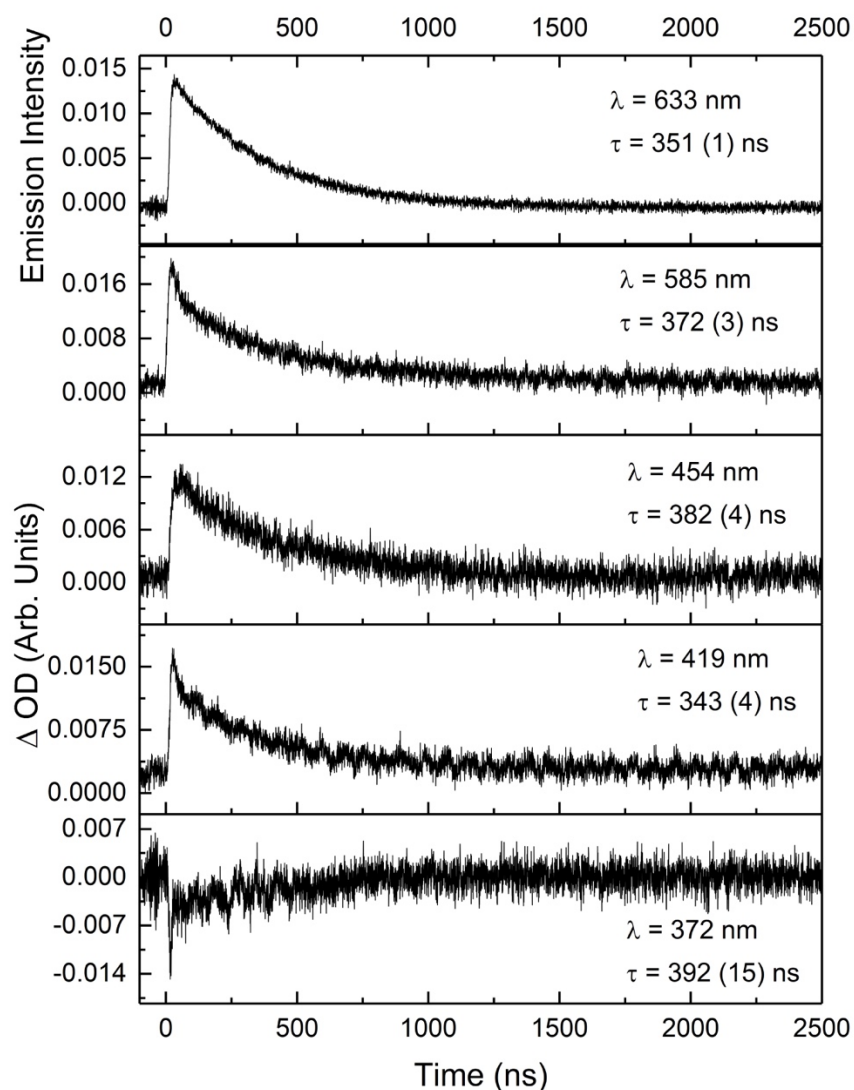


Figure 50 Transient kinetic traces of the major features of the $\text{Ir}(\text{L}2)_2(\text{pyra})$ complex. Fit errors in nanoseconds are shown in parentheses.

As in the case of the picolinate complexes, the feature lifetimes of the three pyrazinate-based complexes are very similar to one another. The L2 pyrazinate complex transient kinetic spectra are shown in figure 50 above. The complexes once again all exhibit kinetic profiles that fit to mono-exponential decay functions for all features, again suggestive of a single-state origin. The underlying process responsible appears to be fundamentally the same in all cases for the quinoxaline-based complexes, with only relatively minor alterations to the exact positioning of features and their lifetimes. This is promising from the perspective of designing complexes, as

the fine tuning of spectroscopic features afforded by this process allows for a lot of flexibility to create a bespoke complex, or set of complexes, for any given application.

4.5.3 Diquinoxaline-Pyridine Complexes

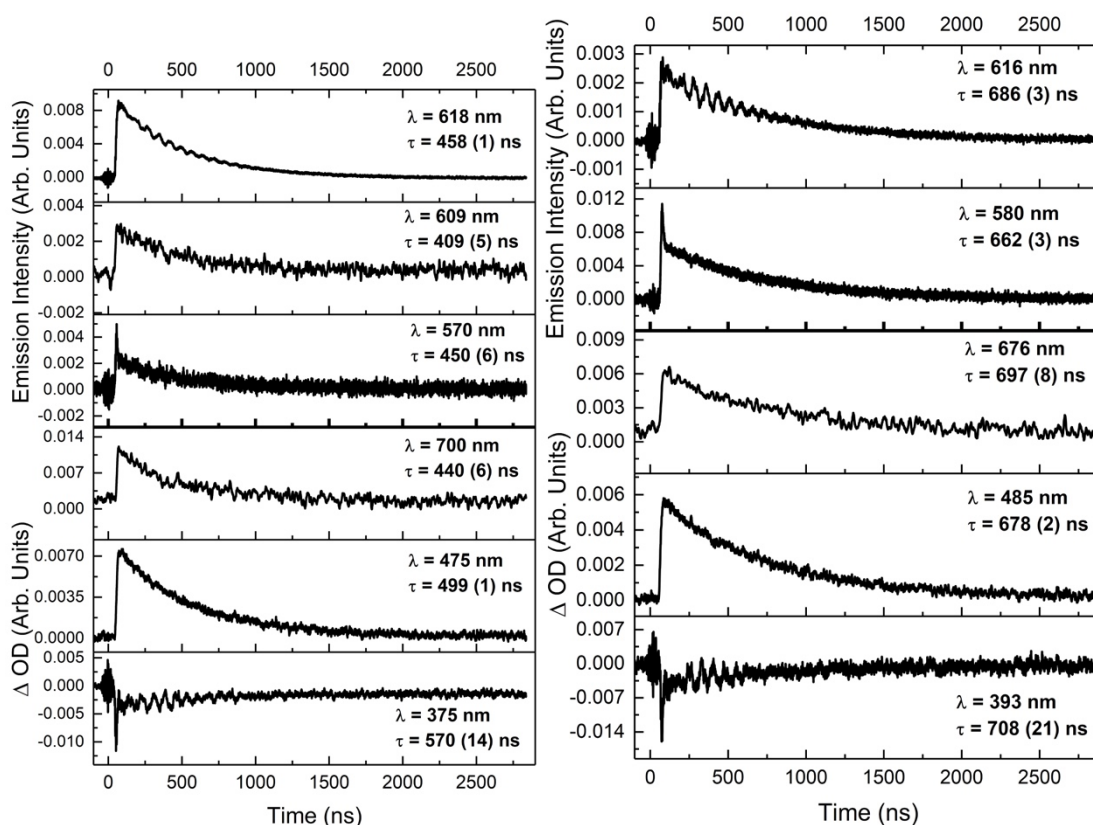


Figure 51 Kinetic traces of the major features of the transient spectra of $[\text{Ir}(\text{L12})_2]\text{PF}_6$ (left) and $[\text{Ir}(\text{L13})_2]\text{PF}_6$ (right) complexes in chloroform. Wavelengths and lifetimes of each trace are inset, with lifetime fit errors in nanoseconds in parentheses.

The transient kinetic spectra of the L12 and L13 complexes are shown in figure 51 above. The emission kinetics were measured at two separate wavelengths to evaluate the additional emission feature observed in low concentration samples. The features all show signs of a single state of origin, with the exception of the bleach features and the shorter wavelength emission features at 570 nm and 580 nm for the L12 and L13 complexes respectively. As can be seen in the above figure, there is a sharp, short-lived peak immediately after $T = 0$ in the 570 nm and 580 nm emission traces, indicative of an additional emissive state. This short-lived feature is suggestive of a fluorescent process, supporting the argument that the additional emission feature observed using

the ICCD detector system is from a spin-allowed process, whilst the longer wavelength feature that dominates the spectrum at higher concentrations is from a spin-forbidden phosphorescent process. The breadth of the emission features observed results in substantial overlap, as was noted in the analysis of the ICCD spectra in the emission section of this chapter, meaning that the longer lifetime feature observed in the 570 nm and 580 nm decay traces above are due to the phosphorescent emission.

Transient Feature	L12 Complex Lifetime (ns)	L13 Complex Lifetime (ns)
Bleach (~390 nm)	570 (14)	708 (21)
ESA (~480 nm)	499 (1)	678 (2)
ESA (~700 nm)	440 (6)	697 (8)
Emission (~575 nm)	450 (6)	662 (3)
Emission (609 nm)	409 (5)	-
Emission (~618 nm)	458 (1)	686 (3)

Table 22 Lifetimes of transient kinetic features of the diquinoxaline-pyridine complexes, $[\text{Ir}(\text{L12})_2]\text{PF}_6$ and $[\text{Ir}(\text{L13})_2]\text{PF}_6$. Fit errors in nanoseconds are shown in parentheses after each lifetime.

Each kinetic feature was fitted to a mono-exponential decay function in order to obtain a lifetime, shown inset next to each trace in figure 51 and itemised in table 22 above. In the cases of the bleach and shorter wavelength emission features fitting was applied from immediately after the initial short-lived peak. The lifetimes of the methylated L13 complex features are longer than those of the L12 basis complex, making this set of complexes similar to the previously observed bidentate cases in this regard. The lifetimes obtained for the two complexes are significantly longer than those previously observed.

4.6. DFT Analysis of Benzoquinoxaline Ir (III) Complexes

The analysis of the four benzoquinoxaline complexes was carried out entirely by DFT methods in support of an experimental study performed by the Pope group at Cardiff

University. The complexes were found by experiment to emit both in the visible and near-infrared (NIR) regions and a DFT study was performed with a primary focus on assessing if the methodology applied to iridium complexes thus far would reflect this significant change in emission energy and to determine the origin of the longer-wavelength emission. This is an important test of the usefulness of DFT methods from the perspective of developing a rational design framework, potentially saving time and cost in the laboratory by allowing complexes to be pre-screened for their spectroscopic properties prior to synthesis. Once again, the B3-LYP functional was used alongside the 6-31G* basis set for the lighter atoms and the Stuttgart – Dresden basis set and core potential for the iridium atom.

4.6.1 Molecular Orbital Decomposition

Analysis of the molecular orbitals proceeded in the same way as the other sets of Iridium complexes, with the percentage contributions of each ligand to the frontier orbitals being considered as well as that of the metal centre. The optimised singlet ground state geometry of each complex was used and the GaussSum software package was employed to perform the decomposition analysis. Table 23 shows the results of this analysis for the L8 complex.

Ir(L8)₂(bpy)	Moiety Contribution to Orbital (%)			
	Ir (5d)	Bipy	BQ1	BQ2
LUMO +4	2	7	45	47
LUMO +3	2	30	36	33
LUMO +2	2	96	1	1
LUMO +1	3	1	48	48
LUMO	3	1	48	47
HOMO	26	1	36	36
HOMO -1	4	1	47	48
HOMO -2	12	1	44	43
HOMO -3	1	0	49	49
HOMO -4	5	1	47	47

Table 23 Percentage contribution of each group to the frontier molecular orbitals of the L8 bipyridine complex.

The molecular orbitals of the benzoquinoxaline complexes L8 and L9 bear a strong resemblance to those of the first set of iridium bipyridine complexes, L1 – L7. Both benzoquinoxaline ligands contribute evenly to the HOMO and LUMO, and generally function as a degenerate pair for all of the frontier orbitals. The HOMO is divided between the metal centre and the benzoquinoxaline ligands, whilst the LUMO is predominantly centred on just the benzoquinoxaline moieties. The metal centre largely plays no role in the unoccupied orbitals calculated, and the bipyridine generally doesn't contribute to most orbitals, save for the LUMO +2 orbital, where it makes the dominant contribution, and the LUMO +3 orbital, where it contributes just under a third of the total orbital. The orbital contributions of the L10 and L11 complexes slightly differ, in that the HOMO is made up of larger contributions from the benzoquinoxaline ligands to the detriment of contributions from the metal centre. The benzoquinoxaline ligands also display a loss of degeneracy in these two complexes, so whilst the general trend of contributions to each orbital from each moiety remain the same, the benzoquinoxalines lack parity in the extent of their individual contributions. The results of decomposition analysis for the L11 complex are shown in table 24.

Ir(L11)₂(bpy)	Moiety Contribution to Orbital (%)			
	Ir (5d)	Bipy	L1	L2
LUMO +4	2	4	35	60
LUMO +3	1	11	56	31
LUMO +2	2	97	1	1
LUMO +1	3	0	47	50
LUMO	3	1	49	46
HOMO	13	0	44	42
HOMO -1	3	1	47	49
HOMO -2	20	1	39	39
HOMO -3	1	0	50	49
HOMO -4	12	1	43	44

Table 24 Percentage contribution of each group to the frontier molecular orbitals of the L11 bipyridine complex.

The loss of degeneracy resembles that observed in the pyrazinate and picolinate complexes, with the two ligands forming pairs of pseudo-degenerate orbital contributions. This suggests that the two complexes, L10 and L11 have geometries that aren't as close to the C2 point group as those of the L8 and L9 complexes.

4.6.2 Simulation of Spectroscopic Features

4.6.2.1 Simulation of Complex Features

The triplet geometries of each complex were optimised using the singlet ground state optimised geometry as a starting point. Using these two geometries to perform stationary point energy evaluations, the vertical transition values for spin-forbidden absorption and emission of each complex were then obtained, as shown in table 25.

Complex	S₀ - T_n Abs.(nm)	T₁ - S₀ Em. (nm)
[Ir(L8) ₂ (bpy)]PF ₆	557.1	993.2
[Ir(L9) ₂ (bpy)]PF ₆	602.3	979.5
[Ir(L10) ₂ (bpy)]PF ₆	582.6	962.3
[Ir(L11) ₂ (bpy)]PF ₆	589.9	1019.1

Table 25 Calculated electronic component of the spin-forbidden absorption and emission between the singlet ground state and the excited triplet state for each of the benzoquinoxaline complexes.

The simulated emission wavelengths for the complexes predict that the triplet-to-singlet emission falls in the NIR region, which is matched by experiment, and the spin-forbidden absorption from the singlet ground state to the triplet excited state also matches weak absorption bands assigned as such observed in the UV-Vis absorption spectra of the compounds. The difference between the absorption and emission bands being so pronounced suggests a large difference in geometry between the ground state singlet and lowest energy triplet state, or alternatively that the absorption occurs from the ground state to a higher-level triplet state. To assess this first hypothesis, the optimised geometries of the ground singlet state and triplet state were compared, and

are shown for the L8 complex in figure 52 below. The RMSD values are shown in table 26 for complexes L8 – L11.

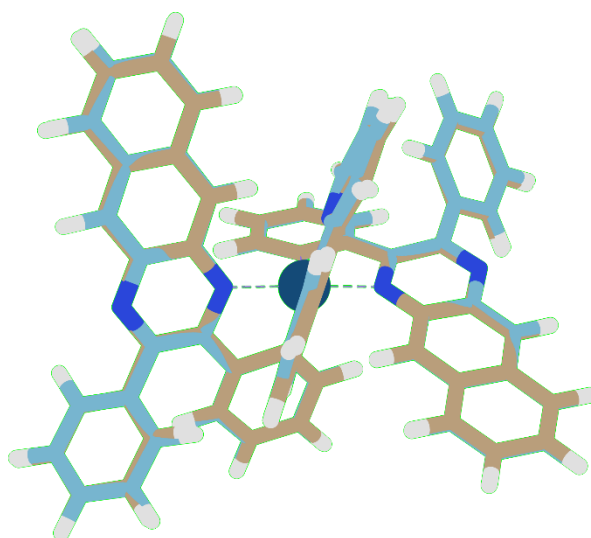


Figure 52 Comparison of the optimised singlet (blue) and triplet (brown) geometries of $\text{Ir}(\text{L8})_2(\text{bpy})$ (RMSD = 0.141 Å)

Complex	$S_0 - T_1$ RMSD (Å)
$\text{Ir}(\text{L8})_2(\text{bpy})$	0.141
$\text{Ir}(\text{L9})_2(\text{bpy})$	0.148
$\text{Ir}(\text{L10})_2(\text{bpy})$	0.149
$\text{Ir}(\text{L11})_2(\text{bpy})$	0.185

Table 26 RMSD values for the geometry difference between the singlet and triplet geometries of the benzoquinoxaline complexes.

As can be observed in the above table, the most pronounced change in geometry is experienced by the halogenated complex, $\text{Ir}(\text{L11})_2(\text{bpy})$, which also possesses the lowest calculated phosphorescent emission energy and one of the largest differences between absorption and emission energy. This is indicative of geometric relaxation

following the electronic promotion to the triplet excited state playing a significant role in the fine tuning of the emission centre wavelength.

Using TD-DFT calculations, the first five singlet excited states of each complex were estimated as well as their contributing molecular orbitals. The results of this analysis are shown for the L8 complex in table 27.

Ir(L8)₂(bpy)	
Excited State	Contributing Transitions
1 (432.75 nm, f=0.037)	HOMO -1 -> LUMO +1 (10.01%) HOMO -> LUMO (72.46%)
2 (425.77 nm, f=0.1092)	HOMO -1 -> LUMO (15.64%) HOMO -> LUMO +1 (65.41%)
3 (401.41 nm, f=0.2957)	HOMO -2 -> LUMO +1 (48.96%) HOMO -1 -> LUMO (38.76%)
4 (397.42 nm, f=0.0084)	HOMO -2 -> LUMO (55.12%) HOMO -1 -> LUMO +1 (34.49%)
5 (353.95 nm, f=0.1783)	HOMO -4 -> LUMO (39.8%) HOMO -3 -> LUMO +1 (37.77%)

Table 27 The wavelength, force oscillator strengths and contributing molecular orbital transitions of the first 5 singlet-to-singlet excited states for the Ir(L8)₂(bpy) complex.

The L8 complex is fairly representative of the behaviour of the set as a whole, as the first excited state is predominantly driven by HOMO to LUMO transition. The calculations suggest that singlet-to-singlet absorption doesn't contribute to the UV-Vis spectrum beyond ~435 nm, supporting the assignment of these parts of the UV-Vis spectrum as being due to spin forbidden in nature. The predominant contribution for the first three excitations arises from the HOMO and HOMO -2 orbitals, which are the orbitals that feature the greatest contributions from the metal centre for the L8, L9 and L11 cases. The L10 complex also features contributions that arise from the metal centre, but these originate from the HOMO -1 in the case of this complex. The transitions all primarily feature promotion into orbitals centred almost entirely on the benzoquinoxaline ligands, as the bipyridine centred LUMO +2 and LUMO +3 orbitals

are not involved in any of the first five excitations. This suggests that the longer wavelength spin-allowed absorption transitions of the complexes are $^1\text{MLCT}$ in nature.

4.6.2.2 Simulation of Ligand Emission

The emission spectrum of the free ligand was also obtained for the L8 ligand and compared to the L8 complex emission in the visible region. The emission of the L8 ligand was simulated using Franck-Condon vibronic simulations from calculations of the excited state and ground state geometries. Figure 53 shows the comparison of the simulated and experimental spectra.

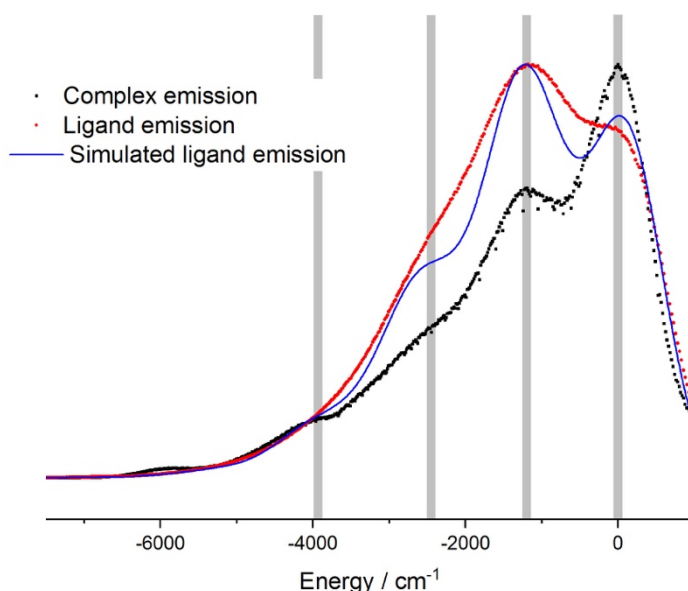


Figure 53 Simulated L8 emission (blue), superimposed on the $\text{Ir}(\text{L8})_2(\text{bpy})$ (black) and L8 ligand emission (red).

The emissions are offset by their vibronic origin for comparison. It can be seen that the visible region emission corresponds well with the emission features of both the ligand and complex, suggesting that the visible region emissive state of the complex is ligand centred. The different ratio of Franck-Condon intensities between the free ligand and the complex emission can be surmised to be due to geometric constraints imposed on the ligand through its bonds to the metal. This rigidity induced by metal bonding likely induces steeper potential energy surfaces in these normal mode coordinates (consistent with an increasing force constant in a classical picture), whilst simultaneously reducing differences in minimum energy geometries between

electronic states. This in turn alters the degree of overlap between the ground state and the emissive vibronic states in comparison to the unbound ligand.

4.7 Discussion of Ligand Effects

4.7.1 Comparison of Bipyridine, Picolinate and Pyrazinate Effects in Quinoxaline Complexes

By examining the differences between the three sets of quinoxaline complexes, the effect of the ancillary ligand can be determined. The bipyridine and picolinate sets can be directly compared in their entirety, whilst only the L2, L5 and L7 complexes can be evaluated entirely. Using the L2 complex of each set as an example, a comparison of their most effectively tuneable feature, their emission spectra, clearly demonstrates the effect of the ancillary ligand, shown in figure 54.

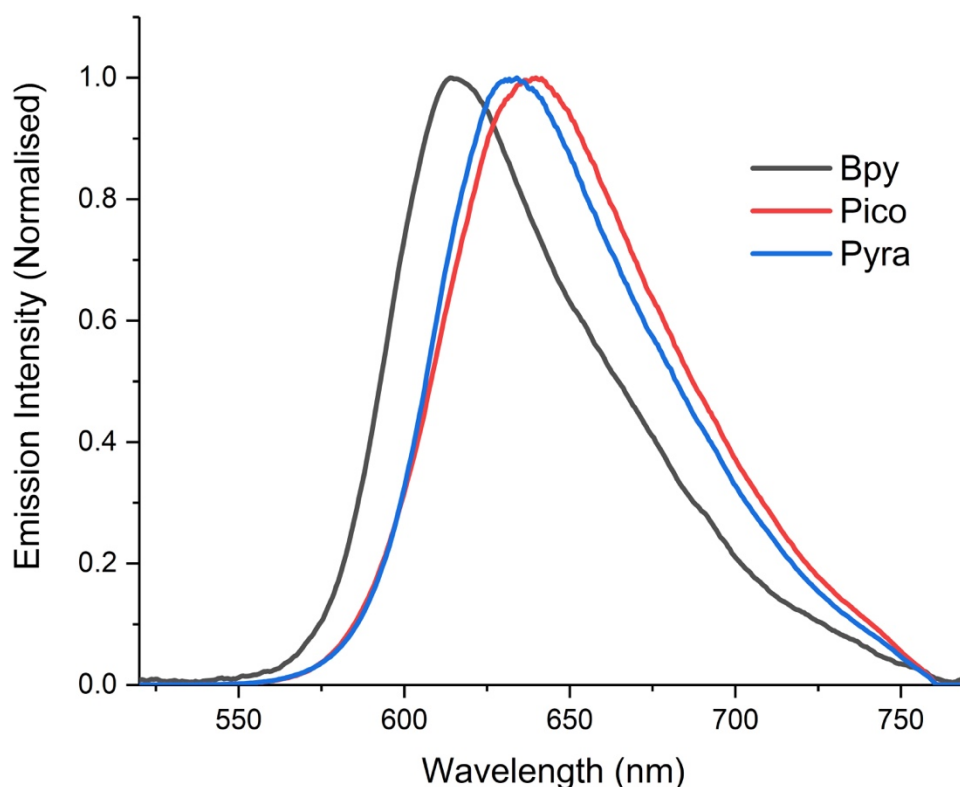


Figure 54 Comparison of the emission spectra of the L2 variant of each complex type. These spectra are overlaid to highlight the effect of the ancillary ligand on the emission peak maximum and normalised to the peak maxima for comparison purposes.

As can be seen from the above figure 54, the peak maxima of the picolinate and the pyrazinate complexes are significantly red-shifted compared to their bipyridine analogue. The pyrazinate and picolinate emission are more similarly positioned to one another, as is to be expected given their close chemical similarity.

Complex	HOMO (eV)	LUMO (eV)	ΔE (eV)
Ir(L2) ₂ (pico)	-5.33	-2.32	3.01
Ir(L1) ₂ (pico)	-5.42	-2.45	2.97
Ir(L5) ₂ (pico)	-5.34	-2.38	2.96
Ir(L4) ₂ (pico)	-5.53	-2.6	2.93
Ir(L7) ₂ (pico)	-5.53	-2.65	2.88
Ir(L3) ₂ (pico)	-5.6	-2.75	2.85
Ir(L6) ₂ (pico)	-5.61	-2.79	2.82
Ir(L2) ₂ (pyra)	-5.43	-2.41	3.02
Ir(L5) ₂ (pyra)	-5.44	-2.46	2.98
Ir(L7) ₂ (pyra)	-5.63	-2.73	2.9

Table 28 Singlet ground state HOMO to LUMO gaps for the picolinate and pyrazinate complexes, ordered from highest energy difference to lowest.

The energy difference between the HOMO and LUMO orbitals of the pyrazinate and picolinate complexes, seen in table 28, show a consistent trend throughout, identical in nature to the bipyridine complexes seen in the previous chapter. Once again there's a clear trend in the HOMO energy levels, with halogenated complexes showing a significantly lower energy relative to L1 and conversely the demethylated complexes L2 and L5 showing a significant destabilisation in the case of the picolinate complexes. The pyrazinate complexes show a similar trend, with the L2 and L5 HOMO energy levels significantly exceeding that of the L7. Like the bipyridine set, the LUMO energy values for all are affected in the same way as the HOMO, but to differing degrees, once again accounting for the differing emission values and ordering. The average frontier orbital energies for each ancillary ligand set are shown in table 29.

Complex set	Avg. HOMO (eV)	Avg. LUMO (eV)	Avg. ΔE (eV)
Bipyridine	-6.26	-3.2	3.06
Picolinate	-5.48	-2.56	2.92
Pyrazinate	-5.5	-2.53	2.97

Table 29 Average energies for the singlet state frontier orbitals of the complex sets

Notable features are the difference in the values of the energy gap between the HOMO and LUMO as well as the absolute energies of the molecular orbitals themselves. In the case of the picolinate and pyrazinate complexes, the energy gaps are substantially lower than the bipyridine complexes, for which all but one exceeds 3 eV. The values of the HOMO are around 0.8 eV higher on average in the picolinate and pyrazinate cases compared to the bipyridine set, and the LUMO values are around 0.65 eV higher on average. This gives insight into the differences in emission wavelength between the complex sets, as the different degrees of elevation in energy of the frontier orbitals by the ancillary ligands is readily explainable by the position and composition of the ligands themselves. The HOMO of each of these complexes is centred far more heavily on the iridium metal core than the LUMO, which is predominantly quinoxaline based. The metal-bonded ancillary ligand can therefore be inferred to be exerting a stabilising or destabilising effect on the HOMO more so than on the LUMO, and this effect depends on the nature of the ligand. The bipyridine ligand is bonded to the metal via two N – Ir bonds and is electron-withdrawing in character, lowering the energy of the HOMO. Conversely, the picolinate and pyrazinate ligands are bonded via a N – Ir bond and an electron-rich carboxylate group, which is electron-donating in character. This destabilises the HOMO in those cases, raising its energy. The difference between the picolinate and pyrazinate complexes can be explained by the additional nitrogen atom of the pyrazine moiety in that ligand structure, increasing the electron-withdrawing effect exerted by that portion of the ligand through increased electron deficiency of the heterocyclic ring.

4.7.2 Effect of Extended Conjugation on Quinoxaline Ligand

It can be observed from the DFT analysis of the benzoquinoxaline ligands that extending the conjugation of the bidentate quinoxaline ligand 'backbone' can further bathochromically shift the emission wavelength into the near-IR region. Varying the substituents of the phenyl groups bound to the benzoquinoxaline moieties was once again shown to have a fine-tuning effect, indicative of subtle tuning compared to the coarser tuning induced by directly altering the quinoxaline main structure. Given the results of the DFT analysis suggesting that the emissive state is predominantly centred on the benzoquinoxaline, and thus the emission is likely $^3\text{MLCT}$ and ^3LC in character, this result is to be expected.

4.7.3 Speculative Prediction of Complex Properties

Given the observed behaviour of the complexes it is speculated that a complex of the form $\text{Ir}(\text{L3})_2(\text{pico})$ substituted with bromine or iodine in place of the chlorine substituent would possess an emission wavelength centre bathochromically shifted relative to the rest of the complex set, with an emission centre at around 690 nm, and that a similar substitution of the complex $\text{Ir}(\text{L6})_2(\text{pico})$ would result in a further bathochromic shift to around 700 – 710 nm.

4.8 Conclusion

The methodology developed in analysing the behaviour of bipyridine-based quinoxaline complexes has proven effective when applied to a range of similar complexes, giving insight into the role of each of the ligand types in addition to that of the cyclometallating variety. Varying the ancillary ligand of the bidentate complexes is shown to have an indirect effect on the emission properties of the complexes via stabilisation effects of the frontier orbitals, equating to a 'coarse' tuning as opposed to the fine-tuning afforded through alteration of the quinoxalines. This is evidenced by the emission wavelength ordering of each of the groups of complexes, which remained consistent in response to alterations made to the quinoxaline groups but altered more

considerably, and within a consistent range, to alterations in the ancillary ligand. The methodology employed proved to consistently predict the relative ordering of spectroscopic features of the whole range of complexes considered, demonstrating the efficacy of the technique.

The alteration of the ancillary ligand structure in the quinoxaline complex group to include a carboxylate group in place of one of the pyridine rings resulted in a significant bathochromic shift in emission centre in comparison to the original bipyridine set discussed in the previous chapter, attributed to the effects discussed above. Between the two new quinoxaline-based complex sets discussed, those with picolinate ancillary ligands showed a greater bathochromic shift overall, with the difference in emission centre between picolinate and pyrazinate being relatively minor. This is attributed to the differing stabilisation effects on the HOMO of the complex by the ancillary ligand, lowering or raising the energy gap between the frontier orbitals. Bipyridine stabilises the HOMO, whilst picolinate and pyrazinate ligands destabilise it, resulting in a smaller energy gap for complexes with the latter two as ancillary ligands.

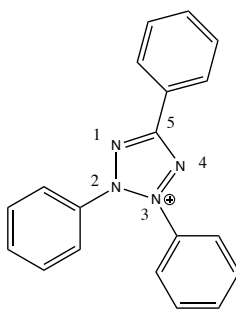
Application of the methodology established in analysing the quinoxaline complexes was also applied to a pair of novel tridentate diquinoxaline-pyridine complexes, consisting of an unsubstituted basis complex and a methylated version. The two new complexes display similar transient absorption profiles to those of the original quinoxaline pair, with a substantial shift between the two. The absence of an ancillary ligand results in the electron density distribution becoming more diverse across each molecule, with greater ligand contributions to both the HOMO and LUMO and an increase in ILCT character in the transition between them. The molecular orbital decomposition analysis used here was more granular than in previous analyses, to account for the greater ligand complexity. The utilisation of a similarly deep approach in analysing the bidentate complexes discussed previously would potentially allow for interrogation of the subtle effects of substitution on the ligand electron density distribution and should be considered as an avenue for future development.

Computational analysis of benzoquinoxaline bipyridine based iridium complexes confirmed a substantial bathochromic shift in the spin-forbidden emission, with extended conjugation of the quinoxaline ligands driving the emission band centre into the near-infrared region of the electromagnetic spectrum. This was a match for experimental results obtained by the Pope group at Cardiff University. Analysis of the molecular orbital distribution across the four complexes suggests that the HOMO and LUMO distribution resembles to that of the bidentate quinoxaline complexes, with the principal absorption transitions being MLCT in nature and the emission LMCT in nature.

5. Inhibiting the Photoreductive Pathway of 2,3,5-Triphenyltetrazolium via Selective Substitution

5.1 Introduction and Background

Triphenyltetrazolium, shown in figure 55, is a cationic compound possessing four nitrogen atoms in a heterocyclic ring, with phenyl rings bonded to the 2, 3 and 5 positions of this tetrazolium ring.



Tri-Phenyl Tetrazolium

Figure 55 The chemical structure of 2,3,5-triphenyltetrazolium, with the positions of the tetrazolium ring numbered.

This compound is commonly used in its chloride salt form (TTC) and is highly photosensitive, with the outcome of the subsequent photoreaction depending on the solvent environment.⁸⁶ Triphenyltetrazolium readily undergoes a reduction reaction to triphenylformazan (TPF), involving the severance of the N – N bond between positions 2 and 3 on the azo ring. The reduction reaction of TTC has an associated colour change when it results in formazan formation, with solutions of triphenyltetrazolium changing from colourless to a deep red colour upon conversion to triphenylformazan.

Depending on the structure of the tetrazolium being reduced, the formazan can possess different spectroscopic and chemical properties. TPF exists in a multitude of conformers, and these were used as the basis for spectroscopic simulation of the absorption spectrum of formazan later in this work, shown in figure 62.

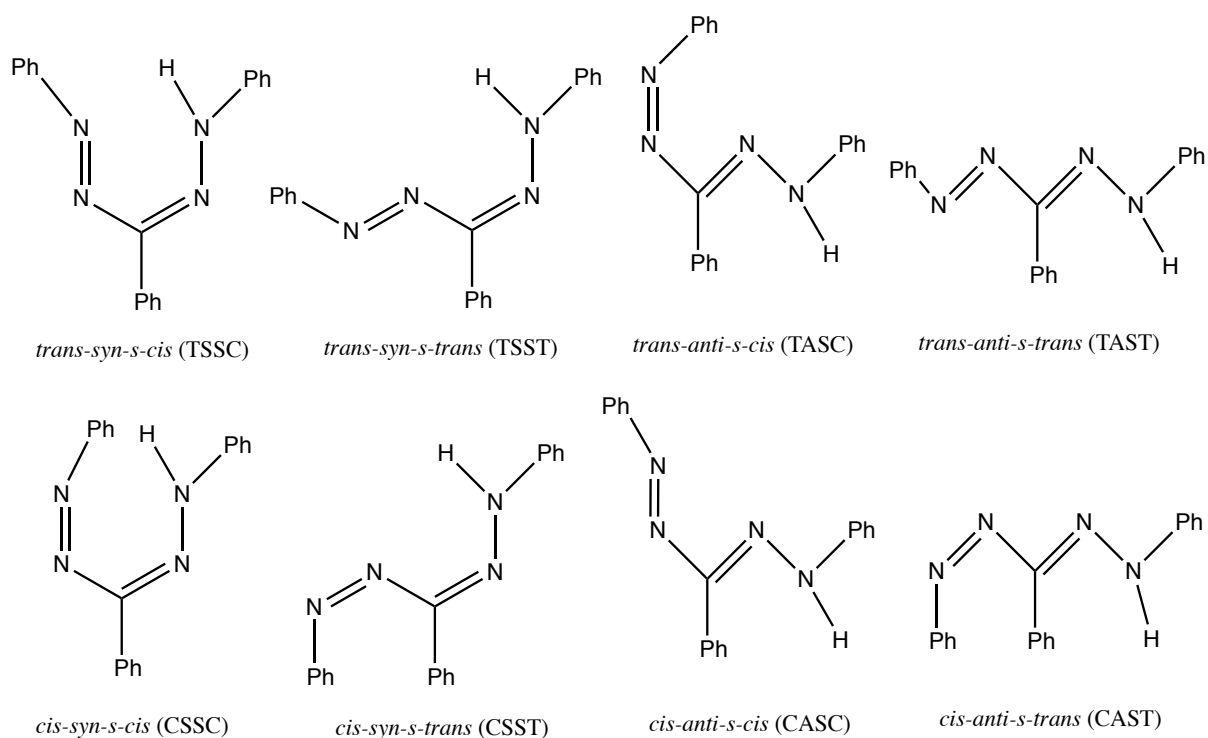


Figure 56 The eight conformers of triphenylformazan considered in this work.

2,3,5-Triphenyltetrazolium hexafluorophosphate (TTP) was used as a basis for this study to facilitate dissolution in acetonitrile, which the chloride form is insoluble in. This was to allow for a solvent system that could accommodate both the TTP and the TPF, otherwise the latter would precipitate on the surface of the sample cuvette. Selective modifications were made to the TTP substituents in order to inhibit this photoreductive potential and attempt to understand the process and develop a mechanistic explanation. To this end, a study was devised based around literature theories on the nature of the photoreduction of triphenyltetrazolium and three variations on the base compound were produced.

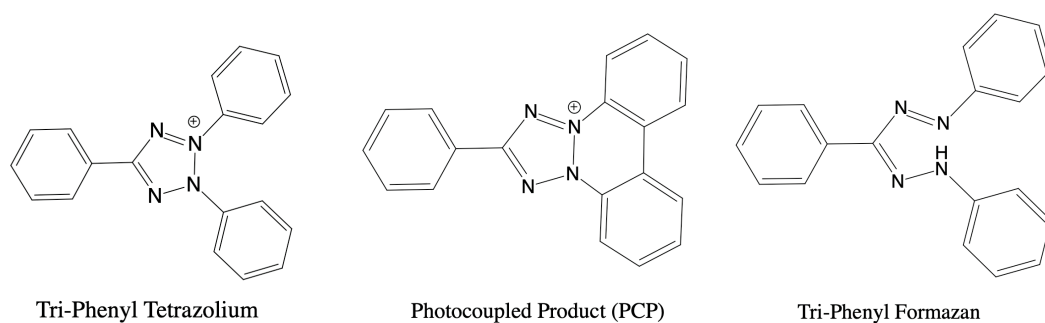


Figure 57 The basis compound triphenyltetrazolium and the photocoupled and formazan products formed from its photoreduction.

Investigations into this system in the literature have proposed the existence of a photocoupled product in addition to the formazan, produced under certain circumstances depending on the solvent environment.^{86–89} The photocoupled product (PCP) is proposed to be formed following the generation of tetrazonilyl radical species induced by photoexcitation and the acquisition of an electron from solution. Two equivalents of this then undergo a disproportionation reaction to produce the formazan and photocoupled product, shown in figure 58.⁸⁶

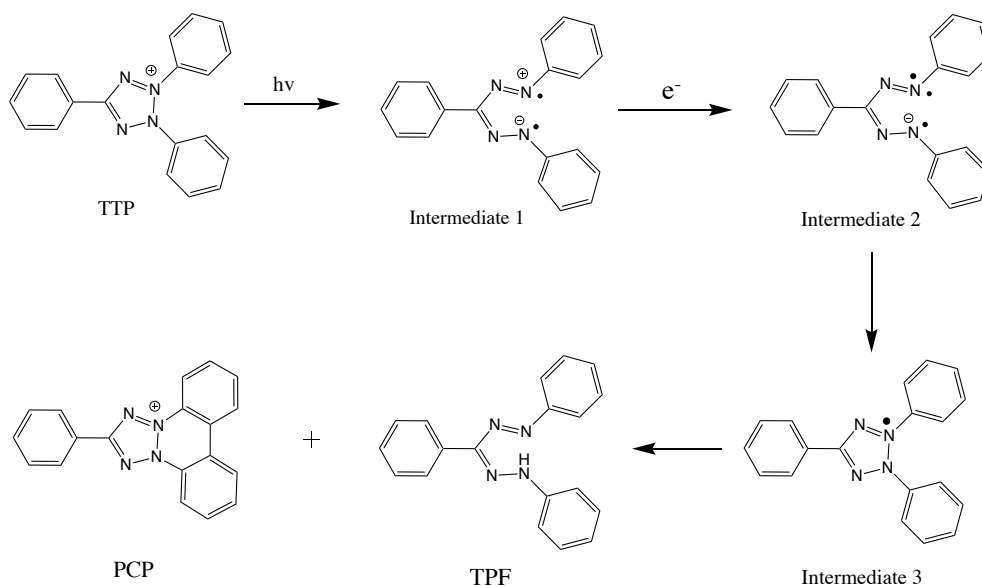


Figure 58 The proposed mechanism of the photoreaction of triphenyltetrazolium, leading to the formation of triphenylformazan and the photocoupled product species.

5.2 Compound Structures

The aim of this study was to inhibit the photochemistry of TTP by blocking the sites that are involved in the bridging reaction that allows for the formation of the tetrazonilyl radical. The proposed mechanism for PCP formation occurs via a bridging reaction between the ortho sites of the phenyl rings bonded to positions 2 and 3 of the tetrazolium ring, as described in figure 58. It was postulated that substitution on these sites could inhibit the formation of PCP via steric interference or chemical inhibition of the elimination reaction of the ortho substituents. Novel synthesis of TTP variants by the Fallis group at Cardiff University was carried out to produce candidates for the inhibition of the photochemistry that leads to PCP and TPF. Due to TTPs potential as a chemical agent sensor via chemical reduction, it would be beneficial to prevent false positives due to light exposure, so a photostable tetrazolium compound would be ideal for such applications.

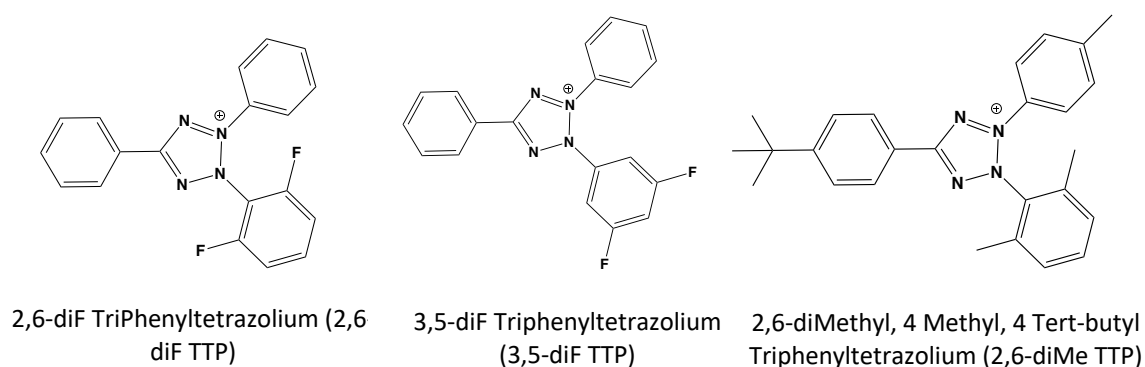


Figure 59 The three substituted variants of TTP involved in this study.

As can be seen in figure 59 the substituents were placed in the 2,6 and 3,5 positions of one of the N-phenyl rings to assess the effect it would have on the rate of formation of the photocoupled product. It was postulated that in the 2,6 substituted cases there would be direct inhibition of the formation of PCP and TPF through steric hindrance of the ortho phenyl-phenyl bond formation, whilst the 3,5 substituted case was to assess the effect, if any, the substituents presence elsewhere on the ring would have. The different substituents, Me and F, used in the 2,6- substituted cases were chosen to compare the effects of steric hindrance on the degree of inhibition. For brevity, the

compounds are referred to by the main substituents placed on the bridging phenyl ring, i.e. 3,5-diF, 2,6-diF and 2,6-diMe, as shown in figure 59. It was proposed that using the spectroscopic technique of flash photolysis, supported by kinetics and DFT, that these novel TTP variants could be examined and the postulate of photochemical inhibition tested, and the nature of the photoproducts ascertained.

5.3 Steady State UV-Vis Absorption Spectra

The steady state absorption spectra of each of the tetrazolium compounds were acquired for the purposes of determining the pump wavelength required in the flash photolysis experiments.

5.3.1 Triphenyltetrazolium (TTP)

5.3.1.1 Steady State UV-Vis Absorption

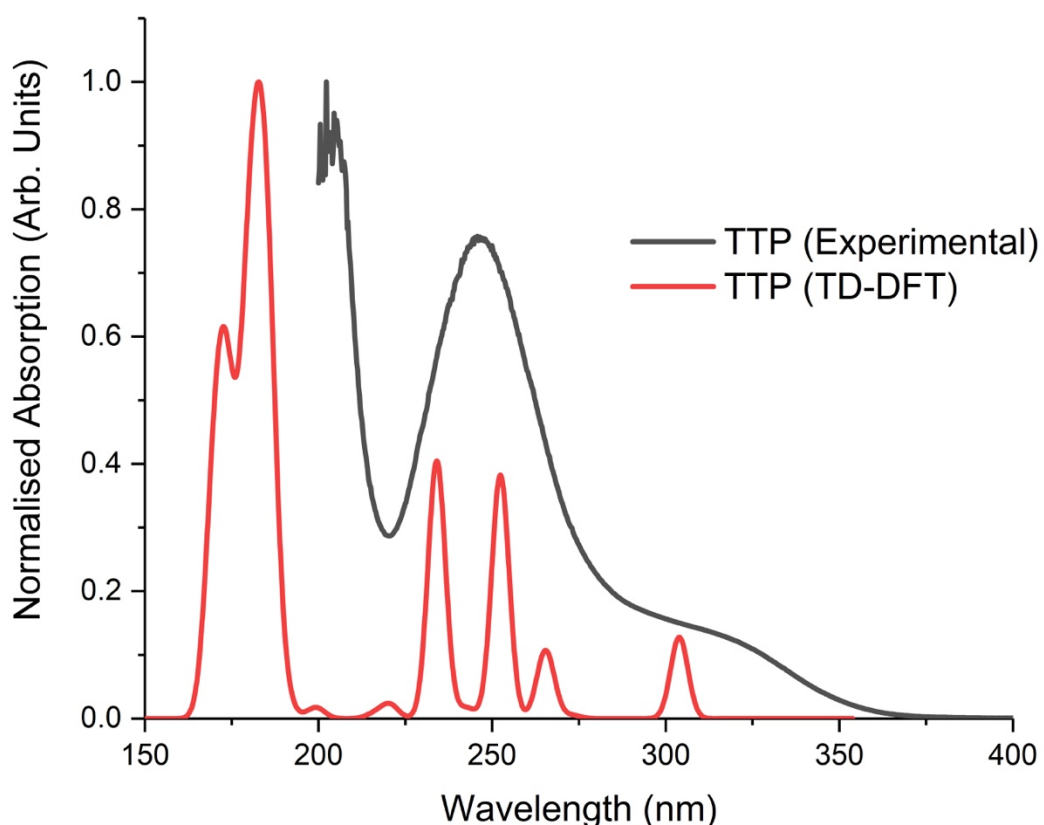


Figure 60 Normalised UV-Vis absorption spectrum of TTP in acetonitrile (100 μM) (black trace). The TD-DFT derived spectrum is also displayed (red trace).

The absorption spectrum of the TTP base compound, shown in figure 60, displays three notable features: an intense absorption band <225 nm, a moderately intense band centred at 250 nm and a weakly intense, less defined band between 300 – 375 nm. The TD-DFT derived spectrum is an effective emulation of the experimental spectrum, suggesting that the absorption spectrum is dominated by spin-allowed singlet-to-singlet transitions. The TD-DFT spectrum displayed here was calculated using the methods outlined in the experimental section above. For ease of comparison with experimental data, the calculated transitions were scaled by their associated oscillator strengths and convoluted with a 20 nm bandwidth Gaussian function. The broadening is intended as a guide to the eye, intended to allow for the comparison of datasets. Analysis of the TD-DFT spectrum coupled with decomposition analysis of the molecular orbitals of the singlet ground state gives a greater insight into the nature of the transitions that result in the cleavage of the tetrazolium ring, discussed in the DFT section of this chapter.

5.3.1.2 Molecular Orbital Decomposition Analysis

The frontier molecular orbitals of the tetrazolium species were examined using decomposition analysis and used in conjunction with the TD-DFT calculations to gain insight into the initial excitation that drives the photoreaction being studied. The results of this analysis for the base TTP compound are shown in table 30.

Molecular Orbital	Tetrazo Ring (%)	N – Phenyl 1 (%)	N – Phenyl 2 (%)	C – Phenyl (%)
LUMO +4	9	44	44	2
LUMO +3	5	47	47	0
LUMO +2	9	44	44	3
LUMO +1	43	3	3	51
LUMO	81	9	9	0
HOMO	17	8	8	68
HOMO -1	0	0	0	100
HOMO -2	1	46	46	7
HOMO -3	1	50	50	0
HOMO -4	4	42	42	11

Table 30 Percentage contribution of each of the groups to the frontier orbitals of the singlet ground state of triphenyltetrazolium.

The molecular orbital contributions from the phenyl rings situated at positions 2 and 3 of the tetrazolium ring (N-Phenyl 1 and 2) are equal for all orbitals, suggesting that they are functionally degenerate. The HOMO is centred predominantly on the phenyl ring situated on the 5 position (C – Phenyl), whilst the LUMO is positioned primarily on the central tetrazolium ring. Renderings of the orbitals are displayed in figure 61.

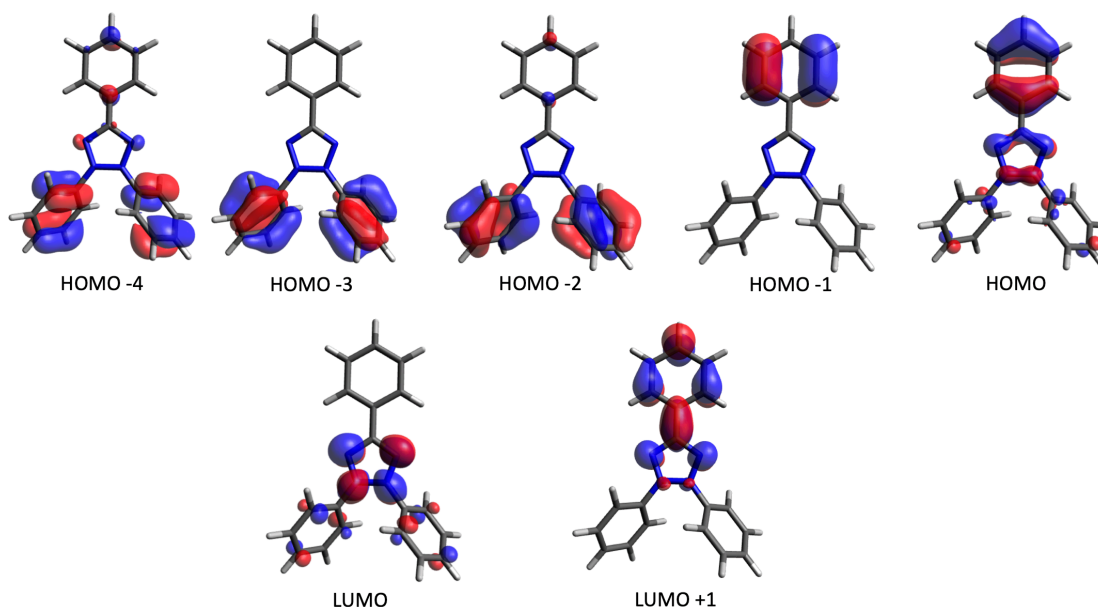


Figure 61 Rendered frontier molecular orbitals of the singlet ground state of triphenyltetrazolium.

5.3.1.3 Simulation of Excited States

Excited State	Contributing Transitions
1 (303.90 nm, $f = 0.1575$)	HOMO \rightarrow LUMO (78.35%)
2 (272.91 nm, $f = 0.0063$)	HOMO -2 \rightarrow LUMO (79.62%) HOMO \rightarrow LUMO (13.08%)
3 (266.13 nm, $f = 0.0378$)	HOMO -4 \rightarrow LUMO (80.46%)
4 (265.19 nm, $f = 0.0963$)	HOMO -3 \rightarrow LUMO (90.3%)
5 (256.76 nm, $f = 0.0006$)	HOMO -1 \rightarrow LUMO (95.99%)

Table 31 The first five calculated singlet states of triphenyltetrazolium from the singlet ground state.

Using TD-DFT calculations the first five excited singlet states were derived for the TTP basis compound. The first three excited states involved promotion from the HOMO, HOMO -2 and HOMO -4 to the LUMO exclusively, suggestive of charge transfer from the phenyl ring moieties to the tetrazolium ring. The primary contributions to the 4th and 5th states also support this, originating from the N – phenyl rings and C – phenyl ring respectively. Although these calculations support concept of photoexcited charge transfer on to tetrazolium ring, the LUMO orbital is π^* in character, and unlikely to

lead to direct bond fission. Instead, it is anticipated that the time evolution of the excited state leads to $\pi-\sigma^*$ character that ultimately cleaves the N-N bond.

5.3.1.4 Triphenylformazan (TPF)

The steady state UV-Vis absorption spectrum of triphenylformazan was obtained for characterisation purposes and is shown below in figure 62.

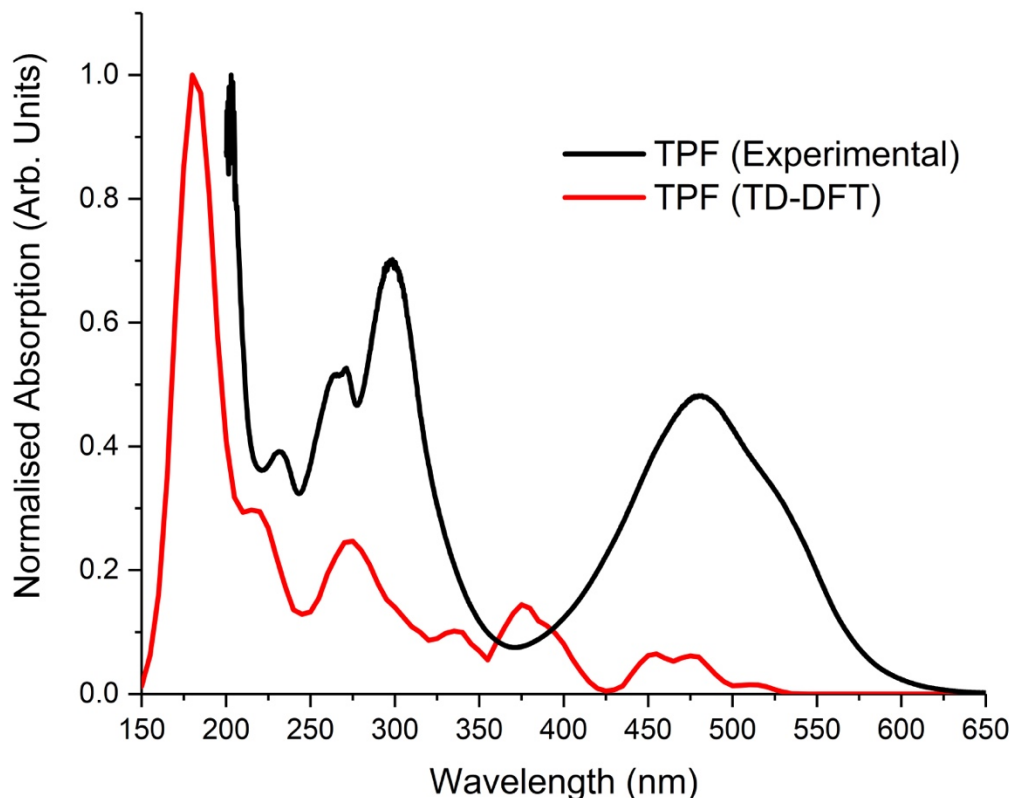


Figure 62 Normalised steady state UV-Vis absorption spectrum of triphenylformazan in acetonitrile (10 μM) (black trace). The TD-DFT derived spectrum is also displayed (red trace).

The steady state absorption spectrum of TPF features significantly more structure than that of the TTP starting material and this is attributed to the convolution of the spectra of the different possible conformers of TPF. The experimental spectrum displayed above is a good match for that observed in prior literature.⁹⁰ The simulated spectrum shown in figure 62 is a composite of the simulated singlet-to-singlet spectra of the 8 different conformers visible in figure 56, each adjusted according to a Boltzmann distribution derived from the relative energies of their optimised singlet geometries. The full spectrum of TPF cannot be fully accounted for by the simulated spectrum of

any one conformer, suggesting that TPF is present in several conformers in solution. The Boltzmann distribution appears to provide insufficient intensity in portions of the spectrum, namely the absorption band between 400 – 600 nm, suggesting that the formazan conformers are potentially not produced in ratios consistent with this treatment. The predicted spectra of the *cis* conformers feature transitions corresponding to the absorption feature centred at ~475 nm in the experimental spectrum, suggesting that the population of these conformers in solution is dramatically underestimated by this method. This is likely because the electrostatic environment provided by solution varies from the approximations made in the computational treatment, leading to underestimation of the stabilisation energies of certain conformers.

5.3.2 3,5-diF Triphenyltetrazolium (3,5-diF TTP)

5.3.2.1 Steady State UV-Vis Absorption

The steady state absorption spectrum of the 3,5 diF variant of TTP is functionally identical to that of the TTP spectrum and can be found in the appendix. Apart from slight differences between the oscillator strengths of the predicted transitions, the TD-DFT spectrum also bears the same profile, suggesting that the substitution of the phenyl ring hasn't significantly altered the electronic structure of the TTP, making a direct comparison between these compounds valid.

5.3.2.2 Molecular Orbital Decomposition Analysis

The molecular orbital decomposition analysis of the 3,5-diF triphenyltetrazolium shows an expected loss of degeneracy between the contributions from the nitrogen-based phenyl ring moieties, as a result of the fluorine substitution of the 2-position phenyl ring. The table of molecular contributions is shown in figure 63 below.

Molecular Orbital	Tetrazolium Ring (%)	3,5-diF Ring (%)	N – Phenyl Ring (%)	C – Phenyl Ring (%)
LUMO +4	7	23	69	1
LUMO +3	7	34	58	1
LUMO +2	12	67	16	5
LUMO +1	42	5	4	48
LUMO	80	10	9	0
HOMO	17	4	7	73
HOMO -1	0	0	0	100
HOMO -2	0	79	19	2
HOMO -3	0	17	82	0
HOMO -4	6	26	57	11

Figure 63 Percentage contribution of each of the groups to the frontier orbitals of the singlet ground state of 3,5-diF triphenyltetrazolium.

The overall contribution from each of the moieties is similar to that of the basis triphenyltetrazolium compound, with the HOMO -1 still being entirely located on the C – phenyl ring as an example. This suggests that despite the loss of degeneracy between the two nitrogen-based ring moieties, the overall electronic structure of the compound is very similar to the basis compound.

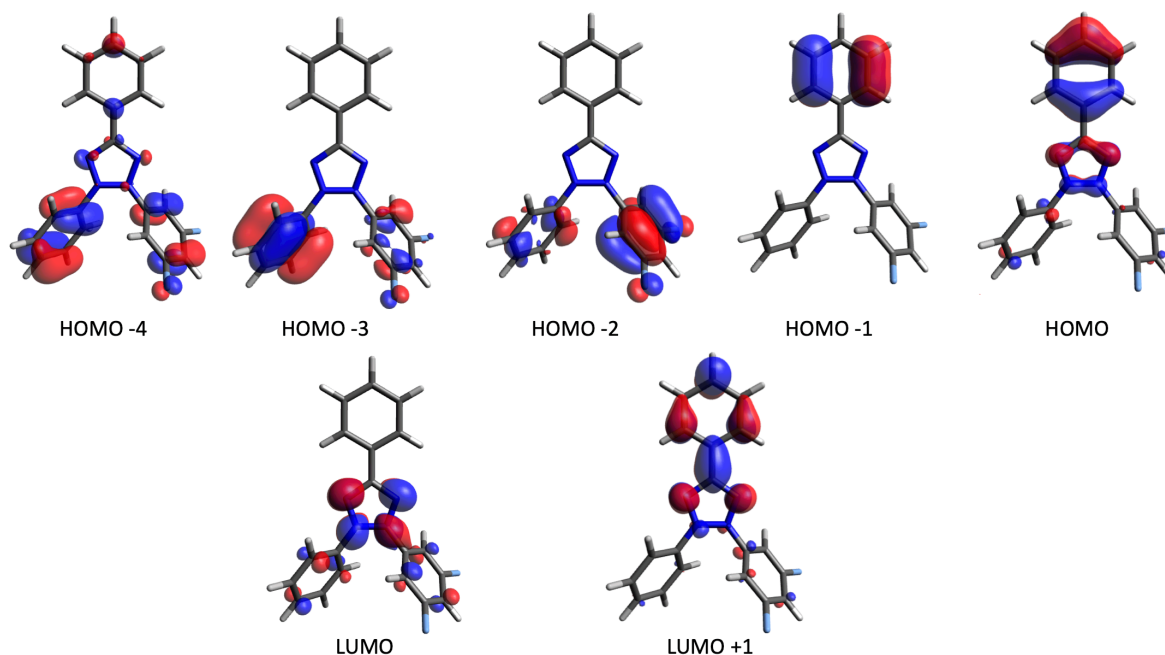


Figure 64 Rendered frontier molecular orbitals of the singlet ground state of 3,5-diF triphenyltetrazolium.

The molecular orbital distribution, visualised in figure 64, is similar to that of the TTP basis molecule, with exceptions in the distributions of electron density around the nitrogen-based phenyl rings, indicative of the loss of degeneracy caused by the fluorine substitution. The LUMO is still primarily located on the tetrazolium ring suggestive of the same excited state dynamics.

5.3.2.3 Simulation of Excited States

Excited State	Contributing Orbitals
1 (305.83 nm, $f = 0.1386$)	HOMO \rightarrow LUMO (82.33%)
2 (281.96 nm, $f = 0.0195$)	HOMO -2 \rightarrow LUMO (89.96%)
3 (271.73 nm, $f = 0.0785$)	HOMO -4 \rightarrow LUMO (45.75%) HOMO -3 \rightarrow LUMO (40.77%)
4 (270.31 nm, $f = 0.0184$)	HOMO -4 \rightarrow LUMO (36.48%) HOMO -3 \rightarrow LUMO (53.51%)
5 (263.52 nm, $f = 0.0007$)	HOMO -1 \rightarrow LUMO (96.77%)

Table 32 The first five calculated singlet states of 3,5-diF triphenyltetrazolium from the singlet ground state.

The first five excited states of the 3,5-diF TTP are shown in table 32. The contributions of each of the excited states are similar to that of the triphenyltetrazolium basis compound, originating primarily from the HOMO -4, HOMO -2 and HOMO and contributing to the LUMO. The energy values of the predicted transitions are slightly bathochromically shifted relative to the basis TTP.

5.3.3 2,6-diF Triphenyltetrazolium (2,6-diF TTP)

5.3.3.1 Steady State UV-Vis Absorption

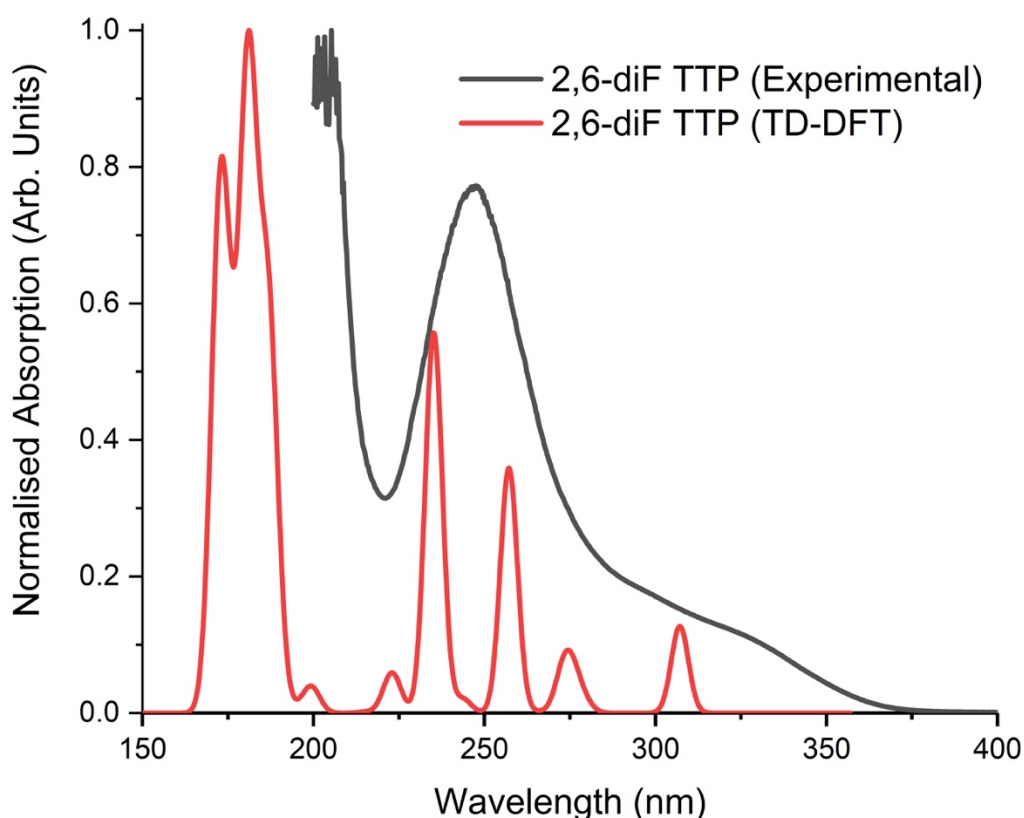


Figure 65 Normalised UV-Vis absorption spectrum of 2,6-diF TTP in acetonitrile (100 μ M). The TD-DFT singlet-to-singlet spectrum is also displayed, derived from the calculated singlet ground state.

The 2,6-diF TTP once more has an identical absorption profile to the TTP basis molecule, reinforcing the argument that the substitution of two fluorine atoms to one of the N-phenyl rings has little effect on the overall character of the compound. This is likely due to the contributions from the N-phenyl rings to the frontier orbitals being

relatively small, and this is discussed in more detail in the next subsection. The TD-DFT simulation suggests that the transitions that make up the absorption spectrum have undergone a slight hypsochromic shift. The spectrum is shown in figure 65.

5.3.3.2 Molecular Orbital Decomposition Analysis

The molecular decomposition analysis of the 2,6-diF TTP compound, shown in table 33, suggests that the electronic structure is similar to that of 3,5-diF TTP, with contributions from the moieties to each of the orbitals closely correlating in both. This suggests that the electronic structure of the TTP molecule is not significantly perturbed by the difluorine substitution, and that the position of the substitution does not have a significant impact on the contributions of the phenyl ring at position 2 to the frontier molecular orbitals.

Molecular Orbital	Tetrazolium Ring (%)	2,6-diF Ring (%)	N – Phenyl Ring (%)	C – Phenyl Ring (%)
LUMO +4	3	32	65	0
LUMO +3	10	15	74	1
LUMO +2	11	77	9	3
LUMO +1	43	4	3	49
LUMO	82	8	10	0
HOMO	16	3	6	75
HOMO -1	0	0	0	100
HOMO -2	0	88	12	0
HOMO -3	0	19	80	1
HOMO -4	6	9	75	10

Table 33 Percentage contribution of each of the groups to the frontier orbitals of the singlet ground state of 2,6-diF triphenyltetrazolium.

The rendered frontier orbitals of the 2,6-diF TTP singlet ground state, shown below in figure 66, show the almost identical electron distribution of the 2,6-diF TTP to the 3,5-diF TTP singlet ground state.

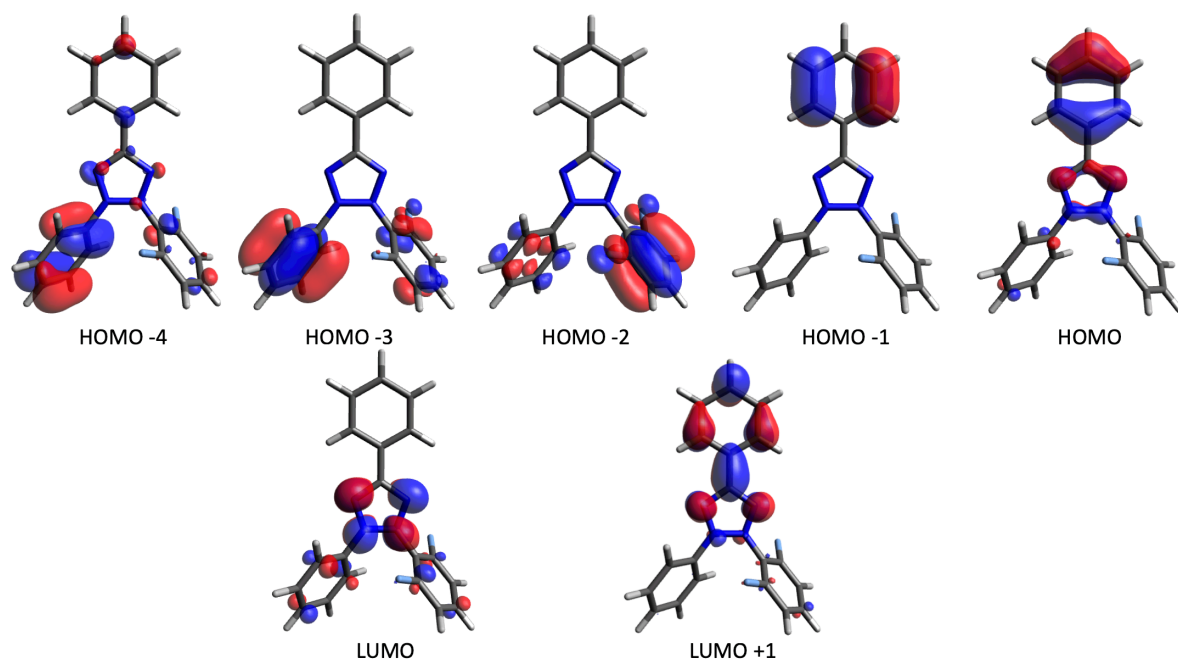


Figure 66 Rendered frontier molecular orbitals of the singlet ground state of 2,6-diF TTP

5.3.3.3 Simulation of Excited States

Excited State	Contributing Orbitals
1 (307.07 nm, f = 0.1342)	HOMO -4 → LUMO (10.57%) HOMO → LUMO (81.96%)
2 (279.24 nm, f = 0.0147)	HOMO -3 → LUMO (13.82%) HOMO -2 → LUMO (76.41%)
3 (275.85 nm, f = 0.0496)	HOMO -4 → LUMO (41.95%) HOMO -3 → LUMO (24.8%) HOMO -2 → LUMO (15.77%)
4 (273.12 nm, f = 0.0605)	HOMO -4 → LUMO (36.66%) HOMO -3 → LUMO (51.37%)
5 (265.53 nm, f = 0.0021)	HOMO -1 → LUMO (96.63%)

Table 34 The first five calculated singlet states of 2,6-diF triphenyltetrazolium from the singlet ground state.

Table 34 shows the first five excited states for the 2,6-diF TTP singlet state. The predominant contributions to the excited states of the 2,6-diF TTP are similar to that of the basis TTP molecule and 3,5-diF TTP variant, suggesting that substitution has not significantly altered the electronic structure of the molecule. The energy values of each

excitation are slightly bathochromically shifted relative to the 3,5-diF and TTP values. The LUMO remains the exclusive orbital transitioned to, and the contributing occupied orbitals remain the same as those in the TTP and 3,5-diF TTP compounds. This suggests that the 2,6-diF substitution of the phenyl located at the 2 position of the tetrazolium ring would not inhibit the initial photolysis of the compound at the tetrazolium ring.

5.3.4 2,6-diMethyl, 4-Methyl, 4-Tert-butyl Triphenyltetrazolium (2,6-diMe TTP)

5.3.4.1 Steady State UV-Vis Absorption

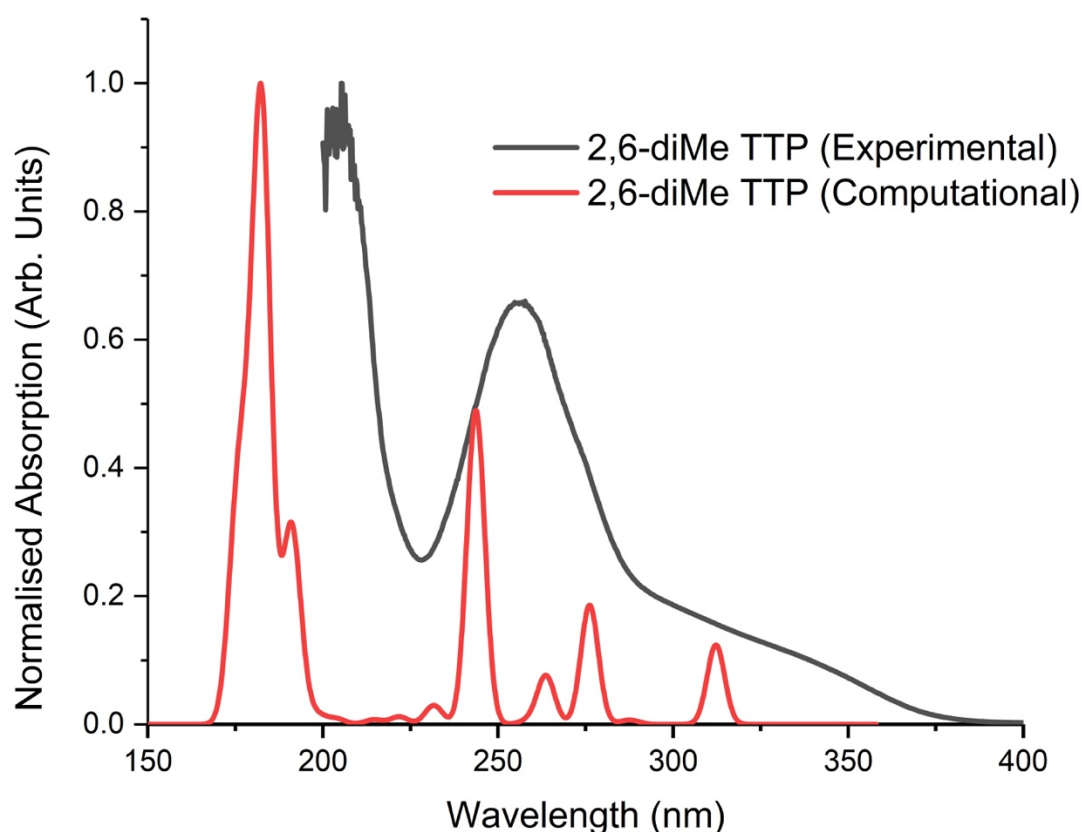


Figure 67 Normalised UV-Vis absorption spectrum of 2,6-diMe TTP in acetonitrile (100 μ M). The TD-DFT derived spectrum of singlet-to-singlet transitions calculated from the singlet ground state is also displayed.

The UV-Vis absorption spectrum of the 2,6-diMe TTP compound, shown in figure 67, shows the same profile as the other tetrazolium compounds, but features a distinct bathochromic shift in the features, most strongly in the medium intensity feature centred around 250 nm. This can be rationalised by considering the sites of

substitution that this compound features compared to the others, with all three phenyl rings featuring differing substitutions. This would alter the energies of both the HOMO and LUMO of the compound, resulting in a shifting of the energies, whilst the overall structural similarity of the compound to the TTP basis molecule results in an absorption spectrum bearing a similar profile.

5.3.4.2 Molecular Orbital Decomposition

Molecular Orbital	Tetrazolium Ring (%)	2,6-diMe Ph (%)	4-Me Ph (%)	4-TertButyl Ph (%)
LUMO +4	9	9	80	2
LUMO +3	4	13	82	1
LUMO +2	8	81	9	1
LUMO +1	44	2	2	52
LUMO	82	4	14	0
HOMO	15	2	8	76
HOMO -1	0	99	1	0
HOMO -2	0	0	0	99
HOMO -3	6	21	63	11
HOMO -4	3	29	67	1

Table 35 Molecular orbital contributions from each of the constituent groups of the calculated geometry of singlet 2,6-diMe TTP

The molecular orbital contributions from each of the moieties of 2,6-diMe to the frontier molecular orbitals of the singlet geometry, seen in table 35, show a similar general structure to that of the other two substituted variants of TTP. A notable deviation from the trend is the contributions from the HOMO -1 and -2, visible in the renderings of the orbitals in figure 68 below, as it appears these two orbitals have a different energy ordering to those of the other 3 compounds. This is likely an effect due to the substitution of the C-phenyl ring bonded at the 5 position of the tetrazolium ring, as contributions from this phenyl ring make up the majority of the HOMO -1 in the other 3 compounds, yet make up the majority of the HOMO -2 orbital in this case.

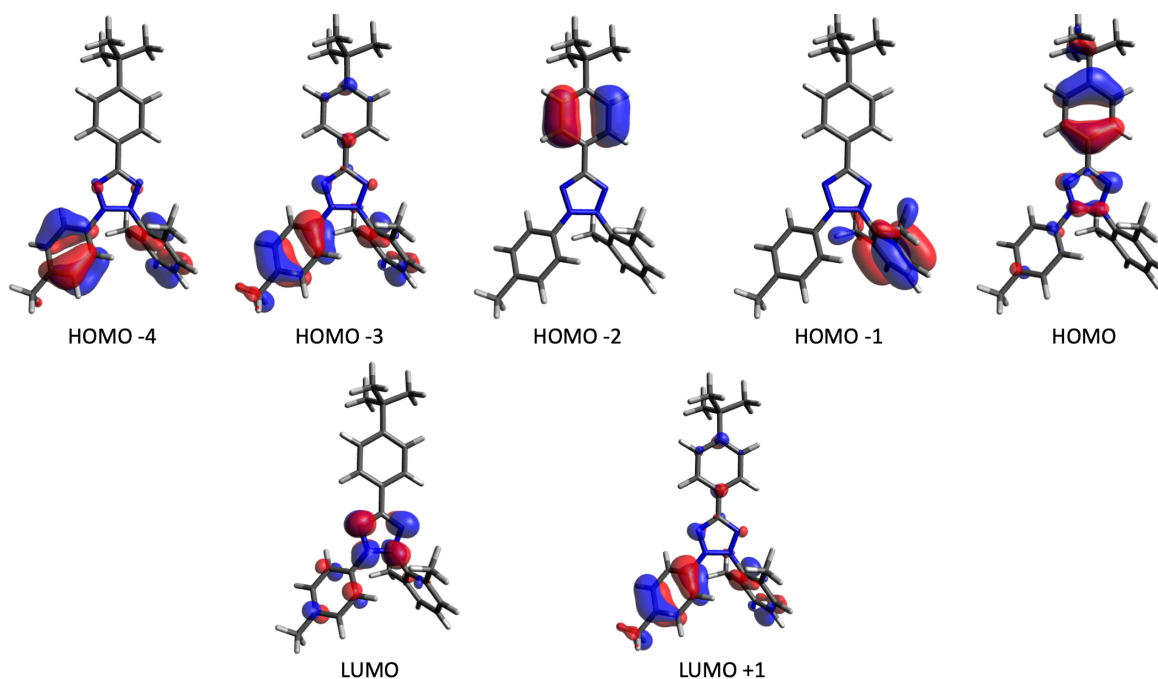


Figure 68 Rendered frontier molecular orbitals of the singlet ground state of 2,6-diMe TTP

The rendered molecular orbitals of the singlet ground state 2,6-diMe TTP, shown in figure 68, show the same motif as the other TTP variants, as the occupied orbitals predominantly arise from the phenyl moieties, whilst the unoccupied orbitals are centred predominantly on the tetrazolium ring, with some contribution from the N-phenyl rings.

5.3.4.3 Simulation of Excited States

Excited State	Contributing Orbitals
1 (312.16 nm, $f = 0.2077$)	HOMO -3 \rightarrow LUMO (17.91%) HOMO \rightarrow LUMO (76.27%)
2 (288.11 nm, $f = 0.009$)	HOMO -1 \rightarrow LUMO (95.55%)
3 (285.68 nm, $f = 0.0036$)	HOMO -4 \rightarrow LUMO (25.27%) HOMO -3 \rightarrow LUMO (43.98%) HOMO \rightarrow LUMO (15.63%)
4 (276.19 nm, $f = 0.3114$)	HOMO -4 \rightarrow LUMO (58.61%) HOMO -3 \rightarrow LUMO (27.49%)
5 (263.70 nm, $f = 0.1275$)	HOMO -5 \rightarrow LUMO (79.47%)

Table 36 The first five excited singlet states of 2,6-diMe TTP

Examination of the first five excited singlet states of 2,6-diMe TTP, shown in table 36, shows similar behaviour to that of the other 3 TTP compounds, suggesting once again that the overall electronic structure of the compound is defined by the 4 ring structures, with substitution altering the relative energies of the orbitals. The simulated transitions arise from the HOMO and HOMO -3 and -4 orbitals and transition exclusively to the LUMO, in keeping with the behaviour of the other 3 compounds, and again suggesting that the substituents do not prevent the weakening of the tetrazolium ring following photoexcitation. The oscillator strengths of the transitions are on the whole significantly higher than those of the other 3, suggesting that this compound will possess a larger molar extinction coefficient in the UV region than the other 3 variants.

5.4. Flash Photolysis Study

Due to the photolytic nature of the compounds being studied, the acquisition of any transient spectra will induce a photoreaction in the sample. The transient spectra will therefore alter over time, as the reaction induced by the pump source progresses. The instrument is therefore functioning as a flash laser photolysis (FLP) spectrometer in these cases, and there is expected to be a permanent difference in the spectrum of the sample that doesn't fade as a function of time, representing the completion of the reaction.

5.4.1 Triphenyltetrazolium (TTP)

The flash photolysis spectra of TTP was obtained in acetonitrile with no additional agents added. The products of the reduction of TTP depend largely on the conditions of the environment, affected by the polarity of the solvent and pH of the solution, with a number of agents, such as ascorbic acid or sodium hydroxide, able to induce the reduction reaction to the corresponding formazan. These conditions were considered to evaluate solely the effect the light had on the compound, as any chemical reduction agent present would potentially convolute the results by altering the rate of the reaction or induce the production of formazan via a chemical, rather than photochemical pathway.

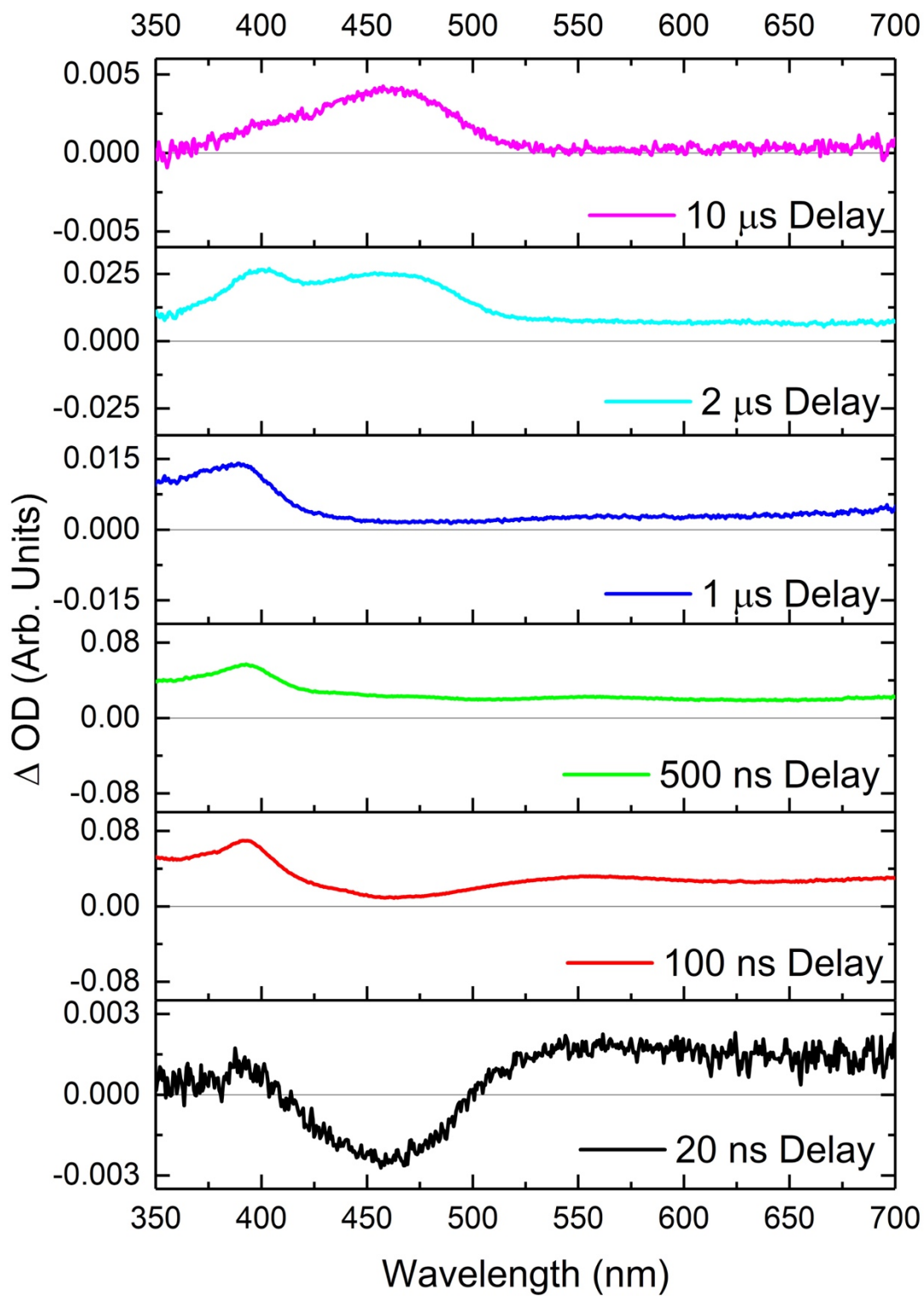


Figure 69 Luminescence subtracted transient absorption/FLP spectrum of TTP (100 μM) in acetonitrile at different time delays from the laser pulse ($\lambda_{\text{ex}} = 266 \text{ nm}$). All spectra are placed on their own scale to allow comparison, due to intensity differences.

As can be observed in the above figure 69, the spectrum evolves with time. Each measurement was conducted using a fresh sample for each time delay and the same amount of averaging was used in the acquisition of each trace. The strong absorption feature <400 nm that dominates the early time spectra and the absorption feature that grows in at 460 nm in later time delays are ascribed to the formation of the two intermediary TTP radicals postulated in the literature.⁸⁶ The bleach and absorption features at longer wavelengths (> 400 nm), observed most prominently at early timescales, match profiles assigned as belonging to the transient absorption spectrum of the corresponding formazan, as assigned in the literature. The features of the spectrum are hypsochromically shifted and evolve at a much longer timescale than those observations made in the literature and these are believed to be accounted for by solvent environment differences. In this study, the solvent environment chosen was relatively absent of potential reduction agents, and is dramatically different to the study cited above, wherein aqueous and methanol solutions were used. A more reducing solvent results in faster observed reaction rates, as the reaction can proceed via reduction from the solution environment, as opposed to purely photonically, as was the aim in this thesis. Solvatochromism could explain the shift in the formazan spectral features and the absence of anything that could conceivably function as a reducing agent could inhibit the formations of intermediate 2 from the photoexcitation induced intermediate 1 via the proposed mechanism, explaining the differences in temporal evolution of the system. An additional factor for consideration is the choice of ion pairing for the tetrazolium cation, as this can impact the reaction rate through differences in the immediate environment of the tetrazolium cation. Hexafluorophosphate anions were used in this study in order to facilitate solution in acetonitrile, whilst chloride anions were used in the 2015 Kanal *et al* study.⁸⁶ In order to assess the impact choice of anion pairing and solution environment has on the reaction rate, a further study would be required, beyond the time constraints and scope of this thesis. However, some preliminary work undertaken suggests that working with the chloride salts poses experimental challenges: the precursor tetrazolium and formazan photoproducts have marked different solubilities in those solvents suitable to hold the precursor. Thus, the formazan frequently precipitated out of solution during the photolysis, making these experiments untenable. Similarly, one

must consider the strength of the ion pair of choice in solution- often discussed in terms of 'innocence', namely whether the ion pair has long-lasting/long range association in solution. Ideally, one would wish to use an innocent counter ion, which does not alter the photophysics of the tetrazolium in solution. Chloride is not an innocent ion in comparison to hexafluorophosphate. Ideally, however, future work might examine the use of tetrakis(3,5-bis(trifluoromethyl)phenyl)borate, often considered among the most innocent of counter ions. The longer wavelength features (>400 nm) are indicative of the build-up of permanent product residue from previous measurements, resulting in the convolution of successive measurements. The lowering of the number of averages and the acquisition of multiple spectra from the same sample without refreshing the cuvette show these longer wavelength features begin to appear as successive spectra are acquired. Lowering the number of averages also reduces the signal-to-noise ratio of the acquired data. As the sample is repeatedly probed, more of the TTP contained within the cuvette is converted into the photoproducts of the reaction, altering the spectrum considerably from prior measurements. This is particularly an issue for transient absorption/flash photolysis measurements as the baseline measurement used for comparison will alter with the composition of the probed volume giving rise to features from residues of previous measurements, as observed above. In the static 4 cm³ cuvette used for this study this problem is exacerbated by the low levels of sample movement within the small volume of the sample holder, meaning that the even smaller volume of sample probed by the spectrometer (~1 cm³) will have a higher effective concentration of the photoproducts and will build up these photoproducts more rapidly, making a prolonged study difficult. Visually, the sample changes from a colourless solution to a light yellow one, with the intensity of this increasing with light exposure. This was unexpected given the reduction to TPF from TTP is normally associated with a deep red colour change, suggesting the formation of another photoproduct, and is ascribed to PCP formation.

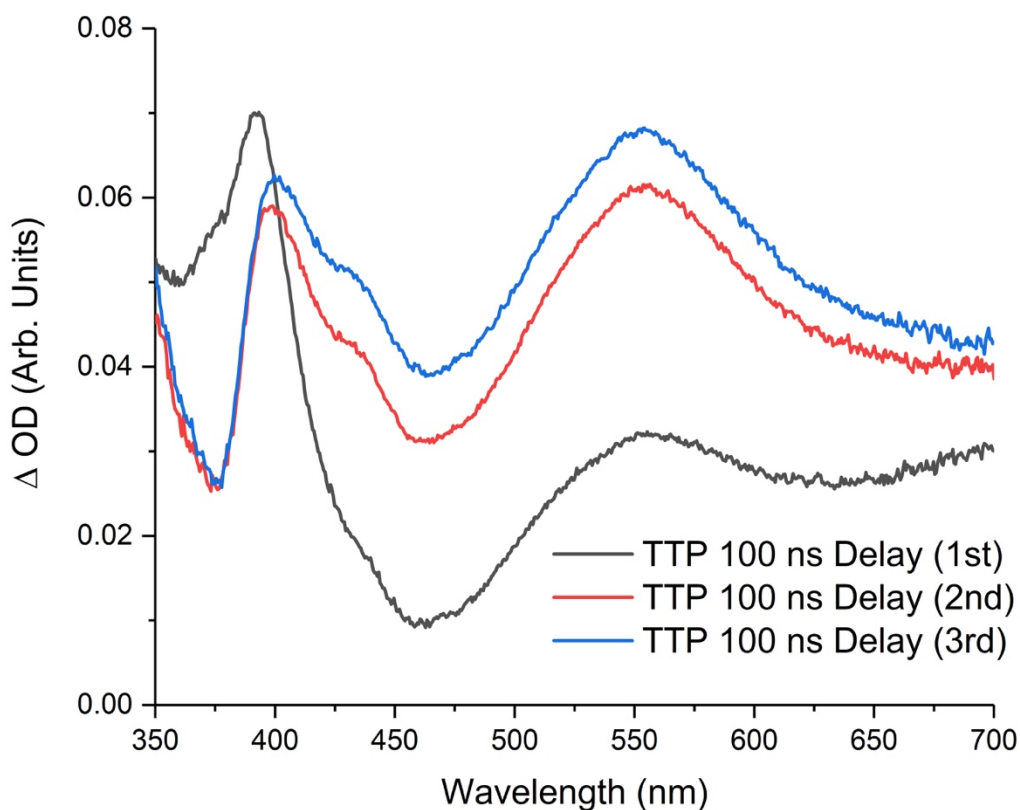


Figure 70 Successive acquisitions of luminescence corrected transient absorption/FLP spectra at the same time delay from a sample of TTP in acetonitrile (100 μM), demonstrating the progressive alteration of the sample composition with cumulative light exposure.

Figure 70 shows successive transient absorption spectra of TTP in acetonitrile. The blue trace, shown as the third successive measurement bears a strong resemblance to the spectrum of TPF assigned in the work of Kanal et al.⁸⁶ Studying the dynamics of the tetrazolium photoreduction is thus not likely to be successfully carried out using this static cell method without interference from the spectral features of residual photoproducts of previous acquisitions. The evident differences between the initially acquired measurement and the successive subsequently acquired measurements, visible in figure 70 above, are due to the averaging applied to each measurement, as the conditions of the 2nd and 3rd measurements, visible in the red and blue traces respectively, include less tetrazolium and more photoproducts throughout the measurement. This indicates that any spectrum obtained with a reasonable amount of averaging as to be useable will inherently contain photoproduct contamination. To rectify this problem, a flow cuvette was employed in conjunction with a larger

reservoir of TTP solution, allowing the sample to be refreshed continuously and a baseline of TTP to be more readily attained. The larger reservoir of TTP solution (100 ml), along with the small volume being actively probed, results in a much slower build-up of detectable photoproduct, meaning that this solution also allows for extended study at multiple timeframes without interference from the transient spectra of any residual species from prior probing. Figure 71 shows the results obtained from the use of this flow cell.

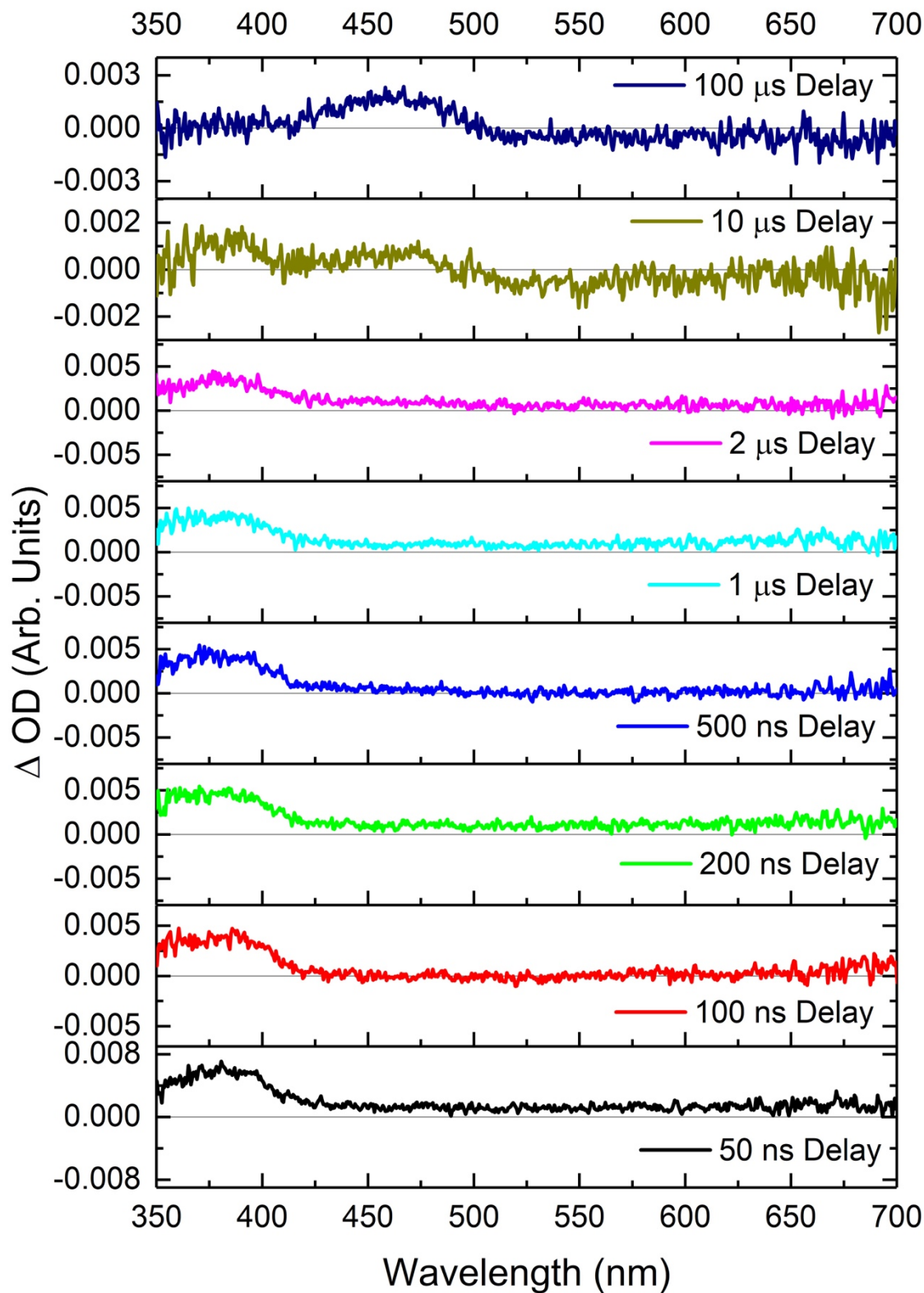


Figure 71 Luminescence corrected transient absorption/FLP spectra of TTP (100 μM) in acetonitrile under flow at a variety of different gate delays relative to pulse ($\lambda_{\text{ex}} = 266 \text{ nm}$)

By flowing the sample, the features $> 425 \text{ nm}$ in the sub-microsecond timescale are removed from the spectra, whilst the features assigned to the radical intermediates⁸⁶

of the TTP photoreaction remain for all timescales. The absorption feature in the region 400 – 500 nm, ascribed to the formation of the intermediate 3 species in the mechanism proposed in figure 58 appears faintly in the 10 μ s spectrum alongside the feature ascribed to the formation of intermediate 2. In the 100 μ s spectrum it is the only remaining feature, suggestive of the completion of the conversion of the excited TTP population into intermediate 3. Following prolonged irradiation of the larger reservoir the features ascribed to the photoproducts begin to return. This is indicative of different origins for each of the spectral features, with those features that persist upon the activation of the flow system being ascribed to transient features originating from the TTP excited by the pump laser, as they are present in all solutions probed, whilst the features assigned to the formazan by the literature are indeed due to the build-up of photoproducts from previous acquisitions, as they are not present in continually refreshed sample volumes. The use of the flow sample cell does result in a reduction of the signal-to-noise ratio of the sample, but this is offset by its capacity to deconvolute the sample compared to a static volume. The flow cell system offers a more consistent response than the standard cell, which would exhibit less consistent responses at certain timeframes likely due to the variable consistency of the probed volume, which is dictated entirely by molecular motion within the cuvette. In contrast, the flow cell displays a far more consistent spectrum at all timeframes, with a more stable baseline for the Δ OD measurements, suggesting that the probed volume is being refreshed throughout the measurement.

For comparison with the spectra acquired in the above measurements, the transient spectrum of triphenylformazan (TPF) is shown below in figure 72.

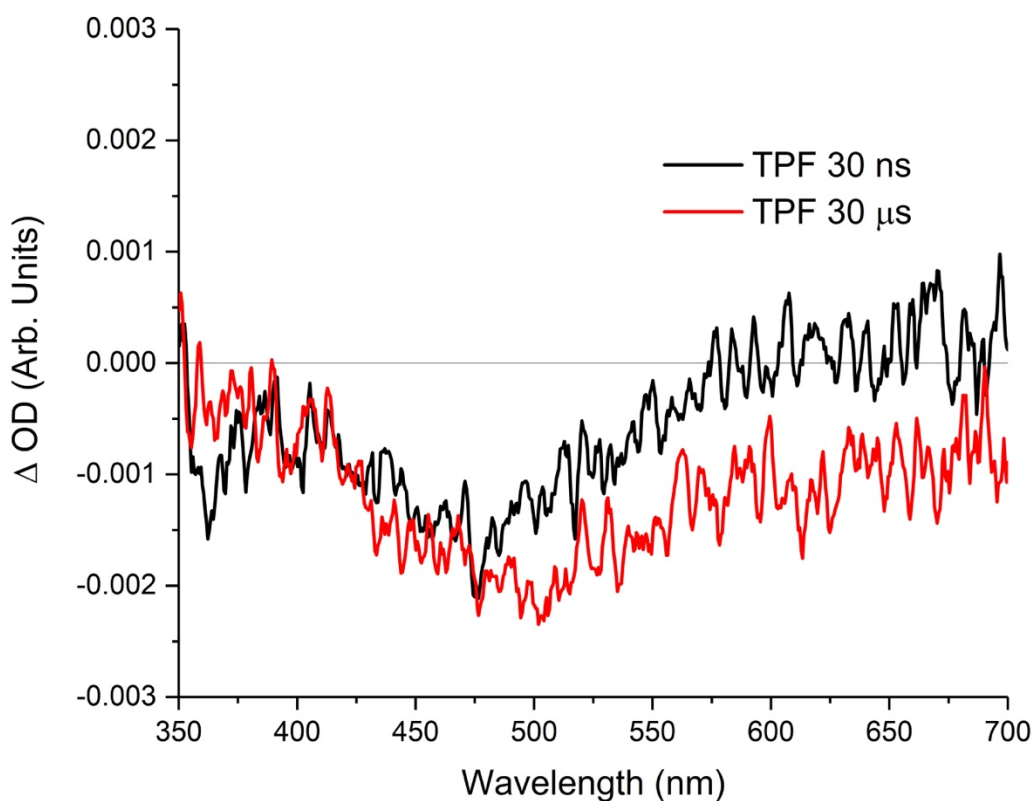


Figure 72 Luminescence corrected transient absorption spectrum of TPF in acetonitrile (10 μM)
($\lambda_{\text{EX}} = 266 \text{ nm}$)

The chemically produced formazan displays faint transient absorption features at both a short and long acquisition delay time relative to the excitation pulse, suggestive of a slight difference between the ground state and excited state absorption spectra. The spectrum features a broad negative feature between 400 – 600 nm, assigned as a ground state bleach of the absorption features at this region in the steady state formazan spectrum, visible in figure 62 in the steady state absorption subsection of this chapter. This ground state bleach feature persists into the microsecond regime, and is still visible at $t = 30 \mu\text{s}$.

5.4.2 3,5-diF Triphenyltetrazolium (3,5-diF TTP)

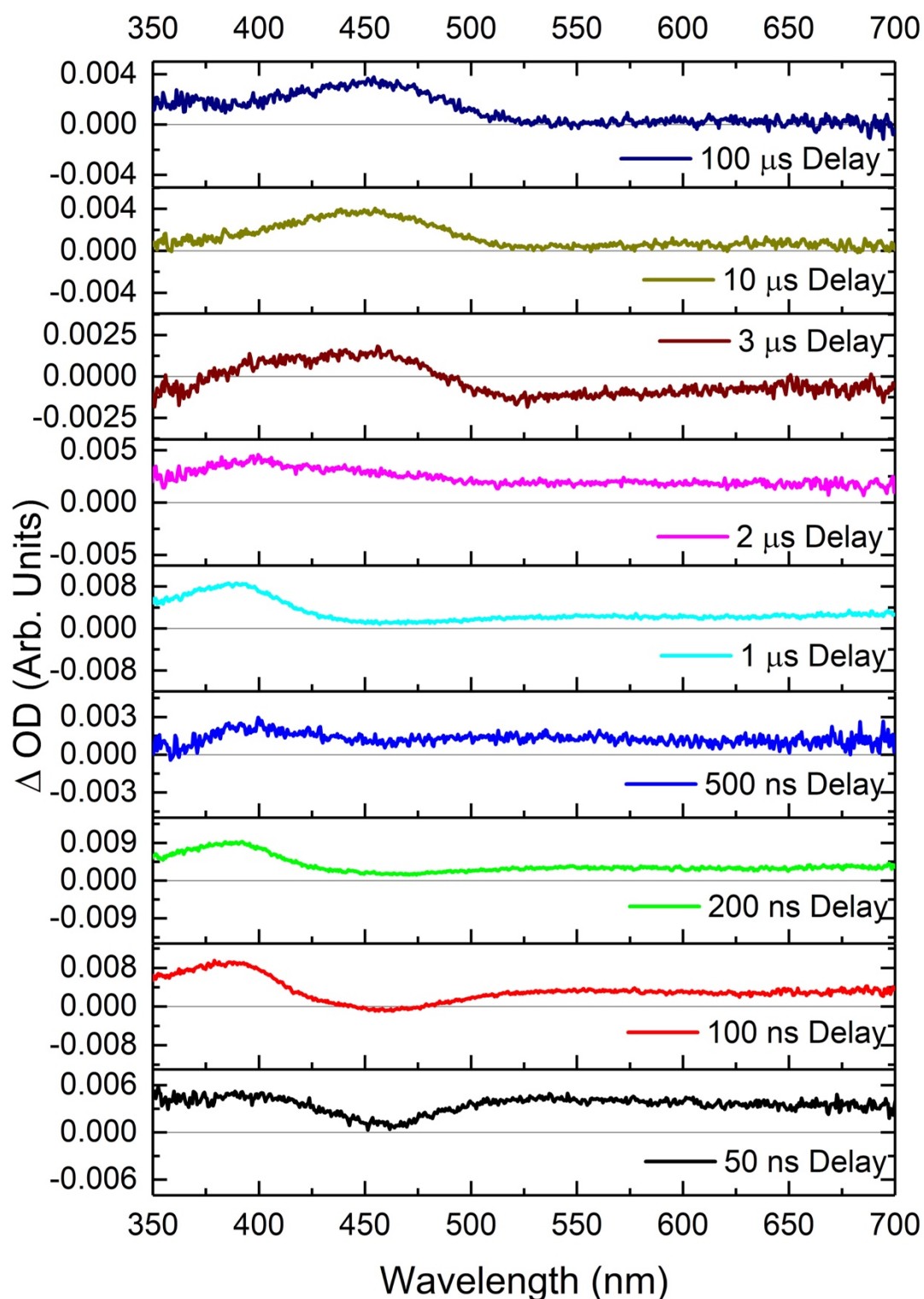


Figure 73 Luminescence corrected transient absorption/FLP spectrum of 3,5-diF TTP (100 μM) in acetonitrile at different time delays from the laser pulse ($\lambda_{\text{ex}} = 266 \text{ nm}$). All spectra are placed on their own scale to allow comparison, due to intensity differences.

The transient absorption/FLP spectra of 3,5-diF TTP in a standard cuvette, shown in figure 73, bear a close resemblance to that of the basis TTP compound. There is a persistent broad absorption at wavelengths beyond 500 nm, corresponding to the formation of the formazan photoproduct of the reaction. In the early timescale there is also evidence of a decrease in optical density at the wavelength region 400 – 500 nm, which also corresponds with the formation of the formazan. This is indicative of the photoreaction process being unaffected by substitution at these positions, which is to be expected given that the substitution doesn't physically impede the bridging sites on either of the phenyl rings involved in the formation of the photoproduct resulting from the initiation of the photoreaction. The spectrum appears to evolve in a similar fashion across a similar timescale, suggesting that the addition of two fluorine atoms has not significantly altered the kinetics.

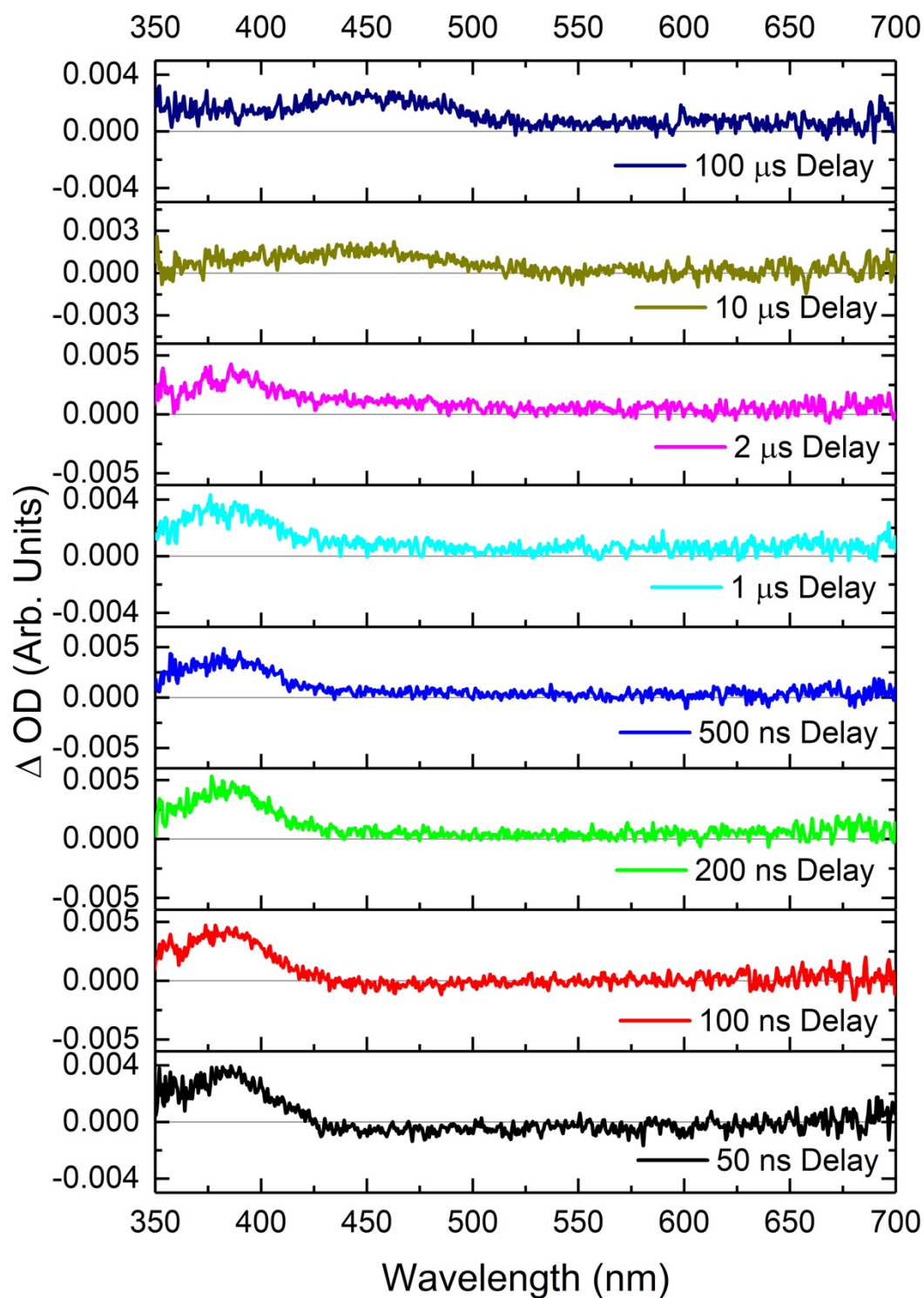


Figure 74 Luminescence corrected transient absorption/FLP spectra of 3,5-diF TTP (100 μM) in acetonitrile under flow at a variety of different delays relative to pulse ($\lambda_{\text{ex}} = 266 \text{ nm}$)

A sample of the 3,5-diF TTP was also examined using the flow cell system and similar results to the TTP basis compound were observed, shown in figure 74. The features

attributed to the formazan species are absent from spectra obtained using the flow system, suggesting that the flow system is functioning as desired, removing residual products from previous interrogations of the sample. The system evolves along a similar timescale as the TTP basis compound, but in both the standard and flow cell systems there appears to be a more rapid formation of intermediate 3 from intermediate 2 along the suggested mechanism.

5.4.3 2,6-diF Triphenyltetrazolium (2,6-diF TTP)

The 2,6-diF variation of TTP displays no discernible features in its transient absorption/FLP spectra, at any timescale, shown in figure 75. This is a good indication that the photochemical processes that are being induced in the basis TTP molecule are being strongly inhibited by the presence of the fluorine substituents in the 2,6-diF bridging position. The expectation was that the features formally ascribed to the radical intermediate species in the reaction scheme proposed in the literature would remain in the spectra of this compound, but that the build-up of permanent photoproducts would not be present or at least would be present in reduced amounts. When subjected to a similar degree of averaging and largely identical conditions, the 2,6-diF TTP sample shows no indication of any light-induced activity using transient absorption/flash photolysis spectroscopy, suggesting that ascribing the features to the intermediates in the proposed reaction scheme (figure 58) may not be complete, and that the photoreduction may proceed via a route involving the ortho sites of the N-phenyls instead of the proposed mechanism.

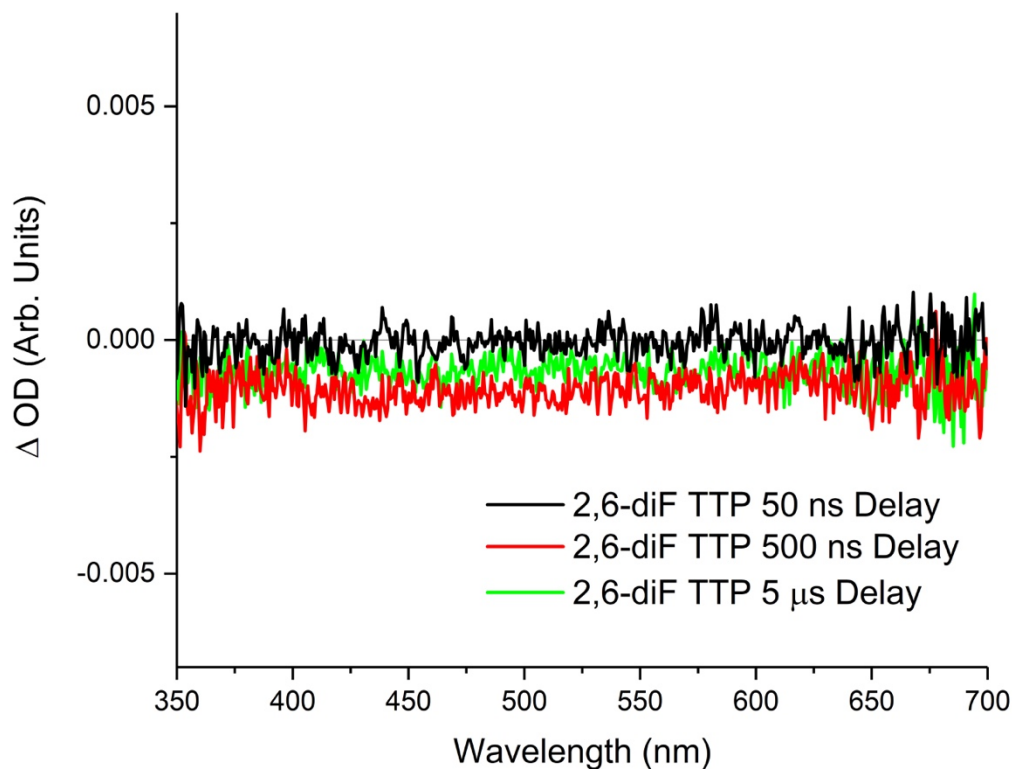


Figure 75 Luminescence corrected transient absorption/FLP spectrum of 2,6-diF TTP (100 μM) in acetonitrile at different time delays from the laser pulse ($\lambda_{\text{ex}} = 266 \text{ nm}$).

The sample displays no colour change following light exposure, unlike the TTP and 3,5-diF TTP variants, suggesting that the light-based reaction has been inhibited. To assess the early time frame of this compounds spectral dynamics, a map was obtained using the PMT-monochromator detection system, shown in figure 76.

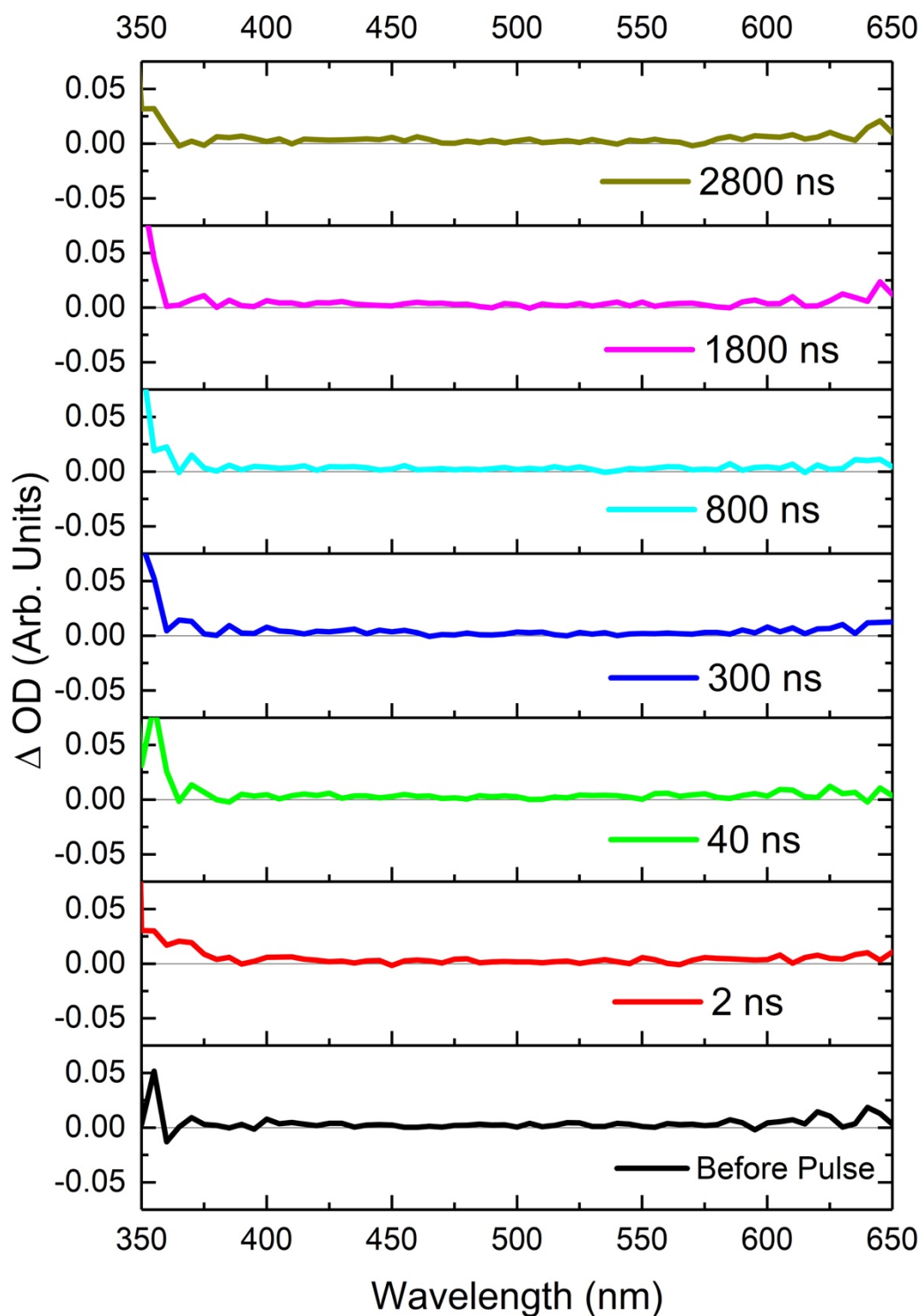


Figure 76 Luminescence corrected transient absorption/FLP spectra of 2,6-diF TTP (100 μM) in acetonitrile at different time delays from the laser pulse, acquired using the PMT/monochromator detector system ($\lambda_{\text{ex}} = 266 \text{ nm}$).

Using this method, a portion of the spectrum is displayed prior to the onset of the pump excitation, and a time slice of this region is included as a comparison. The

progression of time frames displayed here are chosen from intervals across the PMT map in order to provide an examination into the behaviour at early and late time delays from the pulse. As can be seen above, save for a few instrument artefacts at either end of the observable wavelength region, there is no activity in the spectra at any time frame, suggestive of complete inhibition of the photoreductive process.

5.4.4 2,6-diMethyl, 4-Methyl, 4-Tert-butyl Triphenyltetrazolium (2,6-diMe TTP)

The 2,6-diMe TTP compound displays no features in its transient absorption spectrum, shown in figure 77, again indicative of the inhibition of the photoreaction. The compound was probed at a 50 ns delay from the laser pulse and showed no activity or development with successive acquisitions.

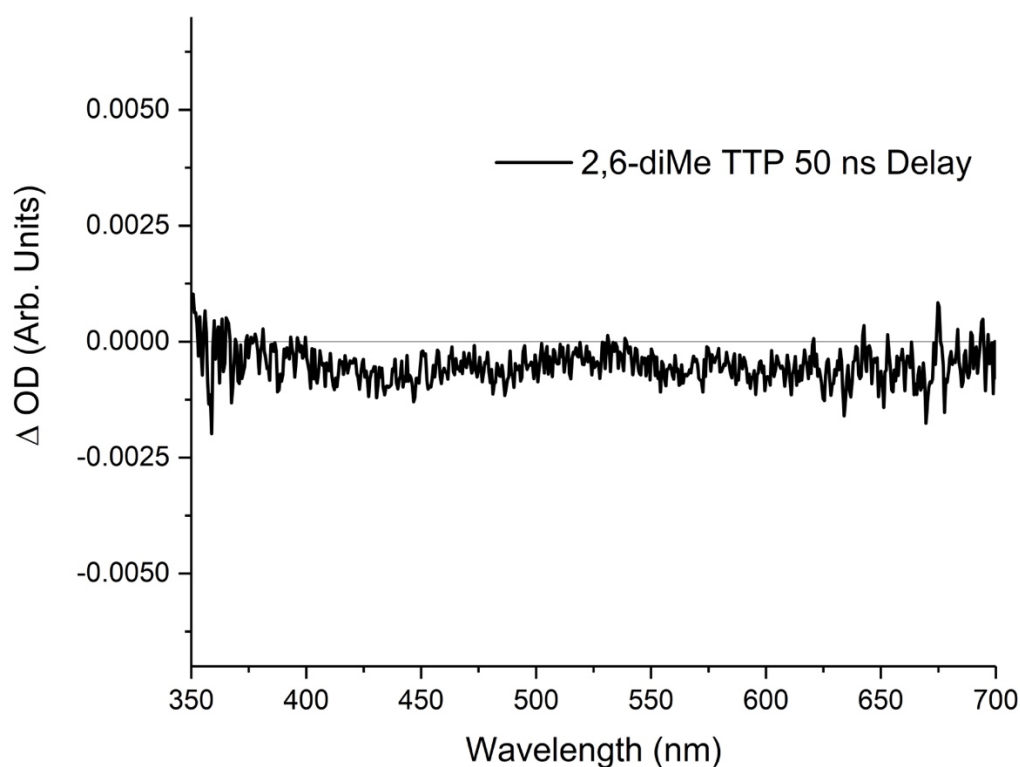


Figure 77 Luminescence corrected transient absorption/FLP spectrum of 2,6-diMe TTP (100 μ M) in acetonitrile at 50 ns delay from the pulse ($\lambda_{ex} = 266$ nm)

The lack of activity within the spectrum suggests that the photoreaction has been inhibited. The sample also does not undergo any colour change following light

exposure. This implies that the inhibition of the 2,6 positions of one of the phenyl rings is sufficient to inhibit the photochemical transition of TTP to PCP and the corresponding formazan to a point not observable by this method.

5.5 Emission Spectra

5.5.1 Triphenyltetrazolium (TTP)

The emission spectrum of the TTP compound was recorded in order to study the progression of the reaction as a function of cumulative light exposure and is shown in figure 78. Any change in the emission spectra of the TTP compound as a function of time or exposure could be used to monitor the progression of the photoreaction, and thus be used as a comparison with the variations of the TTP molecule to aid in their characterisation.

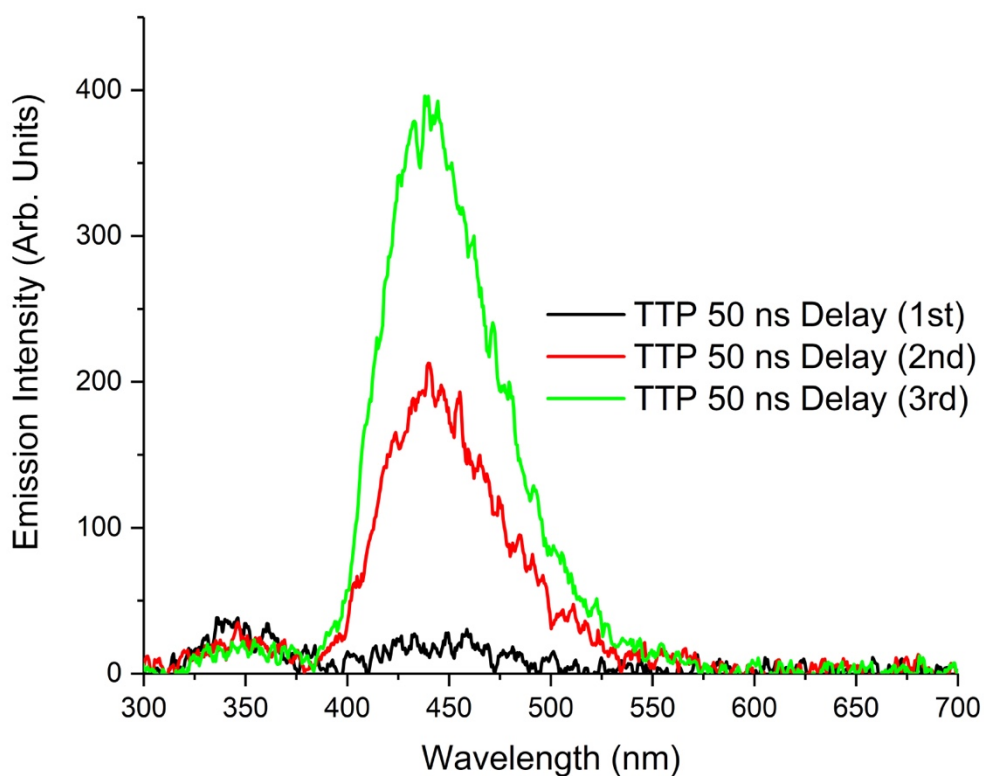


Figure 78 Emission spectra of the TTP compound (100 μ M) at 50 ns from the laser pulse, multiple acquisitions ($\lambda_{ex} = 266$ nm), static cell.

The emission spectrum of the TTP basis compound evolves as a function of light exposure, which is to be expected given the light sensitive nature of the system. There is a persistent minor feature centred at 350 nm, which is ascribed to the fluorescence of the PCP photoproduct previously reported in the literature.⁸⁸ The most prominent feature of the spectrum is the growing emission centred at 440 nm, which is also assigned as fluorescence originating from the PCP in the literature. This assignment of both features to the same species would appear to be incorrect given that the two features do not share the same relative intensity throughout the measurement process. The growth of the feature at 440 nm with light exposure suggests that it arises from a permanent product of the reaction. The relative stability of the shorter wavelength feature suggests it arises from either an intermediate in the photochemical process itself or the starting TTP, assuming a similar amount of TTP is exposed to each successive pulse. An assignment to the PCP is therefore made for the feature at 440 nm based on its accumulative nature as a function of laser exposure and the literature observations of emission from this species.⁸⁸

Under flow, the emission spectrum displays a single broad emission band with low intensity, shown in figure 79. The clear effect of the flow cell on the emission spectrum, all but removing the 440 nm feature, suggests that the two emission bands originate from different species.

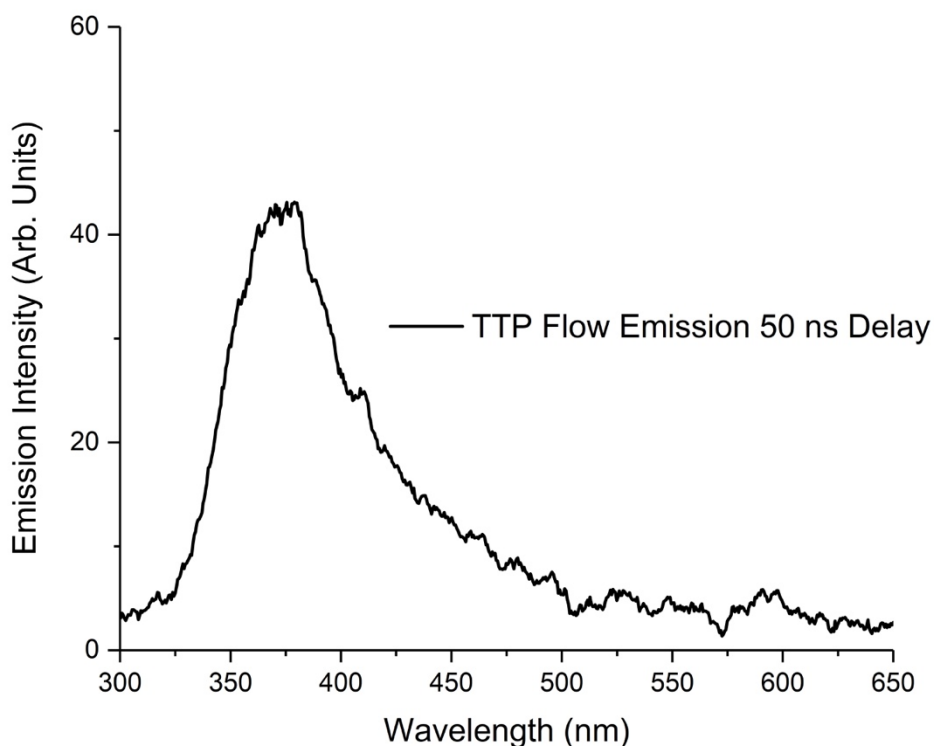


Figure 79 Emission spectra of the TTP compound in acetonitrile (100 μM) under flow at 50 ns from the laser pulse ($\lambda_{\text{EX}} = 266 \text{ nm}$). Smoothing applied for presentation purposes.

The emission spectrum under flow has a peak maximum centred at 375 nm, and a much broader shoulder extending to longer wavelengths. This is suggestive of the removal of the species from which the longer wavelength feature arises in the static solution cell, leaving only the less intense fluorescence that appears insensitive to light exposure. The different appearance of the spectrum under flow can be attributed to convolution of the two peaks, as it's possible that some of the species that produces the longer wavelength emission remains in the volume or is formed via the photochemical process. The feature at 375 nm is ascribed to laser induced fluorescence of the intermediate 2, based on the similarities in position of the transient absorption feature of this species.

5.5.2 3,5-diF Triphenyltetrazolium (3,5-diF TTP)

The emission spectral profile of the 3,5-diF TTP compound is very similar to the TTP base compound, further supporting the hypothesis that the two follow the same photochemical process. The same two features are present and are assigned to their

3,5-diF equivalent species, as is the growth of the more prominent feature at the longer wavelength. The emission spectrum for 3,5-diF TTP in the static cell is shown in figure 80.

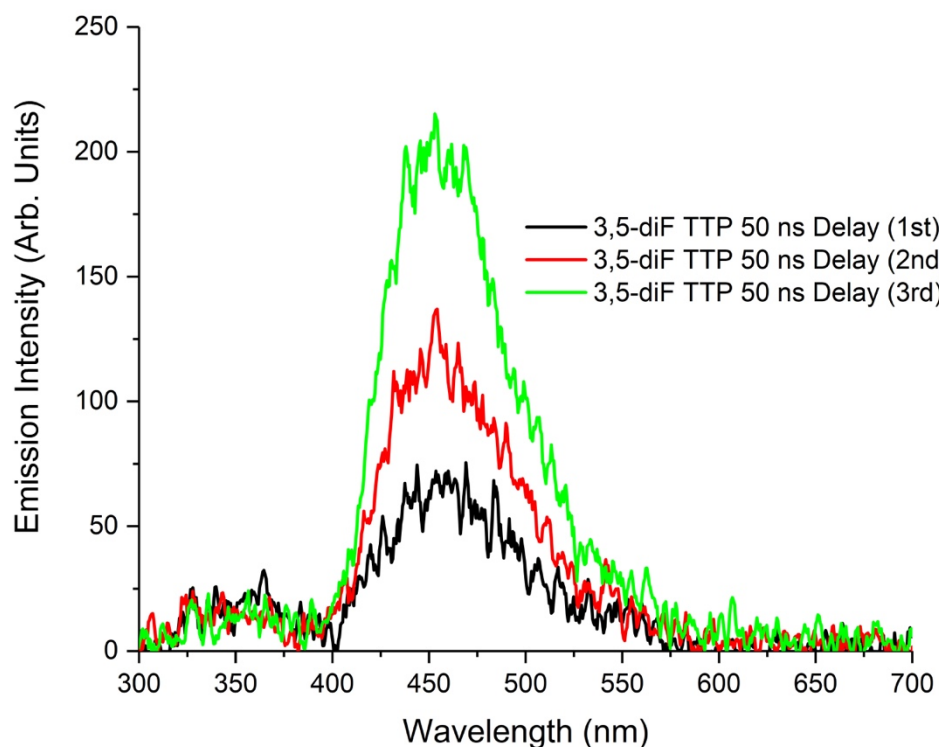


Figure 80 Emission spectra of the 3,5-diF TTP compound in acetonitrile (100 μM) at 50 ns from the laser pulse, multiple acquisitions ($\lambda_{\text{EX}} = 266 \text{ nm}$), static cell.

The feature that grows in is bathochromically shifted relative to its equivalent in the TTP spectra, centring on 460 nm in this case. This feature is also present in the first instance of acquisition, suggesting that the onset of the photoreaction occurs at a more rapid rate in the 3,5-diF TTP case or that the 3,5-diF variant is more photosensitive than the standard TTP. The minor feature present at $\sim 350 \text{ nm}$ remains in the spectrum of the 3,5-diF TTP also, and once again is unaffected by continuous light exposure.

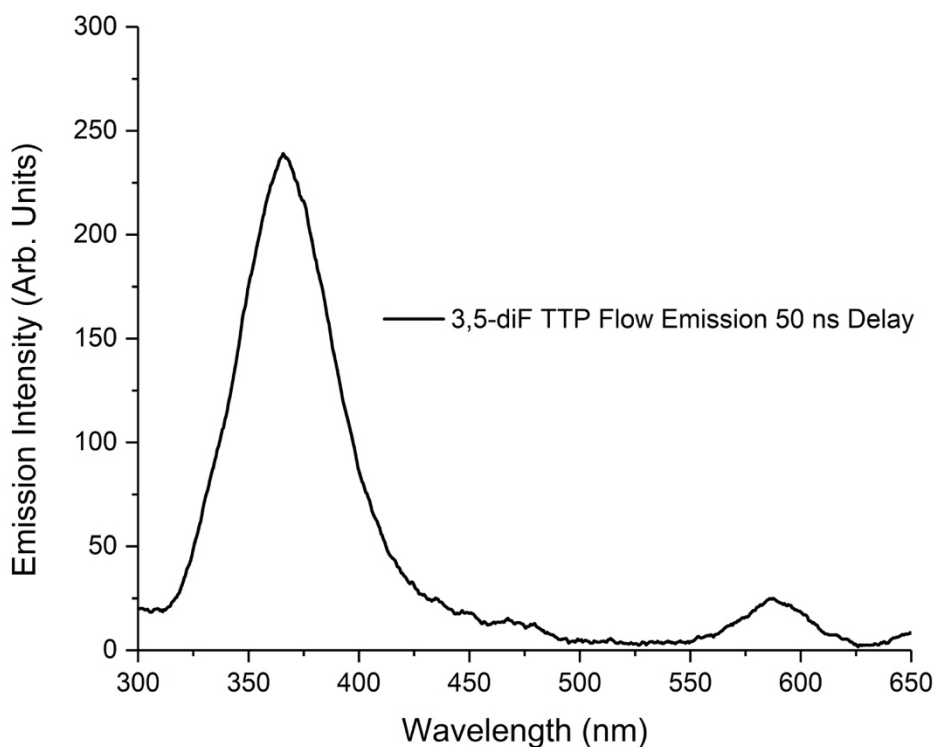


Figure 81 Emission spectra of the 3,5-diF TTP compound in acetonitrile (100 μ M) under flow at 50 ns from the laser pulse ($\lambda_{\text{ex}} = 266$ nm). Smoothing applied for presentation purposes.

The emission spectrum of 3,5-diF TTP under flow, shown in figure 81, resembles that of the standard TTP at 50 ns from the pulse. The short wavelength emission remains whilst the emission at 440 nm is depleted. A small feature is visible at ~ 590 nm, but this remains unassigned, and is possibly due to a contaminant in the flow apparatus.

5.5.3 2,6-diF Triphenyltetrazolium (2,6-diF TTP)

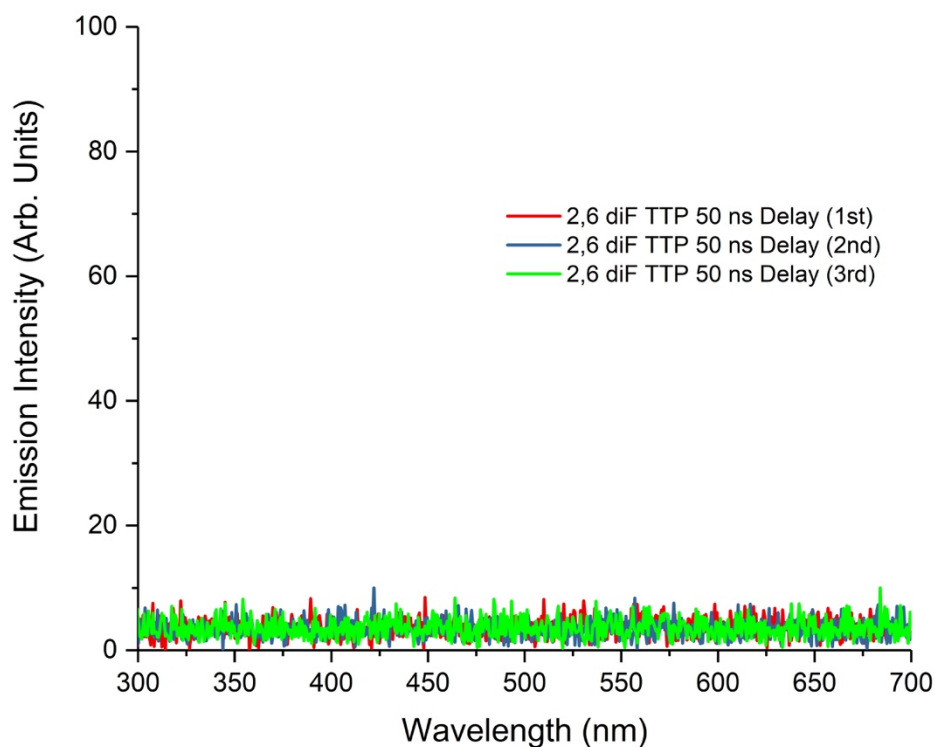


Figure 82 Emission spectra of the 2,6-diF TTP compound in acetonitrile (100 μM) at 50 ns from the laser pulse, multiple acquisitions ($\lambda_{\text{Ex}} = 266 \text{ nm}$)

The 2,6-diF variant of TTP exhibits no emission at 50 ns from the laser pulse, shown in figure 82, suggestive of an absence of long-lived fluorescence or phosphorescence. The compound does not display any features at this timescale even when subjected to increased light exposure, suggestive of significant inhibition of the photoreactive process that caused emission feature growth in the other TTP compounds. The PMT acquisition process used in the flash photolysis spectra section of this chapter includes a laser-only emission background step for each acquired wavelength as a means to correct for luminescence when acquiring a transient absorption spectrum. This emission background suggests the presence of a short-lived fluorescence feature for wavelengths between 350 – 625 nm. Using the method employed for the flash photolysis spectrum, the intensity value for each wavelength is plotted for a time delay of 20 ns after the pulse, chosen for when the emission intensity is at its maximum, and is shown below in figure 83.

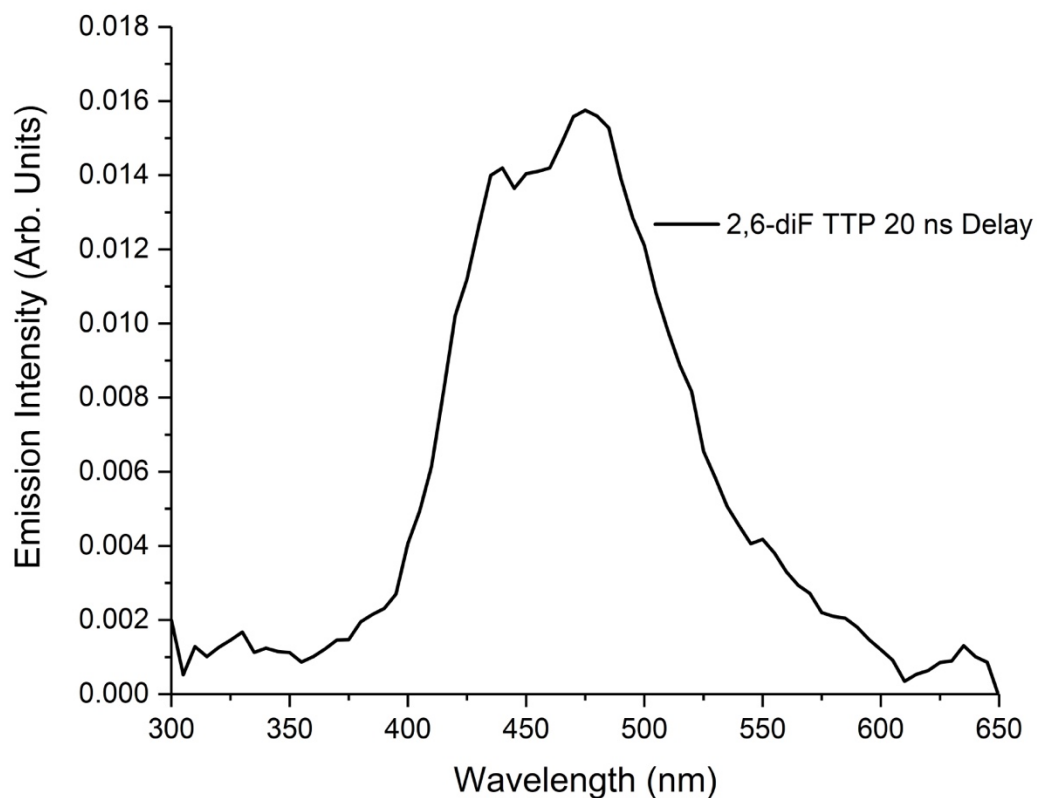


Figure 83 Emission spectra of the 2,6-diF TTP compound in acetonitrile (100 μ M) at 20 ns from the laser pulse ($\lambda_{Ex} = 266$ nm) acquired using wavelength stepped PMT mapping. Smoothing applied for presentation purposes.

The emission spectrum above resembles that observed in the 3,5-diF and base variants of TTP following extended light exposure, suggesting the presence of the photocoupled product. In the PMT emission spectrum there appears to be two visible peak features in the emission, so an ICCD spectrum of the emission was also obtained at a 30 ns delay in light of this finding in an attempt to develop a clearer image of this spectrum as a whole, as the wavelength stepped nature of the PMT map reduces the resolution of the spectrum. The ICCD spectrum is shown below in figure 84.

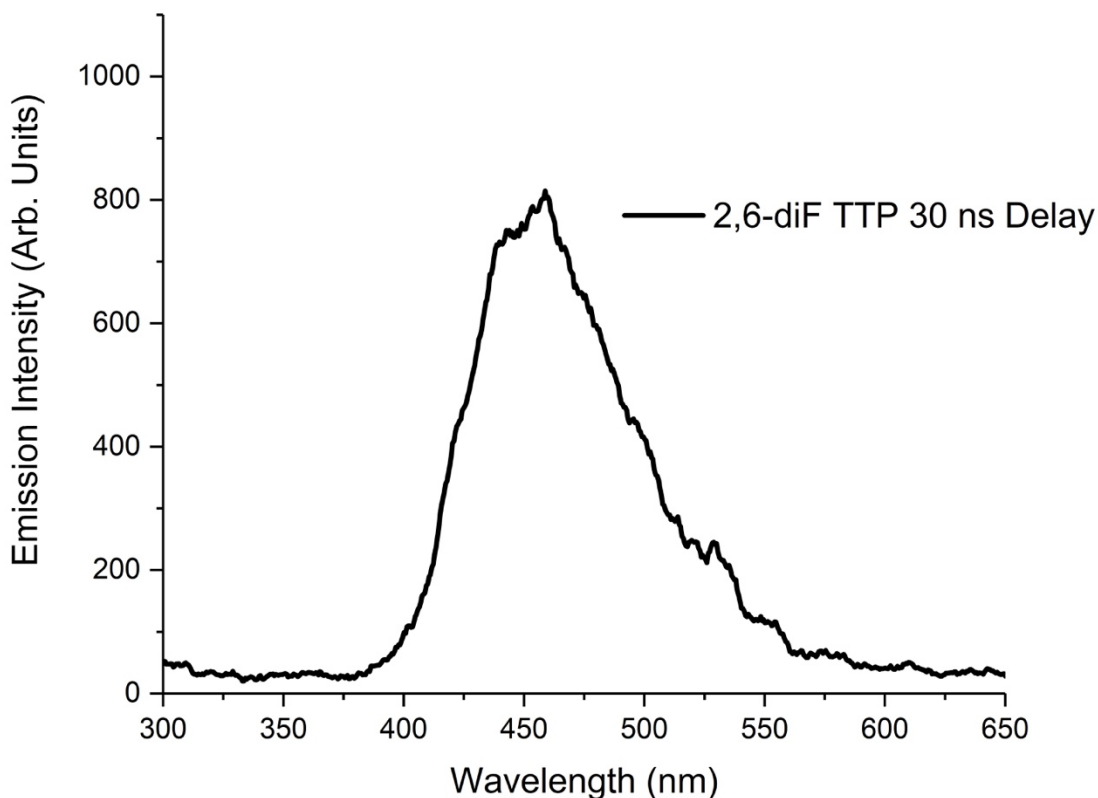


Figure 84 Emission spectra of the 2,6-diF TTP compound in acetonitrile (100 μM) at 30 ns from the laser pulse ($\lambda_{\text{ex}} = 266 \text{ nm}$). Smoothing applied for presentation purposes.

The emission feature appears broad and without any significant shoulder features at 30 ns from the delay. The shoulder feature observed around 530 nm matches a parasitic output wavelength present in the laser excitation pulse (532 nm output) and is likely distortion due to residual laser scatter from this. It is difficult to determine from these measurements alone the nature of the photoreaction, if any, that the 2,6-diF TTP compound is undergoing, although the emission spectrum retains its profile irrespective of the amount of laser excitation, as evidenced by the PMT map spectrum which remains consistent despite the number of measurements required to obtain it. Given the low intensity of the emission, and the lack of response at any time scale in the transient absorption spectrum that might correspond to chemical change, the emission observed likely originates from either the 2,6-diF TTP itself, or small quantities of the corresponding photocoupled product.

5.5.4 2,6-diMethyl, 4-Methyl, 4-Tert-butyl Triphenyltetrazolium (2,6-diMe TTP)

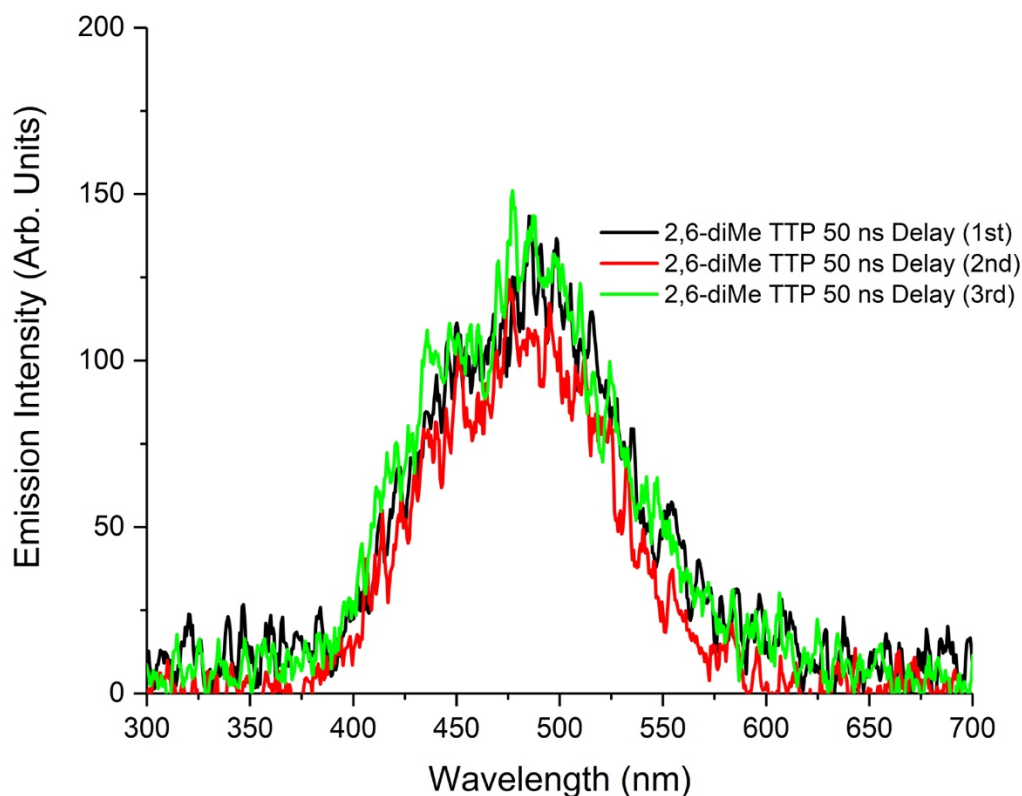


Figure 85 Emission spectra of the 2,6-diMe TTP compound in acetonitrile (100 μ M) at 50 ns from the laser pulse, first three acquisitions ($\lambda_{\text{ex}} = 266$ nm)

The emission spectrum of the 2,6-diMe TTP compound, shown in figure 85, is markedly different from the other compounds. There is a single broad emission feature present at 50 ns from laser excitation, with a global maximum centred at ~ 490 nm and a shoulder peak at 450 nm. The two peaks are ascribed to the same origins as those observed in the spectra of the 3,5-diF and basis TTP compounds. Given that the 2,6-diMe TTP compound has the greatest number of modifications of all the TTP variants, it is unsurprising that the spectrum has undergone a more significant degree of chromatic shift. The spectrum remains unchanged upon a similar degree of excitation as the other compounds, suggesting that the species from which they originate are more photostable than either the TTP or 3,5-diF TTP compounds. To test the degree to which the emission spectrum of this sample of 2,6-diMe TTP is stable with respect to light exposure, subsequent acquisitions were performed, shown in figure 86.

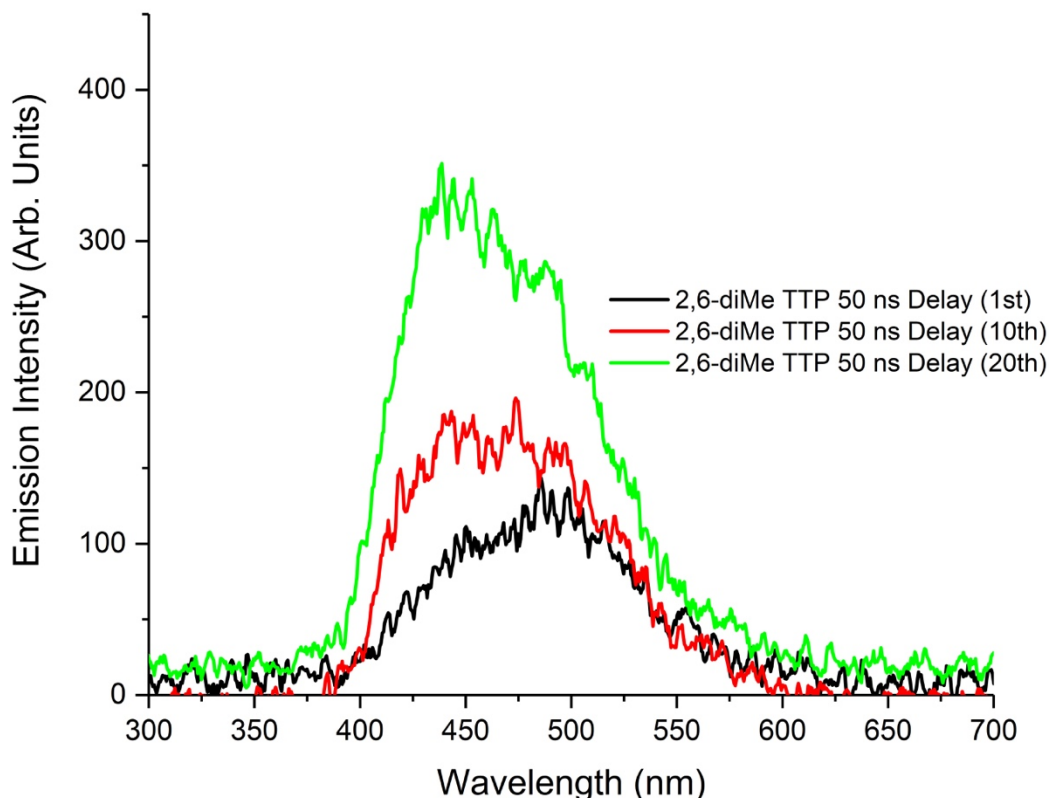


Figure 86 Emission spectra of the 2,6-diMe TTP compound in acetonitrile (100 μ M) at 50 ns from the laser pulse, multiple acquisitions ($\lambda_{\text{ex}} = 266$ nm)

Upon extended light exposure, the spectrum begins to alter. The feature observed at 450 nm begins to increase in magnitude and shifts to ~ 440 nm. This shift is possibly as a result of the increased resolution due to the greater intensity of emission. The two emission bands have significant overlap, making it difficult to distinguish their exact relative intensities, however it is clear from the spectra above that the shorter wavelength band increases in intensity more so than the longer wavelength band. This strongly indicates that the two have different origins and is in keeping with the observations made in the emission spectra of the 3,5-diF TTP and basis TTP molecules. Hence the feature localised around 490 nm is ascribed to the same origin as the peak centred at 360 nm found in those two compounds, albeit bathochromically shifted. This assignment is based on the similar behaviours exhibited by the compounds, as the increased substitution of the phenyl rings of the 2,6-diMe TTP is likely to have a more pronounced effect on the emission bands, given that the phenyl rings are heavily involved in the frontier orbitals of the compound. The observations made in this emission study suggest that the 2,6-diMe TTP compound has a greater inhibition to the

onset of the photoreaction than the 3,5-diF or standard TTP compounds, but that it still is susceptible to undergoing the reaction given sufficient light exposure. This is also likely why it displayed no activity in the TA spectra presented and discussed above, as the progression of the reaction proceeded at a rate insufficient to produce a measurable response from the sample.

5.6 Transient Kinetic Study

Using the PMT/monochromator detection system, individual wavelengths of interest can be selected and probed across a relatively long timescale. Whilst this process has been used in this work primarily to analyse the progression of single-origin emission and transient absorption features in the case of the iridium complexes, this method can also be used to monitor the progression of a changing chemical system. The change induced by the laser in the sample should induce a variety of transient absorption, emission and bleach features depending on the stage of the reaction and proportion of chemical species present in solution at a given timeframe. To that end, the kinetics of the TTP compounds were examined at significant wavelengths based on the ICCD transient absorption and emission spectra.

5.6.1 Triphenyltetrazolium (TTP)

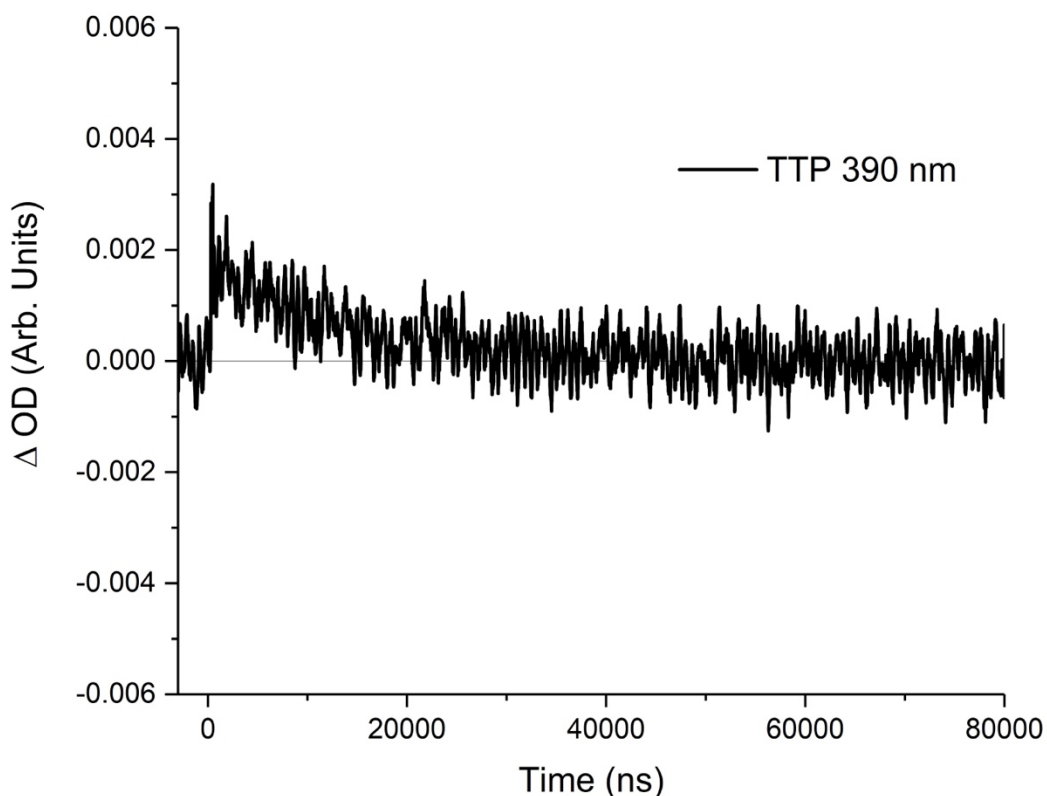


Figure 87 Luminescence corrected kinetic transient absorption spectrum of TTP in acetonitrile ($100 \mu\text{M}$) at 390 nm ($\lambda_{\text{EX}} = 266 \text{ nm}$). For presentation purposes smoothing has been applied.

A transient kinetic spectrum was obtained for the TTP basis compound at the main absorption peak observed in the ICCD spectrum at 390 nm and is shown in figure 87. The measurements obtained with the PMT/monochromator system match those obtained with the ICCD, in that the feature arises in the early timescale and persists into the tens of microseconds. The absorption feature appears almost immediately following the laser pulse and proceeds to decay in a mono-exponential fashion, with an obtained lifetime of $13.5 (\pm 1.2) \mu\text{s}$. The data has a relatively low signal-to-noise ratio in comparison with the kinetic measurements obtained from the iridium complexes earlier in this work, inducing a higher degree of error into the fitting.

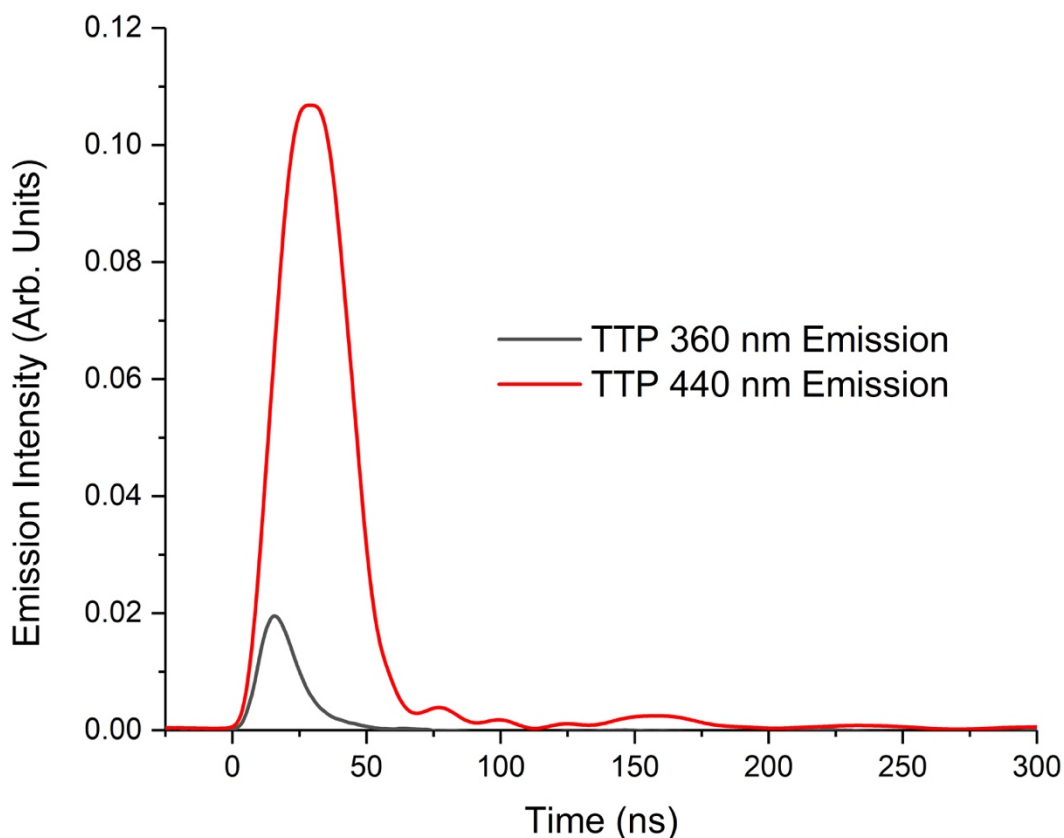


Figure 88 Kinetic emission spectra of TTP in acetonitrile (100 μM) ($\lambda_{\text{Ex}} = 266 \text{ nm}$). For presentation purposes smoothing has been applied.

Analysis of the major emission bands observed in the TTP spectra using the PMT detector system corroborates the results of the ICCD detector, and are shown in figure 88. Both emission traces are short-lived, with Gaussian-like temporal profiles, indicative of fluorescence. The emission band at 440 nm is far more intense than that observed at 360 nm and is significantly prevalent up to around 70 ns after the onset of the excitation pulse. Both were fitted to a mono-exponential decay function from the maximum intensity to the base, giving lifetimes of 12.1 (± 0.3) ns and 22.1 (± 1.9) ns for 360 nm and 440 nm respectively. The features arising after the main emission peak in the 440 nm trace are attributed to instrument noise.

5.6.2 2,6-diF Triphenyltetrazolium (2,6-diF TTP)

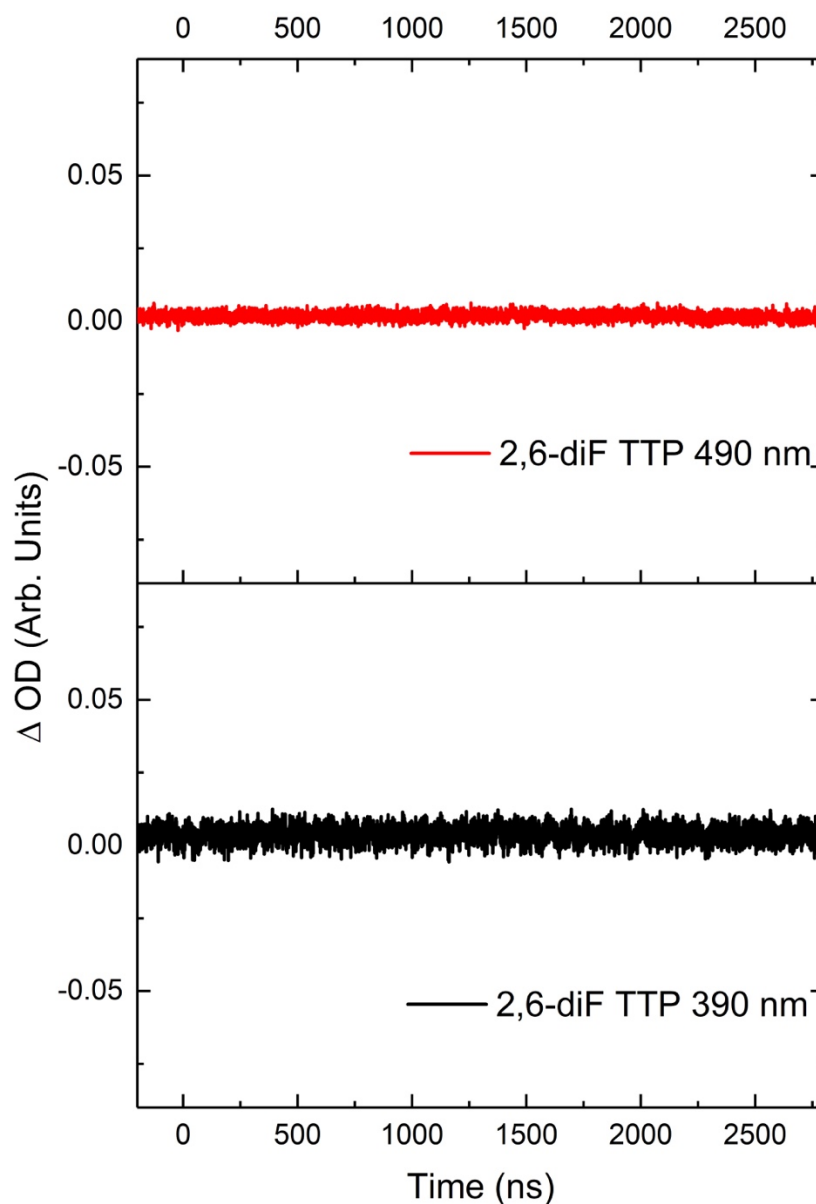


Figure 89 Luminescence corrected kinetic transient absorption spectrum of 2,6-diF TTP in acetonitrile (100 μM) at 390 nm and 490 nm ($\lambda_{\text{ex}} = 266$ nm).

The transient absorption kinetics of 2,6-diF TTP, shown in figure 89, yield no response at any of the examined wavelengths, suggestive of no permanent change to the sample and no alteration in the absorption properties of the ground state upon excitation into the excited state. The two kinetic traces above are shown above as examples, showing the clear lack of response from the sample.

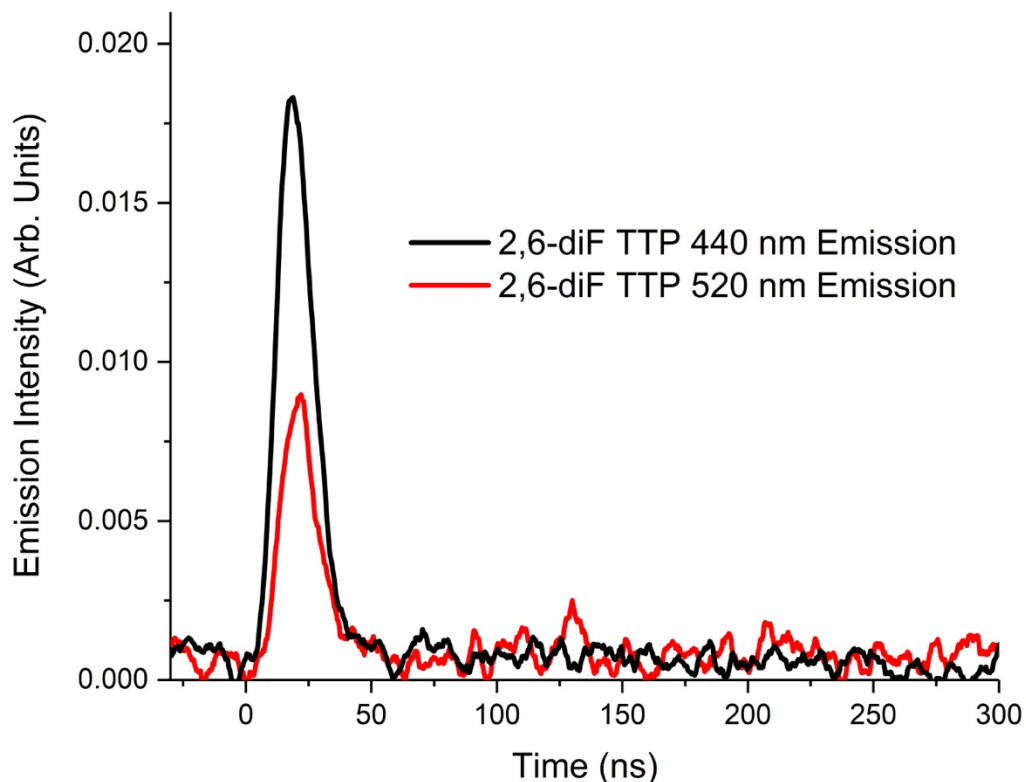


Figure 90 Kinetic emission spectra of 2,6-diF TTP in acetonitrile (100 μM) ($\lambda_{\text{ex}} = 266 \text{ nm}$). For presentation purposes smoothing has been applied.

The emission kinetics of the 2,6-diF TTP, shown in figure 90, yield similar lifetimes for each wavelength of the emission band differing only in maximum intensity, suggestive of a shared origin emissive state for all wavelengths across the band, in contrast with the spectrum of the base TTP compound. Shown in the figure above, two wavelengths were chosen from either side of the emission band maximum, 440 nm and 520 nm. Each were fitted to a mono-exponential decay function and both exhibited decay lifetimes of around 9 ns (9.0 (± 0.4) ns and 9.1 (± 0.6) ns for 440 and 520 nm respectively), suggestive of fluorescence. The presence of a short-lived fluorescence feature and the absence of any permanent change in the sample, as indicated by the lack of transient absorption response, suggest that in the 2,6-diF TTP case the photochemical reaction has been strongly inhibited.

5.7 Mass Spectrometry

Time of flight mass spectrometry (TOF-MS) was used to analyse the products of the photoreaction in order to ascertain the nature of the chemically stable end results of the reaction following light exposure. This is a technique that can accurately determine the mass-to-charge ratio (m/z) of a sample compound through acceleration of the ionised compound by an electric field of known strength across a known distance, whereupon an ion impact event is registered by a detector. The time taken for a compound to reach the detector can then be used to determine the m/z ratio, allowing for the composition of compounds in a sample to be more accurately determined. The experiment normally is conducted under vacuum, in order to allow for the uninterrupted flight of the sample ions to the detector, and to prevent interference from the detection of atmospheric contaminants. The sample is normally subject to pre-ionisation, normally through the use of an electron spray method, although this could potentially damage the sample. The compounds in this thesis chapter were analysed using a direct injection method, meaning the ionisation step was omitted, to prevent damage to the compounds. In this manner we detect only those ions already present in solution and assume, in doing so, that once solvated the precursor tetrazolium species dissociate from their ion pair. This technique was also used to confirm whether or not the mechanism had been completely or partially inhibited in the 2,6-diF TTP case, as the conclusions from the flash photolysis studies suggest that the reaction does not proceed, but may not be sufficiently sensitive to detect any small amounts that may have been produced over the course of the experiment. To this end, samples of the TTP and 2,6-diF TTP compounds in acetonitrile were exposed to the pump laser output for different amounts of time and then examined using direct injection TOF-MS.

5.7.1 Triphenyltetrazolium (TTP)

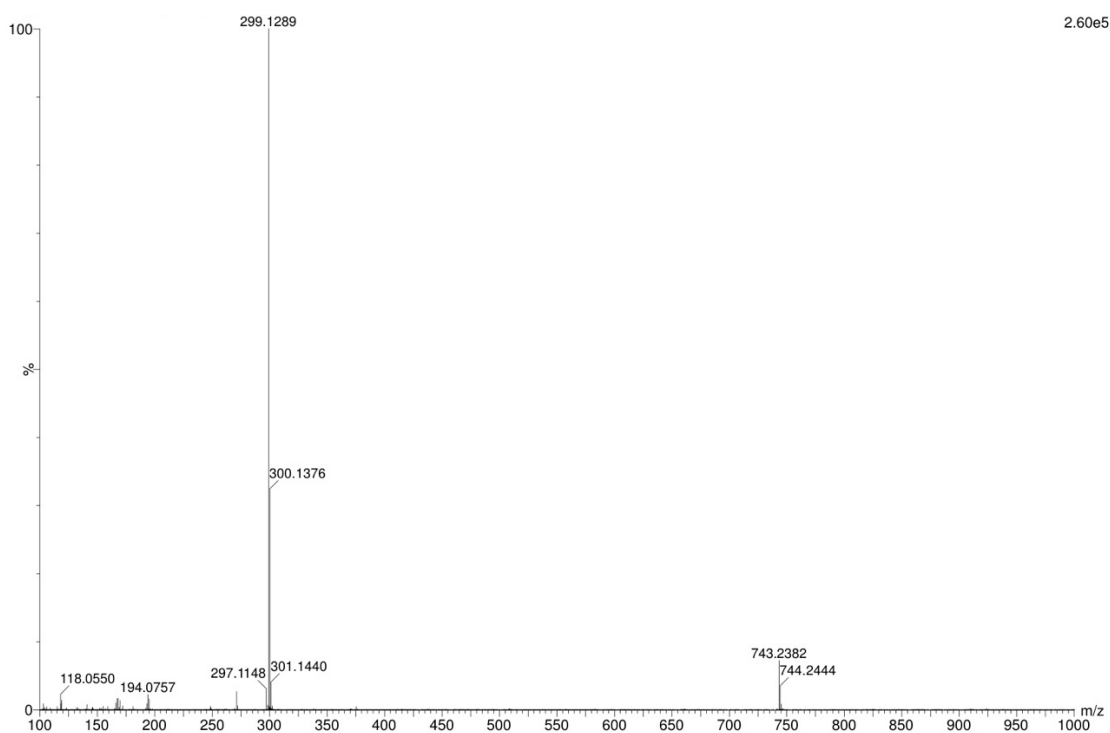


Figure 91 Time-of-flight mass spectrum of TTP in acetonitrile (100 μ M), no laser exposure.

The TOF-MS spectrum of the non-irradiated TTP sample, shown in figure 91, shows a dominant peak at 299.1289, as well as minor peaks at 300.1376 and 301.1440, which correspond to the expected m/z values for the triphenyltetrazolium cation and its isotopic variants. The pair of peaks at 743.2384 and 744.2444 corresponds closely to a pair of deprotonated triphenylformazan photoproducts coupled to a PF₆ anion, with

isotopic differences accounting for the two. The peak visible at 300.1376 matches closely with the expected value of a single non-deprotonated formazan molecule (300.14). There is a minor peak detected at 297.1148, corresponding to the PCP molecule. These are likely present due to ambient light exposure driving the photoreaction, owing to the light sensitivity of the TTP base compound. A sample taken from the same stock solution was exposed to the output of the Nd:YAG pump laser at 266 nm for approximately 2 hours and a mass spectrum obtained, shown in figure 92.

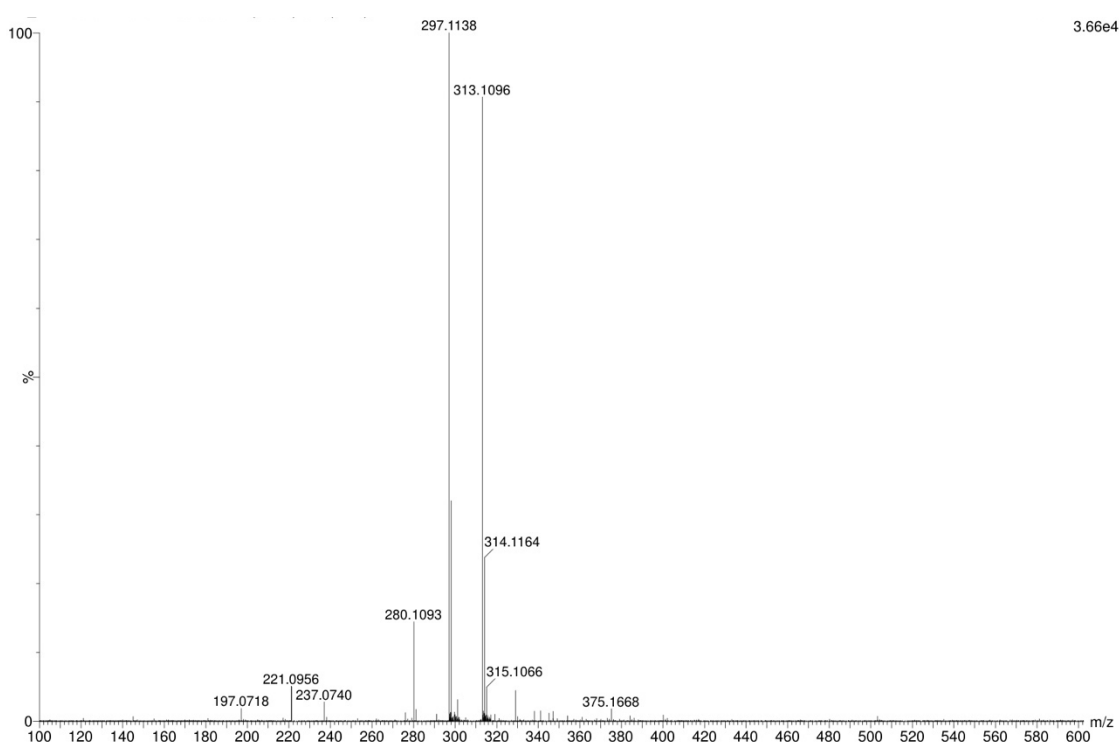


Figure 92 Time-of-flight mass spectrum of TTP in acetonitrile (100 μ M), 2 hours laser exposure.

The mass spectrum of the heavily exposed sample shows a complete depletion of the m/z value corresponding to the triphenyltetrazolium starting material and a massive increase in the 297.11 m/z value corresponding to the PCP. The value of the formazan end product is expected at 300.14, but this is not significantly apparent in this spectrum and neither are the peaks around 740 assigned to the formazan pairings, omitted from this spectrum due to inactivity. Of significant interest is the presence of a very strong peak at 313.1096 and an accompanying pair of peaks at 314.1164 and

315.1066. These correspond to a mass value equivalent to the PCP plus an atom of oxygen, and fit the ratios expected with isotopic variation. This strongly suggests that the PCP undergoes a further oxidation, and quite readily given the high population of this oxidation product, designated oxidised photocoupled product (O-PCP). To initially and relatively inexpensively test this hypothesis, four additional samples of the TTP solution were prepared for TOF-MS, with different exposure times and different volumes of oxygen present. Two samples were thoroughly degassed using a freeze-thaw procedure, removing the atmosphere of the cuvette and replacing it with nitrogen, a procedure repeated 8 times for each sample to ensure a low level of oxygen. These were then exposed to the laser output for 10 and 45 mins, with the TOF-MS spectra of each visible in figures 95 and 96 respectively. Two additional samples were left in normal atmospheric conditions with no degassing performed and exposed for the same times. The TOF-MS spectra of each are shown below in figures 93 and 94 respectively.

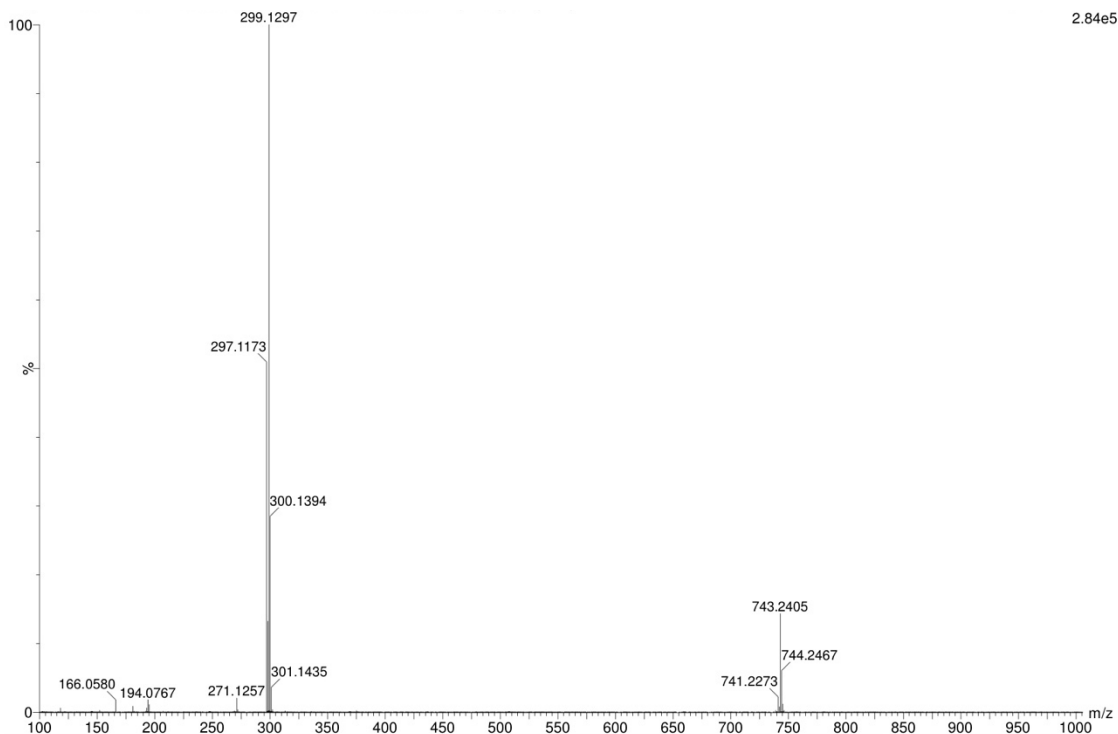


Figure 93 Time-of-flight mass spectrum of TTP in acetonitrile (100 μ M), 10 minutes laser exposure

Evident in the spectrum above is the progression of the reaction towards the formation of the PCP, with the triphenyltetrazolium still dominating the mass spectrum. The PCP peak is more prominent than in that of the non-exposed sample, now corresponding to the second most abundant species overall. The peak present at 300.1394 corresponds closely to the triphenylformazan, expected at 300.14, suggesting that a significant amount of this is formed also. There is no sign indicating the formation of the oxidised PCP species at this level of exposure, indicating that it is likely formed from a secondary reaction or at the least a far slower rate than the PCP.

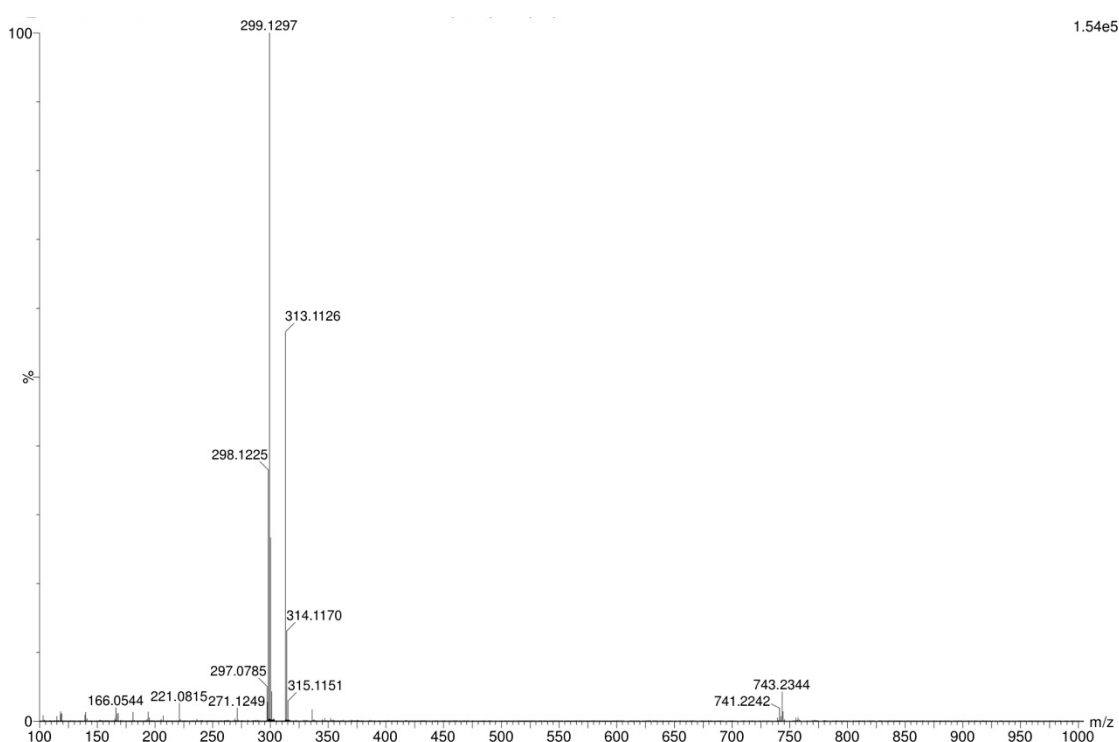


Figure 94 Time-of-flight mass spectrum of TTP in acetonitrile (100 μ M), 45 minutes laser exposure

Following more prolonged exposure, features corresponding to the oxidised form of PCP begin to become more prominent. The feature corresponding to the triphenyltetrazolium starting material is still the most prominent feature, suggesting that the majority of the solution remains unchanged after 45 minutes of laser exposure. The predominant photoproduct here appears to be the oxidised PCP, as there is no detectable sign of the formazan photoproduct in the mass spectrum, as in the case of the 2-hour laser exposure spectrum. It would appear as though the corresponding formazan is only present at lower levels of laser exposure, and that it is

potentially depleted by further photon exposure. The peak at 298.1225 corresponds to an isotopic variant of the PCP species.

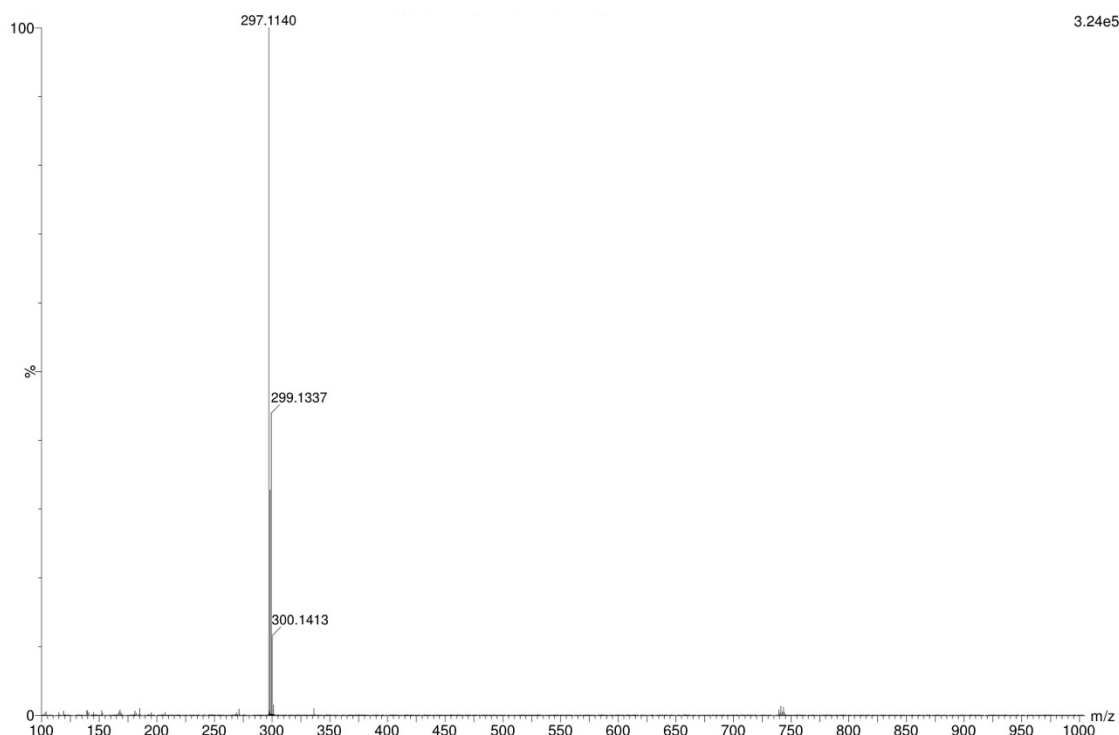


Figure 95 Time-of-flight mass spectrum of degassed TTP in acetonitrile (100 μ M), 10 minutes laser exposure.

In the absence of an oxygenated environment, the spectrum becomes much cleaner, shown in figure 95, with clear evidence of the triphenyltetrazolium, the PCP and the triphenylformazan present in solution. Small peaks are visible at \sim 740 – 745, suggestive of coupled pairs joining with PF_6 ions, but in much smaller amounts. At 45 minutes of exposure, a similar case is observed, with the PCP being the dominant species present (297.1134 and 298.1194) and the triphenyltetrazolium starting material (299.1301) still remaining, albeit in a much smaller amount as a percentage of the whole. The lack of development of the feature at \sim 313 – 315 mu of in either of the degassed spectra constitutes indirect evidence supporting an assignment to the oxidised PCP species. The mass spectrum for the 45 minutes exposure time degassed sample of TTP is shown in figure 96 below.

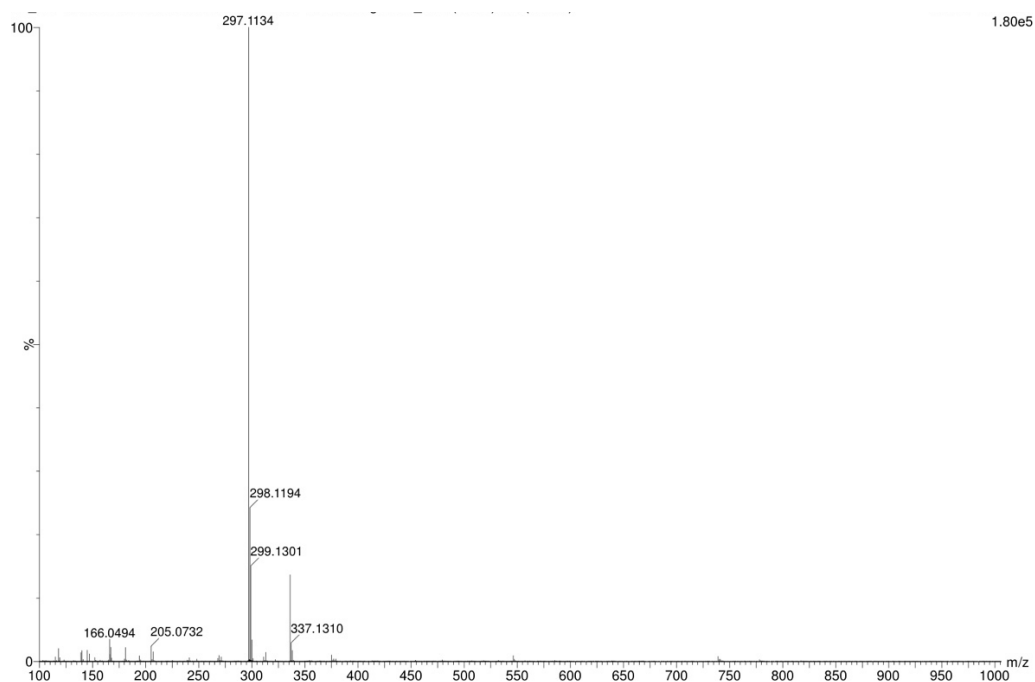


Figure 96 Time-of-flight mass spectrum of degassed TTP in acetonitrile (100 μ M), 45 minutes laser exposure.

5.7.1.1 Oxidised Photocoupled Product

Given the mass number of the oxidised photocoupled product, the likeliest site for oxidation would be the central tetrazolium ring, with a proposed structure shown in figure 97.

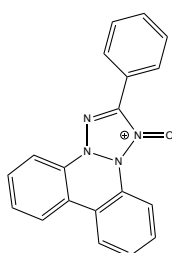


Figure 97 Theorised structure for the oxidised photocoupled product.

An isotopic mass spectrum study and/or NMR study would allow for a confirmation of this structure but given the lack of substitution implied by the mass number, direct addition of an oxygen atom to the phenyl ring is the most likely outcome. Insertion of

an oxygen atom into one of the C-H bonds of the phenyl rings is another possibility and shows the need for an NMR study to confirm the structure of this species.

5.7.2 2,6-diF Triphenyltetrazolium (2,6-diF TTP)

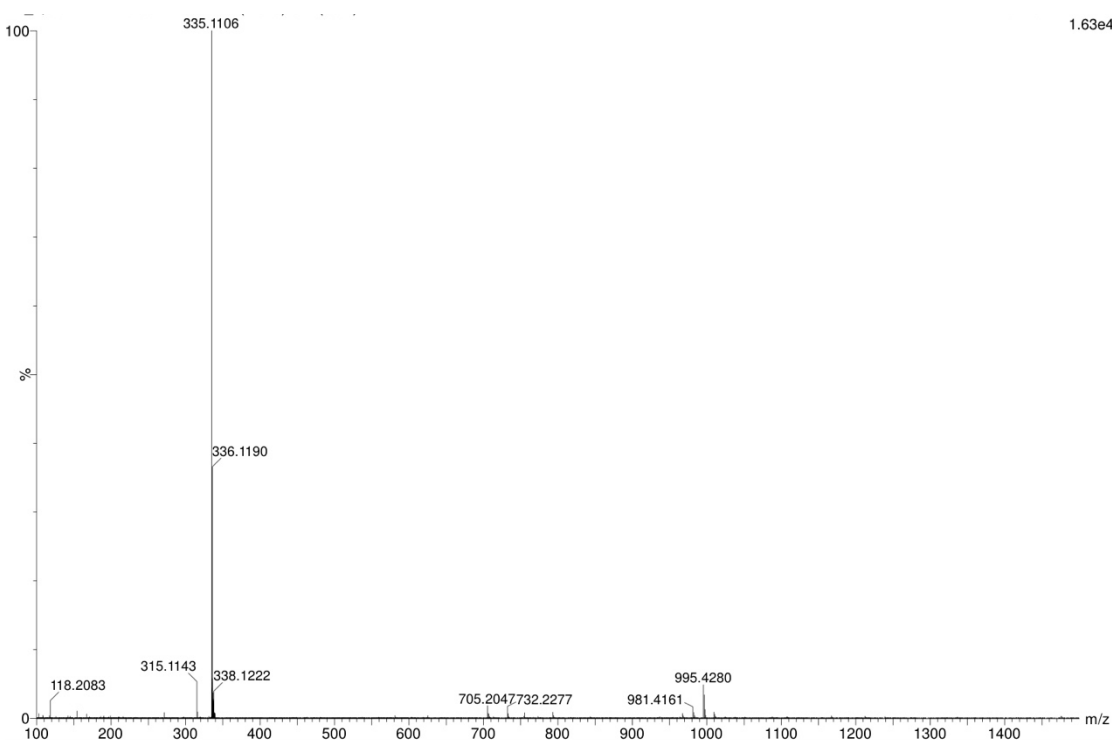


Figure 98 Time-of-flight mass spectrum of 2,6-diF TTP in acetonitrile (100 μ M)

Analysis of the mass spectra of the 2,6-diF TTP, figure 98, shows that the solution is composed primarily of the 2,6-diF triphenyltetrazolium starting material (335.1106). The value at 336.1190 is attributed to the corresponding formazan (expected at 336.12). This is possibly due to ambient light exposure over time due to the age of the sample but suggests that the sample is nonetheless photosensitive to some degree. A small peak at 315.1143 suggests the presence of the corresponding photocoupled product. This also implies HF elimination through the formation of the bond between the two N-based phenyl rings. Similar photoelimination has been observed in fluorohelicene compounds.⁹¹

Extensive laser exposure was employed in order to determine the degree to which the photoreaction is inhibited relative to the standard TTP molecule, and the results of this are shown in figure 99.

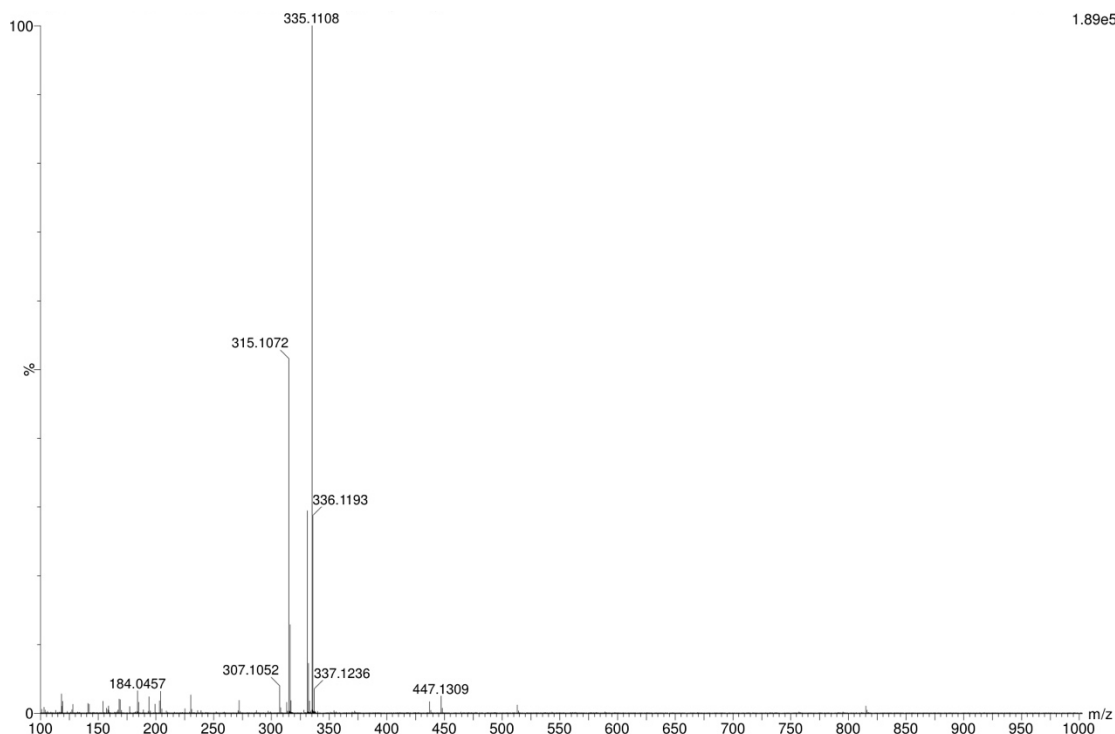


Figure 99 Time-of-flight mass spectrum of 2,6-diF TTP in acetonitrile (100 μ M), 2 hours laser exposure.

Following 2 hours of laser exposure, the most prominent feature remains the 2,6-diF triphenyltetrazolium starting material. The relative amount of the corresponding formazan is similar following photo-exposure whilst the amount of the photocoupled product has increased significantly (315.1072). Whilst the photoreaction is not completely deactivated in the 2,6-diF case, it does appear to be strongly inhibited, as the starting material is still the most prevalent species in contrast to the standard TTP molecule, which was completely depleted following the same degree of exposure.

5.8 Conclusion

Analysis of triphenyltetrazolium and its variants using flash photolysis showed that the photoreduction reaction could be inhibited through the selective placement of substituents on the phenyl ring bound to the 2 position of the central tetrazolium ring. Placement of substituents at the ortho position of the ring inhibited the photoreaction as evidenced by the removal of features from the transient absorption spectra indicative of the formation of photoproducts and the slowing of the cumulative evolution of the emission spectra, also indicative of photoproduct formation. Fluorine appeared to be a more successful inhibitor when placed at the ortho position, evidenced by its apparent spectral inactivity despite light exposure. Placement at the meta position of this phenyl ring appeared to have no inhibitive effect and appeared to actually slightly increase the rate of photoreaction. Spectroscopic analysis showed to be a good match for literature observations of the formation of TPF and PCP. Crucially, in combination with the computational molecular orbital decomposition, these data suggest that the photoreaction can be inhibited without altering the electronic chemistry of the system, suggesting the chemical reduction of 2,6-diF TTP might still be a useful colourimetric indicator, but will be insensitive to light as a false positive.

Mass spectral studies of TTP and 2,6-diF TTP species suggest that the 2,6-diF TTP does undergo the photoreduction forming the corresponding PCP, albeit at a vastly reduced rate compared to the base TTP. This is also indirectly indicative of HF liberation, removed in the PCP formation from 2,6-diF TTP. A species with a mass number corresponding to a further oxidation product of PCP was also observed in the mass spectrum and the formation of this photoproduct is inhibited through the removal of oxygen from the atmosphere during irradiation, suggesting it is a product of a further photoreaction between the PCP molecule and oxygen in solution. A further study employing NMR and isotopic oxygen analysis would confirm this assignment and yield a more definitive explanation of the structure of this species but was not completed here due to time constraints.

6. Design and Development of a mid-IR Cavity Ringdown Spectrometer

6.1. Introduction and Background

6.1.1 Cavity Ringdown Spectroscopy

Cavity ringdown absorption spectroscopy (CRDS) is an analytical technique used in the gas phase that relies on the use of an optical cavity to enhance the path length of a standard absorption spectrometer, providing a vast increase in sensitivity compared to standard absorption techniques, with sensitivities on the order of ppm – ppb frequently accomplished.^{53,92} A pair of high reflectivity mirrors, normally >99.9% reflectivity, are used to form the optical cavity, within the confines of which the sample being examined is placed. Curved mirrors are commonly used to aid in the alignment of the cavity, as they will refocus any reflected light towards a point. A light source, almost exclusively a laser, is then used to probe the sample through the cavity, via direct injection of light into the first mirror of the cavity, along the principal axis of the optical cavity. The principle of the method (as is the case with all cavity enhanced methods that use high reflectivity mirrors in this fashion) is that, whilst the vast majority of any probe light used to interrogate the sample will be rejected by the initial mirror of the cavity due to its extreme reflectivity, a very small amount will be transmitted through. In CRDS, the injected light will then oscillate between the two mirrors via repeated reflections, interacting with the sample contained within, resulting in a massively increased path length compared to conventional spectrometers. The interrogating beam is shut off at a certain point, either using fast electronics or a chopper wheel. The light will then ‘leak’ out of the cavity through both mirrors on each successive reflection ($1 - R$, where R is the mirror reflectivity),⁹² and this is monitored by a detector positioned on the ‘far’ side of the cavity, positioned behind the second mirror of the optical cavity, normally equipped with a lens to collect the light and transfer it to the detector more efficiently. Figure 100 shows a basic optical cavity scheme.

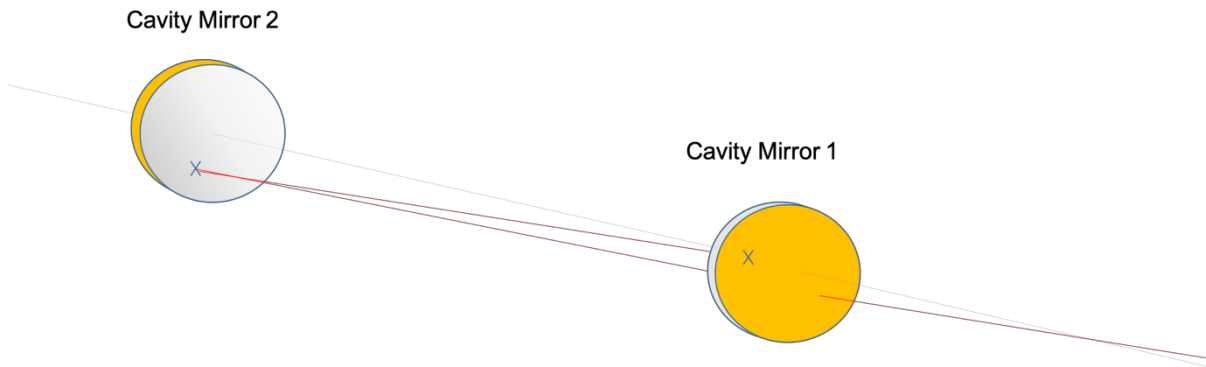


Figure 100 Diagram of an off-axis injection optical cavity setup with one reflection shown.

By examining the signal strength perceived by the detector as a function of time, a rate of decay can be obtained for the signal, the inverse of which is called the ‘ringdown’ time.⁵³ The equation below describes the relationship between the cavity decay rate and the properties of the instrument:

$$k = \frac{1}{\tau} = \frac{(1 - R)c}{L}$$

Equation 6 Empty cavity decay rate. k = decay rate coefficient, τ = ringdown time, L = distance between mirrors, R = reflectivity of mirrors, c = speed of light.

The ringdown time represents the average time a photon will last within the cavity, and from this relationship, the effective path length, or average distance travelled within the cavity, can be deduced, shown in equation 7.

$$L_{eff} = \frac{L}{(1 - R)} = \tau c$$

Equation 7 Mean distance travelled by light within the cavity, L_{eff} .

This effective path length can reach very large values for even relatively short cavities and is largely dependent on the reflectivity of the mirrors, but also the distance between them. For example, a cavity of length 1 metre with mirrors of 99.98% reflectivity would have a mean distance travelled of 5 kilometres for an empty cavity.

CRDS works well for a large portion of the electromagnetic spectrum, the limitations of the experiment primarily being the availability of high-reflectivity mirrors and sufficiently powerful light sources at the desired wavelength range.

By comparing the rate of decay for an empty cavity compared with one containing a sample, the absorption spectrum of the sample can be obtained. This is explained using the Beer-Lambert law, as the molar extinction coefficient of the sample will cause the light to be attenuated in the case of the filled cavity, whilst this factor will be absent for the empty cavity, resulting in an increased decay rate proportional to the samples molar extinction coefficient at any of the measured wavelengths.

$$I = I_0 e^{-tk} \quad k = \frac{L_{cav} + \alpha l_{RT}}{t_{RT}} = \frac{L_{cav}}{t_{RT}} + c\epsilon C$$

Equation 8 *The relationship of transmitted intensity to absorptivity . I = transmitted intensity, I_0 = initial intensity, t = time, k = decay rate, L_{cav} = round-trip cavity losses, l_{RT} = cavity round-trip length, t_{RT} = cavity round-trip time, α = absorption coefficient of sample, c = speed of light, C = concentration of sample, ϵ = molar extinction coefficient of sample.*

The equations above relate the observed intensity decay to the properties of the sample and cavity.⁹³ The round-trip time is given by $2L/c$, where L is the cavity length and c is the speed of light.

In atmospheric studies, cavity enhanced techniques are favoured for their sensitivities, which can be described as the minimum absorption a spectrometer is able to detect, defined typically by absorbances greater than standard deviations in baseline noise levels. Cavity ringdown spectroscopy is somewhat immune to input source variation noise, as the above relationship shows, as it measures a rate of decay in intensity as opposed to a change in absolute absorption. Cavity ringdown spectrometers can be operated in either continuous wave or pulsed configurations. In a pulsed configuration, an incident laser pulse is injected into the cavity, whereupon it will 'bounce' from the surface of each of the mirror faces, losing a small amount of intensity on each pass. On each mirror impingement the laser pulse will lose intensity due to range of loss mechanisms (e.g. scattering) but also because a small fraction of light will be

transmitted through the mirrors. As the light in the optical cavity diminishes over time, so does the intensity of light passing through the optics on each pass, according to the losses of the cavity described in the above equation 8. Most detection equipment will be of a bandwidth sufficiently high that this reduction in light intensity leaking through the cavity optics is recorded as a single decay trace of light intensity with time. Pulsed cavity ring down instruments are particularly favourable because the frequency bandwidth of each pulse is sufficient to overlap with several cavity modes and additionally will be many times the free spectral range of the instrument. This typically reduces the complexity of the instrument, and reduces mode matching requirements, albeit that the better aligned the system the longer the ring down time (hence one can typically observe smaller changes in the ring down time and achieve better sensitivities). The instrument in this thesis is operated in a pulsed configuration, with an off-axis injection design which makes alignment of the system considerably more complex, but is designed to preclude back reflections from the cavity optics reaching, and damaging, the laser system. More in-depth discussions of mode-matching are beyond the scope of this thesis.

6.1.2 Herriott Cell

Another multipass optical cavity configuration is the Herriott cell. It is a relatively simple design analogous to a CRDS optical cavity, consisting of two spherical mirrors facing one another to form an optical cavity, with the exception that an injection aperture is made in the primary mirror to allow light to be injected into the cavity. This aperture can be placed anywhere on the mirror surface but is typically near the edge. The simplest such design would feature two identical mirrors of equal focal length separated by a distance ≤ 4 times their focal length.^{94,95} An injected beam will be reflected between the mirrors and refocussed on each successive reflection such that it forms a spot pattern in the shape of an ellipse on the surface of the mirrors, with each spot being separated by an advance angle. After a given number of reflections, the exact number of which is dependent on the specifications of the setup, the light beam will be directed out of the cavity via the injection aperture, called the 'closure' or 're-entrant' condition.^{94,95} The upper limit on the cells achievable path length for a

given mirror separation is practically limited by the diameter of the individual laser spots relative to the input aperture, as this will limit the density of spots in an ellipse due to clipping of the beam upon overlap with the input aperture.⁹⁵ Upon achieving the re-entrant condition, the beam will exit the cell and can be measured to perform direct absorption spectroscopy with an enhanced path length.

6.1.3 Criegee Intermediates

Criegee intermediates are a class of reaction intermediates formed in the atmosphere during the ozonolysis of alkenes, named for Rudolph Criegee, who first proposed their existence in 1969.⁹⁶ The reaction scheme involves the production of a Criegee intermediate (CI) and a ketone through fissure of the alkene double bond following the formation of a primary ozonide of the alkene via 1,3-cycloaddition, followed by decomposition to the CI and ketone.⁹⁷ Figure 101 shows an example of this scheme.

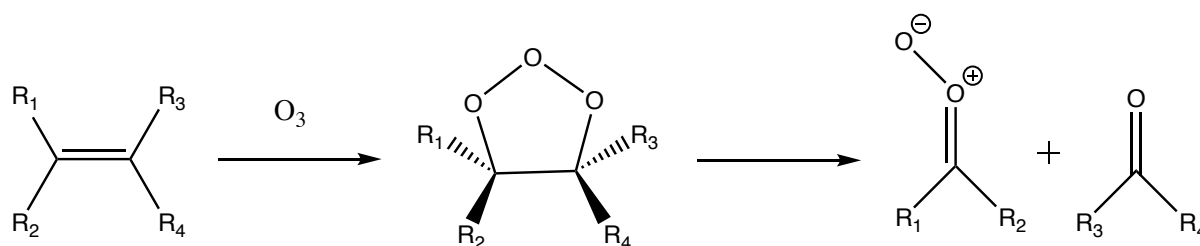


Figure 101 Ozonolysis of an example alkene, forming a Criegee intermediate and a ketone via a primary ozonide. An R₃, R₄ CI and R₁, R₂ ketone are also possible.

The global population of alkenes primarily consists of biogenic emissions, mainly isoprene and monoterpenes, and these species are particularly prominent in forested areas,³⁸ but smaller alkenes arising from anthropogenic emissions can be prevalent in urban areas.^{38,40–42} CIs can form via the ozonolysis of most of these alkenes, which is significant, as CIs have been implicated in a number of atmospheric processes, including the loss mechanisms of both biogenic and anthropogenic alkene populations in the troposphere,⁹⁸ the formation of OH radicals from CI unimolecular decay and aerosol formation.^{39–41,99} OH radicals are responsible for the oxidation of many species in the atmosphere, including SO₂ and NO, making them an atmospherically important species.⁹⁸ Under low UV conditions, such as during the night or winter, CI unimolecular

decay is the dominant pathway for the formation of OH radicals, highlighting the importance of these species.⁴¹ CIs have also been implicated in the formation of secondary organic aerosols,^{100,101} which can lead to urban haze and present a respiratory hazard, emphasising the importance of studying them.

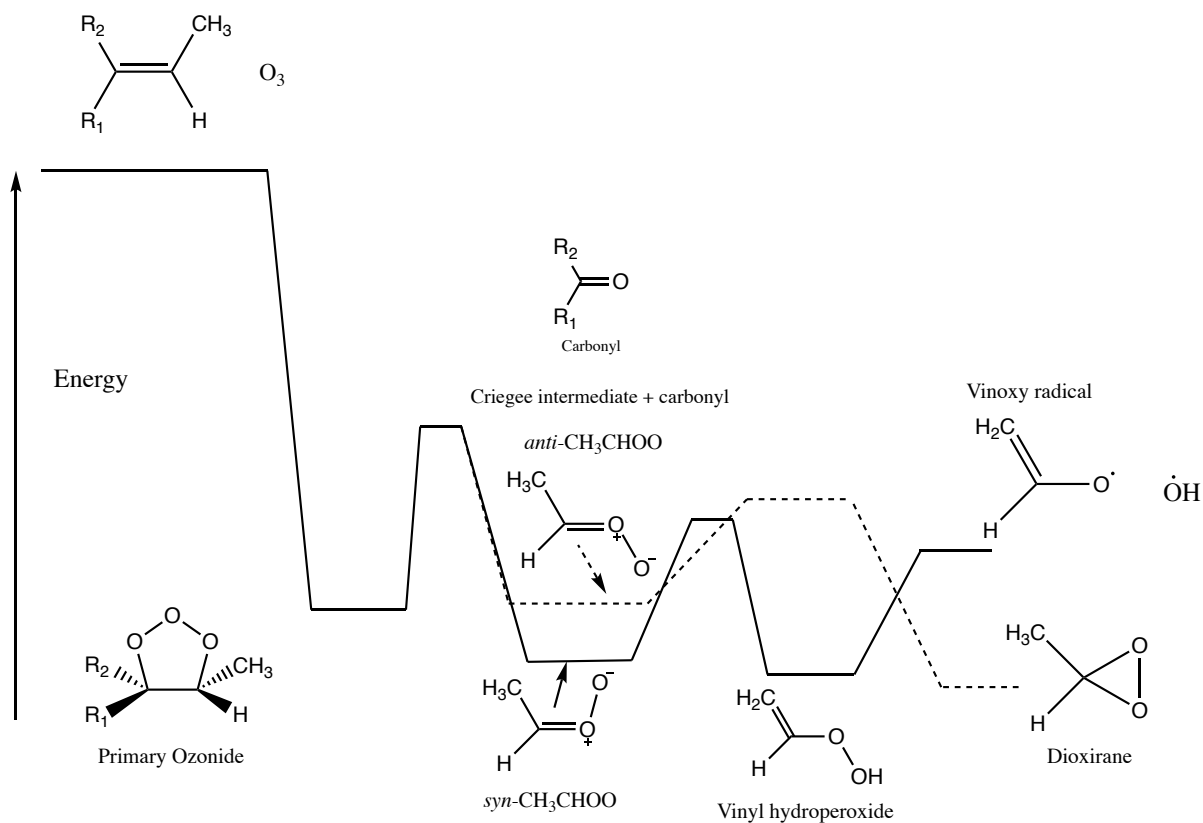


Figure 102 Basic reaction coordinate showing the *syn*- and *anti*- conformers of a simple Criegee intermediate

Figure 102 shows a basic reaction coordinate for the formation of the Criegee intermediate CH₃CHOO. An important feature of the above diagram is that for alkenes with differing R substituents, the Criegee intermediates can form in one of two possible conformers defined by the carbon substituents position relative to the O – O bond, the *syn*- and *anti*- conformers, which possess differing unimolecular decay chemistries,^{102,103} as shown in the above diagram (fig. 102). These conformers also interact differently with atmospheric species, such as NO/NO₂, with the *anti*-conformer being the more reactive in this case.¹⁰³ Criegee intermediates can be readily synthesised in a lab environment through the photolysis of diiodoalkanes in the presence of oxygen,^{102–105} so this route will be used to study the Criegee intermediates

formed from target alkenes such as isoprene, one of the most abundant alkenes in the troposphere as noted above.

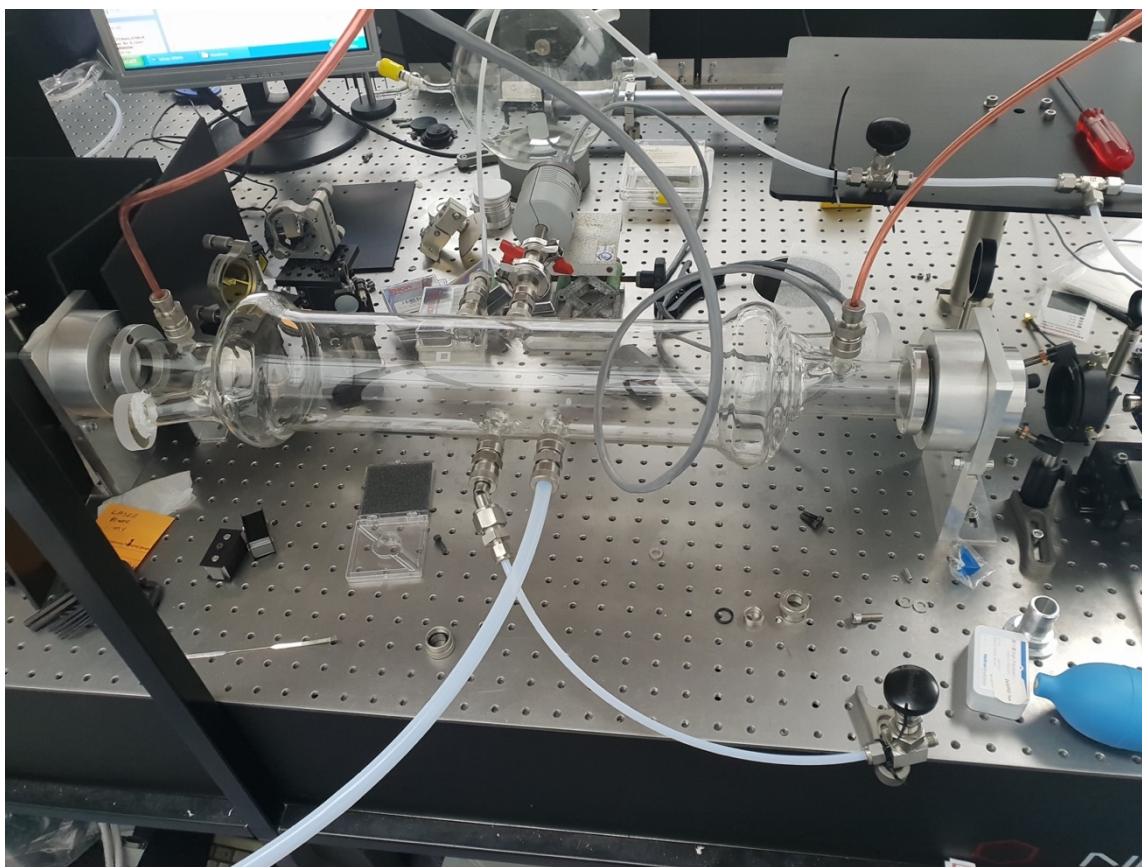
Perhaps most significantly, although Criegee intermediates can be detected using the strong B-X electronic absorption band ($350 \text{ nm} < \lambda < 400 \text{ nm}$), the electronic spectra are broad and relatively unstructured. This means that it is not straight forward to detect and individual intermediate from within a mixture. This would not inherently be of scientific concern if all the Criegee intermediates displayed similar chemistries, however a simple change in conformation for CH_3CHOO leads to changes in reactivity with water of several orders of magnitude. Therefore, it is desirable to produce conformer specific reaction rate coefficients and reaction mechanisms for these intermediates to better understand their impact on Earth's atmosphere. This can be accomplished through the use of mid-IR spectroscopy, which will provide fingerprint spectra of each conformer, and thus can be used to deconvolute their chemistries in experimental mixtures.

6.2. Design and Components

6.2.1 Main Cavity

The main ringdown cavity was formed from a pair of 2-inch high reflectivity mirrors (II-VI Infrared, 99.96% reflectivity, $f = 1 \text{ m}$), positioned facing one another 80.3 cm apart in bespoke mounts. The main sample chamber was a single-piece bespoke glass unit constructed by GPE Scientific, which was supported by the optical cavity mounts. The sample chamber includes ports to allow the monitoring and control of the atmosphere within the chamber, as well as the introduction of chemical species for interrogation. Atmospheric control is achieved using mass flow controllers to adjust the relative amounts of species in the reaction mixture injected into the sample chamber. Through this and a vacuum pump, the pressure within the sample chamber can also be regulated. Input ports are placed immediately after the high-reflectivity mirrors to allow for the injection of nitrogen or other inert gases, generating positive pressure in order to protect the mirror surfaces from chemical attack or deposition. In addition to the ports, there is also an additional input channel off-axis relative to the primary optical cavity to allow for the injection of laser radiation in order to drive

photoreactions within the chamber for study through bond photolysis. Photographs of the spectrometer are shown below in figure 103.



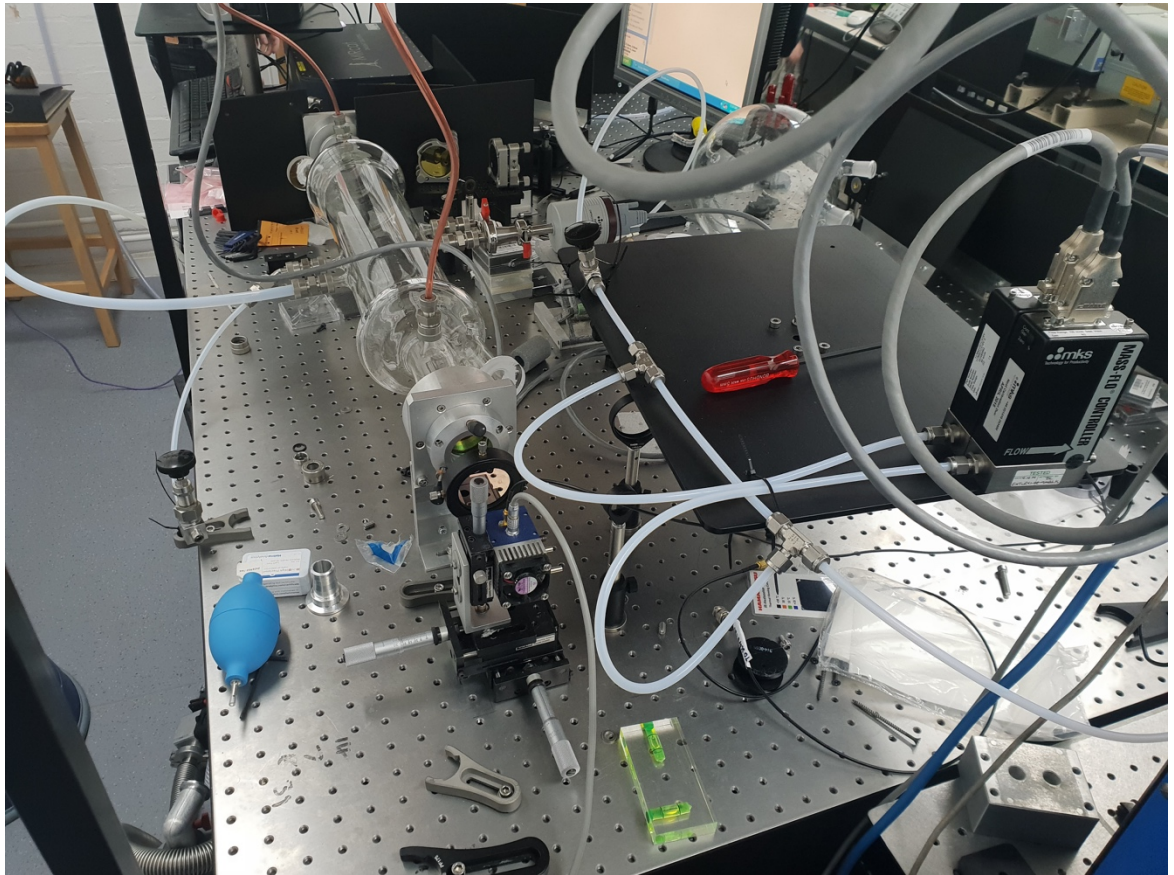


Figure 103 Side-on (top) and end-on (bottom) views of the spectrometer system in development.

Following the main optical cavity, a 2-inch germanium lens (Edmund Optics, $f = 5$ cm) is used to direct transmitted light from the cavity towards the detector system. Two thermoelectrically cooled MCT (Mercury Cadmium Telluride) photovoltaic detector systems are used in order to cover the whole wavelength range employed, both manufactured by VIGO System, one centred on $6 \mu\text{m}$ (model PV-3TE-6) and $8 \mu\text{m}$ (model PV-3TE-8). The PV-3TE-6 model is around an order of magnitude more sensitive than the PV-3TE-8 model and was thus used for alignment of the instrument. The laser source used is a tuneable quantum cascade laser system (Daylight Solutions MIRcat, $5.75 - 6.58 \mu\text{m}$, $7.5 - 8.57 \mu\text{m}$, 300 mW pulsed output, 500 ns pulse). The waveform produced by the detector system is digitised and visualised using a LeCroy Waverunner oscilloscope, which is operated in the externally triggered mode using the laser system as a trigger source. The ionising laser source is a tuneable multi-stage dye laser system, composed of a Continuum Powerlite II driving a Sirah dye laser system. Prior to the main optical cavity, a planned additional cavity is to be placed, discussed more in the

next subsection. An above view schematic of the spectrometer setup is shown below in figure 104.

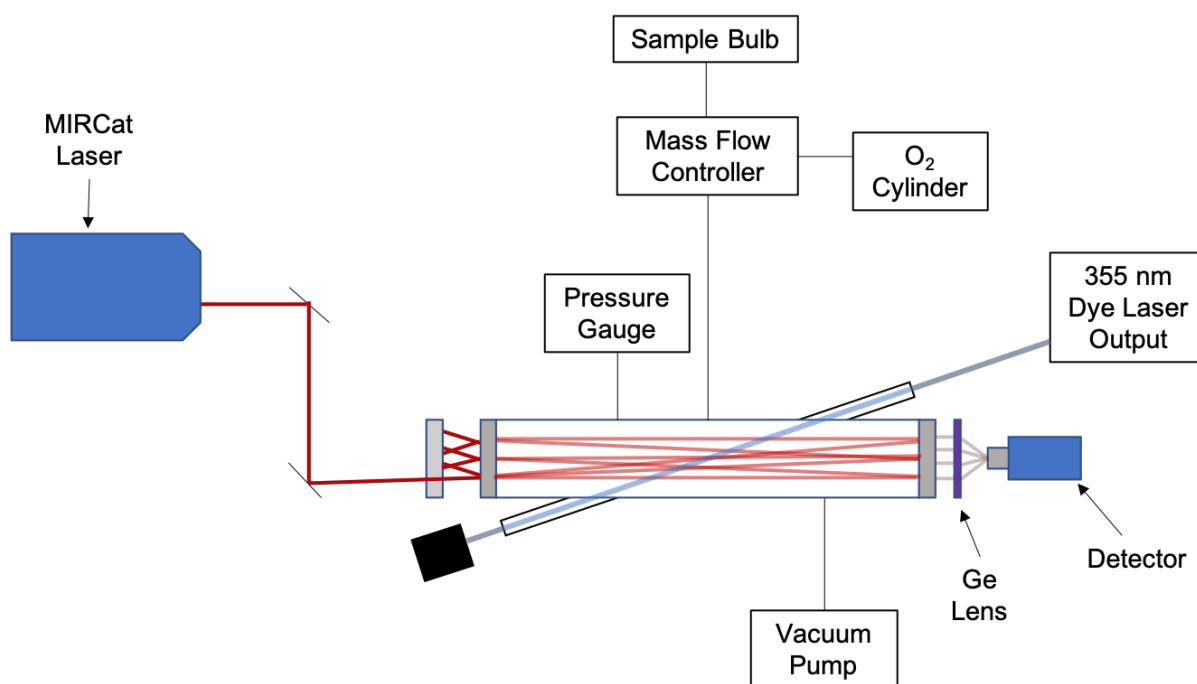


Figure 104 Above view diagram of the cavity ringdown setup in development.

6.2.2 Re-injection Cavity

The design of the mid-IR cavity ringdown spectrometer was based on a design found in the literature using an additional mirror to generate an optical cavity in addition to the main ringdown cavity.¹⁰⁶ This additional cavity was to be implemented in order to enhance the signal-to-noise ratio of the spectrometer by increasing the power transmitted to the main cavity. The high reflectivity of the mirrors used in the main cavity means that the vast majority of the light directed into the cavity is rejected by the cavity, meaning upwards of 99% of the laser input is wasted. By inserting an additional mirror prior to the cavity, in a Herriott cell configuration, this otherwise wasted light from a laser pulse can be reflected back at the main cavity and increase the power injected on each pulse. The mirror used was a 2-inch gold spherical mirror with properties matched as closely to that of the re-injection mirror employed by O’Keefe et al as feasible, featuring a hole ~5 mm drilled approximately ~12 mm from

the centre of the optic, to permit the laser through to the main cavity, and a focal length of 20 cm.¹⁰⁶ The re-injection mirror was mounted 10 cm from the initial cavity mirror, in accordance with the stability region relationship displayed in equation 9, concentric with the principal axis of the cavity.

$$0 \leq \left(1 - \frac{L}{R_{RIM}}\right) \left(1 - \frac{L}{R_F}\right) \leq 1$$

Equation 9 *The stability region of a re-injection cavity. L = mirror separation, R_{RIM} = radius of re-injection mirror, R_F = radius of front cavity mirror.*

6.2.3 Alignment of Cavity

The cavity was designed to have an off-axis injection mode of operation relative to the principal axis of the optical cavity, with the laser input being injected off-centre into the back of the initial mirror. A Herriott cell type arrangement using a 2-inch aluminium mirror with a hole ~5 mm drilled ~12 mm from the centre, matching the focal length of the cavity mirrors, was used to design the input path in combination with a red diode laser matched to the path of the MIRcat laser. This is due to limitations of the method used to detect the path of the MIRcat output, as heat-sensitive cards were used to detect the beam path and these did not function beyond the first cavity mirror due to the massive depletion in transmitted power due to the reflectivity. Photographs of the spot patterns of this setup are shown in figure 105.



Figure 105 Spot patterns traced by the red diode alignment beam on the surfaces of the aluminium alignment mirror (top left), the opposing cavity mirror (top right) in optic mounts from initial optical cavity testing, and on the surface of the secondary cavity mirror mounted in the sample chamber (bottom).

The optical cavity was initially modelled using 2-inch optical mounts sat opposed to one another, allowing for a better view of the spot pattern traced by the diode laser. The spot pattern was optimised through simple adjustment of the input beam using two 1-inch turning mirrors and angular adjustment of the cavity mirrors to create a circular pattern on the face of each mirror, so as to cover as much of the volume of the optical cavity as possible and ensure the containment of the beam to the optical cavity (barring escape through the entry aperture following a complete round-trip). Following this, the MIRcat infrared beam was projected into the cavity along the same initial path as the diode laser and the spot pattern checked using the heat sensitive cards. The aluminium mirror was then replaced with the first cavity optic, whilst maintaining the path set out for the infrared probe laser. The detector for the set-up was mounted on a 3-dimensional translation stage, enabling the adjustment of the position to

optimise the output from the cavity collected by the post-cavity lens. Through fine adjustment of the cavity components, a signal was obtainable at a wavelength of 5.8 microns. The signal was relatively weak and consequently distorted by detector noise and artefacts. In an effort to improve upon the signal magnitude, the re-injection mirror was inserted 10 cm prior to the principal cavity mirror, in line with the optical cavity, and the infrared beam directed through the input hole. The re-injection optic provided several additional reflections of the main infrared pulse into the optical cavity, increasing the magnitude of the detectable signal by ~5.5 times, shown in figure 106.

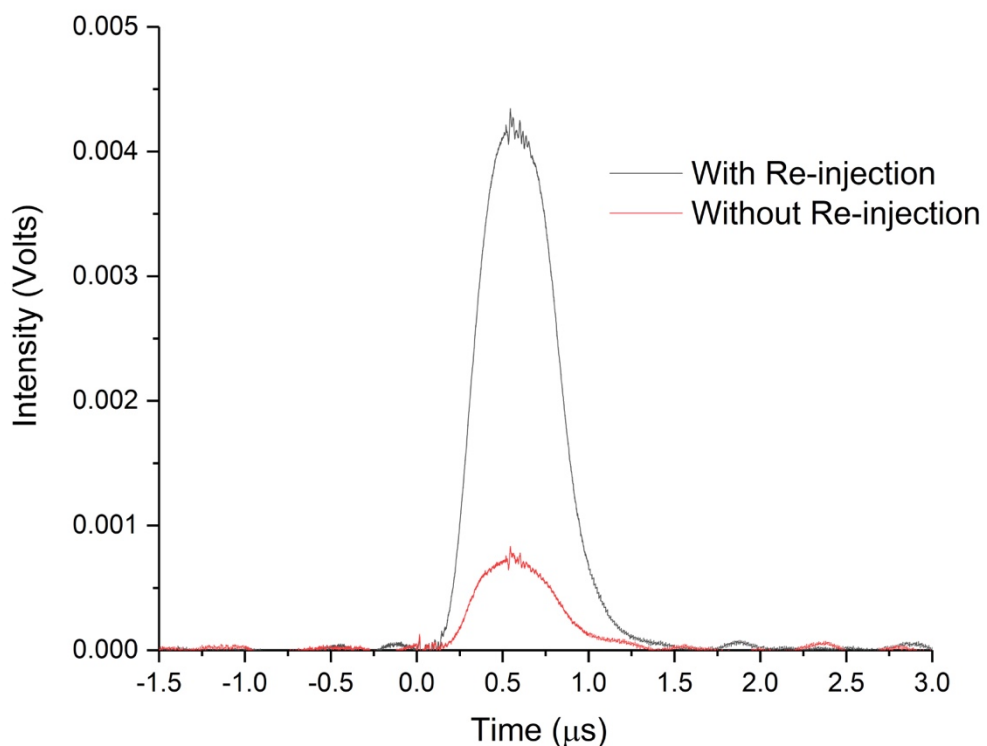


Figure 106 Comparison of the signal obtained through the optical cavity with and without the re-injection mirror in position.

Although the signal intensity was greatly increased, the degree of discernible ringdown character was not noticeably improved and did not function at a useable level. Attempts to reproduce these results in the sample chamber cavity were unsuccessful. Given the success in producing a Herriott cell-type arrangement using the diode laser in the main cavity, it would be feasible to create a cavity enhanced absorption

application using such an arrangement with the infrared pulsed beam. This would require the addition of an optical window prior to the principal cavity mirror to seal the chamber due to the hole in the optic used, but should provide a far greater usable signal intensity, the absolute absorption of which could be monitored in the presence of a sample. Given the multi-pass nature of this arrangement, the path lengths observed should still provide good sensitivity, which can be improved upon through the adjustment of the input beam, or the use of a different mirror, to produce denser spot patterns, and thus more passes per pulse.

6.3 Conclusion and Future Work

Initial development of a re-injection enhanced cavity ringdown spectrometer was undertaken for the purpose of investigating the chemistry of atmospherically significant intermediates, called Criegee intermediates. A Herriott cell configuration was used to assist in the alignment of the cavity and although a signal could be detected through the optical cavity, no ringdown characteristics could be observed. The re-injection mirror system was shown to be functional, enhancing the detectable power injected into the cavity per pulse by approximately 5.5 times. For future work, it is recommended that the cavity be converted into a Herriott cell configuration and operated as a cavity enhanced absorption spectrometer. This configuration would retain some of the sensitivity enhancements provided by a multi-pass system and allow for a significant increase in signal strength due to the direct injection of the full laser pulse into the cavity. Additional solutions would be to use less reflective cavity mirrors, as this would potentially reduce the amount of light rejected by the cavity, allowing for more power to be injected into the system, whilst also increasing the rate of decay through the corresponding increased amount of light lost per pass. These factors would result in a greater observed signal strength whilst still retaining a higher sensitivity than that of a Herriott cell configuration.

Summary and Perspective

In this chapter, an overview of the key aspects and results of the thesis will be given.

Iridium (III) Complexes

Much of this thesis has focussed on the influence of ligand substitution on the spectroscopic properties of a variety of iridium (III) complexes built upon variations of quinoxaline ligand structures. The primary experimental methodology used for this purpose was transient absorption spectroscopy and kinetic analysis, allowing the examination of the excited state features of these complexes in contrast to the ground state. Computational techniques, principally density functional theory, were employed alongside this experimental treatment in order to deepen the understanding of the electronic processes behind the spectroscopic results. The primary interest of this analysis was to determine the effect of ligand substitution on the band positions of ligand spectroscopic profiles, particularly the emission feature, and develop a methodology for doing so reliably.

Chapter three details the initial effort to analyse a set of seven complexes based around a ligand structure of two quinoxaline moieties and a bipyridine moiety, with the simplest complex forming the basis of the set. The remaining six complexes can be divided into two sets depending on whether they feature phenyl ring substitution in place of a methyl group on the quinoxaline moieties or not, and otherwise feature methyl, fluorine or chlorine substitution. Transient absorption and emission spectroscopy showed that all complexes featured similar profiles with feature positions shifting in a way that was readily relatable to the substitutions made to the quinoxaline ligands. Methyl substitution was shown to induce a hypsochromic shift in the emission band position, whilst halogenation induces a bathochromic shift.

Phenylated versions of complexes feature a slight bathochromic shift in their emission in comparison to their non-phenylated counterparts. Computational analysis gave a good approximation of the absorption and emission properties of each complex, and most importantly was able to correctly predict the degree of band-shifting in the emission profiles of each complex. DFT analysis was also useful in giving insight into

the electronic structure of the complexes, allowing for the assignment of charge transfer properties involved in the transitions of the absorption spectra through molecular orbital decomposition analysis. It was found that the division of contributions to the HOMO of each complex was approximately equal between the metal centre and the two quinoxaline moieties, each contributing a third of the total. In contrast, the LUMO was primarily centred on the quinoxalines, suggesting that the absorption processes of the complexes are MLCT in nature. This was confirmed using TD-DFT analysis of the singlet to singlet absorption transitions in conjunction with the decomposition analysis results.

Chapter four built on the work established in chapter three, applying the methodology to a variety of novel iridium complexes. Among these were two new sets of quinoxaline-based complexes, with identical cyclometallating ligands to those discussed in chapter three, but with variation introduced to the ancillary ligand. A complete set of seven picolinate analogues to the bipyridine complexes of chapter three were evaluated, and three were produced featuring pyrazinate ancillary ligands. This enabled a comparative study to be performed between complexes to evaluate the effect the ancillary ligand plays in the spectroscopic profile, which previous orbital decomposition analysis suggested should be minor. What was discovered was that the ancillary ligand made a significant difference to the properties of the complex, with a far greater impact on the emission band position. This was theorised to be due to variations in stabilisation of the complex frontier orbitals that the different ligands exerted, resulting in a 'broad' or 'coarse' emission tuning effect, in contrast to the quinoxaline ligands 'fine' tuning. The picolinate and pyrazinate complexes retained their emission band position ordering relative to the other complexes within their respective sets, suggesting that the fine-tuning effects of the quinoxaline ligand alterations still have a similar effect here as in the bipyridine complexes. The results of this chapter's work are promising, as they contain the beginnings of a more extensive rational design methodology. The capacity of DFT to accurately relate complexes to one another allows for a more informed selection process when postulating new ligand designs, allowing for a more targeted approach when synthesising complexes for their spectroscopic properties.

Two other ligand variations were also investigated in this chapter, including more extensive alterations to the quinoxaline-based ligand structures seen previously. Four bidentate complexes utilising benzoquinoxaline cyclometallating ligands and a bipyridine ancillary ligand were evaluated using DFT alone, in order to obtain a deeper understanding of the electronic basis for their emission spectra, which featured a significant bathochromic shift in comparison with those discussed prior. DFT analysis confirmed that the spin-forbidden emission of the complexes lay in the mid-infrared, with extended conjugation of the quinoxaline-based ligands assigned as the cause.

Finally, a pair of tridentate complexes were also analysed using the joint spectroscopic and DFT methods, utilising ligand structures based on a pair of quinoxaline moieties joined by a pyridine group. One of the complexes featured additional methyl group substitution on terminal positions of the quinoxaline moieties but was otherwise identical to the other. Due to the extended ligand structure and absence of ancillary ligand, a more granular decomposition analysis procedure was applied, with the ligand moieties broken down into more sections. This analysis showed that there was an increase in intraligand charge transfer between the frontier orbitals of these species, which is to be expected given the larger ligand backbone. A similarly granular approach could be applied in future to complexes such as those discussed previously, with the aim of deducing the finer effects of substitution on the ligand structure, as opposed to the broader categorisation used in this thesis.

In future, the use of the DFT methodology outlined in this thesis would ideally be used to predict the properties of a yet to be synthesised set of complexes. This would serve as confirmation of the validity of this approach and a significant milestone in the development of a rational design framework. With regards to the development of new complexes, exploration of differing substituents on the spectroscopic band positions would be desirable. The employment of a more significantly electron withdrawing ancillary ligand would be a useful test to validate the analysis carried out in chapter four with regards to the stabilisation of the HOMO and carries a prediction of a more hypsochromically shifted emission band.

All of the analysis within chapters 3 and 4, with the exception of the tridentate species, has formed the basis of published works.^{107–109}

Triphenyltetrazolium Compounds

Chapter 5 of this thesis focussed on a different chemical system with a separate aim, but nonetheless used a thematically similar analytical approach as that utilised in the study of the iridium complexes, with the same apparatus and methodology used for both. The chemical system targeted was 2,3,5-triphenyltetrazolium (TTP), a light-sensitive organic compound, and the aim was to determine whether the light-induced reduction mechanism of this species could be inhibited through site-selective substitution, preventing the conversion to a corresponding triphenylformazan (TPF) and photocoupled product (PCP). The suggested mechanism of the photoreduction involves the formation of an intermediate species with a bond formed between two of the compound's phenyl ring groups, at the ortho position of each. In order to inhibit this bond formation, 3 variants of the parent triphenyltetrazolium compound were synthesised by the Fallis group at Cardiff University with substitutions made at relevant positions on the phenyl rings. The three variants included versions with a fluorine substitution at the 2 and 6 positions of one of the phenyl rings, a 3 and 5 position fluorine substitution and a 2 and 6 position methyl substitution, although this last variant also included additional substitutions on the other two phenyl rings. The aim of this study was to determine to what extent these substitutions would inhibit the photoreduction, and to carry out this assessment a flash photolysis study was performed. As stated above, flash photolysis differs from transient absorption only in the effect on the sample had by the measurement process, in that flash photolysis causes degradation in the starting sample through photonically induced bond fission. It was found that through analysis of the flash photolysis and emission spectra at different time delays, the degree of inhibition of the reaction can be determined for the different compound variants. This process was complicated by the fact that the sample composition was altered by the act of measurement, so a flow system was

employed to continually refresh the sample, facilitating the assignment of features visible in the flash photolysis spectrum. The use of this flow system to distinguish the spectral features present proved effective, as the features removed were able to be more confidently assigned to the permanent photoproducts, whilst those that remained are assigned to intermediates within the reaction.

Through this flash photolysis analysis, it was shown that fluorine substitution in the 3 and 5 positions of the relevant phenyl group was ineffective at inhibiting the photoreduction reaction, with sample degradation proceeding at a similar rate to the parent compound. Meanwhile, substitution in the 2 and 6 positions of the phenyl ring with both fluorine and a methyl group proved effective at reducing the rate of degradation, with flash photolysis features assigned to the reaction intermediates being undetectable in the case of both variants. Further exposure to photoexcitation revealed that the 2,6 diMe TTP variant emission spectrum showed progressive alteration as a function of exposure, suggesting that the inhibition of the reaction wasn't complete, but partial. A mass spectrometry study confirmed that the 2,6 diF TTP also underwent some degree of photoreduction, but at a much lower rate than the parent TTP compound. In addition, it was noted that protracted laser exposure of the TTP parent compound under atmospheric conditions gave rise to a species matching the mass number of a PCP molecule plus an additional oxygen atom, a species that was not present following a similar degree of exposure under a nitrogen atmosphere. To confirm the assignment of this species a more involved study would need to be carried out, involving techniques such as NMR spectroscopy and an isotopic oxygen exposure study, however not performed here due to time constraints.

With regards to future work, exploration of the effect additional substituents have on the rate of photoreduction would be advisable, as the application of the above techniques would allow for an assessment of the effects of different groups. The attachment of a greater sterically hindering group, such as tert-butyl, to the 2,6 and 3,5 positions of the N-phenyl rings would allow for an assessment of steric versus electron withdrawing effects on the reaction inhibition, for instance. As mentioned within chapter five, the progression of spectroscopic features was noted to be

considerably slower in comparison with prior literature, and a study involving the alteration of the solvent environment would hopefully shed light on the cause. Similarly, adjustment of the pairing anion for the tetrazolium moiety would also be desirable, as this likely also plays a role in the rate of reaction due to its effects on the immediate solvation shell.

Development of a Cavity Ringdown Infrared Spectrometer

The development of a multipass spectrometer is discussed in chapter 6, with the ultimate aim of producing a spectrometer system fit for use when studying trace atmospheric intermediates in the ozonolysis of simple alkenes, such as isoprene. The target system is a species of compounds known as Criegee intermediates (CIs), which are generally present in very small concentrations in the atmosphere and when synthesised under laboratory conditions, such that conventional absorption spectrometers are insufficient when trying to detect them empirically. To this end, development of a multipass absorption spectrometer was undertaken, as this class of instrument provides far greater sensitivity over conventional absorption spectrometers, achieved through vastly longer path lengths of the interrogation beam. The design principle of the spectrometer in this case consists of two highly reflective (~99.97%) mirrors set facing each other along the same principal axis, with a collecting lens and detector positioned behind one of the mirrors. On the opposing side of the mirror set-up, a mid-infrared laser system is positioned. The high reflectivity mirrors form an optical cavity, such that when the mid-IR laser beam is injected into the back of one of the mirrors, the small percentage of light that isn't rejected will enter the cavity and be repeatedly reflected between the two mirrors, transmitting a small percentage of light through each mirror on each successive reflection. It is this 'leakage' of light that the detector system will be used to monitor, as the time taken for the injected laser light within the cavity to decrease to zero intensity (the 'ringdown time') through this leakage process can be compared for an empty cavity and one containing the chemical system one wishes to study and used to obtain an absorption spectrum. The repetitive exposure to the sample volume the interrogation pulse experiences during this process gives the technique its high sensitivity when

compared to conventional spectrometers, which normally have path lengths of around a centimetre. An additional component was incorporated into the design in the form of an additional mirror prior to the optical cavity, with an opening to allow the laser input through. This additional mirror aims to reinject any light rejected by the cavity, increasing the potential power transmitted to the optical cavity per pulse.

Development of the infrared spectrometer was only partially successful, with some signal intensity observed through the cavity, but with no observable ringdown decay character. The application of the reinjection mirror was a success, with notable improvements on the signal strength following its introduction. Steps that could be taken to improve the system include the use of less reflective mirrors, as this can improve the signal transmission whilst still retaining an extended path length sufficient to detect trace species. In addition, a change to the design to that of a Herriot cell could prove beneficial, as this would involve direct injection through an opening in one of the main cavity mirrors, rather than depending on a small amount of the laser radiation entering the cavity through the mirror itself. A downside to this design would be a significantly lower path length, among other issues such as sensitivity to laser power fluctuations, but the path lengths achievable with Herriot cells are still considerably more than those of conventional, single pass spectrometers.

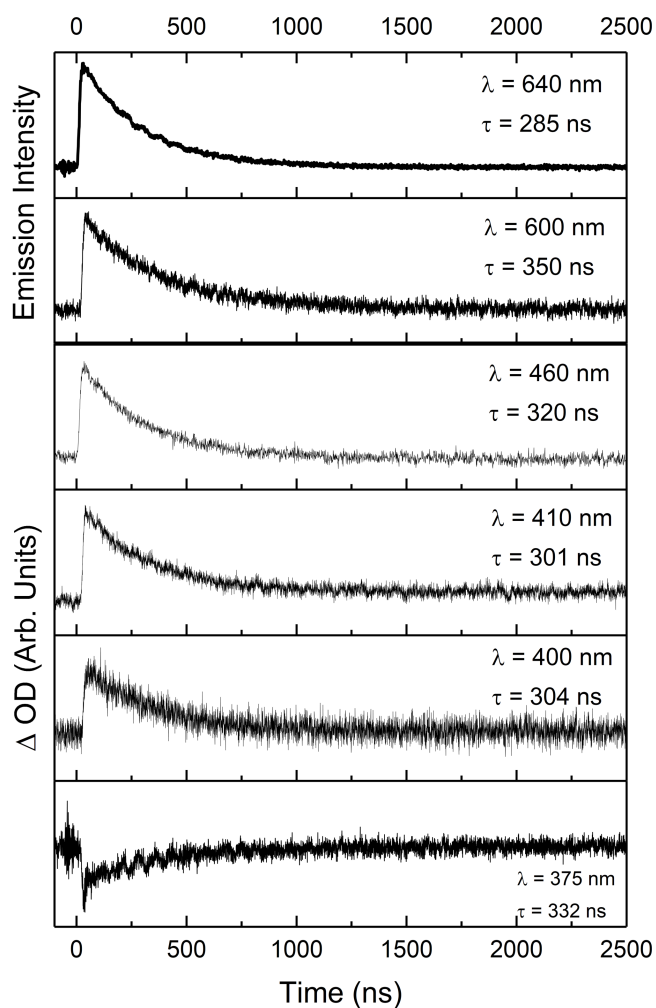
Appendices

Effect of Ligand Structure on the Spectroscopic Properties of Iridium (III) Complexes

Complexes

Picolinate Complexes

$Ir(L2)_2(pico)$



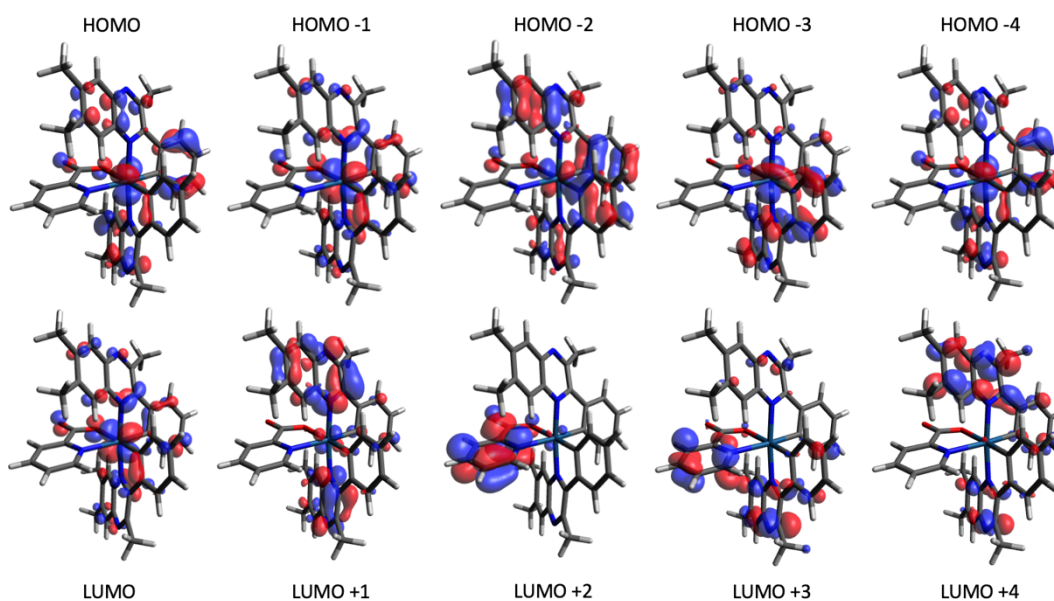
Kinetic traces of $Ir(L2)_2(pico)$ at major feature wavelengths, obtained with a PMT detector. Top 2 traces are emission, whilst the bottom 4 are ΔOD . All traces were fitted to mono-exponential functions and the lifetimes determined are reported next to each trace.

Orbital	Ir (5d)	Picolinate	L1	L2
LUMO +4	1	1	72	26
LUMO +3	1	37	12	50
LUMO +2	2	96	2	0
LUMO +1	4	1	60	34
LUMO	4	2	34	60
HOMO	39	4	29	27
HOMO -1	37	11	28	24
HOMO -2	12	7	49	32
HOMO -3	28	4	18	49
HOMO -4	21	7	43	29

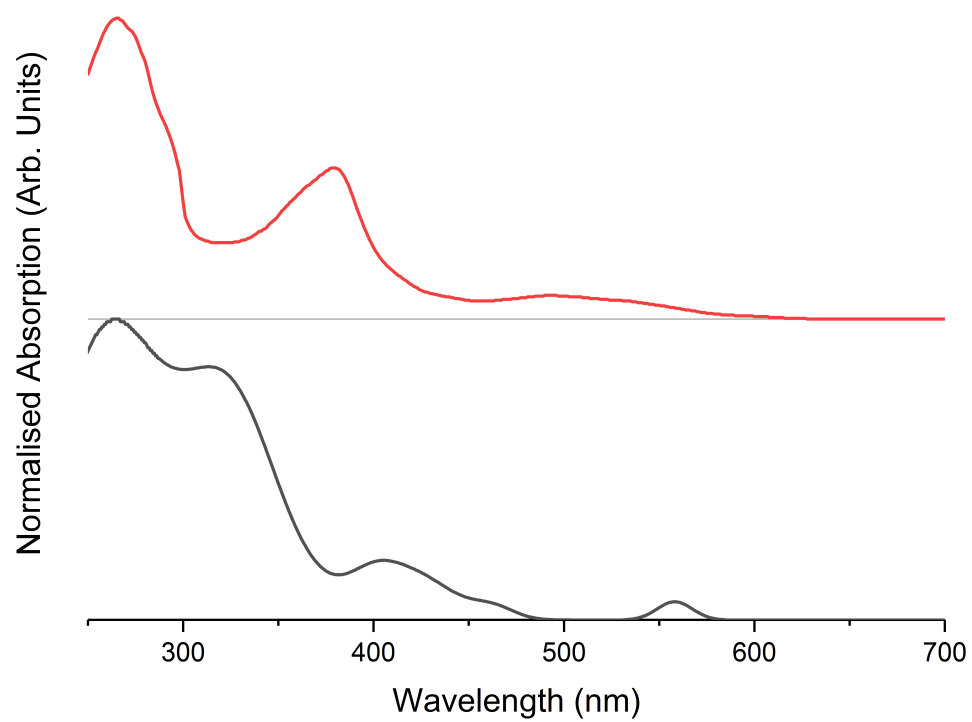
Table of percentage contributions to each MO from each part of the Ir(L2)₂(pico) complex, L1 and L2 are the quinoxalines

Excited State	Contributing Transitions
1 (419.34 nm, f = 0.0504)	HOMO → LUMO (85.27%)
2 (411.06 nm, f = 0.1529)	HOMO → LUMO +1 (82.55%)
3 (340.5 nm, f = 0.0887)	HOMO -2 → LUMO (57.02%) HOMO -1 → LUMO (22.52%)
4 (327.66 nm, f = 0.0527)	HOMO -2 → LUMO +1 (31.72%) HOMO -1 → LUMO +1 (33.53%)
5 (323.41 nm, f = 0.3255)	HOMO -2 → LUMO +1 (18.87%) HOMO -1 → LUMO (16.18%) HOMO -1 → LUMO +1 (19%)

First five singlet transitions of the Ir(L2)₂(pico) complex and a breakdown of their corresponding formative transitions.

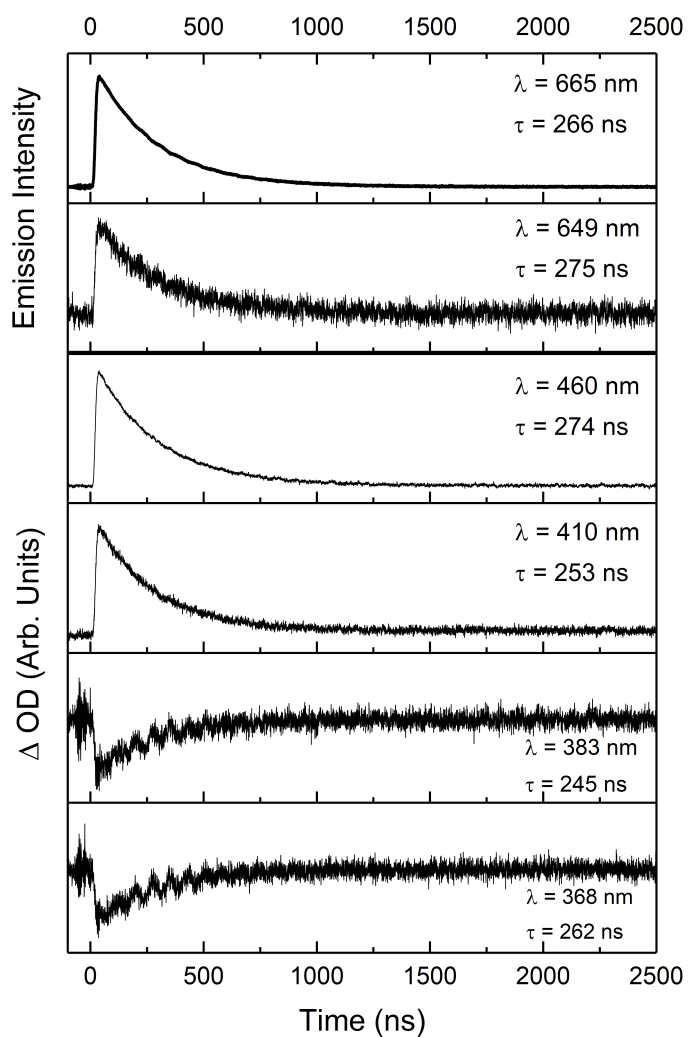


Renderings of the frontier MOs of the Ir(L2)₂(pico) complex.



Comparison of the experimental (red) and simulated (black) absorption spectra for $\text{Ir}(\text{L2})_2(\text{pico})$. The simulated spectrum is comprised of singlet and triplet transitions from the singlet ground state.

Ir(L3)₂(pico)



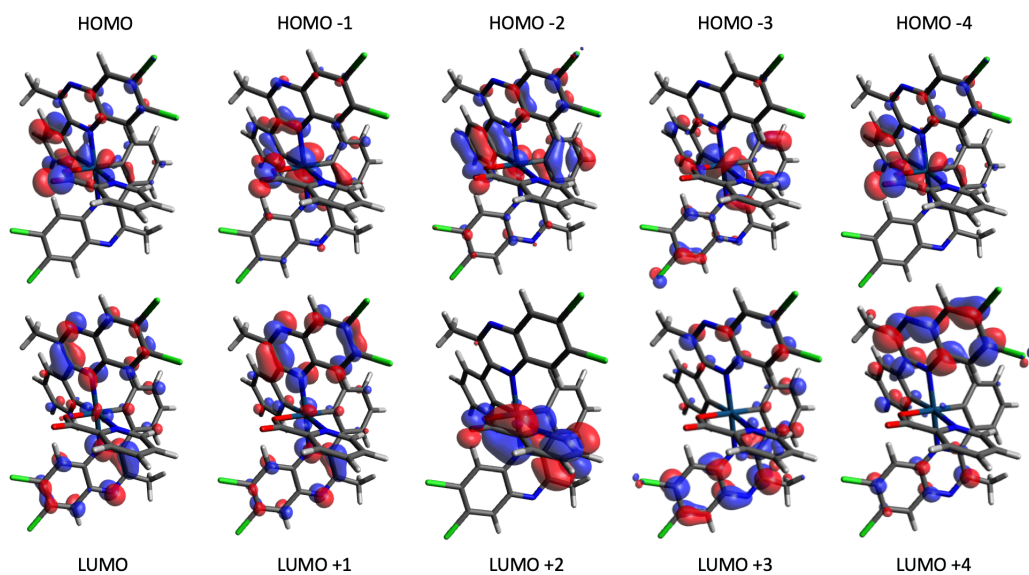
Kinetic traces of *Ir(L3)₂(pico)* at major feature wavelengths, obtained with a PMT detector. The top 2 traces are emission, whilst the bottom 4 are Δ OD. All traces were fitted to mono-exponential functions and the lifetimes determined are reported next to each trace.

Orbital	Ir (5d)	Picolinate	L1	L2
LUMO +4	1	1	75	22
LUMO +3	1	7	20	72
LUMO +2	2	94	3	1
LUMO +1	4	1	55	40
LUMO	4	1	40	55
HOMO	39	4	29	28
HOMO -1	41	14	25	20
HOMO -2	10	10	48	33
HOMO -3	26	4	20	50
HOMO -4	17	25	48	11

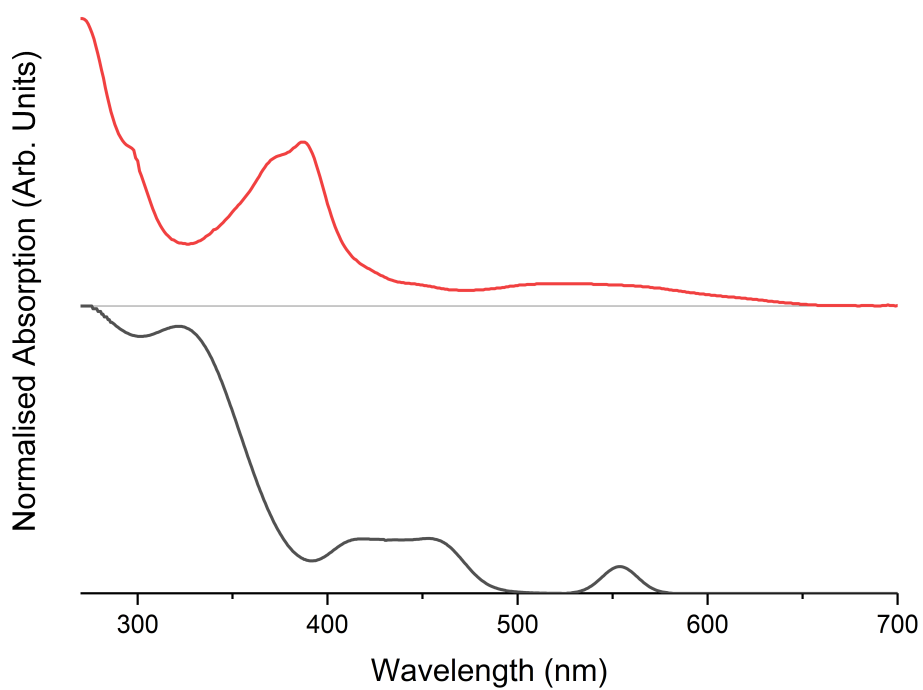
Table of contributions to each MO from each part of the Ir(L3)₂(pico) complex, L1 and L2 are the quinoxalines.

Excited State	Contributing Transitions
1 (439.97 nm, f = 0.0392)	HOMO → LUMO (87.01%)
2 (431.02 nm, f = 0.1577)	HOMO → LUMO +1 (84.08%)
3 (351.22 nm, f = 0.08)	HOMO -2 → LUMO (43.83%) HOMO -1 → LUMO (35.23%)
4 (337.03 nm, f = 0.0784)	HOMO -2 → LUMO +1 (18%) HOMO -1 → LUMO +1 (51.28%)
5 (330.3 nm, f = 0.2889)	HOMO -3 → LUMO (13.46%) HOMO -2 → LUMO (14.55%) HOMO -2 → LUMO +1 (25.73%) HOMO -1 → LUMO (10.65%)

First five singlet transitions of the Ir(L3)₂(pico) complex and a breakdown of their corresponding formative transitions.

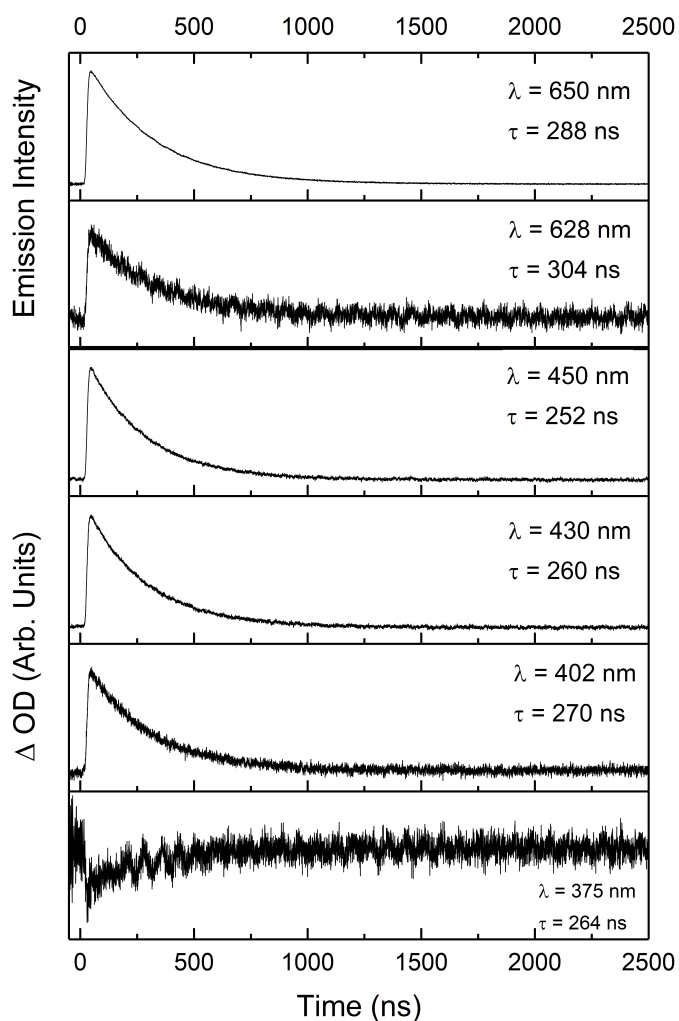


Renderings of the frontier MOs of the Ir(L3)₂(pico) complex.



Comparison of the experimental (red) and simulated (black) absorption spectra for Ir(L3)₂(pico). The simulated spectrum is comprised of singlet and triplet transitions from the singlet ground state.

Ir(L4)₂(pico)



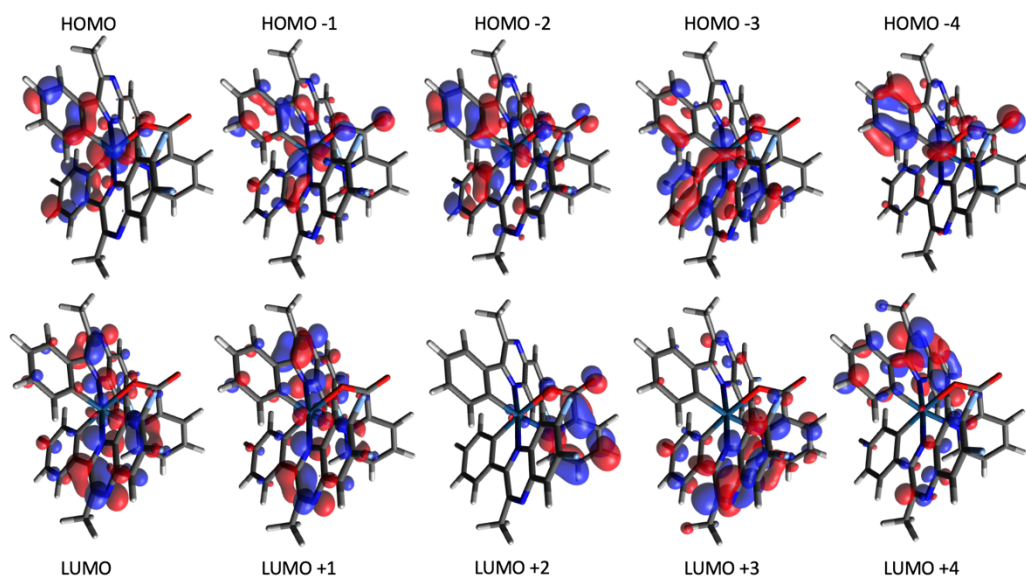
Kinetic traces of *Ir(L4)₂(pico)* at major feature wavelengths, obtained with a PMT detector. Top 2 traces are emission, whilst the bottom 4 are ΔOD . All traces were fitted to mono-exponential functions and the lifetimes determined are reported next to each trace.

Orbital	Ir (5d)	Picolinate	L1	L2
LUMO +4	1	1	79	19
LUMO +3	1	16	15	68
LUMO +2	2	96	2	0
LUMO +1	4	1	56	39
LUMO	4	1	39	56
HOMO	39	4	29	28
HOMO -1	40	13	27	20
HOMO -2	13	9	46	13
HOMO -3	23	4	22	51
HOMO -4	24	18	46	13

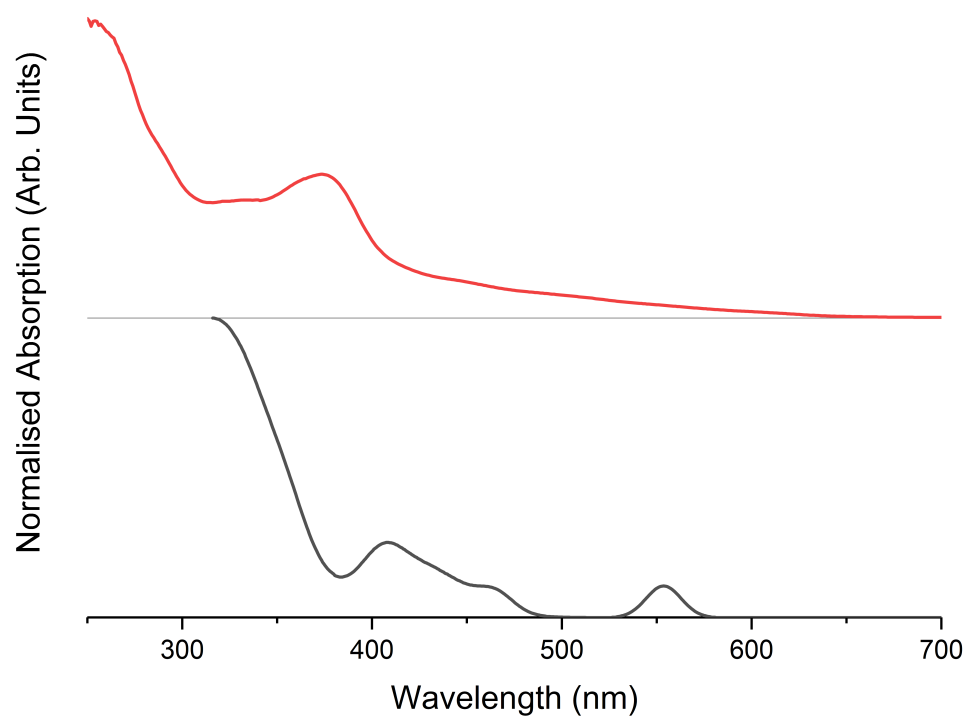
Table of contributions to each MO from each part of the Ir(L4)₂(pico) complex, L1 and L2 are the quinoxalines.

Excited State	Contributing Transitions
1 (428.5 nm, f = 0.0373)	HOMO → LUMO (86.11%)
2 (420.47 nm, f = 0.1344)	HOMO → LUMO +1 (83.26%)
3 (342.9 nm, f = 0.0827)	HOMO -2 → LUMO (53.96%) HOMO -1 → LUMO (25.45%)
4 (330.2 nm, f = 0.0823)	HOMO -2 → LUMO +1 (23.91%) HOMO -1 → LUMO +1 (45.01%)
5 (325.06 nm, f = 0.2908)	HOMO -3 → LUMO +1 (10.93%) HOMO -2 → LUMO (12.36%) HOMO -2 → LUMO +1 (23.28%) HOMO -1 → LUMO (18.4%)

First five singlet transitions of the Ir(L4)₂(pico) complex and a breakdown of their corresponding formative transitions.

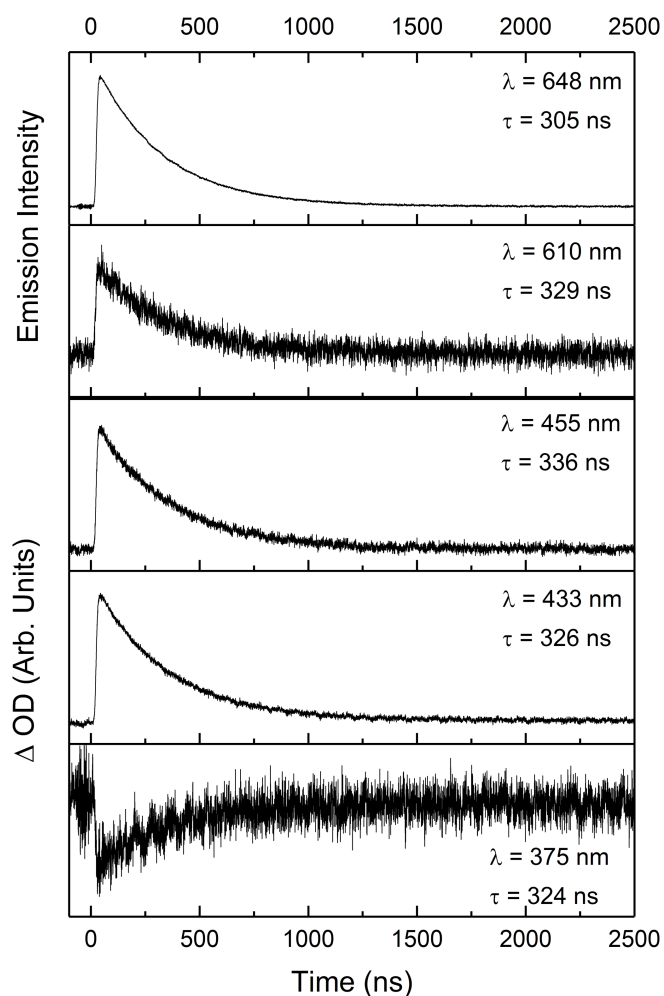


Rendered frontier MOs of the Ir(L4)₂(pico) complex



Comparison of the experimental (red) and simulated (black) absorption spectra for Ir(L4)₂(pico). The simulated spectrum is comprised of singlet and triplet transitions from the singlet ground state.

Ir(L5)₂(pico)



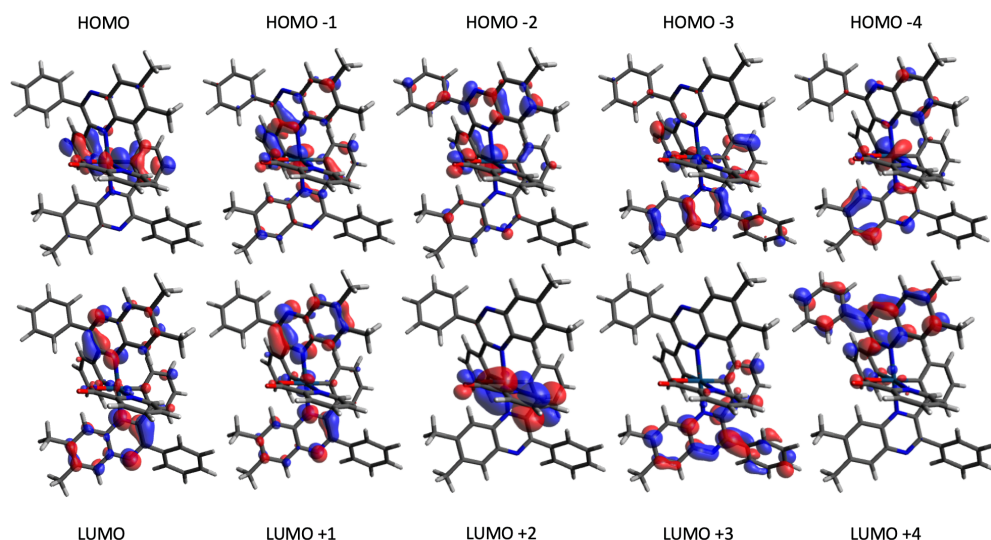
Kinetic traces of *Ir(L5)₂(pico)* at major feature wavelengths, obtained with a PMT detector. The top 2 traces are emission, whilst the bottom 3 are ΔOD . All traces were fitted to mono-exponential functions and the lifetimes determined are reported next to each trace.

Orbital	Ir (5d)	Picolinate	L1	L2
LUMO +4	1	2	92	4
LUMO +3	1	5	4	91
LUMO +2	2	94	3	1
LUMO +1	4	1	57	38
LUMO	4	1	38	57
HOMO	38	4	30	28
HOMO -1	21	5	46	29
HOMO -2	25	10	43	21
HOMO -3	5	2	30	63
HOMO -4	37	4	23	36

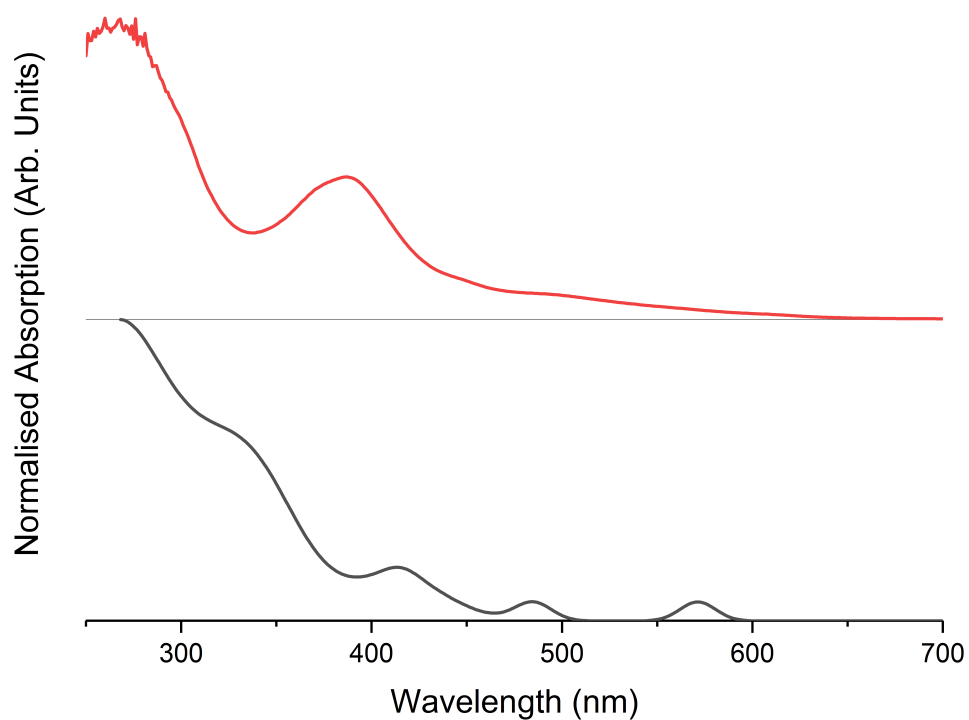
Table of contributions to each MO from each part of the Ir(L5)₂(pico) complex, L1 and L2 are the quinoxalines

Excited State	Contributing Transitions
1 (424.82 nm, f = 0.0334)	HOMO → LUMO (87.75%)
2 (411.7 nm, f = 0.1952)	HOMO → LUMO +1 (82.18%)
3 (346.14 nm, f = 0.996)	HOMO -3 → LUMO (20.66%) HOMO -2 → LUMO (49.1%)
4 (336.8 nm, f = 0.2223)	HOMO -3 → LUMO (14.68%) HOMO -2 → LUMO (12.45%) HOMO -1 → LUMO (11.42%) HOMO -1 → LUMO +1 (37.9%)
5 (334.84 nm, f = 0.3983)	HOMO -3 → LUMO (24.62%) HOMO -3 → LUMO +1 (13.09%) HOMO -2 → LUMO +1 (10.62%) HOMO -1 → LUMO (31.09%)

First five singlet transitions of the Ir(L5)₂(pico) complex and a breakdown of their corresponding formative transitions.

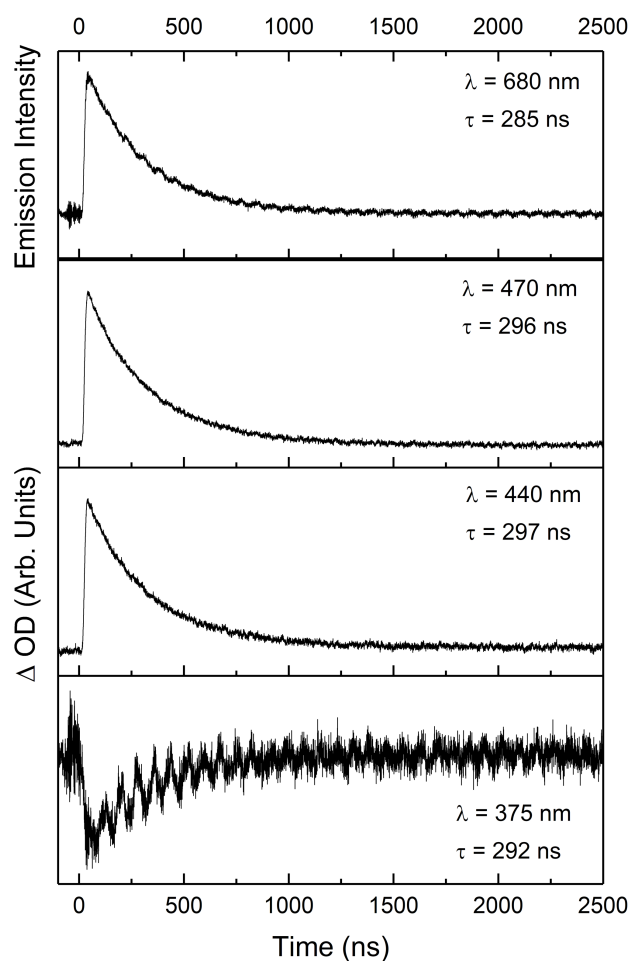


Renderings of the frontier orbitals of Ir(L5)₂(pico)



Comparison of the experimental (red) and simulated (black) absorption spectra for Ir(L5)₂(pico). The simulated spectrum is comprised of singlet and triplet transitions from the singlet ground state.

Ir(L6)₂(pico)



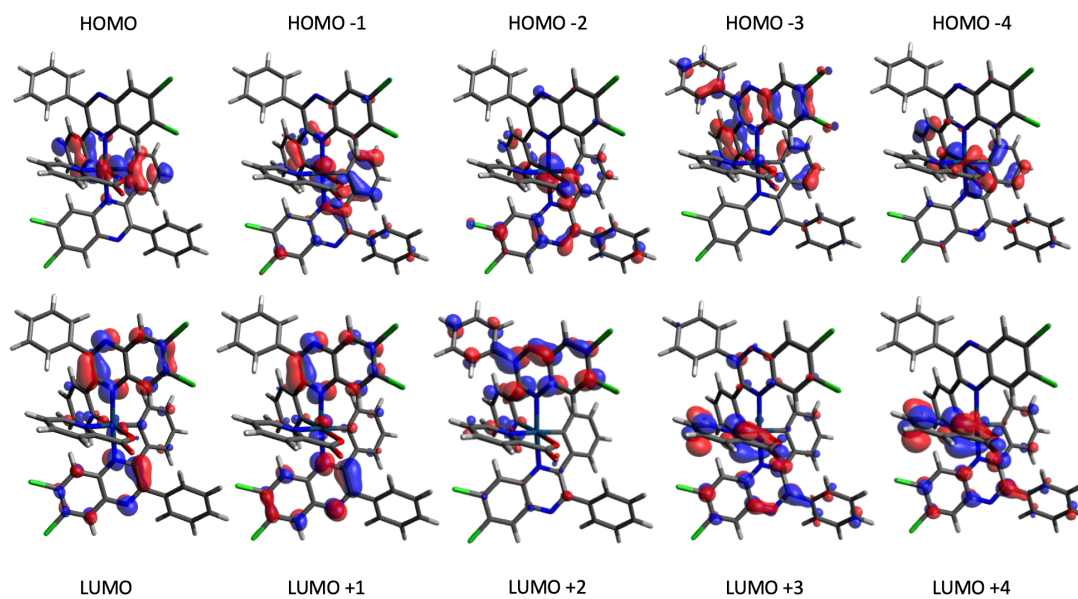
Kinetic traces of *Ir(L6)₂(pico)* at major feature wavelengths, obtained with a PMT detector. The top trace is emission, whilst the bottom 3 are ΔOD . All traces were fitted to mono-exponential functions and the lifetimes determined are reported next to each trace.

Orbital	Ir (5d)	Picolinate	L1	L2
LUMO +4	2	55	42	1
LUMO +3	1	37	45	16
LUMO +2	1	6	12	81
LUMO +1	4	1	53	42
LUMO	4	1	42	53
HOMO	38	4	30	28
HOMO -1	21	5	49	25
HOMO -2	25	13	43	19
HOMO -3	5	2	27	66
HOMO -4	31	12	31	26

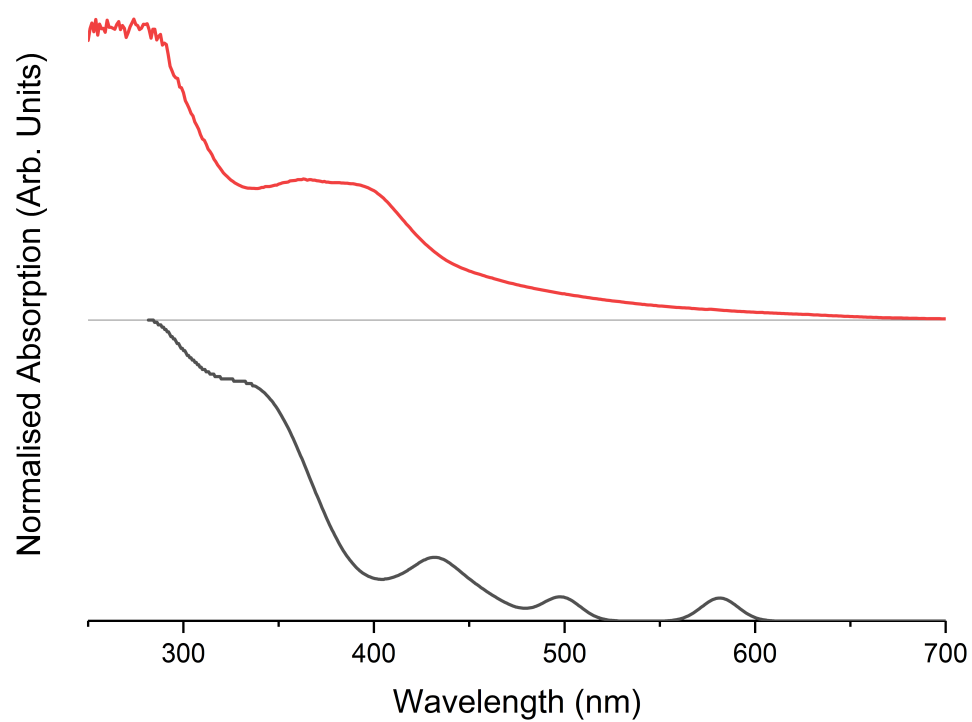
Table of contributions to each MO from each part of the Ir(L6)₂(pico) complex, L1 and L2 are the quinoxalines.

Excited State	Contributing Transitions
1 (445.39 nm, f = 0.0273)	HOMO → LUMO (88.66%)
2 (430.72 nm, f = 0.1950)	HOMO → LUMO +1 (83.14%)
3 (356.62 nm, f = 0.1279)	HOMO -3 → LUMO (46.6%) HOMO -1 → LUMO (24.7%)
4 (347.51 nm, f = 0.2361)	HOMO -2 → LUMO (30.68%) HOMO -1 → LUMO (10.98%) HOMO -1 → LUMO +1 (44.13%)
5 (342.51 nm, f = 0.4185)	HOMO -3 → LUMO (23.94%) HOMO -2 → LUMO (10.17%) HOMO -2 → LUMO +1 (25.63%) HOMO -1 → LUMO (20.47%)

First five singlet transitions of the Ir(L6)₂(pico) complex and a breakdown of their corresponding formative transitions.

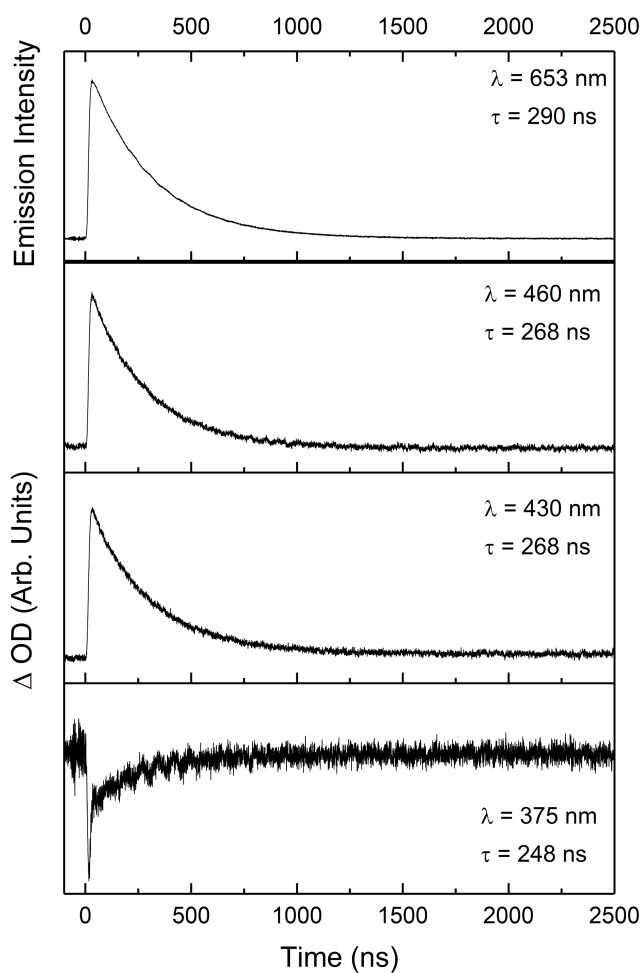


Renderings of the frontier MOs of the Ir(L6)₂(pico) complex.



Comparison of the experimental (red) and simulated (black) absorption spectra for Ir(L6)₂(pico). The simulated spectrum is comprised of singlet and triplet transitions from the singlet ground state.

Ir(L7)₂(pico)



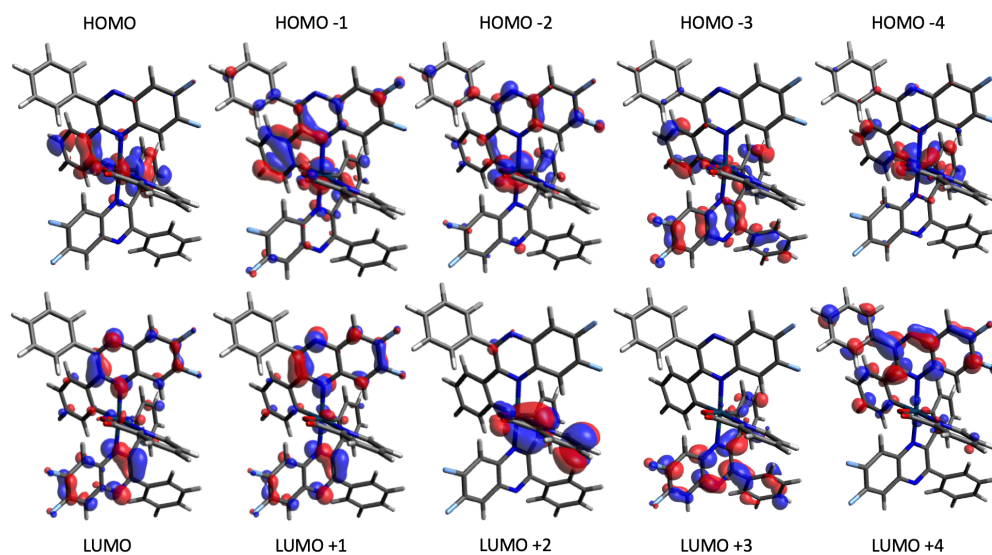
Kinetic traces of *Ir(L7)₂(pico)* at major feature wavelengths, obtained with a PMT detector. The top traces is emission, whilst the bottom 3 are ΔOD . All traces were fitted to mono-exponential functions and the lifetimes determined are reported next to each trace.

Orbital	Ir (5d)	Picolinate	L1	L2
LUMO +4	2	6	89	3
LUMO +3	1	4	2	93
LUMO +2	2	90	8	1
LUMO +1	4	1	54	41
LUMO	4	1	41	54
HOMO	38	4	30	28
HOMO -1	16	4	54	26
HOMO -2	32	14	36	18
HOMO -3	5	2	28	65
HOMO -4	34	10	30	26

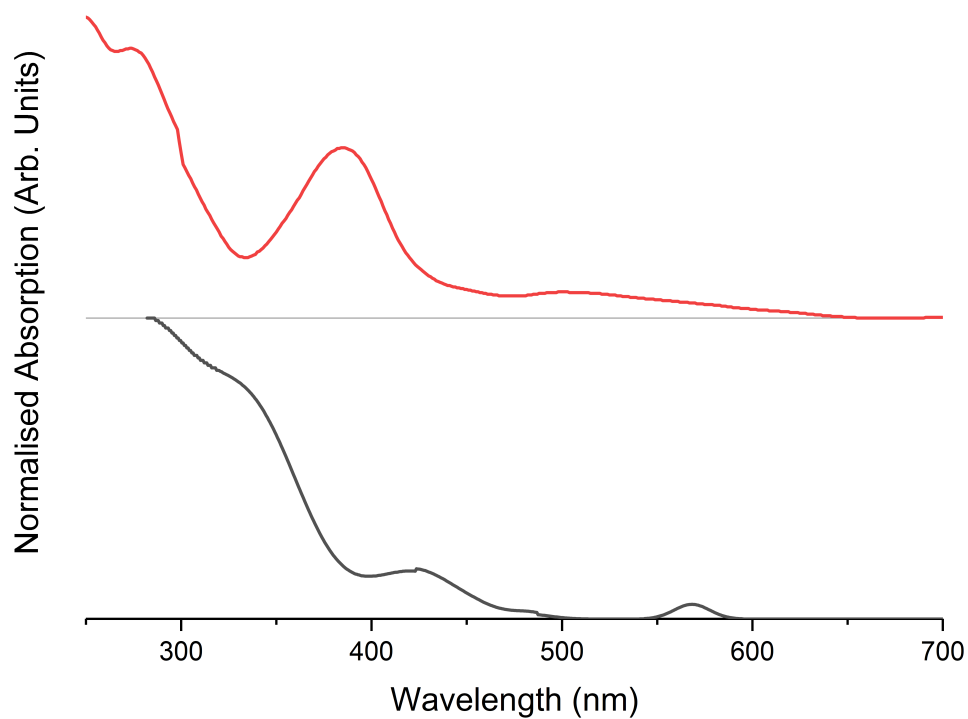
Table of contributions to each MO from each part of the Ir(L7)₂(pico) complex, L1 and L2 are the quinoxalines.

Excited State	Contributing Transitions
1 (434.13 nm, f = 0.0253)	HOMO → LUMO (88.4%)
2 (420.48 nm, f = 0.1668)	HOMO → LUMO +1 (82.89%)
3 (348.37 nm, f = 0.1302)	HOMO -3 → LUMO (54.66%) HOMO -1 → LUMO (19.6%)
4 (341.03 nm, f = 0.2244)	HOMO -2 → LUMO (27.17%) HOMO → LUMO (13.18%) HOMO → LUMO +1 (43.33%)
5 (336.66 nm, f = 0.3471)	HOMO -3 → LUMO (18.07%) HOMO -2 → LUMO (16.35%) HOMO -2 → LUMO +1 (24%) HOMO -1 → LUMO (21.64%)

First five singlet transitions of the Ir(L7)₂(pico) complex and a breakdown of their corresponding formative transitions.

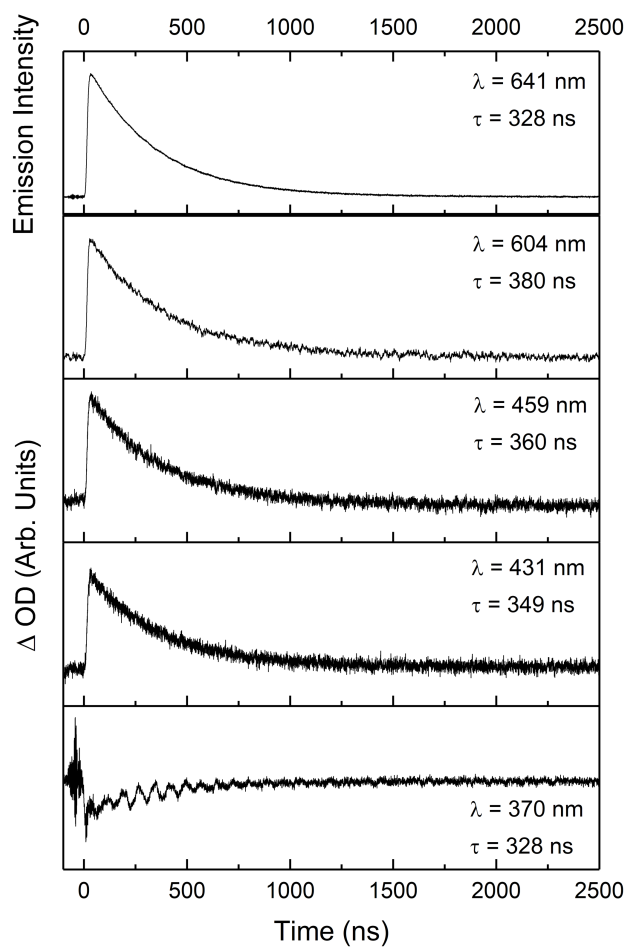
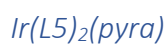


Renderings of the frontier MOs of the Ir(L7)₂(pico) complex.



Comparison of the experimental (red) and simulated (black) absorption spectra for Ir(L7)₂(pico). The simulated spectrum is comprised of singlet and triplet transitions from the singlet ground state.

Pyrazinate Complexes



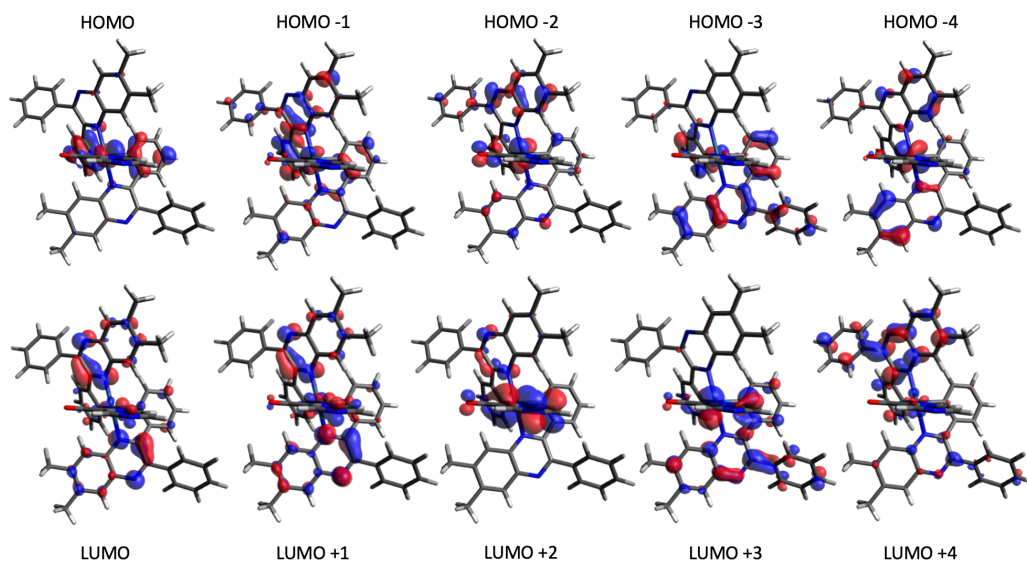
Kinetic traces of *Ir(L5)₂(pyra)* at major feature wavelengths, obtained with a PMT detector. The top trace is emission, whilst the bottom 4 are ΔOD . All traces were fitted to mono-exponential functions and the lifetimes determined are reported next to each trace.

Orbital	Ir (5d)	Pyrazine	L1	L2
LUMO +4	2	4	72	22
LUMO +3	1	34	8	57
LUMO +2	4	76	20	1
LUMO +1	3	14	35	48
LUMO	4	8	41	47
HOMO	37	4	31	28
HOMO -1	10	2	57	31
HOMO -2	31	11	36	22
HOMO -3	6	2	29	64
HOMO -4	29	4	27	40

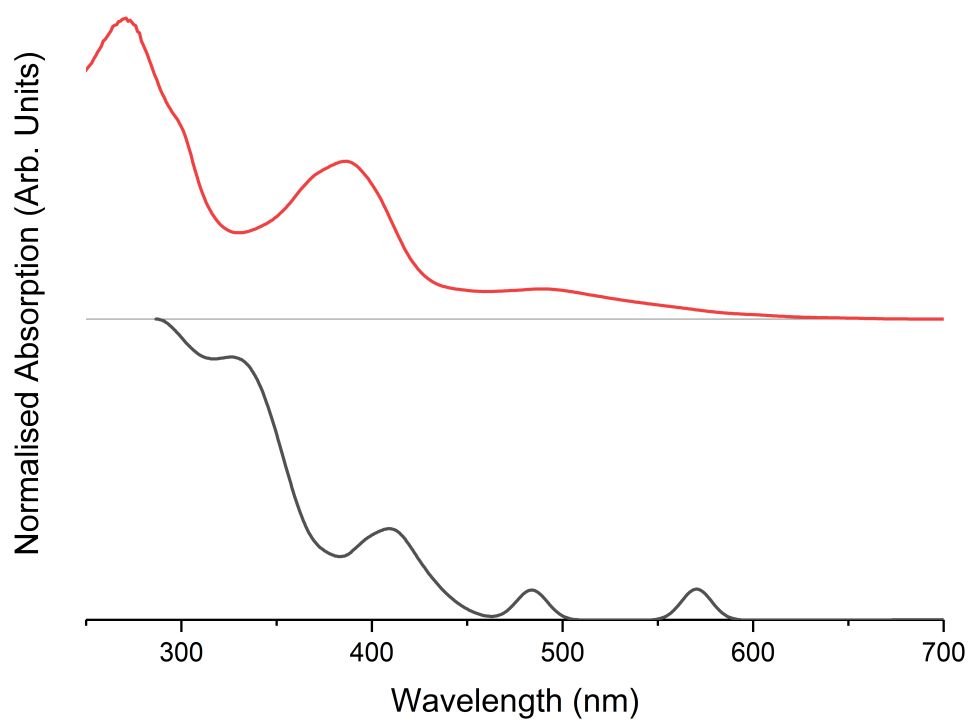
Table of contributions to each MO from each part of the Ir(L5)₂(pyra) complex, L1 and L2 are the quinoxalines

Excited State	Contributing Transitions
1 (421.51 nm, f = 0.032)	HOMO → LUMO (87.45%)
2 (408.15 nm, f = 0.2089)	HOMO → LUMO +1 (79.48%)
3 (349.39 nm, f = 0.0223)	HOMO → LUMO +2 (80.64%)
4 (342.61 nm, f = 0.0938)	HOMO -3 → LUMO (56.78%) HOMO -2 → LUMO (11.4%)
5 (336.78 nm, f = 0.2254)	HOMO -2 → LUMO (20.42%) HOMO -1 → LUMO (17.73%) HOMO -1 → LUMO +1 (30.27%)

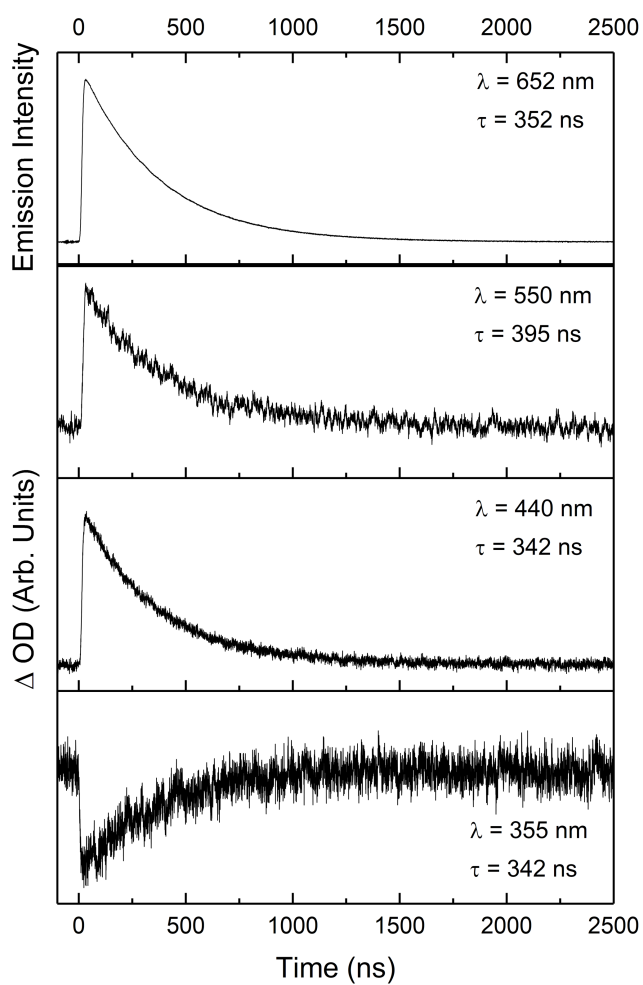
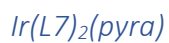
First five singlet transitions of the Ir(L5)₂(pyra) complex and a breakdown of their corresponding formative transitions.



Renderings of the frontier MOs of the Ir(L5)₂(pyra) complex



Comparison of the experimental (red) and simulated (black) absorption spectra for Ir(L5)₂(pyra). The simulated spectrum is comprised of singlet and triplet transitions from the singlet ground state.



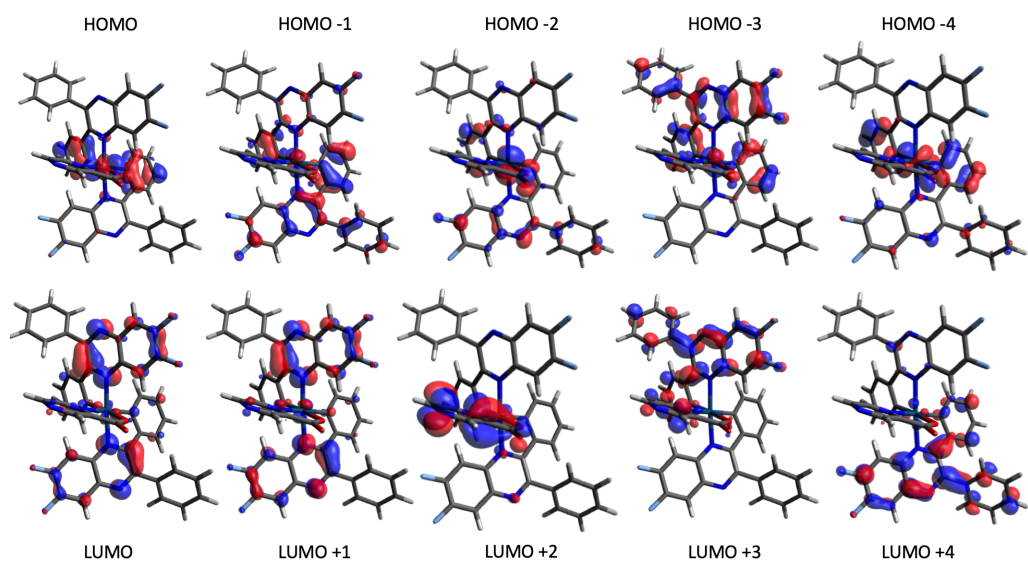
Kinetic traces of $\text{Ir(L7)}_2(\text{pyra})$ at major feature wavelengths, obtained with a PMT detector. The top trace is emission, whilst the bottom 3 are Δ OD. All traces were fitted to mono-exponential functions and the lifetimes determined are reported next to each trace.

Orbital	Ir (5d)	Pyrazine	L1	L2
LUMO +4	2	3	86	10
LUMO +3	1	16	6	77
LUMO +2	3	89	7	0
LUMO +1	4	4	46	46
LUMO	4	4	44	49
HOMO	37	4	31	28
HOMO -1	8	2	63	27
HOMO -2	32	12	31	25
HOMO -3	10	4	27	60
HOMO -4	23	10	38	29

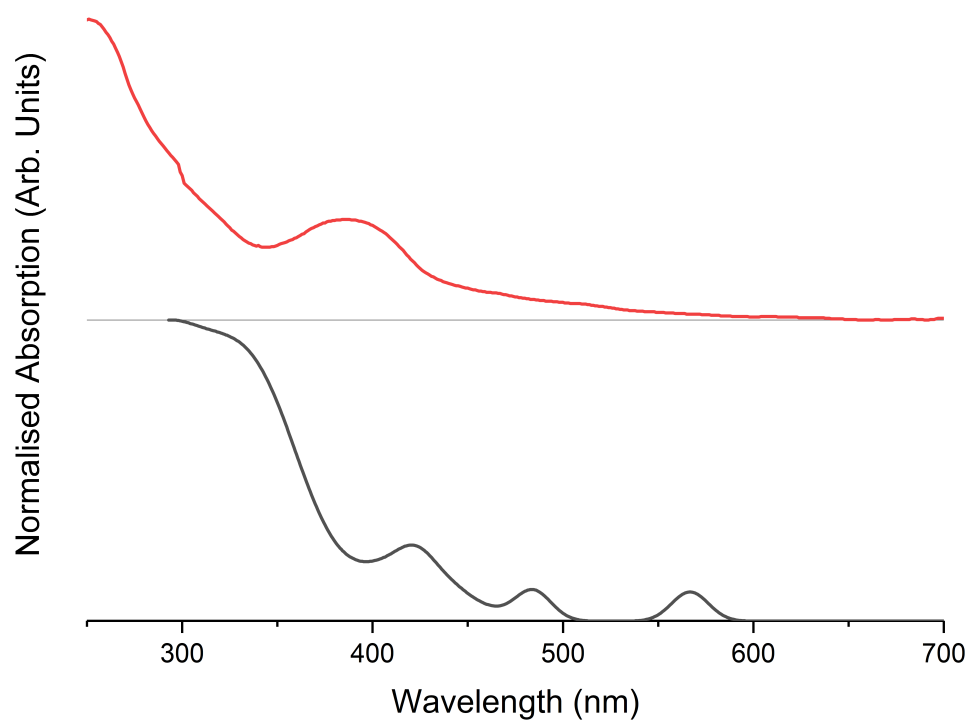
Table of contributions to each MO from each part of the Ir(L7)₂(pyra) complex, L1 and L2 are the quinoxalines.

Excited State	Contributing Transitions
1 (430.81 nm, f = 0.0248)	HOMO → LUMO (88.25%)
2 (416.68 nm, f = 0.1779)	HOMO → LUMO +1 (81.53%)
3 (344.58 nm, f = 0.1607)	HOMO -3 → LUMO (46.24%) HOMO -1 → LUMO (24.74%)
4 (343.25 nm, f = 0.1002)	HOMO -2 → LUMO (15.02%) HOMO -1 → LUMO +1 (19.47%) HOMO → LUMO +2 (50.87%)
5 (340.02 nm, f = 0.2894)	HOMO -2 → LUMO (12.85%) HOMO -1 → LUMO (11.89%) HOMO -1 → LUMO +1 (20.73%) HOMO → LUMO +2 (25.41%)

First five singlet transitions of the Ir(L7)₂(pyra) complex and a breakdown of their corresponding formative transitions.



Renderings of the frontier MOs of the Ir(L7)₂(pyra) complex



Comparison of the experimental (red) and simulated (black) absorption spectra for Ir(L7)₂(pyra). The simulated spectrum is comprised of singlet and triplet transitions from the singlet ground state.

Benzoquinoline Complexes

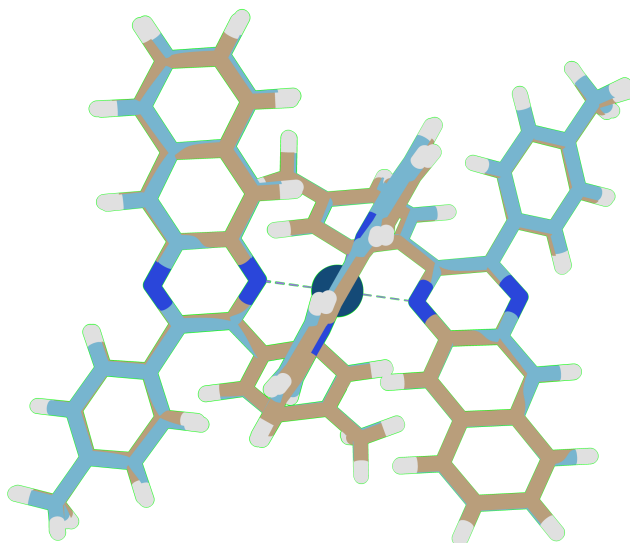
Ir(L9)₂(bpy)

Ir(L9)₂(bpy)	Moiety Contribution to Orbital (%)			
	Ir (5d)	Bipy	L1	L2
LUMO +4	2	10	44	44
LUMO +3	2	40	29	29
LUMO +2	2	96	1	1
LUMO +1	3	1	48	48
LUMO	3	2	47	48
HOMO	26	1	37	36
HOMO -1	4	1	47	48
HOMO -2	8	1	46	45
HOMO -3	1	0	49	50
HOMO -4	9	1	46	45

Ir(L9)₂(bpy) frontier orbital decomposition.

Orbital Contribution to Excited State	
Excited State	Contributing Transitions
1 (434.4 nm, f=0.0611)	HOMO -1 -> LUMO +1 (10.26%) HOMO -> LUMO (74.26%)
2 (428.05 nm, f=0.1761)	HOMO -1 -> LUMO (14.92%) HOMO -> LUMO +1 (66.58%)
3 (399.38 nm, f=0.2821)	HOMO -2 -> LUMO +1 (45.67%) HOMO -1 -> LUMO (38.68%)
4 (395.41 nm, f=0.0137)	HOMO -2 -> LUMO (53.18%) HOMO -1 -> LUMO +1 (32.99%)
5 (358.83 nm, f=0.1907)	HOMO -4 -> LUMO (40.01%) HOMO -3 -> LUMO +1 (34.33%)

Ir(L9)₂(bpy) first five excited singlet states.



Optimised Singlet (blue) and Triplet (brown) geometries of Ir(L9)₂(bpy), RMSD = 0.148 Å

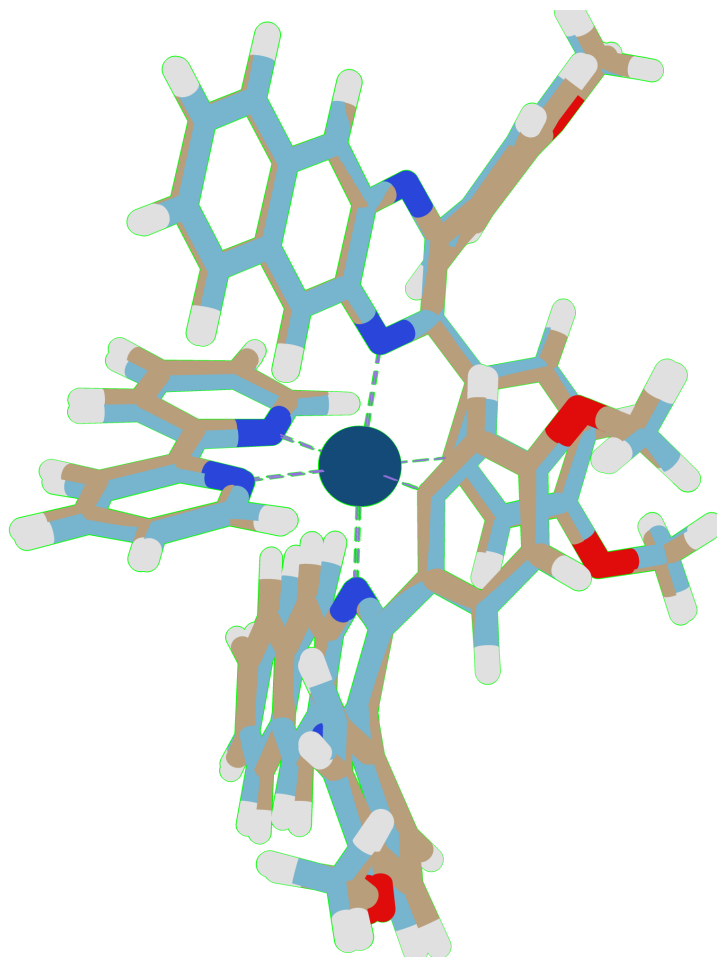
Ir(L10)₂(bpy)

Ir(L10)₂(bpy)	Moiety Contribution to Orbital (%)			
	Ir (5d)	Bipy	L1	L2
LUMO +4	1	16	44	39
LUMO +3	2	56	18	25
LUMO +2	2	96	1	1
LUMO +1	3	0	49	47
LUMO	3	2	47	49
HOMO	16	1	40	43
HOMO -1	5	1	49	45
HOMO -2	1	0	44	55
HOMO -3	0	0	55	45
HOMO -4	28	2	35	34

Ir(L10)₂(bpy) frontier orbital decomposition.

Excited State	Contributing Transitions
1 (427.75 nm, f=0.1508)	HOMO -1 -> LUMO +1 (22.26%) HOMO -> LUMO (64.51%)
2 (423.31 nm, f=0.3062)	HOMO -1 -> LUMO (32.99%) HOMO -> LUMO +1 (53.06%)
3 (397.48 nm, f=0.3685)	HOMO -3 -> LUMO (33.1%) HOMO -2 -> LUMO +1 (40.01%) HOMO -1 -> LUMO (12.58%)
4 (395.21 nm, f=0.0461)	HOMO -3 -> LUMO +1 (30.48%) HOMO -2 -> LUMO (48.42%) HOMO -1 -> LUMO +1 (10.92%)
5 (364.39 nm, f=0.1483)	HOMO -4 -> LUMO (41.34%) HOMO -1 -> LUMO +1 (21.54%)

$\text{Ir}(\text{L10})_2(\text{bpy})$ first five excited singlet states.



Optimised Singlet (blue) and triplet (brown) geometries for $\text{Ir}(\text{L10})_2(\text{bpy})$, RMSD = 0.149 Å

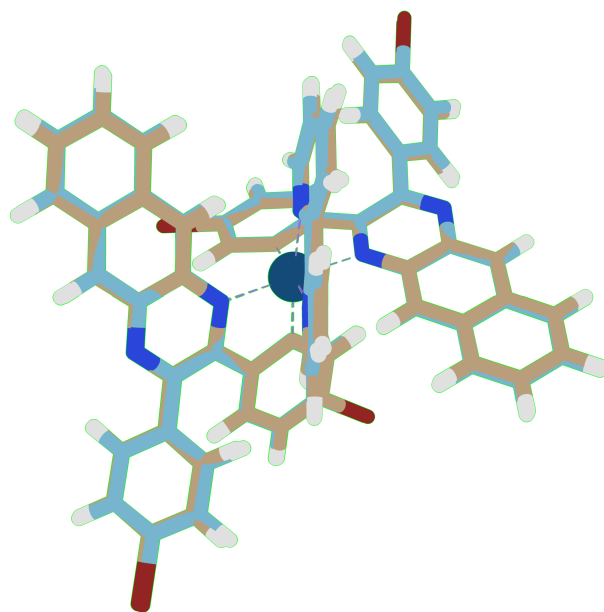
Ir(L11)₂(bpy)

Ir(L11)₂(bpy)	Moiety Contribution to Orbital (%)			
	Ir (5d)	Bipy	L1	L2
LUMO +4	2	4	35	60
LUMO +3	1	11	56	31
LUMO +2	2	97	1	1
LUMO +1	3	0	47	50
LUMO	3	1	49	46
HOMO	13	0	44	42
HOMO -1	3	1	47	49
HOMO -2	20	1	39	39
HOMO -3	1	0	50	49
HOMO -4	12	1	43	44

Ir(L11)₂(bpy) frontier orbital decomposition.

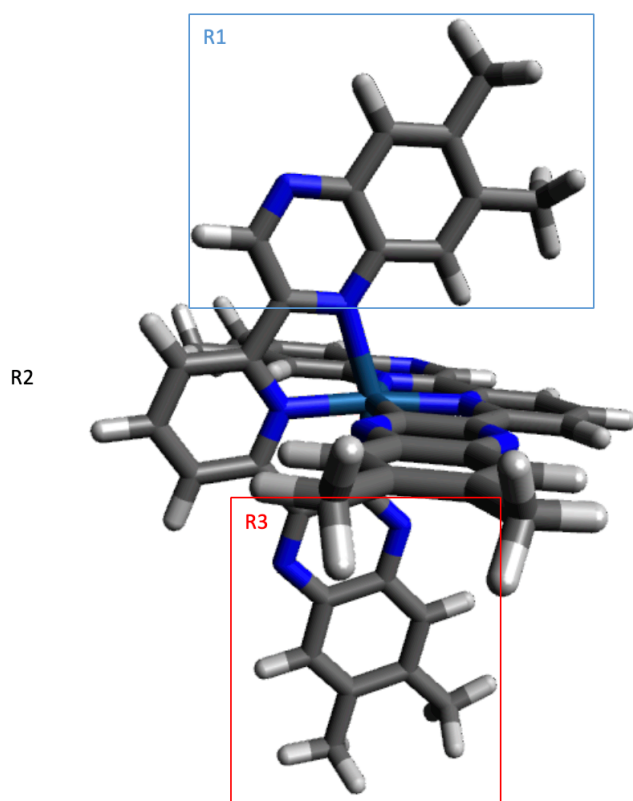
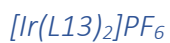
Orbital Contribution to Excited State	
Excited State	Contributing Transitions
1 (427.81 nm, f=0.0467)	HOMO -1 -> LUMO +1 (22.1%) HOMO -> LUMO (58.93%)
2 (423.85 nm, f=0.0492)	HOMO -1 -> LUMO (37.61%) HOMO -> LUMO +1 (50.87%)
3 (402.04 nm, f=0.4275)	HOMO -3 -> LUMO (12.9%) HOMO -2 -> LUMO +1 (57.52%) HOMO -1 -> LUMO (14.9%)
4 (400.92 nm, f=0.0656)	HOMO -2 -> LUMO (57.21%) HOMO -1 -> LUMO +1 (20.51%)
5 (352.76 nm, f=0.1948)	HOMO -4 -> LUMO (37.09%) HOMO -3 -> LUMO +1 (31.69%)

Ir(L11)₂(bpy) first five singlet excited states



Optimised singlet (blue) and triplet (brown) geometries for Ir(L11)₂(bpy), RMSD = 0.185 Å

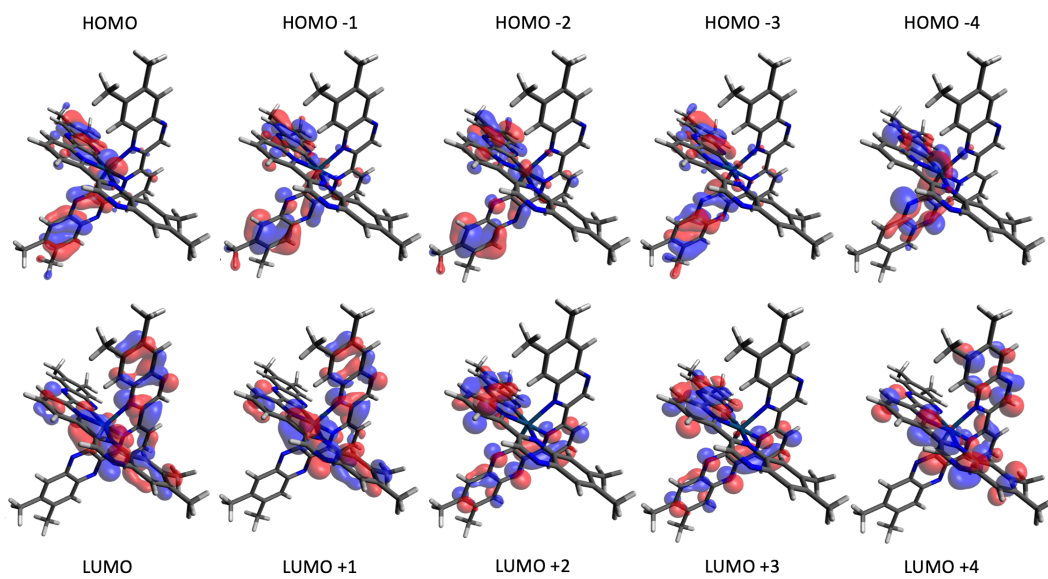
Diquinoxaline-Pyridinyl Complexes



$[Ir(L13)_2]$ with the orbital contributing moieties highlighted for one ligand.

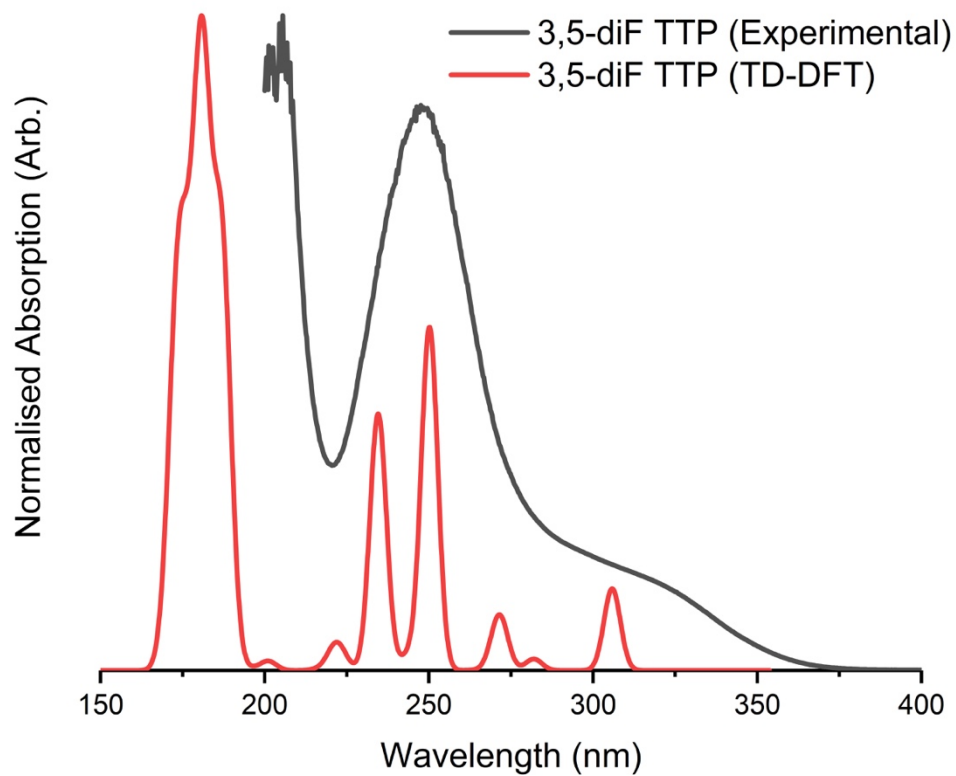
$[Ir(L13)_2]$	Ir (5d) (%)	Q1 R1 (%)	Q1 R2 (%)	Q1 R3 (%)	Q2 R1 (%)	Q2 R2 (%)	Q2 R3 (%)
LUMO +4	1	34	16	0	33	15	0
LUMO +3	1	0	22	27	0	22	27
LUMO +2	1	1	20	29	1	20	29
LUMO +1	4	40	12	0	33	10	0
LUMO	4	31	11	1	39	14	1
HOMO	26	2	3	32	2	3	32
HOMO -1	4	2	4	40	2	5	43
HOMO -2	6	1	5	42	1	5	39
HOMO -3	2	2	4	42	2	4	42
HOMO -4	8	2	1	43	2	1	42

$[Ir(L13)_2]$ frontier orbital decomposition



Rendered frontier orbitals for Ir(L13)₂

Inhibiting the Photoreductive Pathway of 2,3,5-Triphenyltetrazolium via Selective Substitution



Normalised UV-Vis absorption spectrum of 3,5-diF TTP in acetonitrile (100 μ M). The TD-DFT derived spectrum is also displayed.

Bibliography

- 1 W.-K. Hu, S.-H. Li, X.-F. Ma, S.-X. Zhou, Q. Zhang, J.-Y. Xu, P. Shi, B.-H. Tong, M.-K. Fung and L. Fu, *Dyes Pigments*, 2018, **150**, 284–292.
- 2 A. Sinopoli, C. J. Wood, E. A. Gibson and P. I. P. Elliott, *Dyes Pigments*, 2017, **140**, 269–277.
- 3 J. Sun, W. Wu, H. Guo and J. Zhao, *Eur. J. Inorg. Chem.*, 2011, **2011**, 3165–3173.
- 4 S. Koseki, D. G. Fedorov, M. W. Schmidt and M. S. Gordon, *J. Phys. Chem. A*, 2001, **105**, 8262–8268.
- 5 A. R. G. Smith, P. L. Burn and B. J. Powell, *ChemPhysChem*, 2011, **12**, 2429–2438.
- 6 D.-L. Ma, S. Lin, W. Wang, C. Yang and C.-H. Leung, *Chem. Sci.*, 2017, **8**, 878–889.
- 7 F. Gärtner, D. Cozzula, S. Losse, A. Boddien, G. Anilkumar, H. Junge, T. Schulz, N. Marquet, A. Spannenberg, S. Gladiali and M. Beller, *Chem. - Eur. J.*, 2011, **17**, 6998–7006.
- 8 F. Gärtner, S. Denurra, S. Losse, A. Neubauer, A. Boddien, A. Gopinathan, A. Spannenberg, H. Junge, S. Lochbrunner, M. Blug, S. Hoch, J. Busse, S. Gladiali and M. Beller, *Chem. – Eur. J.*, 2012, **18**, 3220–3225.
- 9 N. D. McDaniel, F. J. Coughlin, L. L. Tinker and S. Bernhard, *J. Am. Chem. Soc.*, 2008, **130**, 210–217.
- 10 M. Li, K. Takada, J. I. Goldsmith and S. Bernhard, *Inorg. Chem.*, 2016, **55**, 518–526.
- 11 P. N. Curtin, L. L. Tinker, C. M. Burgess, E. D. Cline and S. Bernhard, *Inorg. Chem.*, 2009, **48**, 10498–10506.
- 12 H. Huo, X. Shen, C. Wang, L. Zhang, P. Röse, L.-A. Chen, K. Harms, M. Marsch, G. Hilt and E. Meggers, *Nature*, 2014, **515**, 100–103.
- 13 E. Meggers, *Chem. Commun.*, 2015, **51**, 3290–3301.
- 14 W.-J. Xu, S.-J. Liu, X.-Y. Zhao, S. Sun, S. Cheng, T.-C. Ma, H.-B. Sun, Q. Zhao and W. Huang, *Chem. – Eur. J.*, 2010, **16**, 7125–7133.
- 15 R. Yao, D. Liu, Y. Mei and R. Dong, *J. Photochem. Photobiol. Chem.*, 2018, **355**, 136–140.
- 16 M. Chen, L.-D. Wang, Y. Wang, Y.-Y. Zhou, C.-G. Hu, B.-H. Tong, Z.-Q. Bian, L. Fu, Q.-F. Zhang and P. Wang, *Org. Electron.*, 2019, **75**, 105439.
- 17 Y.-Y. Hu, W. Luo, Y. Wang, B.-H. Tong, M.-K. Fung and Q.-F. Zhang, *Inorganica Chim. Acta*, 2019, 119168.
- 18 Q.-Y. Mei, M. Chen, J. Shu, S.-X. Zhou, B.-H. Tong, M.-K. Fung and S. Wang, *Inorganica Chim. Acta*, 2019, **495**, 118942.
- 19 N. Su, C.-Z. Shen and Y.-X. Zheng, *J. Organomet. Chem.*, 2019, **896**, 188–193.
- 20 Y.-H. Zhou, D. Jiang and Y.-X. Zheng, *J. Organomet. Chem.*, 2018, **876**, 26–34.
- 21 V. V. Grushin, N. Herron, D. D. LeCloux, W. J. Marshall, V. A. Petrov and Y. Wang, *Chem. Commun.*, 2001, 1494–1495.
- 22 I. R. Laskar and T.-M. Chen, *Chem. Mater.*, 2004, **16**, 111–117.
- 23 P. Coppo, E. A. Plummer and L. D. Cola, *Chem. Commun.*, 2004, 1774–1775.
- 24 Q. Zhao, M. Yu, L. Shi, S. Liu, C. Li, M. Shi, Z. Zhou, C. Huang and F. Li, *Organometallics*, 2010, **29**, 1085–1091.
- 25 T. Huang, Q. Yu, S. Liu, K. Y. Zhang, W. Huang and Q. Zhao, *ChemBioChem*, 2019, **20**, 576–586.
- 26 F.-M. Hwang, H.-Y. Chen, P.-S. Chen, C.-S. Liu, Y. Chi, C.-F. Shu, F.-I. Wu, P.-T. Chou, S.-M. Peng and G.-H. Lee, *Inorg. Chem.*, 2005, **44**, 1344–1353.

- 27 T.-Y. Li, J. Wu, Z.-G. Wu, Y.-X. Zheng, J.-L. Zuo and Y. Pan, *Coord. Chem. Rev.*, 2018, **374**, 55–92.
- 28 L. Lopez Del Egado, D. Navarro-Miró, V. Martinez-Heredia, P. E. Toorop and P. P. M. Iannetta, *Front. Plant Sci.*, 2017, **8**, 747, DOI:10.3389/fpls.2017.00747.
- 29 M. H. Olesen, P. Nikneshan, S. Shrestha, A. Tadayyon, L. C. Deleuran, B. Boelt and R. Gislum, *Sensors*, 2015, **15**, 4592–4604.
- 30 J. C. Stockert, A. Blázquez-Castro, M. Cañete, R. W. Horobin and Á. Villanueva, *Acta Histochem.*, 2012, **114**, 785–796.
- 31 F. M. Young, W. Phungtamdet and B. J. S. Sanderson, *Toxicol. In Vitro*, 2005, **19**, 1051–1059.
- 32 M. M. Nociari, A. Shalev, P. Benias and C. Russo, *J. Immunol. Methods*, 1998, **213**, 157–167.
- 33 H. Wang, H. Cheng, F. Wang, D. Wei and X. Wang, *J. Microbiol. Methods*, 2010, **82**, 330–333.
- 34 E. Severin, J. Stellmach and H.-M. Nachtigal, *Anal. Chim. Acta*, 1985, **170**, 341–346.
- 35 V. V. Minin, V. M. Ostrovskaya, V. V. Avdeeva, E. A. Ugolkova and D. O. Shchepilov, *Talanta*, 2019, **195**, 599–603.
- 36 F. A. Neugebauer, *Tetrahedron Lett.*, 1968, **9**, 2129–2132.
- 37 F. A. Neugebauer and G. A. Russell, *J. Org. Chem.*, 1968, **33**, 2744–2746.
- 38 *Global Aspects of Atmospheric Chemistry*, Springer Science & Business Media, 1999.
- 39 D. E. Heard, L. J. Carpenter, D. J. Creasey, J. R. Hopkins, J. D. Lee, A. C. Lewis, M. J. Pilling, P. W. Seakins, N. Carslaw and K. M. Emmerson, *Geophys. Res. Lett.*, 2004, **31**, L18112.
- 40 R. M. Harrison, J. Yin, R. M. Tilling, X. Cai, P. W. Seakins, J. R. Hopkins, D. L. Lansley, A. C. Lewis, M. C. Hunter, D. E. Heard, L. J. Carpenter, D. J. Creasey, J. D. Lee, M. J. Pilling, N. Carslaw, K. M. Emmerson, A. Redington, R. G. Derwent, D. Ryall, G. Mills and S. A. Penkett, *Sci. Total Environ.*, 2006, **360**, 5–25.
- 41 R. Sommariva, M. J. Pilling, W. J. Bloss, D. E. Heard, J. D. Lee, Z. L. Fleming, P. S. Monks, J. M. C. Plane, A. Saiz-Lopez, S. M. Ball, M. Bitter, R. L. Jones, N. Brough, S. A. Penkett, J. R. Hopkins, A. C. Lewis and K. A. Read, *Atmos Chem Phys*, 2007, **7**, 587–598.
- 42 Z. Rao, Z. Chen, H. Liang, L. Huang and D. Huang, *Atmos. Environ.*, 2016, **124**, 207–216, DOI:10.1016/j.atmosenv.2015.06.050.
- 43 W. Armerding, F. J. Comes and B. Schuelke, *J. Phys. Chem.*, 1995, **99**, 3137–3143.
- 44 M. C. McCarthy, V. Lattanzi, D. Kokkin, O. Martinez and J. F. Stanton, *J. Chem. Phys.*, 2012, **136**, 034303.
- 45 T. Gherman, D. S. Venables, S. Vaughan, J. Orphal and A. A. Ruth, *Environ. Sci. Technol.*, 2008, **42**, 890–895.
- 46 T. Wu, W. Chen, E. Fertein, F. Cazier, D. Dewaele and X. Gao, *Appl. Phys. B*, 2012, **106**, 501–509.
- 47 C. Jain, P. Morajkar, C. Schoemaeker, B. Viskolcz and C. Fittschen, *J. Phys. Chem. A*, 2011, **115**, 10720–10728.
- 48 S. A. Nizkorodov and P. O. Wennberg, *J. Phys. Chem. A*, 2002, **106**, 855–859.
- 49 B. D. Bean, A. K. Mollner, S. A. Nizkorodov, G. Nair, M. Okumura, S. P. Sander, K. A. Peterson and J. S. Francisco, *J. Phys. Chem. A*, 2003, **107**, 6974–6985.

- 50 R. A. Washenfelder, N. L. Wagner, W. P. Dube and S. S. Brown, *Environ. Sci. Technol.*, 2011, **45**, 2938–2944.
- 51 Y. Liu and J. Zhang, *Anal. Chem.*, 2014, **86**, 5391–5398.
- 52 M. Becker, N. Andersen, B. Fiedler, P. Fietzek, A. Körtzinger, T. Steinhoff and G. Friedrichs, *Limnol. Oceanogr. Methods*, 2012, **10**, 752–766.
- 53 K. K. Lehmann, G. Berden and R. Engeln, in *Cavity Ring-Down Spectroscopy*, eds. G. Berden and R. Engeln, John Wiley & Sons, Ltd, 2009, pp. 1–26.
- 54 M. Li, H. Zeng, Y. Meng, H. Sun, S. Liu, Z. Lu, Y. Huang and X. Pu, *Dalton Trans.*, 2011, **40**, 7153–7164.
- 55 F.-Q. Bai, J. Wang, B.-H. Xia, Q.-J. Pan and H.-X. Zhang, *Dalton Trans.*, 2012, **41**, 8441.
- 56 Z.-F. Xie, F.-Q. Bai, J. Wang and H.-X. Zhang, *Mol. Phys.*, 2011, **109**, 1657–1675.
- 57 J. Wang, F.-Q. Bai, B.-H. Xia and H.-X. Zhang, *J. Phys. Chem. A*, 2011, **115**, 11689–11695.
- 58 G.-N. Li, Y. Zou, Y.-D. Yang, J. Liang, F. Cui, T. Zheng, H. Xie and Z.-G. Niu, *J. Fluoresc.*, 2014, **24**, 1545–1552.
- 59 N. Zhao, Y.-H. Wu, R.-M. Wang, L.-X. Shi and Z.-N. Chen, *The Analyst*, 2011, **136**, 2277.
- 60 L. Shi, B. Hong, W. Guan, Z. Wu and Z. Su, *J. Phys. Chem. A*, 2010, **114**, 6559–6564.
- 61 M. Kasha, *Discuss. Faraday Soc.*, 1950, **9**, 14–19.
- 62 B. A. Thrush, *Photochem. Photobiol. Sci.*, 2003, **2**, 453–454.
- 63 R. G. W. Norrish and G. Porter, *Discuss. Faraday Soc.*, 1947, **2**, 97–104.
- 64 R. G. W. Norrish and G. Porter, *Nature*, 1949, **164**, 658–658.
- 65 R. G. W. Norrish and G. Porter, *Proc. R. Soc. Lond. Ser. Math. Phys. Sci.*, 1952, **210**, 439–460.
- 66 R. G. W. Norrish, G. Porter and B. A. Thrush, *Nature*, 1953, **172**, 71–72.
- 67 G. Porter and M. R. Topp, *Proc. R. Soc. Lond. Math. Phys. Sci.*, 1970, **315**, 163–184.
- 68 T. Yanai, D. P. Tew and N. C. Handy, *Chem. Phys. Lett.*, 2004, **393**, 51–57.
- 69 A. D. Becke, *Phys. Rev. A*, 1988, **38**, 3098–3100.
- 70 C. Lee, W. Yang and R. G. Parr, *Phys. Rev. B*, 1988, **37**, 785–789.
- 71 T. Asada, S. Hamamura, T. Matsushita and S. Koseki, *Res. Chem. Intermed.*, 2009, **35**, 851–863.
- 72 H.-H. Kuo, Z. Zhu, C.-S. Lee, Y.-K. Chen, S.-H. Liu, P.-T. Chou, A. K.-Y. Jen and Y. Chi, *Adv. Sci.*, 2018, **5**, 1800846.
- 73 A. C. Jacko, B. J. Powell and R. H. McKenzie, *J. Chem. Phys.*, 2010, **133**, 124314.
- 74 S. Ladouceur and E. Zysman-Colman, *Eur. J. Inorg. Chem.*, **2013**, 2985–3007.
- 75 Y. Kawamura, K. Goushi, J. Brooks, J. J. Brown, H. Sasabe and C. Adachi, *Appl. Phys. Lett.*, 2005, **86**, 071104.
- 76 S. Lamansky, P. Djurovich, D. Murphy, F. Abdel-Razzaq, H.-E. Lee, C. Adachi, P. E. Burrows, S. R. Forrest and M. E. Thompson, *J. Am. Chem. Soc.*, 2001, **123**, 4304–4312.
- 77 Y. Ohsawa, S. Sprouse, K. A. King, M. K. DeArmond, K. W. Hanck and R. J. Watts, *J. Phys. Chem.*, 1987, **91**, 1047–1054.
- 78 Y. You and S. Y. Park, *J. Am. Chem. Soc.*, 2005, **127**, 12438–12439.
- 79 G. A. Carlson, P. I. Djurovich and R. J. Watts, *Inorg. Chem.*, 1993, **32**, 4483–4484.
- 80 S. Lamansky, P. Djurovich, D. Murphy, F. Abdel-Razzaq, R. Kwong, I. Tsyba, M. Bortz, B. Mui, R. Bau and M. E. Thompson, *Inorg. Chem.*, 2001, **40**, 1704–1711.

- 81 F. O. Garces, K. A. King and R. J. Watts, *Inorg. Chem.*, 1988, **27**, 3464–3471.
- 82 Q. Yang, H. Jin, Y. Gao, J. Lin, H. Yang and S. Yang, *ACS Appl. Mater. Interfaces*, 2019, **11**, 15417–15425.
- 83 C. Yang, F. Mehmood, T. L. Lam, S. L.-F. Chan, Y. Wu, C.-S. Yeung, X. Guan, K. Li, C. Y.-S. Chung, C.-Y. Zhou, T. Zou and C.-M. Che, *Chem. Sci.*, 2016, **7**, 3123–3136.
- 84 S. Schmidbauer, A. Hohenleutner and B. König, *Beilstein J. Org. Chem.*, 2013, **9**, 2088–2096.
- 85 T. Keane, T. W. Rees, E. Baranoff and B. F. E. Curchod, *J. Mater. Chem. C*, 2019, **7**, 6564–6570.
- 86 F. Kanal, D. Schleier and P. Nuernberger, *ChemPhysChem*, 2015, **16**, 3143–3146.
- 87 A. W. Nineham, *Chem. Rev.*, 1955, **55**, 355–483.
- 88 T. Bolze, J.-L. Wree, F. Kanal, D. Schleier and P. Nuernberger, *ChemPhysChem*, 2018, **19**, 138–147.
- 89 M. C. Gonzalez and E. San Roman, *J. Phys. Chem.*, 1989, **93**, 3536–3540.
- 90 K. Umemoto, *Bull. Chem. Soc. Jpn.*, 1985, **58**, 2051–2055.
- 91 F. B. Mallory and C. W. Mallory, *J. Org. Chem.*, 1983, **48**, 526–532.
- 92 A. O’Keefe, J. B. Paul, R. J. Saykally and J. J. Scherer, *Chem Rev*, 1997, **1**, 25–52.
- 93 B. A. Paldus and A. A. Kachanov, *Can. J. Phys.*, 2005, **83**, 975–999.
- 94 J. Altmann, R. Baumgart and C. Weitkamp, *Appl. Opt.*, 1981, **20**, 995–999.
- 95 J. A. Silver, *Appl. Opt.*, 2005, **44**, 6545–6556.
- 96 R. Chhantyal-Pun, A. Davey, D. E. Shallcross, C. J. Percival and A. J. Orr-Ewing, *Phys. Chem. Chem. Phys.*, 2015, **17**, 3617–3626.
- 97 M. A. H. Khan, C. J. Percival, R. L. Caravan, C. A. Taatjes and D. E. Shallcross, *Environ. Sci. Process. Impacts*, 2018, **20**, 437–453, DOI:10.1039/C7EM00585G.
- 98 D. Johnson and G. Marston, *Chem. Soc. Rev.*, 2008, **37**, 699–716.
- 99 N. M. Donahue, J. H. Kroll, J. G. Anderson and K. L. Demerjian, *Geophys. Res. Lett.*, 1998, **25**, 59–62.
- 100 M. Kanakidou, J. H. Seinfeld, S. N. Pandis, I. Barnes, F. J. Dentener, M. C. Facchini, R. V. Dingenen, B. Ervens, A. Nenes, C. J. Nielsen, E. Swietlicki, J. P. Putaud, Y. Balkanski, S. Fuzzi, J. Horth, G. K. Moortgat, R. Winterhalter, C. E. L. Myhre, K. Tsigaridis, E. Vignati, E. G. Stephanou and J. Wilson, *Atmospheric Chem. Phys.*, 2005, **5**, 1053–1123.
- 101 M. Hallquist, J. C. Wenger, U. Baltensperger, Y. Rudich, D. Simpson, M. Claeys, J. Dommen, N. M. Donahue, C. George, A. H. Goldstein, J. F. Hamilton, H. Herrmann, T. Hoffmann, Y. Iinuma, M. Jang, M. E. Jenkin, J. L. Jimenez, A. Kiendler-Scharr, W. Maenhaut, G. McFiggans, T. F. Mentel, A. Monod, A. S. H. Prévôt, J. H. Seinfeld, J. D. Surratt, R. Szmigielski and J. Wildt, *Atmospheric Chem. Phys.*, 2009, **9**, 5155–5236.
- 102 J. M. Beames, F. Liu, L. Lu and M. I. Lester, *J. Chem. Phys.*, 2013, **138**, 244307.
- 103 H.-Y. Lin, Y.-H. Huang, X. Wang, J. M. Bowman, Y. Nishimura, H. A. Witek and Y.-P. Lee, *Nat. Commun.*, 2015, **6**, 7012.
- 104 O. Welz, J. D. Savee, D. L. Osborn, S. S. Vasu, C. J. Percival, D. E. Shallcross and C. A. Taatjes, *Science*, 2012, **335**, 204–207.
- 105 D. Stone, M. Blitz, L. Daubney, T. Ingham and P. Seakins, *Phys. Chem. Chem. Phys.*, 2013, **15**, 19119–19124.
- 106 J. B. Leen and A. O’Keefe, *Rev. Sci. Instrum.*, 2014, **85(9)**, 093101, DOI:10.1063/1.4893972.

- 107K. A. Phillips, T. M. Stonelake, K. Chen, Y. Hou, J. Zhao, S. J. Coles, P. N. Horton, S. J. Keane, E. C. Stokes, I. A. Fallis, A. J. Hallett, S. P. O’Kell, J. M. Beames and S. J. A. Pope, *Chem. – Eur. J.*, 2018, **24**, 8577–8588.
- 108K. A. Phillips, T. M. Stonelake, P. N. Horton, S. J. Coles, A. J. Hallett, S. P. O’Kell, J. M. Beames and S. J. A. Pope, *J. Organomet. Chem.*, 2019, **893**, 11–20.
- 109T. M. Stonelake, K. A. Phillips, H. Y. Otaif, Z. C. Edwardson, P. N. Horton, S. J. Coles, J. M. Beames and S. J. A. Pope, *Inorg. Chem.*, 2020, **59**, 2266–2277.